Étude des performances mécaniques et de la résistance à la corrosion des joints soudés laser entre alliages Ti6Al4V et AA7075 avec couches intermédiaires d'argent et de cuivre pour des applications aérospatiales

Thèse présentée

dans le cadre du programme de doctorat en ingénierie (3737)

en vue de l'obtention du grade de Philosophiae doctor (Ph.D.)

PAR

© Asim Iltaf

Mai 2025

Composition du jury :

Abderrazak El Ouafi, président du jury, Université du Québec à Rimouski, UQAR

Noureddine Barka, directeur de recherche, Université du Québec à Rimouski, UQAR

Jacopo Profili, examinateur, Université du Québec à Rimouski, UQAR

Ayoub Tanji, examinateur externe, Centre de métallurgie du Québec - CMQ

Dépôt initial le 17 décembre 2024 Dépôt final le 27 mai 2025

À ma mère, mon père et mes sœurs, à vous qui êtes toujours à mes côtés et dans mon cœur, même si des milliers de kilomètres nous séparent, je pense à vous chaque jour et vous garde près de moi.

REMERCIEMENTS

Je voudrais avant tout exprimer ma profonde reconnaissance à Dieu le Tout-Puissant, qui m'a donné la force, la patience et la santé nécessaires pour mener à bien cette thèse de doctorat.

Je tiens également à exprimer toute ma gratitude à mon directeur de thèse, monsieur Noureddine Barka, dont le soutien indéfectible et la disponibilité constante ont été des éléments cruciaux tout au long de ce projet. Il a su être présent à chaque étape, me guidant avec une approche méthodique et rigoureuse qui a permis de structurer mes recherches de manière efficace. Ses conseils avisés, toujours empreints de pertinence et de clarté, m'ont non seulement aidé à surmonter les obstacles rencontrés, mais ont également enrichi ma réflexion et orienté mes travaux vers des résultats de qualité. Sans son aide précieuse, ses encouragements constants et ses orientations éclairées, cette thèse n'aurait jamais pu atteindre le niveau d'aboutissement que je présente aujourd'hui. Son expertise et son engagement ont été pour moi une source d'inspiration tout au long de ce parcours.

Je tiens également à exprimer ma reconnaissance aux membres du jury. Tout d'abord, je remercie monsieur Abderrazak El Ouafi, professeur à l'Université du Québec à Rimouski (UQAR), d'avoir accepté de présider le jury de cette thèse. Je suis également profondément reconnaissant envers monsieur Jacopo Profili, professeur à l'Université du Québec à Rimouski (UQAR), pour sa participation au jury. Enfin, je remercie monsieur Ayoub Tanji, chercheur au Centre de métallurgie du Québec, d'avoir accepté d'agir en tant qu'évaluateur externe de ma thèse.

Je tiens également à exprimer ma profonde reconnaissance envers l'organisation Mitacs, dont le soutien financier a été essentiel pour la réalisation de cette thèse. Grâce à leur aide, j'ai pu approfondir mes recherches sur le soudage et l'assemblage de matériaux

dissemblables, un domaine complexe et crucial pour les applications industrielles avancées. Leur contribution m'a permis de développer de nouvelles compétences et d'explorer des solutions innovantes dans ce domaine.

Je tiens particulièrement à remercier monsieur Claude Belzile (Institut des Sciences de la Mer de Rimouski) pour son aide précieuse tout au long de mon séjour à l'UQAR. Je tiens également à exprimer ma gratitude au personnel du Département de mathématiques, d'informatique et de génie pour leur soutien notamment Karel, Suzie et Richard. Je remercie également madame Farrah Fiset. Enfin, je remercie du fond du cœur ma famille et mes amis, sans qui cette réalisation n'aurait pas été possible.

RÉSUMÉ

Dans les applications d'ingénierie avancées, notamment dans les secteurs aérospatial et automobile, la demande pour des structures légères offrant de hautes performances mécaniques a conduit à l'intégration d'alliages métalliques dissemblables. L'assemblage de matériaux tels que l'aluminium et le titane permet de tirer parti de leurs propriétés respectives : la faible densité de l'aluminium et la résistance élevée ainsi que la résistance à la corrosion du titane. Toutefois, l'assemblage de ces alliages dissemblables pose d'importants défis métallurgiques, principalement en raison de la formation de composés intermétalliques (IMC) fragiles à l'interface, ce qui dégrade l'intégrité des joints.

Pour relever ces défis, l'utilisation de matériaux intercalaires insérés entre les alliages de base lors du soudage a été proposée comme stratégie efficace. Les intercalaires peuvent modifier le chemin de solidification et la diffusion élémentaire à travers l'interface, contrôlant ainsi la formation et la morphologie des IMC. Le choix d'un intercalaire approprié est crucial ; il doit non seulement agir comme une barrière de diffusion, mais aussi améliorer la compatibilité mécanique et chimique entre les métaux de base. Dans ce contexte, l'argent (Ag) et le cuivre (Cu), tous deux connus pour leur haute conductivité thermique et électrique, sont des candidats potentiels. Leurs interactions métallurgiques avec l'aluminium et le titane sont différentes, offrant ainsi des voies distinctes pour optimiser la microstructure et les propriétés des joints. De plus, le soudage laser, grâce à sa haute précision et son apport d'énergie localisé, s'est imposé comme une technique prometteuse pour ces applications.

La présente recherche se concentre sur le soudage laser de l'alliage d'aluminium AA7075 et de l'alliage de titane Ti6Al4V en utilisant des intercalaires en Ag et en Cu commercialement disponibles (pureté de 99,9 %, fournis par McMaster-Carr). Les deux intercalaires ont été appliqués sous forme de feuilles minces (380 μm), et les paramètres de

soudage ont été optimisés pour tenir compte des différences de conductivité thermique et de comportement à la fusion. L'étude vise à évaluer et comparer les effets de ces intercalaires sur la microstructure du joint, sa performance mécanique, sa résistance à la corrosion et son comportement au fluage à l'échelle nanométrique. La microscopie optique et la microscopie électronique à balayage (MEB) ont été utilisées pour examiner la morphologie des grains et la distribution des phases. Des tests de microdureté et de nanoindentation ont permis d'analyser les gradients mécaniques dans les soudures, tandis que le comportement au fluage à l'échelle nanométrique a été évalué par des essais de fluage par nanoindentation à profondeur contrôlée. La résistance à la corrosion a été analysée par spectroscopie d'impédance électrochimique (EIS), polarisation cyclique et tests potentiodynamiques.

Des différences significatives ont été observées quant à l'effet des intercalaires Ag et Cu sur les caractéristiques des joints. L'intercalaire en Ag s'est révélé particulièrement efficace pour supprimer la formation de composés intermétalliques fragiles du type Al_3Ti et $TiAl_3$ dans la zone fondue (zone de fusion formée par le soudage). Cela a contribué à une microstructure plus homogène et plus fine, améliorant la stabilité mécanique. En revanche, l'intercalaire en Cu a réduit les interactions aluminium–titane, mais a favorisé la formation d'IMC à base de cuivre, tels que Cu_3Ti_2. Bien que cela ait renforcé la résistance mécanique locale, cela a également introduit une certaine fragilité localisée.

Sur le plan des performances mécaniques, les joints avec intercalaire Ag ont présenté des valeurs de microdureté plus élevées dans la zone fondue que ceux avec intercalaire Cu. La dureté la plus élevée a été enregistrée dans la zone affectée thermiquement (ZAT) du Ti6Al4V, où la formation de phase martensitique α' a été observée, contribuant à une augmentation de la résistance. Pour les joints avec intercalaire Cu, l'interface entre le cuivre et le Ti6Al4V a montré une dureté et un module d'élasticité élevés, indiquant une bonne liaison mécanique, bien que la zone fondue ait présenté une dureté inférieure à celle du joint avec Ag.

La résistance au fluage à l'échelle nanométrique a également mis en évidence une meilleure performance du joint avec intercalaire Ag. Celui-ci a montré une résistance supérieure au fluage dans la zone fondue, probablement en raison de sa capacité à supprimer les IMC fragiles et à influencer la diffusion élémentaire. Les mécanismes de fluage variaient selon les régions : le fluage par ascension des dislocations dominait dans le Ti6Al4V, tandis que le fluage par diffusion était plus marqué dans l'AA7075. L'intercalaire Ag semblait faciliter un gradient de diffusion plus favorable, menant à un meilleur contrôle de la déformation par fluage. En comparaison, l'intercalaire Cu montrait une résistance inférieure au fluage dans la zone fondue.

Concernant le comportement à la corrosion, les joints avec intercalaire Ag ont démontré une meilleure résistance dans une solution de NaCl à 3,5 %, attribuée à une microstructure affinée et à la réduction des interactions galvaniques. À l'inverse, bien que le joint avec intercalaire Cu soit toujours plus performant qu'un assemblage direct aluminium–titane, son efficacité restait inférieure en raison de la présence d'IMC riches en Cu (Cu_3Ti_2), susceptibles d'agir comme sites d'initiation de la corrosion localisée.

Ces résultats contribuent au développement de joints plus fiables et durables pour des applications structurelles à haute performance. De plus, cette étude approfondie met en évidence les effets bé001néfiques de l'utilisation d'intercalaires dans le soudage laser d'alliages dissemblables.

Mots clés : Soudage laser dissemblable ; Intercalaire en cuivre et en argent ; Optimisation des paramètres de soudage laser ; Évolution microstructurale de la zone fondue ; Composés intermétalliques ; Performance mécanique des assemblages dissemblables ; Analyse du fluage à l'échelle nanométrique ; Résistance à la corrosion des joints.

ABSTRACT

In advanced engineering applications particularly in the aerospace and automotive sectors the demand for lightweight structures with high mechanical performance has driven the integration of dissimilar metal alloys. Joining materials like aluminum and titanium can leverage their individual strengths: aluminum's low density and titanium's high strength and corrosion resistance. However, joining these dissimilar alloys presents significant metallurgical challenges, particularly due to the formation of brittle intermetallic compounds (IMCs) at the interface, which degrade joint integrity.

To address these challenges, the use of interlayers materials inserted between the base alloys during welding has been proposed as an effective strategy. Interlayers can modify the solidification path and elemental diffusion across the interface, thus controlling the formation and morphology of IMCs. Selecting an appropriate interlayer is critical; it should not only act as a diffusion barrier but also improve mechanical and chemical compatibility between the base metals. In this context, silver (Ag) and copper (Cu) both known for their high thermal and electrical conductivity are potential candidates. Their metallurgical interactions with both aluminum and titanium are distinct, offering different pathways for optimizing the joint microstructure and properties. Additionally, laser welding, with its high precision and localized energy input, has emerged as a promising technique for such applications.

The present research focuses on laser welding of AA7075 aluminium alloy and Ti6Al4V titanium alloy using commercially available Ag and Cu interlayers (99.9% pure, sourced from McMaster). Both interlayers were applied as thin foils (380 μm), and welding parameters were optimized to accommodate differences in thermal conductivity and melting behavior. The study aims to assess and compare the effects of these interlayers on the joint's microstructure, mechanical performance, corrosion resistance, and nanoscale creep behavior.

Optical microscopy and scanning electron microscopy (SEM) were employed to examine grain morphology and phase distribution. Microhardness and nanoindentation tests provided insights into mechanical gradients across the welds, while nanoscale creep behavior was evaluated using depth-controlled nanoindentation creep tests. Corrosion resistance was analyzed using electrochemical impedance spectroscopy (EIS), cyclic polarization, and potentiodynamic tests.

Significant differences were observed in how Ag and Cu affected the joint characteristics. The Ag interlayer was particularly effective in suppressing the formation of brittle titanium–aluminum IMCs such as Al_3Ti and $TiAl_3$ in the fusion zone (melt zone formed welding). This contributed to a more homogeneous and refined microstructure, improving mechanical stability. In contrast, the Cu interlayer reduced aluminum–titanium interactions but promoted the formation of copper-based IMCs, such as Cu_3Ti_2. While this enhanced local mechanical strength, it also introduced some localized brittleness.

From a mechanical performance, the Ag-interlayered joints exhibited higher microhardness values in the fusion zone compared to those with Cu. The highest hardness overall was recorded in the Ti6Al4V HAZ (zone affected by heat near the fusion zone), where martensitic α′ phase formation was observed, contributing to increased strength. For joints using Cu, the interface between Cu interlayer and Ti6Al4V displayed high hardness and elastic modulus, indicating good mechanical bonding, though the fusion zone showed relatively lower hardness compared to its Ag counterpart.

Creep resistance at the nanoscale further distinguished the performance of the two interlayers. The Ag interlayer showed superior creep resistance in the fusion zone, likely due to its suppression of brittle IMCs and its influence on elemental diffusion. Creep mechanisms varied across regions: dislocation climb dominated in Ti6Al4V, while diffusion-based creep was more pronounced in AA7075. The Ag interlayer appeared to facilitate a more favorable diffusion gradient, leading to better control over creep deformation. The Cu interlayer, while showed inferior resistance in the fusion zone compared to Ag interlayer joint.

In terms of corrosion behavior, joints with Ag interlayer demonstrated greater resistance in 3.5% NaCl solution, attributed to the refined microstructure and reduced galvanic interactions. On the other hand, Cu interlayer joint, though still beneficial compared to direct aluminum–titanium welding, was less effective due to the presence of Cu-rich IMCs (Cu_3Ti_2), which can act as localized corrosion initiation sites.

These findings contribute to the development of more reliable and durable joints in high-performance structural applications. Additionally, this comprehensive study provides the beneficial effects of the use of interlayers in laser welding of dissimilar alloys.

Keywords**:** Dissimilar laser welding; Copper and silver interlayer; Laser welding parameters optimization; microstructure evolution of FZ; Intermetallic compounds; Mechanical performance of dissimilar weldments; Nanocreep analysis of joints; Corrosion resistance of joints.

TABLE DES MATIÈRES

LISTE DES TABLEAUX

LISTE DES FIGURES

LISTE DES ABRÉVIATIONS, DES SIGLES ET DES ACRONYMES

BCC	Body Centered Cubic
FCC	Face Centered Cubic
IMC	Intermetallic Compound
CpTi	Commercially pure Titanium
Ti	Titanium
Al	Aluminium
BM	Base metal
HAZ	Heat affected zone
HCP	Hexagonal closed pack
HDSM	Hole drill strain measurement
OM	Optical microscopy
SEM	Scanning electron microscopy
AFM	Atomic force microscopy
EBW	Electron beam welding
LBW	Laser beam welding
TIG	Tungsten inert gas welding
CRSS	Critical resolved shear stress

CP	Cyclic polarization
EIS	Electrochemical impedance spectroscopy
UTS	Ultimate tensile strength
SFE	Stacking Fault Energy
TCP	Tetragonal Closed Pack
EDS	Energy dispersive spectroscopy
ASTM	American standard of testing metals

LISTE DES SYMBOLES

α	Alpha
α'	Martensite phase
β	Beta
δ	Delta
σ	Sigma
γ	Gamma
γ''	Gamma double prime
μ	Mu
gf	Gram force
mm	Millimeter
KN	Kilo newton
g/cc	Gram per centimeter cube
MPa	Mega pascals

INTRODUCTION GÉNÉRALE

CONTEXTE

Les matériaux aérospatiaux, en particulier les alliages, sont utilisés comme éléments de structure soutenant la cellule d'un aéronef lors de diverses phases de vol, telles que le roulage, le décollage, la croisière et l'atterrissage. L'industrie aérospatiale a historiquement été à l'avant-garde de la recherche et de la mise en œuvre de matériaux structuraux avancés. Les exigences de performance des composants, souvent des éléments clés dans des systèmes techniques complexes, stimulent la demande pour ces matériaux. Dans le secteur aérospatial, la réduction du poids et l'amélioration des performances à haute température sont les principaux objectifs du développement de nouveaux matériaux structuraux. Des propriétés essentielles telles que la densité, la résistance à l'oxydation et à la corrosion, la résistance mécanique, la limite d'élasticité, la ténacité et la conductivité thermique sont déterminantes pour la performance des aéronefs. Ces matériaux sont appliqués dans des composants critiques pour la sécurité, comme les ailes, le fuselage, le train d'atterrissage et l'empennage, mais aussi dans les hélicoptères (booms de queue, fuselage et pales de rotor).

Dans de nombreux secteurs à hautes performances, tels que l'aérospatiale, l'automobile et le biomédical, les assemblages de matériaux dissemblables sont de plus en plus requis. Cette tendance permet de combiner les propriétés uniques de différents matériaux au sein d'une même structure. La demande pour de tels assemblages provient du besoin d'optimiser les composants en termes de performance, de poids et de rentabilité. En particulier, l'industrie aérospatiale exige des matériaux offrant un équilibre entre résistance, durabilité et légèreté. L'assemblage de matériaux dissemblables permet, par exemple, de joindre des alliages d'aluminium comme l'AA7075 à des alliages de titane comme le Ti6Al4V, tirant ainsi parti des propriétés supérieures de chacun pour répondre aux exigences strictes du secteur. L'AA7075 est prisé pour son faible poids, sa haute résistance et sa bonne résistance à la

corrosion, tandis que le Ti6Al4V se distingue par d'excellentes propriétés mécaniques, une excellente résistance à la corrosion et une grande stabilité à haute température. La possibilité de combiner ces matériaux dans un seul composant permet de produire des structures hybrides offrant à la fois résistance et légèreté, essentielles pour améliorer l'efficacité énergétique, la capacité de charge et les performances globales dans les applications aérospatiales.

De plus, le soudage par faisceau laser est un procédé de soudage par fusion utilisant un laser pour assembler deux métaux ou alliages en fournissant une source de chaleur hautement concentrée. Cette méthode est fréquemment utilisée dans des applications automatisées et à fort volume de production, comme dans l'industrie automobile. L'un des principaux avantages du soudage laser est sa capacité à faire fondre les bords de la jointure sans affecter une grande zone de la pièce, grâce à sa haute densité d'énergie. Par rapport au soudage à l'arc, le soudage laser offre une densité de puissance supérieure et un apport thermique moindre, produisant ainsi des soudures à haut rapport d'aspect tout en minimisant la quantité de chaleur appliquée.

Dans le cas spécifique de l'assemblage entre l'AA7075 et le Ti6Al4V, le soudage laser constitue une solution pratique pour relever les défis posés par ces deux matériaux. L'AA7075, un alliage d'aluminium, est reconnu pour son excellent rapport résistance/poids, ce qui en fait un choix idéal dans les applications où la réduction de poids est primordiale. Le Ti6Al4V, quant à lui, est un alliage de titane apprécié pour ses excellentes propriétés mécaniques, sa résistance à la corrosion et sa capacité à opérer à haute température. Si ces caractéristiques rendent ces alliages très attractifs pour le secteur aérospatial, leurs propriétés physiques et chimiques très différentes représentent un obstacle pour les procédés de soudage traditionnels. Grâce au soudage laser, ces difficultés peuvent être surmontées, permettant la création de composants hybrides solides, durables et légers. L'utilisation d'intercouches, telles que le cuivre ou l'argent, améliore davantage la qualité de la jointure en jouant le rôle de barrière de diffusion, en limitant la formation de composés intermétalliques fragiles, et en

assurant que la soudure finale présente des propriétés mécaniques favorables aux applications aérospatiales et à haute performance.

Revue de littérature

De nombreuses études ont été menées sur le soudage laser des alliages de titane et d'aluminium, avec pour objectif principal d'améliorer la résistance des joints et de réduire la formation de composés intermétalliques, qui peuvent fragiliser les soudures. Ces composés, souvent fragiles, sont susceptibles de compromettre l'intégrité mécanique des joints soudés, ce qui rend leur contrôle essentiel pour les applications industrielles, notamment dans l'aérospatiale.

Chen et al. (Y. Chen et al., 2010) ont étudié comment les différentes morphologies de la couche de réaction interfaciale influencent l'initiation et la propagation des fissures dans les joints titane/aluminium lors du soudage laser-brasage. Leurs résultats ont indiqué que ces morphologies ont un impact significatif sur l'intégrité structurelle des joints, soulignant l'importance de maîtriser ces réactions pour améliorer la qualité des soudures. Dans une autre étude, Chen et al. (S. Chen, Li, Chen, Dai, et al., 2011a) se sont concentrés sur l'amélioration de l'homogénéité des réactions interfaciales lors du soudage laser-brasage entre l'aluminium et le titane. Leur travail a démontré que le contrôle précis de ces réactions peut non seulement renforcer la résistance du joint, mais aussi réduire les défauts potentiels, ce qui est essentiel pour les applications où la fiabilité est primordiale. Lee et al. (S. J. Lee et al., 2013) ont exploré la soudabilité des métaux dissemblables titane et aluminium en utilisant des lasers à fibre monomode. Leurs résultats ont montré qu'il est possible d'obtenir une résistance du joint acceptable et une microstructure favorable en utilisant cette technologie laser avancée. Cela offre une approche pratique pour le soudage de métaux dissemblables, ouvrant la voie à de nouvelles applications industrielles. Casalino et Mortello (Casalino & Mortello, 2016) ont réalisé une analyse modélisée et expérimentale du soudage laser décalé de joints bout à bout entre l'aluminium et le titane. Ils ont découvert qu'un décalage laser approprié peut conduire à des joints de haute qualité avec des propriétés mécaniques optimales. Cette découverte contribue à l'amélioration des techniques de soudage en permettant un meilleur contrôle des

paramètres du processus pour optimiser les résultats. Poursuivant dans cette voie, Casalino et al. (Casalino et al., 2015) ont étudié le soudage laser Yb-YAG décalé de joints bout à bout entre les alliages AA5754 et T40. Ils ont démontré que cette méthode peut efficacement assembler ces alliages dissemblables tout en produisant des soudures de haute qualité avec de bonnes propriétés mécaniques. Ceci est particulièrement significatif pour les industries cherchant à combiner différents matériaux pour tirer parti de leurs propriétés respectives. Leo et al. (Leo et al., 2018a) ont exploré les effets des traitements thermiques à basse température sur les soudures laser dissemblables entre AA5754 et Ti6Al4V. Ils ont constaté que ces traitements peuvent améliorer la microstructure et les propriétés mécaniques des soudures, améliorant ainsi la performance globale du joint. Cette approche offre une méthode supplémentaire pour optimiser les soudures après le processus initial de soudage. Ni Jia-ming et al. (Qun li Li, 2007) ont examiné les caractéristiques des joints de soudage laser-brasage entre les alliages d'aluminium et de titane. Leur recherche a révélé que cette méthode peut produire des joints dissemblables de haute qualité avec de bonnes propriétés mécaniques, en faisant une technique précieuse pour les applications aérospatiales où la fiabilité et la performance des matériaux sont essentielles. Casalino et al. (Casalino et al., 2017a) ont mené une analyse mécanique et microstructurale des soudures bout à bout réalisées par laser à fibre entre AA6061 et Ti6Al4V. Leurs résultats ont montré que ces joints présentaient des propriétés mécaniques satisfaisantes, une résistance adéquate du joint et une bonne résistance à la fracture. Cela souligne le potentiel de cette technique pour produire des soudures fiables entre des matériaux dissemblables. Chen et al. (S. Chen, Li, Chen, & Huang, 2011a) se sont penchés sur le mécanisme d'assemblage des alliages dissemblables titane/aluminium lors du processus de soudage laser-brasage. Ils ont identifié que ce processus implique la solidification, les réactions interfaciales et la liaison métallurgique, qui sont des facteurs cruciaux pour obtenir des joints de haute qualité. Comprendre ces mécanismes est essentiel pour améliorer les procédés de soudage et la qualité des soudures résultantes. Dans une autre étude, Chen et al. (S. H. Chen et al., 2010) ont investigué le mode de réaction interfaciale et son influence sur la résistance à la traction lors du soudage laser des alliages d'aluminium et de titane. Ils ont conclu que le mode de réaction interfaciale affecte de manière significative

les propriétés mécaniques du joint, ce qui souligne l'importance du contrôle de ces réactions pour optimiser la performance des soudures. Lee et al. (Lee. S et al., n.d.) ont examiné le comportement microstructural dans la zone de fusion des soudures en recouvrement dissemblables aluminium-titane et titane-aluminium en utilisant un laser à fibre monomode. Leur étude a montré que cette technologie laser permet d'obtenir des caractéristiques microstructurales souhaitables dans la zone soudée, ce qui est bénéfique pour la qualité globale du joint. Zhou et al. (X. Zhou et al., 2019) ont exploré la résistance mécanique des joints bout à bout Ti-Al formés par soudage laser-brasage. Leurs résultats ont démontré que ce processus produit des joints avec une résistance mécanique satisfaisante et une qualité appropriée, ce qui est important pour les applications nécessitant une fiabilité élevée. Song et al. (Z. Song et al., 2013) ont étudié la microstructure interfaciale et les propriétés mécaniques des joints dissemblables Ti6Al4V/A6061 produits par brasage laser direct sans métal d'apport. Leurs découvertes ont mis en évidence le potentiel d'obtenir une bonne microstructure interfaciale et des propriétés mécaniques favorables sans avoir besoin de matériaux supplémentaires, simplifiant ainsi le processus de soudage. Vaidya et al. (Vaidya et al., 2009) ont examiné la relation entre la structure et les propriétés des joints dissemblables soudés au laser entre l'aluminium AA6056 et le titane Ti6Al4V pour des applications aéronautiques. Ils ont démontré la résistance des joints à la propagation des fissures de fatigue et à la fracture, les rendant adaptés aux environnements soumis à de fortes contraintes, ce qui est crucial dans l'industrie aérospatiale. Tomashchuk et al. (Tomashchuk et al., 2015a) ont étudié le soudage laser direct à trou traversant de l'aluminium AA5754 et du titane Ti6Al4V. Ils ont conclu que cette méthode peut assembler avec succès ces matériaux dissemblables, résultant en des soudures avec des caractéristiques de joint appropriées, élargissant ainsi les options pour le soudage de matériaux différents. Chen et al. (CHEN et al., 2010) ont investigué le comportement de diffusion du silicium lors du soudage laser-brasage des alliages d'aluminium et de titane en utilisant un fil d'apport Al-12Si. Leur étude a montré que la diffusion du silicium joue un rôle critique dans la détermination de la qualité du joint, influençant la formation de phases interfaciales et les propriétés mécaniques. Xue et al. (Xue et al., 2019) ont exploré les caractéristiques interfaciales des joints en recouvrement

Ti6Al4V/AA6060 produits par soudage laser pulsé Nd. Leurs résultats ont montré que ce processus laser produit des caractéristiques interfaciales souhaitables, contribuant à la qualité globale du joint et à sa performance mécanique. Gao et al. (M. Gao et al., 2014) ont étudié la microstructure et le comportement en traction des alliages dissemblables Al et Ti soudés par une méthode hybride laser-arc. Leurs conclusions ont démontré que cette méthode peut aboutir à une performance de joint satisfaisante en termes de microstructure et de comportement en traction, offrant une alternative efficace pour le soudage de ces matériaux. Lv et al. (S. X. Lv et al., 2012) ont investigué le soudage-brasage à l'arc TIG des alliages dissemblables titane/aluminium en utilisant des métaux d'apport à base d'aluminium. Leur recherche a montré que ce processus assemble efficacement les alliages dissemblables de titane et aluminium, produisant de bonnes propriétés mécaniques, ce qui est important pour les applications industrielles où ces matériaux sont couramment utilisés. Lee et al. (S.-J. ; Lee et al., 2013) ont exploré les caractéristiques microstructurales et les propriétés mécaniques des joints en recouvrement soudés par laser à fibre monomode entre des métaux dissemblables titane et aluminium. Leur étude a démontré le potentiel de cette technique laser pour obtenir des caractéristiques de soudure souhaitables, contribuant à améliorer la fiabilité et la performance des joints soudés. Casalino et al. (Casalino et al., 2018) ont investigué les effets des paramètres de décalage et de focalisation sur le soudage laser à fibre des alliages de titane de grade 5 et d'aluminium 6061. Ils ont trouvé que ces paramètres influencent de manière significative la qualité des soudures, soulignant l'importance d'un réglage précis pour obtenir des résultats optimaux. Gupta (S. P. Gupta, 2002) a examiné la formation de composés intermétalliques dans des couples de diffusion de titane et d'un alliage eutectique aluminium-silicium. Sa recherche a montré que ces composés impactent les propriétés du matériau au niveau du joint, ce qui est crucial pour déterminer la performance mécanique de la soudure et pour développer des méthodes visant à minimiser les effets indésirables. Chen et al. (Y. Chen et al., 2009) ont investigué les effets de l'apport de chaleur sur la microstructure et les propriétés mécaniques des joints titane/aluminium formés par soudage laser-brasage par points rectangulaires. Leurs résultats ont indiqué que l'apport de chaleur joue un rôle significatif dans la détermination de la qualité des joints, affectant la formation

de phases interfaciales et la résistance mécanique globale. Cabibbo et al. (Cabibbo et al., 2005) ont étudié les caractéristiques mécaniques et microstructurales des joints titane-aluminium soudés au laser, trouvant que des paramètres de soudage spécifiques conduisent à des propriétés de joint améliorées. Cette étude contribue à la compréhension de l'optimisation des paramètres de soudage pour obtenir des soudures de haute qualité entre des matériaux dissemblables. Enfin, Tomashchuk et al. (Tomashchuk et al., 2017a) ont exploré le soudage laser-brasage de l'aluminium au titane dans une rainure en V, concluant que cette méthode permet d'obtenir des joints efficaces avec des caractéristiques souhaitables. Cette technique offre une solution pratique pour assembler des matériaux dissemblables avec une géométrie spécifique, élargissant ainsi les possibilités d'application dans diverses industries.

Ces études mettent en évidence les avancées réalisées dans le domaine du soudage laser des alliages dissemblables titane/aluminium, en se concentrant sur le contrôle des réactions interfaciales, l'optimisation des paramètres de soudage et l'amélioration des propriétés mécaniques. Ce corpus de travaux fournit des informations précieuses pour améliorer la performance des joints pour les applications industrielles, en particulier dans le secteur aérospatial où la combinaison de légèreté et de résistance est essentielle.

Énoncé du problématique

La demande de jonction de matériaux dissemblables, tels que l'alliage de titane Ti-6Al-4V et l'alliage d'aluminium AA7075, a considérablement augmenté dans divers secteurs, y compris l'aérospatiale, l'automobile et le biomédical. La combinaison de ces matériaux offre le potentiel de structures légères et haute performance qui optimisent à la fois la résistance et l'efficacité. Dans l'industrie aérospatiale, par exemple, la réduction du poids est cruciale pour améliorer l'efficacité énergétique, tandis que le maintien de la résistance est essentiel pour la sécurité. L'AA7075 et le Ti-6Al-4V sont tous deux largement utilisés dans ce domaine en raison de leurs propriétés distinctes. L'AA7075 est apprécié pour son rapport résistance-poids élevé, son excellente résistance à la fatigue et sa bonne résistance à la corrosion, ce qui le rend idéal pour les composants structurels des aéronefs. D'autre part, le Ti-6Al-4V est connu pour ses propriétés mécaniques supérieures, y compris une excellente résistance à la

corrosion et la capacité de résister à des températures élevées, le rendant adapté aux environnements à haute contrainte. Le défi réside dans la jonction efficace de ces deux matériaux sans compromettre l'intégrité mécanique du joint, ce qui a suscité un intérêt pour des techniques de soudage innovantes.

L'un des principaux défis de la jonction de matériaux dissemblables comme l'AA7075 et le Ti-6Al-4V est la formation de composés intermétalliques fragiles à l'interface. Lorsque ces deux matériaux sont assemblés en utilisant des techniques de soudage conventionnelles, l'interaction entre l'aluminium et le titane à haute température conduit souvent à la formation de ces composés intermétalliques. Ces composés intermétalliques, tels que les aluminures de titane, ont tendance à être fragiles et affaiblissent considérablement le joint, le rendant sujet à la fissuration et à une durabilité réduite. Cela est particulièrement préoccupant dans des industries comme l'aérospatiale, où les composants sont soumis à des conditions extrêmes et où la performance à long terme du joint est critique. La formation d'composés intermétalliques est le résultat de l'incompatibilité métallurgique entre l'aluminium et le titane, aggravée par leurs différentes températures de fusion. L'aluminium fond à une température beaucoup plus basse (~600 °C) que le titane (~1650 °C), ce qui complique le processus de soudage et augmente la probabilité de défauts.

Le soudage au laser a émergé comme une solution prometteuse pour relever les défis de la jonction de matériaux dissemblables comme l'AA7075 et le Ti-6Al-4V. Le soudage au laser offre plusieurs avantages par rapport aux méthodes de soudage traditionnelles, principalement en raison de sa capacité à fournir une source de chaleur hautement concentrée. Cela permet une plus grande précision et un meilleur contrôle pendant le processus de soudage, minimisant la zone affectée thermiquement et réduisant le risque de formation d'IMC. La nature localisée de l'apport de chaleur lors du soudage au laser garantit qu'une petite région autour du joint est affectée, empêchant une fusion excessive et une distorsion thermique des matériaux. Ceci est particulièrement important lors de la jonction de matériaux avec des points de fusion très différents, car cela aide à éviter un chauffage inégal et assure un joint plus stable. De plus, le soudage au laser peut être effectué à des vitesses élevées, ce

qui en fait une option efficace et rentable pour la production à grande échelle dans des industries comme l'aérospatiale et l'automobile.

Malgré les avantages du soudage au laser, le soudage direct de l'AA7075 et du Ti-6Al-4V pose encore des défis en raison des différences inhérentes dans leurs propriétés physiques. Pour surmonter ces défis, je propose une approche novatrice qui intègre des intercouches entre les deux matériaux pendant le processus de soudage. Un intercouche est une fine couche de matériau placée entre les alliages AA7075 et Ti-6Al-4V pour agir comme une barrière de diffusion. L'objectif de l'intercouche est de minimiser la formation de composés intermétalliques fragiles et d'améliorer la qualité globale du joint en favorisant la formation de phases intermédiaires stables qui renforcent les propriétés mécaniques de la soudure. Dans ce contexte, le cuivre et argent ont été identifiés comme des matériaux d'intercouche efficaces.

L'utilisation de cuivre et argent comme intercouches offre plusieurs avantages. Ces matériaux servent de barrières de diffusion, empêchant l'interaction directe entre l'aluminium et le titane, responsable de la formation de composés intermétalliques fragiles. Au lieu de cela, le matériau intercouche réagit avec les matériaux de base pour former des phases plus stables et moins fragiles. Par exemple, le cuivre peut former des intermétalliques cuivre-titane qui, bien que toujours plus durs que les matériaux de base, ont tendance à être moins fragiles que les composés aluminium-titane. De même, l'argent peut réduire la formation de composés intermétalliques titane-aluminium en favorisant la formation de phases plus ductiles. Les intercouches de cuivre et argent améliorent également la mouillabilité globale des matériaux, facilitant une meilleure liaison à l'interface et réduisant la formation de vides. L'introduction d'intercouches ne permet pas seulement de réduire la formation de composés intermétalliques, mais aide également à gérer la différence de dilatation thermique entre les deux matériaux, réduisant les contraintes résiduelles dans le joint et améliorant sa durabilité à long terme.

Le développement de ce nouveau procédé de soudage au laser avec intercouches représente une avancée significative dans le domaine de la jonction de matériaux

dissemblables. En minimisant la formation de composés intermétalliques fragiles et en améliorant les propriétés mécaniques du joint, ce procédé répond aux principaux défis associés à la jonction de l'AA7075 et du Ti-6Al-4V. L'utilisation d'intercouches de cuivre et argent renforce la résistance, la ténacité et la résistance à la corrosion de la soudure, la rendant adaptée aux applications exigeantes dans les industries aérospatiales, automobiles et biomédicales. De plus, la précision et l'efficacité du soudage au laser en font une option très attrayante pour la production à grande échelle, où la qualité et la cohérence de la soudure sont cruciales. La mise en œuvre réussie de ce nouveau procédé de soudage a le potentiel d'élargir la gamme d'applications pour les alliages AA7075 et Ti-6Al-4V, conduisant à une performance et une durabilité améliorée dans les industries de haute performance.

Objectifs de la thèse

Ce projet vise à améliorer la qualité des soudures laser entre les alliages Ti-6Al-4V et AA7075 en utilisant des intercouches. En réduisant la formation de composés intermétalliques grâce à l'utilisation de matériaux tels que le cuivre et l'argent, je cherche à optimiser les propriétés mécaniques des joints soudés. Les objectifs de ce projet sont les suivants :

1. Étudier la compatibilité et l'efficacité de différents matériaux d'intercouche, en particulier le cuivre et l'argent, pour réduire la formation de composés intermétalliques fragiles à l'interface lors du soudage laser d'alliages dissemblables Ti6Al4V (alliage de titane) et AA7075 (alliage d'aluminium). L'objectif est d'évaluer comment ces intercouches influencent la diffusion des éléments, la microstructure de la jointure et la qualité globale de la soudure, en vue d'améliorer les performances mécaniques et l'intégrité structurelle dans des applications d'ingénierie avancée.
2. Obtenir des joints soudés de haute qualité en réduisant la formation de composés intermétalliques fragiles, tout en maintenant les propriétés mécaniques souhaitées, notamment la résistance au fluage à l'échelle nanométrique, essentielle pour assurer la performance et la fiabilité à long terme des assemblages d'alliages dissemblables.

3. Évaluer les propriétés mécaniques et la microstructure des joints soudés y compris la résistance à la traction, la ténacité aux chocs et la dureté afin d'estimer l'efficacité du matériau d'intercouche choisi et de déterminer la performance globale et la fiabilité du joint.
4. Examiner le comportement à la corrosion des soudures entre métaux dissemblables, en tenant compte de son importance essentielle pour la durabilité à long terme et les performances fonctionnelles des composants dans le secteur aérospatial.
5. Développer une compréhension approfondie des mécanismes fondamentaux qui régissent la formation des composés intermétalliques dans le joint soudé, et analyser le rôle de l'intercouche dans leur atténuation et le contrôle de leur distribution.

Originalité de la thèse

L'originalité de ce projet réside dans la combinaison unique de matériaux, la méthode de traitement et la caractérisation approfondie des soudures résultantes, en particulier les études sur le comportement à la corrosion et au fluage nanométrique. Le soudage de métaux dissemblables, spécifiquement le Ti6Al4V et l'AA7075, pose des défis en raison de leurs propriétés physiques, chimiques et mécaniques distinctes. En introduisant un intercouche lors du processus de soudage laser, ce projet vise à surmonter ces défis et à améliorer la compatibilité entre les matériaux, aboutissant finalement à une jonction de haute qualité.

Bien qu'il y ait eu des études sur le soudage laser de métaux dissemblables, l'utilisation d'un intercouche en conjonction avec le soudage laser pour assembler le Ti6Al4V et l'AA7075 est un domaine relativement inexploré. De plus, la caractérisation complète des soudures résultantes including les propriétés mécaniques, la microstructure, les contraintes résiduelles, le comportement à la corrosion et le fluage nanométrique fournit des informations précieuses sur la performance de ces joints sous diverses conditions.

L'originalité de ce projet provient également de ses applications potentielles dans diverses industries, telles que l'aérospatiale, l'automobile et le biomédical, où les matériaux

légers et haute performance sont d'une grande importance. En élargissant notre compréhension de la manière dont ces matériaux dissemblables peuvent être efficacement assemblés et de leur comportement subséquent, cette recherche peut conduire à des solutions de conception novatrices et à une performance améliorée dans de nombreuses applications. Le Ti6Al4V, un alliage de titane, est connu pour son rapport résistance/poids élevé, son excellente résistance à la corrosion et sa stabilité à haute température. En revanche, l'AA7075 est un alliage d'aluminium avec une résistance exceptionnelle, une bonne résistance à la fatigue et des propriétés de légèreté. En joignant avec succès ces deux matériaux, les ingénieurs aérospatiaux pourraient concevoir des composants structurels hybrides qui bénéficient des avantages combinés des deux matériaux.

En résumé, l'originalité de ce projet peut être attribuée à l'approche innovante consistant à assembler le Ti6Al4V et l'AA7075 en utilisant un intercouche et le soudage laser, ainsi qu'à l'investigation approfondie des propriétés et du comportement des soudures, ce qui peut avoir des implications significatives pour diverses industries.

Méthodologie

La méthodologie employée dans cette étude englobe les processus détaillés de soudage au laser et de caractérisation subséquente des joints dissemblables formés entre les alliages AA7075 et Ti6Al4V avec l'incorporation d'intercouches en cuivre et en argent.

Pour évaluer la compatibilité et l'efficacité de l'argent en tant qu'intercouche dans le soudage laser des alliages dissemblables AA7075 et Ti6Al4V, une méthodologie systématique a été employée. Le soudage au faisceau laser a été choisi pour sa précision et sa capacité à minimiser les défauts lors de l'assemblage de métaux dissemblables. Des feuilles d'AA7075 et de Ti6Al4V ont été préparées et nettoyées afin d'éliminer toute contamination, garantissant une adhésion optimale au niveau de l'interface de soudure. Une fine couche d'argent a été placée entre les métaux de base pour agir comme barrière de diffusion, réduisant ainsi la formation de composés intermétalliques fragiles. Les paramètres de soudage, tels que la puissance du laser, la vitesse de soudage et la focalisation du faisceau,

ont été optimisés pour assurer un apport énergétique constant. Une caractérisation microstructurale a été réalisée à l'aide de la microscopie optique et électronique à balayage, tandis que la spectroscopie par dispersion d'énergie a permis d'identifier les compositions des phases. Ces analyses ont permis de comprendre comment l'intercouche en argent influence la formation des composés intermétalliques et la stabilité microstructurale. **(Objectif 1)**

En s'appuyant sur les résultats du chapitre 1, ce chapitre se concentre sur l'utilisation du cuivre en tant qu'intercouche pour améliorer la qualité des joints et réduire la formation d'composés intermétalliques lors du soudage laser des alliages AA7075 et Ti6Al4V. Les mêmes protocoles de préparation et de nettoyage ont été appliqués aux métaux de base et aux intercouches. Le potentiel du cuivre à former des composés intermétalliques cuivre-titane moins fragiles a été exploré en soumettant les joints à des conditions de soudage laser optimisées, similaires à celles utilisées pour l'analyse de l'intercouche en argent. Des tests de microdureté et des essais de traction ont été réalisés pour évaluer les propriétés mécaniques, en particulier à l'interface cuivre-titane. En outre, des tests de nanoindentation ont été effectués pour étudier la nanodureté et le module élastique dans les différentes zones de la soudure, notamment les alliages de base, la zone affectée thermiquement et la zone fondue. Cette évaluation détaillée a permis de comprendre la performance mécanique comparative de l'intercouche en cuivre dans la réduction de la fragilité. **(Objectif 2)**

Pour étudier le comportement nanomécanique des soudures dissemblables réalisées au laser avec une intercouche en argent, ce chapitre a utilisé des essais de fluage par nanoindentation. Les échantillons soudés ont été découpés pour isoler des zones spécifiques, notamment les alliages de base, la zone affectée thermiquement et la zone fondue. Des essais de nanoindentation ont été réalisés sous des charges contrôlées, et les courbes profondeur-temps ont été analysées pour identifier les mécanismes de fluage dominants. Une microscopie avancée, incluant le microscope électronique à balayage et la microscopie à force atomique, a été utilisée pour évaluer le comportement de la matière autour des indentations (pile-up/sink-in). Ces analyses quantitatives ont permis de mieux comprendre la

capacité de l'intercouche en argent à améliorer la résistance au fluage à l'échelle nanométrique, en particulier en supprimant la formation de phases fragiles telles que $TiAl_3$ et Al_3Ti. **(Objectif 3)**

Ce chapitre s'est concentré sur la compréhension de la résistance à la corrosion et du comportement mécanique des joints soudés avec une intercouche en cuivre. Après le soudage laser, les échantillons ont été soumis à une analyse microstructurale et de fractographie pour identifier la distribution des phases et les points de défaillance potentiels. Le comportement mécanique a été caractérisé par des essais de traction et des profils de microdureté, tandis que la résistance à la corrosion a été évaluée à l'aide de techniques électrochimiques. La polarisation potentiodynamique, la polarisation cyclique et la spectroscopie d'impédance électrochimique ont été effectuées dans une solution de NaCl à 3,5 % pour simuler les environnements marins. L'analyse post-corrosion à l'aide du microscope électronique à balayage et de la spectroscopie d'impédance électrochimique a permis d'identifier les mécanismes de dégradation et le rôle de l'intercouche en cuivre dans l'amélioration de la résistance à la corrosion. **(Objectif 4)**

Une étude comparative a été menée pour évaluer la résistance à la corrosion des joints avec intercouches en argent et en cuivre. Des mesures de contraintes résiduelles ont été réalisées à l'aide de techniques de forage à trous pour comprendre comment les contraintes affectaient la susceptibilité à la corrosion. Les tests de corrosion, incluant la spectroscopie d'impédance électrochimique et les études de polarisation, ont été répétés pour les joints avec les deux intercouches dans des conditions identiques. L'analyse microstructurale post-corrosion a permis d'identifier les différences spécifiques aux intercouches dans la stabilité des phases et les modèles de dégradation. Les résultats ont fourni une comparaison détaillée de l'efficacité des intercouches pour maintenir l'intégrité des joints dans des environnements corrosifs. **(Objectif 4)**

Pour évaluer la performance nanomécanique et le comportement au fluage des joints avec une intercouche en cuivre, des essais de nanoindentation ont été réalisés dans toutes les zones de soudure. Les courbes profondeur-temps et fluage-déformation versus contrainte ont

été analysées pour déterminer les mécanismes de fluage spécifiques aux interfaces cuivre/Ti6Al4V et cuivre/AA7075. Des images le microscope électronique à balayage et microscopie à force atomique ont fourni des représentations visuelles des profils d'indentation, corrélant les propriétés mécaniques aux observations microstructurales. Cette analyse a permis de comprendre comment l'intercouche en cuivre améliorait la résistance au fluage et sa performance comparative par rapport aux intercouches en argent étudiées dans les chapitres précédents. **(Objectif 5)**

Organisation de la thèse

Ce qui suit présente la structure de cette thèse, qui est composée de plusieurs chapitres, chacun dédié à un aspect spécifique de la recherche. Chaque chapitre représente une étude distincte, axée sur différents matériaux intercouches. Les chapitres proposent une exploration complète des défis et des solutions liés à l'assemblage des alliages Ti6Al4V et AA7075 à l'aide d'intercouches comme le cuivre et l'argent.

- *Chapitre 1* : Ce chapitre se concentre sur l'utilisation de l'intercouche en argent dans le soudage laser. Il présente les expériences et les résultats concernant l'efficacité de cet intercouche pour réduire la formation de composés intermétalliques et améliorer les propriétés mécaniques des soudures.

- *Chapitre 2* : Ce chapitre examine les propriétés mécaniques des soudures réalisées avec un intercouche en cuivre. Il étudie la résistance à la traction, la dureté et la performance globale des soudures, en mettant en lumière l'influence de l'intercouche de cuivre sur la qualité des joints.

- *Chapitre 3* : Ce chapitre est consacré à l'étude du comportement de fluage nanométrique des soudures utilisant l'intercouche argent. Il évalue l'impact de cet intercouche sur la déformation à long terme sous contrainte continue.

- *Chapitre 4* : Ce chapitre examine le comportement à la corrosion des soudures réalisées avec un intercouche en cuivre. Il se concentre sur la résistance à la corrosion des

soudures dans des environnements sévères, un facteur crucial pour la durabilité des composants aérospatiaux.

- *Chapitre 5* : Dans ce chapitre, la résistance à la corrosion des soudures avec intercouche argent est étudiée et comparée à celle des soudures avec intercouche de cuivre. Il offre une comparaison approfondie pour déterminer quel intercouche offre de meilleures performances en termes de résistance à la corrosion

- *Chapitre 6* : Ce chapitre porte sur l'étude du fluage nanométrique des soudures réalisées avec un intercouche en cuivre. Il examine la performance à long terme en termes de déformation sous contrainte et la compare à celle de l'intercouche en argent.

- *Conclusion générale* : Le dernier chapitre résume les principales conclusions des différents articles, en discutant des implications pour les applications industrielles et les orientations futures de la recherche. Il met l'accent sur le potentiel d'utilisation des intercouches dans le soudage laser pour améliorer la qualité et la performance des soudures de métaux dissemblables.

CHAPITRE 1
ÉVOLUTION MICROSTRUCTURALE ET REPONSE NANOMECANIQUE DES JOINTS DISSEMBLABLES SOUDES AU LASER A FIBRE DES ALLIAGES AA7075-TI-6AL-4V EN UTILISANT D'ARGENT COMME INTERCOUCHE

Titre en français du premier article :

Évolution microstructurale et réponse nanomécanique des joints dissemblables soudés au laser à fibre des alliages AA7075-Ti-6Al-4V en utilisant d'argent comme intercouche.

Titre original (en anglais) :

Microstructural evolution and the nanomechanical response of fiber laser welded dissimilar joints of AA7075-Ti-6Al-4V alloys using Ag as an interlayer.

Auteurs et affiliation :

Asim Iltaf : Étudiant au doctorat, Département de mathématiques, d'informatique et de génie, Université du Québec à Rimouski, Québec, Canada.
Noureddine Barka : Professeur, Département de mathématiques, d'informatique et de génie, Université du Québec à Rimouski, Québec, Canada.
Shayan Dehghan : Chercheur post-doctoral, Département de mathématiques, d'informatique et de génie, Université du Québec à Rimouski, Québec, Canada.

État de l'article :

Publié.

Revue :

The International Journal of Advanced Manufacturing Technology.

Référence :

https://doi.org/10.1007/s00170-024-13555-2.

Résumé en français du premier article

Depuis l'introduction du soudage par faisceau laser, ce procédé s'est imposé comme une technologie de soudage par fusion de haute qualité, affichant une croissance considérable dans de nombreux secteurs industriels. Dans cette étude, un faisceau laser à fibre de 3 kW est utilisé pour le soudage dissemblable de tôles de 1,6 mm d'épaisseur en AA7075 et Ti-6Al-4V avec une intercouche d'argent. Il est à noter que les paramètres laser utilisés dans cette étude sont une puissance de 3 kW, une vitesse de soudage de 50 mm/sec, une distance focale de 310 mm et un diamètre de tache focale de 0,45 mm. L'évolution microstructurale, l'impact de l'argent sur la résistance du joint, la formation de composés intermétalliques et les propriétés nanomécaniques par nanoindentation sont analysés pour les soudures. La nanoindentation et la microscopie à force atomique sont utilisées pour déterminer la nanodureté et le module d'élasticité effectif. Un nanoindenteur à pointe de Berkovich est utilisé, ainsi que la microscopie à force atomique pour mesurer les amas elliptiques autour des indentations. Les modules d'élasticité effectifs et les nanoduretés des alliages de base, des zones affectées thermiquement et de la zone de fusion de la soudure sont déterminés avec la technique d'Oliver-Pharr, la microscopie à force atomique et le travail d'indentation. Les résultats montrent que l'utilisation de l'intercouche d'argent dans le soudage AA7075-Ti-6Al-4V a réduit l'interaction titane-alminium et amélioré la qualité du joint. De plus, la méthode OP surestime la nanodureté en ignorant les zones d'amas. En revanche, l'analyse par microscopie à force atomique indique une nanodureté inférieure à la microdureté. Par ailleurs, les valeurs de nanodureté obtenues par la méthode du travail d'indentation sont en accord étroit avec les valeurs de microdureté (par exemple, la nanodureté de la zone de fusion est de 1,50 GPa, et sa microdureté est de 1,71 GPa), ce qui en fait une méthode adaptée pour caractériser les soudures AA7075-Ti-6Al-4V avec une intercouche d'argent. En ce qui

concerne les résultats de cette recherche, il est recommandé d'appliquer la méthode du travail d'indentation pour évaluer les propriétés nanomécaniques des matériaux métalliques.

Microstructural evolution and the nanomechanical response of fiber laser welded dissimilar joints of AA7075-Ti-6Al-4V alloys using Ag as an interlayer

Asim Iltaf [a, *], Noureddine Barka [a], Shayan Dehghan [a, *]

[a] Department of Mathematics, Computer Science and Engineering, University of Quebec at Rimouski, Rimouski, QC G5L 3A1, Quebec, Canada.

[*]Corresponding authors (Asim Iltaf, Shayan Dehghan): Department of Mathematics, Computer Science and Engineering, University of Quebec at Rimouski, Rimouski, QC G5L 3A1, Quebec, Canada.

E-mail address: asim.iltaf@uqar.ca, shayan.dehghan@uqar.ca

Abstract

Since laser beam welding's inception, this process has established itself as a high-quality fusion joining technology, exhibiting tremendous growth in a broad range of industries. In this study, fiber laser beam welding with 3kW power is used for dissimilar joining of 1.6 mm thick AA7075 and Ti-6Al-4V sheets with an Ag interlayer. It is worth noting that the laser parameters used in this study are laser power of 3 kW, welding speed of 50 mm/sec, focal length of 310 mm, and focal spot diameter of 0.45 mm. In this study microstructural evolution, Ag's impact on joint strength, IMC formation, and nanomechanical properties using nanoindentation are analyzed for weldments. Nanoindentation and AFM are used to determine nanohardness and effective elastic modulus. A Berkovich-tipped nanoindenter is used, along with AFM measuring elliptical pile-ups around indents. The effective elastic moduli and nanohardness of the base alloys, heat-affected zones, and fusion zone of the weldment are determined with the Oliver-Pharr technique, atomic force microscopy (AFM), and work of indentation. The results show that the use of Ag interlayer in AA7075-Ti-6Al-4V joining reduced Ti-Al interaction and improved the joint quality. In addition, the OP method overestimates nanohardness because of the ignoring pile-up areas. In contrast, AFM analysis indicates lower nanohardness

compared to microhardness. Moreover, the work of indentation method's nanohardness values closely aligns with the microhardness values (e.g., the fusion zone nanohardness value is 1.50 GPa, and its microhardness value is 1.71 GPa), making it suitable for characterizing AA7075-Ti-6Al-4V weldments with Ag interlayer. Regarding the findings of this research, it is recommended that the work of indentation method be applied to evaluate the nanomechanical properties of metallic materials.

***Keywords*:** Dissimilar joining, Nanoindentation, Interlayer, Laser welding, SEM

1.1 INTRODUCTION

Recently, welding technology has been increasingly applied to design composite structures with dissimilar Ti/Al alloys. For instance, the honeycomb sandwich structure in aircraft wings, where the titanium alloy skin connects with the aluminum alloy honeycomb core within the wing box. The key advantage lies in weight reduction while simultaneously enhancing fatigue resistance and stability (Aminzadeh et al., 2020; Malekshahi Beiranvand et al., 2020; Schubert et al., 2001; Wadsworth et al., 1983). The primary material employed in the construction of the wing of the NASA YF-12 fighter is a Ti/Al honeycomb core composite board. Airbus has implemented a composite construction consisting of titanium plates and aluminium ribs for components that are susceptible to corrosion, such as aircraft seat rails. This adoption aims to enhance the corrosion resistance, while at the same time reducing the overall weight of the structure and minimizing manufacturing expenses (Kocik et al., 2004; J. Zhao et al., 2023). Moreover, previous studies have indicated the existence of a metallurgical incompatibility between aluminium (Al) and titanium (Ti). This incompatibility arises from their limited ability to dissolve in each other and their propensity to produce numerous brittle intermetallic compounds (IMCs). Consequently, these challenges compromise the overall performance of welded joints between titanium and aluminium (Ti/Al), significantly (F. Li et al., 2005; Mathieu et al., 2006; Ohnuma et al., 2000a).

Researchers have conducted extensive studies on various welding procedures to attain a high-quality joint between Ti and Al, particularly focusing on the IMCs concentration inside the joint. The Ti/Al laser welding technique has gained significant recognition for its simplicity, great efficiency, and versatility in accommodating different types of joints. Moreover, it is worth mentioning the significant concern in Ti/Al welded joints is the development of brittle IMCs at the interface between the Ti and Al (Plaine et al., 2017). This phenomenon has been identified as a crucial factor that restricts the strength and ductility of these joints. Furthermore, Tomashchuk et al. (Tomashchuk et al., 2015b) applied the technique of direct keyhole laser welding to successfully combine Al and Ti. Their outcomes revealed the formation of Ti_3Al, TiAl, and Al_3Ti compounds at the interface. In the context of fusion welding between Ti and Al, the process involves the combination of liquid Al and liquid Ti, resulting in the formation of various IMCs consisting of Ti and Al. The thickness of the IMC layer at the interface between Ti and Al in fusion-welded joints was seen to be considerable, measuring up to several tens of microns. In addition, it was shown that fractures tended to begin and spread inside this IMC layer. Xu et al. (L. Xu et al., 2006) found that the Ti/Al interface of diffusion-bonded Ti/Al couples exhibited the presence of just the Al3Ti phase over the temperature range of 520–650 ℃. It is noteworthy to mention that Sahul et al. (Sahul et al., 2017) observed that an insufficient thickness of the Al_3Ti layer might lead to an absence of a reliable weldment, thus diminishing the load-bearing capability of the joints. According to Zhu et al. (Zhu et al., 2019) findings, it is recommended to maintain a consistent thickness of the Al3Ti layer in the thickness direction at Ti/Al butt joints. This uniform thickness should be around 5 μm to avoid issues such as inadequate weldment and unfavourable wettability in the bottom surface of the joints. Hence, it is essential to inhibit the formation of the Al_3Ti layer at the Ti/Al joints, while ensuring the retention of a certain thickness, to meet the requirements of practical engineering applications. Liu et al. (S. Liu et al., 2022a) employed a pulse wave Nd: YAG laser to weld Ti-6Al4V to AA7075, using Al alloy 4047 filler material. They observed that the modulation of laser pulses had an impact on the dwell time of IMCs at elevated temperatures, resulting in a higher growth rate. Consequently, this phenomenon could potentially influence the thickness of the IMC. Li et

al. (P. Li, Lei, Zhang, & Chen, 2020a) opted for Si-containing solder as filler materials in dual-spot laser welded-brazed Ti-Al joints to examine the impact of Si content on interfacial reactions and mechanical properties. They concluded that the inclusion of Si in the filler metal resulted in an improvement in joint strength. Gu et al. (Gu et al., 2021a) successfully achieved a butt joint between TC4 Ti alloy and 6082 Al alloy using a Nb sheet and an offset pulsed laser beam. They observed that by carefully selecting the offset distance and welding energy, they were able to achieve a metallurgical bonding consisting of two distinct metallurgical joining interfaces.

Gas pressure, types, positioning, and their effects on the joint in laser welding are critical parameters that significantly influence the quality, strength, and properties of the weld. In laser welding, the gas used can either be an inert gas, such as argon or helium, or an active gas like oxygen or nitrogen, depending on the materials being welded and the desired properties of the weld. Inert gases are primarily used to shield the weld area from atmospheric contamination, preventing oxidation and other reactions that could weaken the weld. Active gases, on the other hand, can interact with the material to form stronger or specific weld characteristics. The positioning of the gas nozzle relative to the laser beam and the workpiece is another crucial factor. The nozzle must be positioned to ensure adequate shielding of the weld pool while not interfering with the laser beam's path. The gas pressure plays a critical role in determining the stability of the weld pool, penetration depth, and the expulsion of molten material from the weld area. Higher gas pressures can increase the depth of penetration by ejecting the molten material more effectively but may also lead to increased porosity or spatter if not properly controlled. These aspects of gas selection, positioning, and pressure in laser welding directly impact the quality of the joint.

The strength of the weld zone is indicative of its usefulness and quality (Wu & Wang, 2010). Evaluating the mechanical characteristics of weldments, including hardness and elastic modulus, is crucial to ensure their strength and structural stability throughout use. The significance of hardness is essential in several academic investigations. The advantageousness of high or low hardness depends on the specific uses, especially for

dissimilar joints. The evaluation of material properties at the nanoscale is necessary to observe the underlying physical phenomena associated with the reinforcement of weldments. Microhardness testing does not provide sufficient resolution to accurately discern changes occurring at the level of individual grains. Hence, the use of nanoindentation enables an analysis of the hardness properties of individual grains. Multiple indentations may be made on a single grain to get an average measurement of its hardness. Therefore, it is essential to examine the localized strengthening process in weldments at the grain level (B. Yang & Vehoff, 2005b). Instrumented indentation is a commonly used methodology for the evaluation of various materials, including thin coatings on substrates, welded joints, and biomaterials like dental crowns. Traditionally the assessment of the characteristics of welded joints has relied on the use of destructive methods (Fischer-Cripps, 2011). Oliver and Pharr (Oliver & Pharr, 1992b) proposed a technique for quantifying hardness and elastic modulus with the use of nanoindentation. However, it should be noted that this particular approach applies just to materials that tend to sink in, and it is not effective for materials that pile up during the indentation process (Fadaeifard et al., 2019). Kese et al. (Kese et al., 2004a) used images obtained from an atomic force microscope (AFM) to include the area of pile-up in the residual indents. This additional area was then combined with the area determined using the Oliver and Pharr approach. However, a limitation of AFM imaging is the occurrence of elastic recovery between indentation and imaging. As a result, the measured values may seem to be lower than the true values. Tuck et al. (Tuck et al., 2001a) used an indentation-based methodology to determine the nanoproperties of a thick TiN coating on a substrate composed of tungsten carbide-cobalt. This investigation focused on the characterization of bulk hard materials.

Previous studies lacked comprehensive and in-depth examinations of microstructure and nanomechanical behaviour in dissimilar laser welding of AA7075-Ti-6Al-4V with interlayers. Furthermore, given the extensive applications of AA7075-Ti-6Al-4V joints across various industries, there is a clear need for the development of a new and robust joining technique for these materials. In the present study, dissimilar laser-welded AA7075-Ti-6Al-4V joints with silver (Ag) interlayer, are prepared at optimum laser welding process

parameters. The heat-affected zone (HAZ), base alloy (BA), and fusion zone (FZ) are areas of similar significance in terms of the usage and quality of weldments (Wu et al., 2010). Therefore, the main contribution of this work is to evaluate the weldments in terms of microstructure and nanomechanical behaviour of the distinct regions formed after dissimilar welding of AA7075-Ti-6Al-4V across the weld zone. The Oliver-Pharr method, AFM analysis, and work of indentation are three commonly used techniques for evaluating nano hardness using a nanoindenter and an AFM. The primary objective is to compare these approaches and correlate microstructure with the nanomechanical behavior of the joints. The nanomechanical response is also compared with microhardness testing to understand their underlying concepts to evaluate their suitability for evaluating the strengthening of dissimilar joints of Ti-6Al-4V and AA7075 with Ag interlayer achieved by the laser welding. The work is organized into sections detailing the experimental procedure—including materials, laser welding parameters, and various analysis methods such as microstructural characterization and nanoindentation—and results and discussion, which focus on the welded area's microstructure, nanoindentation analysis, and hardness measurements using different methodologies. The study concludes with a comparison of the obtained results. The current study findings are anticipated to provide valuable insights into microstructural analysis and nanomechanical properties of laser-welded dissimilar materials and to pave the way for more effective laser welding of AA7075-Ti-6Al-4V.

1.2 EXPERIMENTAL PROCEDURE

1.2.1 Materials and laser welding conditions

Regarding the experimental conditions of this work, the annealed sheets of AA7075 and Ti-6Al-4V were welded using the laser beam welding (LBW) process, with dimensions of 80 x 50 x 1.6 mm. An interlayer of Ag foil with a thickness of approximately 380 μm was placed between the AA7075 and Ti-6Al-4V sheets. **Table 1.1** presents the chemical compositions measured using Energy Dispersive Spectroscopy (EDS) of the base alloys. As

can be seen in **Figure 1.1**, the samples were welded using a butt configuration. **Table 1.2** shows the optimal laser welding process parameters used after preliminary experiments.

Tableau 1.1 Chemical composition of Ti-6Al-4V and AA7075 alloys as measured by EDS (wt. %)

Alloys	Elements												
	Al	**Sn**	**Mg**	**V**	**Zn**	**Zr**	**Fe**	**Ti**	**C**	**Nb**	**Cu**	**Mn**	**Si**
Ti6Al4V	5.87	0.076	-	4.12	-	0.021	0.17	Bal.	0.352	0.04	-	-	0.028
AA7075	Bal.	-	0.76	-	5.24	-	0.23	-	-	-	0.21	0.13	0.65

Tableau 1.2 Parameters of laser welding for dissimilar weldments of AA7075 and Ti-6Al-4V with Ag interlayer

Laser power (kW)	**Welding speed (mm/sec)**	**Focal length (mm)**	**Focal spot diameter (mm)**
3	50	310	0.92

The welding process was performed using a fiber laser equipped with an IPG Photonics Ytterbium Laser Systems source model (YLS-3000-ST2). The laser used for the current study is classified as a class 4 laser, with a maximum power output of 3 kilowatts. This laser operates by emitting continuous waves with a wavelength of 1070 nanometers. The laser source is connected to the BIMO HIGHYAG laser head using a method that utilizes high-performance optical fibers with a diameter of 600 μm. The laser head is outfitted with a lens that has a fixed focal length of 310 mm. Additionally, it has a focusing module with a value of $M_{foc} = 1.50$ and a zoom collimator that may be adjusted. The outcome of this process yields a circular focal point with a diameter that varies between 0.3 and 1.53 mm. The specific

dimension is dependent upon the properties of the focusing module, the collimation module, and the diameter of the fiber used. This relationship is mathematically described by Equation Eq. (1):

$$\phi_{focus} = M_{col.}.M_{foc}.\phi_{fiber} \quad (1)$$

The parameter ϕ represents the diameter of the laser spot at the focal plane. The collimation modulus, denoted as M_{col}, is a constant value set at 1.022. The modulus of focalization, denoted as $M_{foc} = 1.5$, is a measure of the focusing capability. Additionally, the diameter of the fiber used in the experiment is denoted as $\phi_{fiber} = 600$ µm. The collimator was adjusted to its lowest level, leading to a focused spot diameter of 0.92 mm. The laser head is attached to a FANUC M-710iC robot, which has a 6-axis articulated arm that enables precise and preprogrammed motions in various directions, as shown in **Figure 1.1**. The robotic system has a payload capacity of 70 kg, a manual linear speed of 250 mm/s, and a maximum automated angular speed ranging from 175 to 355 °/s. **Table 1.2** presents the optimum welding parameters used to achieve complete penetration in butt-joined weldments through LBW. Generally, to enhance the strength of weldments, it is common to ensure that the direction of welding remains perpendicular to the rolling direction of the base plates. Nevertheless, in the current study, the welding process was carried out in alignment with the rolling direction of the base plates.

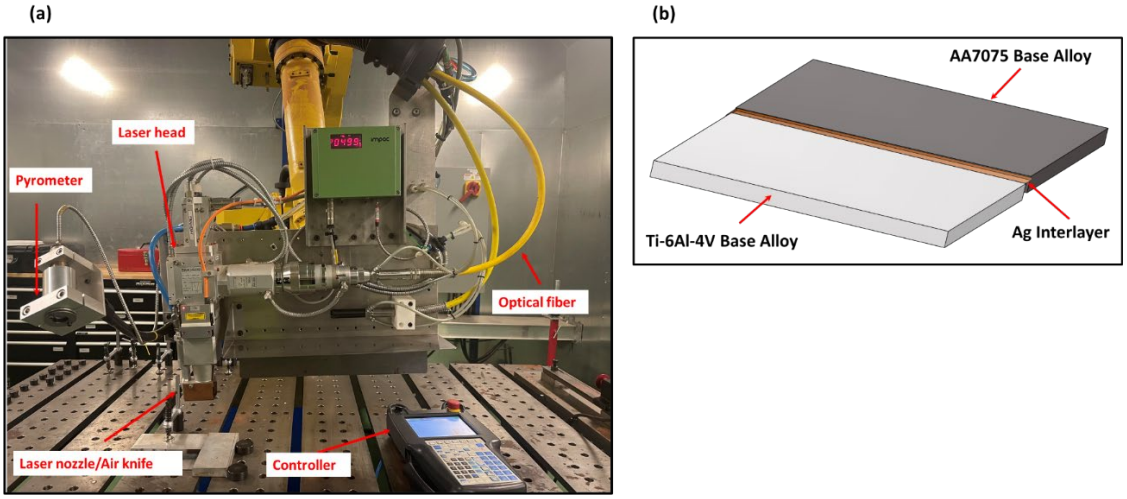

Figure 1.1 (a) Laser cell (3000W: YLS-3000-ST2) mounted on a FANUC robot with 6 axes and (b) Schematic of base alloys used for welding along with interlayer

1.2.2 Microstructural characterization

In order to study the microstructure of the weldments, perpendicular samples were taken, as shown in **Figure 1.2**. Following the machining process, the samples were mounted with epoxy to facilitate metallographic analysis. Subsequently, the mounted sample was ground with the use of SiC grit papers ranging in size from 240 to 4000 microns. After that, the specimens were subjected to polishing using a non-ferrous velvet cloth and 0.05-mm alumina paste. Finally, the sample underwent etching using the Kroll solution, consisting of 6% HNO_3 and 2% HF by volume in distilled water. The microstructure of the specimens was examined using an Olympus BH2-UMA optical microscope.

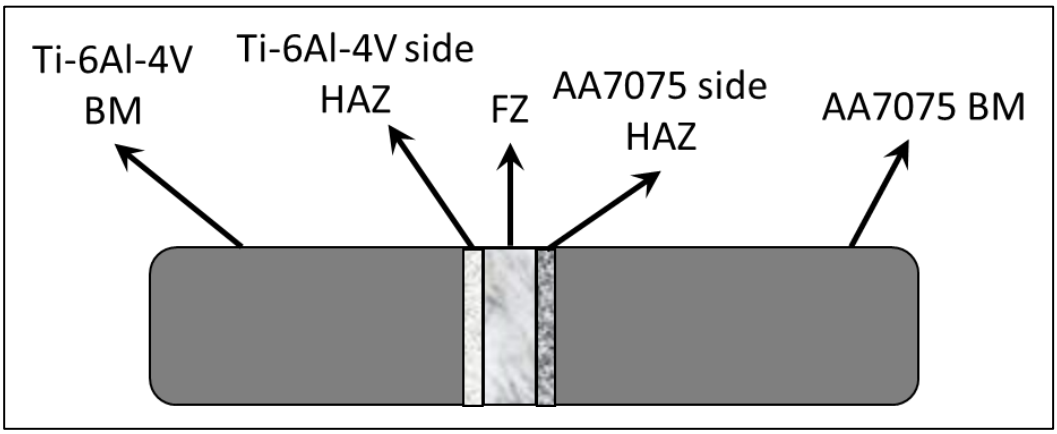

Figure 1.2 Schematic of sample used for microstructural analysis

1.2.3 Sectioning of samples for microstructural, mechanical, and nanomechanical analysis

Specimens for metallographic examination and tensile testing were cut from the welded sheet using wire Electrical Discharge Machining (EDM), as depicted in **Figure 1.3**. Similar specimens were used for EDS, microhardness, and nanoindentation tests. Additionally, the specimens for tensile testing were prepared following the ASTM E8M-04 standard, having a gauge length of 25 mm. The tensile testing was performed on a 100 kN MTS testing machine at a strain rate of 2.5 mm/min.

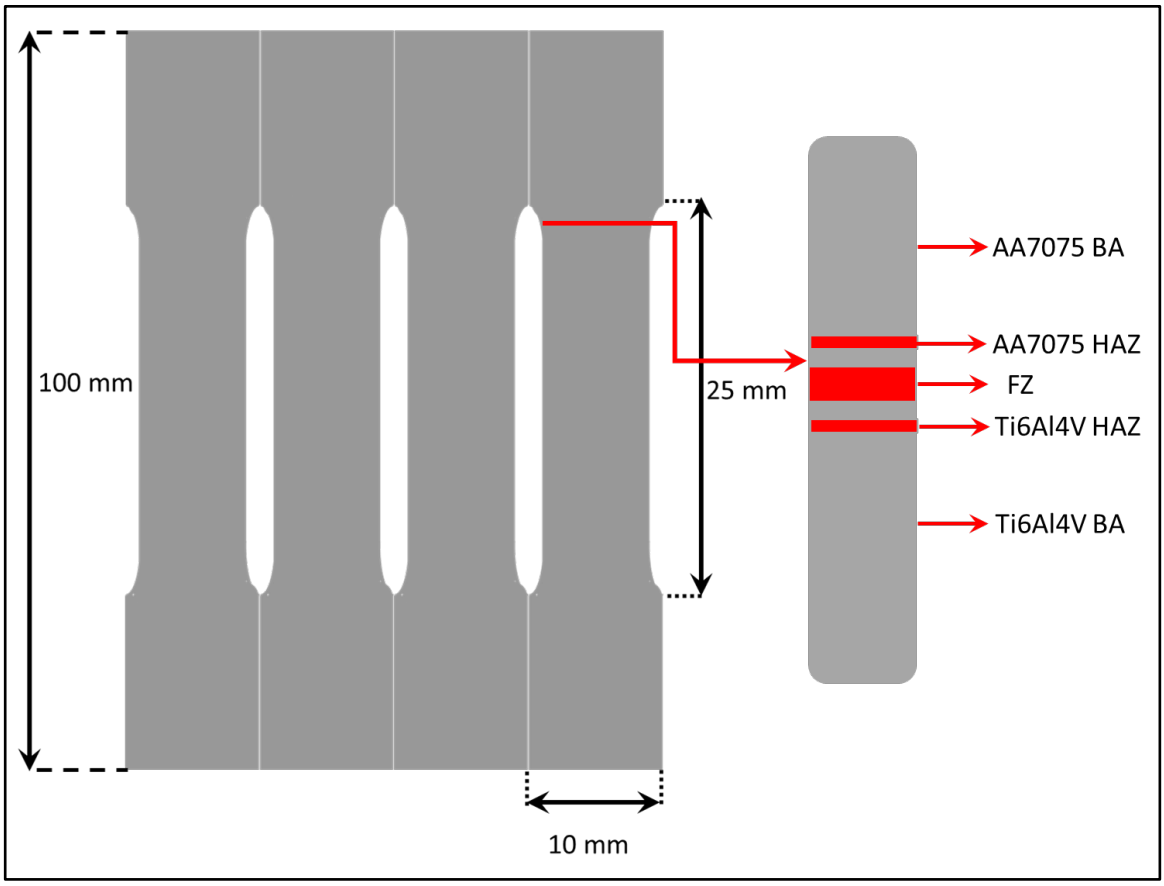

Figure 1.3 Schematic illustration of tensile tests and microstructure analysis samples

1.2.4 Nanoindentation analysis

For the nanoindentation analysis, the metallographic specimens were subsequently tested using a Nano indenter (iMicro from Nanomechanics, Inc.) with a Berkovich indenter tip. The software of the iMicro nanoindenter incorporates a one-of-a-kind tip-calibration system that enables rapid, precise, and automated tip calibration. The nanoindenter has a damping coefficient of 0.05 N-s/m and a drift rate of <0.05 nm/s. At each weld zone i.e., FZ, HAZ on both sides of FZ, and both BAs, a 2x2 grid was positioned for BAs and HAZs while a 3x3 grid was used for FZ due to high variance in it. Using a schematic illustration, this grid is depicted in **Figure 1.4**. The maximum load was maintained at around 200 mN, while the depth was changed within the range of roughly 2000 to 2500 nm for BAs and HAZs. The

selection of the load is based upon many criteria. One example of this phenomenon is that the nanohardness of a bulk material may be greatly overestimated due to surface oxidation. Mante et al. (Mante et al., 1999) investigated the nanohardness of polycrystalline bulk titanium by using different depths of indentations. When the indentation was conducted at depths less than 100 nm, a significant rise of 34% in nano hardness measurement was observed in proximity to the surface. When the indentation was performed at a depth of approximately 2000 nm, the measured hardness values closely matched the established standard values. Many studies have been conducted on the indentation of bulk material to get an appropriate value for the indentation load. The hardness and elastic modulus of Ti and TiB composite materials produced through the process of selective laser melting (SLM) were examined by Attar et al. (Attar et al., 2017). Both materials were subjected to a load of 10 mN, resulting in a depth of 350 nm for titanium (Ti) and 260 nm for the titanium-titanium boride (Ti-TiB) composite. Jamleh et al. (Jamleh et al., 2012) also investigated the use of nanoindentation using the Berkovich indenter tip. They examined the impact of cyclic fatigue on nickel-titanium (NiTi) endodontic equipment. The maximum load was kept at 100 mN and they obtained a resulting depth of 1300 nm. Hassaan et al. (Hassaan et al., 2021) assessed nanohardness and effective elastic moduli in TIG-welded Ti-5Al-2.5Sn alloy using nanoindentation, revealing significant differences due to pile-up morphology and residual stress, with the work of indentation as the preferred assessment method. Based on an analysis of previous studies, an indentation measurement of roughly 2000-2500 nm would be sufficient. This measurement would need the application of a load within the range of 200 mN. In the process of nanoindentation testing, the depth of penetration is continually monitored as the applied stress increases. The loading and unloading curves are obtained, which are then used for the calculation of various properties such as hardness, elastic modulus, and residual stresses of the welded specimen.

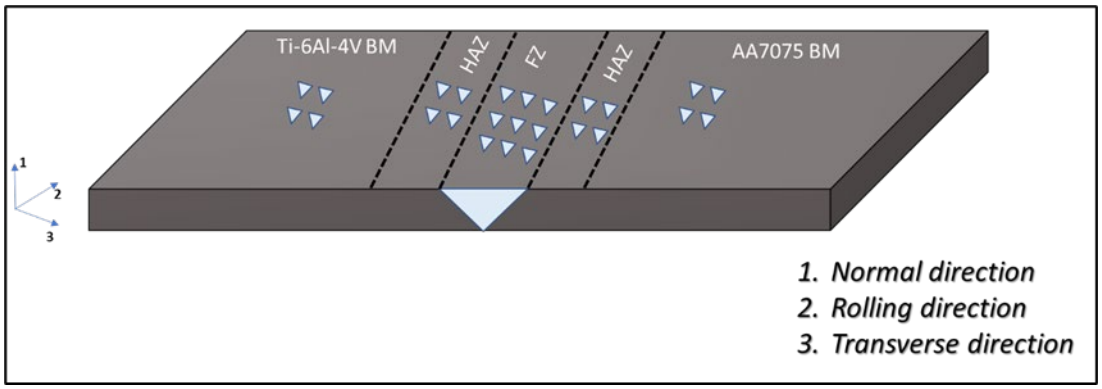

Figure 1.4 A schematic illustration of distinct zones after welding and corresponding indents produced in these zones for nanoindentation

1.2.4.1 Analysis using the Oliver and Pharr method

The Oliver and Pharr (OP) technique serves as the fundamental basis for nanoindentation, providing a framework for quantifying various mechanical properties such as hardness and elastic modulus, as previously outlined by Oliver and Pharr (Oliver & Pharr, 2004a). The equations are provided as follows:

$$H = \frac{P_{max}}{A_C} \tag{2}$$

The expression for A_c is represented as follows:

$$A_C = C_1 h_c^2 + C_2 h_C + \max C_8 h_c^{1/128} \tag{3}$$

The constants C_n are determined using the process of curve fitting (Oliver & Pharr, 2004a). Fixing the indentation depth for all Nanoindenter experiments and then calculating the peak force necessary to achieve the peak depth is a very reasonable approach. The residual stress can be calculated by measuring the difference in peak force (Dean et al., 2011). To account for the impact of Berkovich tip deformation on the elastic modulus of the material at the nanoscale, the effective elastic modulus is used (Oliver & Pharr, 1992c). The technique proposed by Oliver and Pharr involves the determination of the reduced or combined elastic

modulus, which takes into account the elastic deformation of both the specimen and the indenter.

The effective modulus (E_{eff}) may be determined based on the unloading stiffness using the following equation (4):

$$E_{eff} = \frac{S\sqrt{\pi}}{2\beta\sqrt{A}} \quad (4)$$

The parameter 'β' is a dimensionless quantity that takes into consideration the variations in stiffness resulting from the absence of axial symmetry in pyramidal indenters or other physical phenomena. The literature review suggests that there is no clear indication of the individual material's optimal maximum penetration depth. Generally, a penetration depth of roughly 1500 nm is selected for low alloyed and austenitic stainless steels [31], while carbon steel SS400 is chosen to have a range of 200-250 nm (Pham et al., 2014). Aerospace aluminium alloys, on the other hand, are often designed to have a 600 nm indentation depth(Khan et al., 2011), while Al-Mg and Al-Mg-Si alloys are optimized for 200 nm (Charitidis et al., 2012b). There is no universally applicable rule to adhere to these principles; however, the determination of the optimal depth of penetration is dependent upon the specific nature of the problem being investigated. In the case of a material composed of two distinct phases, an indentation depth (h) that is less than the characteristic length 'D' of each phase's microstructure may provide insights into the material property of an individual phase. However, when the indentation depth (h) is greater than the material's characteristic length scale (D), the indentation response may provide information about the typical material qualities in a statistical manner. In the latter scenario, a single indentation will be enough for the test. However, in the former scenario, many indentations are required to determine the phase properties of the material (Constantinides & Ulm, 2007). Additionally, a greater penetration depth might lead to significant accumulation of material at the tip of the indenter (pile up), perhaps causing an overestimation of the hardness value. It is important to acknowledge that the Oliver and Pharr approach is founded upon the absence of pile-up (Bolshakov & Pharr, 1998; Kese et al., 2004a; Saha & Nix, 2001a).

1.2.4.2 Total work method

Tuck et al. were the first to propose this method for determining hardness (Tuck et al., 2001b). In this particular methodology, the measurement of hardness is determined by evaluating the work of indentation, which is derived from the load-depth curve acquired by nanoindentation. The measurement of total work is determined by calculating the area under the loading curve. In contrast, the measurement of elastic work is determined by calculating the area under the unloading curve. As per Tuck et al. (Tuck et al., 2001b), the total work may be measured by calculating the integral of the load-depth curve, which represents the area under the curve as shown in equation 5:

$$W_t = \int_0^{h_{max}} P\, dh \tag{5}$$

As per Kick's law;

$$P = ch^2$$

Therefore, we can modify equation 5 into equation 6 as follows:

$$W_t = \int_0^{h_{max}} ch^2\, dh$$

$$W_t = \frac{Ch_{max}^2}{3} = \frac{P_{max}h_{max}}{3} \tag{6}$$

The determination of hardness may be obtained through the application of either the Vickers or the Berkovich indentation testing methods. In both cases, a generalized formula can be developed to express hardness in terms of the depth of penetration as written below in equation 7:

$$H = \frac{kP}{h^2} \tag{7}$$

The value of k is 0.0378 for the Vickers four-sided pyramidal indenter and 0.0408 for the three-sided Berkovich pyramidal indenter. By rearranging the previous relation, we may get the following expression:

By substituting the given values of P and H into Equation 6 and performing integration:

$$W_t = \int_0^{h_{max}} \frac{Hh^2}{k}\, dh$$

$$\Rightarrow \quad \frac{Hh^2}{3k} = \frac{P_{max}h_{max}}{3} \tag{8}$$

Furthermore, according to equation 8, the value of 'h' is defined as:

$$h = \sqrt{\frac{kP}{H}}$$

Substituting the value of 'h' into equation 8 yields equation 9:

$$H = \frac{kP_{max}^3}{9W_t^2} \tag{9}$$

The definition of hardness specifies that the above-mentioned formulation only includes plastic work. Therefore, if we substitute the total work with plastic work, we get the expression for hardness in terms of plastic work.

1.2.4.3 Plastic work method

As previously mentioned, by substituting the total work with plastic work in the equation for hardness, we can conform to the definition of hardness and get the following equation 10:

$$H = \frac{kP_{max}^3}{9W_p^2} \tag{10}$$

The calculation of plastic work involves the subtraction of elastic work from the overall work as written below:

$$W_P = W_t - W_e$$

The elastic work can be calculated by integrating the unloading curve according to Kick's law:

$$W_e = \int_{h_f}^{h_{max}} P\, dh$$

$$\Rightarrow \frac{P_{max} h_{max}}{3} - \frac{P_f h_f}{3} \quad (11)$$

The plastic work method is used for the determination of hardness value, without considering the area value. Consequently, it will remain unaffected by the pile-ups due to indentation (Tuck et al., 2001c).

1.2.4.4 Atomic force microscopy area measurement method

The circular pile-up phenomenon surrounding the indentation has been studied by Beegan et al. and Saha and Nix (Beegan et al., 2005; Saha & Nix, 2001b). Moreover, Kese et al. (Kese et al., 2004a) characterized the pile-up of material around the indentation as a semi-ellipse. By assuming that the pile-up takes the shape of a semi-ellipse, similar to the one seen in **Figure 1.5**, the pile-ups may be determined by analyzing the AFM images. **Figure 1.5** shows Edge L represents the initiation point of the pile-up, while Edge T corresponds to the location where the pile-up reaches its maximum height. The Berkovich indenter tip has a pyramidal form that exhibits geometric self-similarity, characterized by an included half angle of 65.27°. This leads to the formation of the indentation on the tip, which takes the shape of an equilateral triangle, as seen in the schematic in **Figure 1.6**. The variable "a" represents the length of the minor axis of the semi-ellipse, whereas the variable "b" represents the length of the major axis of the semi-ellipse.

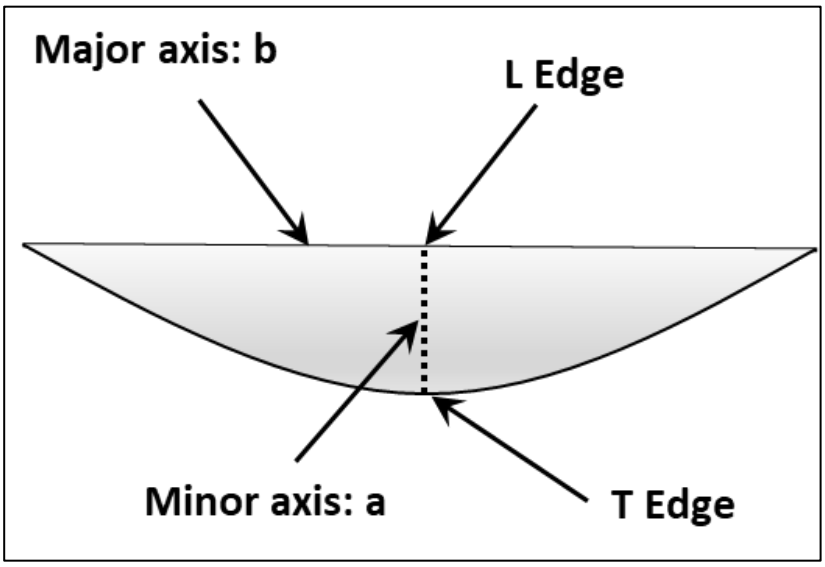

Figure 1.5 Schematic illustration of a semi-ellipse depicting the configuration of material pile up around an indentation

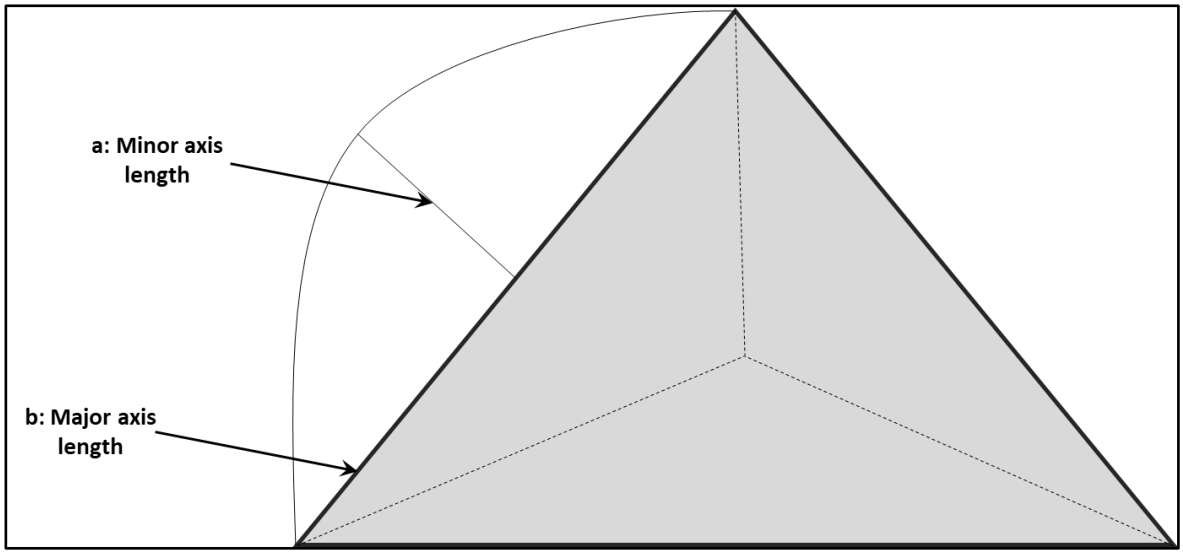

Figure 1.6 Schematic of equilateral triangle indentation resulting from the indentation of a Berkovich tip

The formula for calculating the area of an equilateral triangle is as follows:

$$A_e = \frac{b^2}{4}\tan 60°$$

$$\Rightarrow A_e = 0.433b^2$$

To get an optimal Berkovich tip, the following criteria must be met:

$$A_e = A_c$$

$$24.56h_c^2 = 0.433b^2$$

$$\Rightarrow b = 7.531h_c \quad (12)$$

The symbol "A_c" represents the contact area for a Berkovich tip, assuming ideal conditions and excluding any pile-up effects. Utilizing equation 12, we have successfully determined the magnitude of the principal axis of the semi-elliptical accumulation.

Furthermore, the formula for calculating the area of a semi-ellipse is as follows:

$$A = \frac{ab\pi}{4}$$

As in the case of minor axis (a) value of the of each semi-ellipse in the pile-ups varies, we can see the following relationship:

$$A_{pu} = \frac{\pi b}{4}\sum a_i$$

$$\Rightarrow A_{pu} = 5.914h_c\sum a_i$$

Hence, the overall indentation area is determined by the combined values of the contact area obtained from the application of the Oliver and Pharr method's area function, and the pile-up area as shown below:

$$A = A_{pu} + A_{op}$$

$$A = A_{op} + 5.914h_c\sum a_i \quad (13)$$

Kese et al. (Kese et al., 2004a) used equation 13, to calculate the area containing the pile-ups. Subsequently, this area is used for the computation of nanohardness.

1.3 RESULTS AND DISCUSSION

1.3.1 Microstructural characterization

As mentioned in the methodology section, in this study sheets of the titanium alloy Ti-6Al-4V and the aluminium alloy 7075 (AA7075) with a thickness of 1.6 mm were used along with an Ag interlayer of 380 μm. The Ti-6Al-4V alloy is mostly composed of equiaxed hexagonal close-packed (hcp) α-phase grains, along with an intergranular cubic body-centered cubic (bcc) β-phase present in the alloy as shown in **Figure 1.7(a)**. Additionally, the microstructure of base alloy AA7075 mostly consists of a globular aluminium cubic (fcc) phase, accompanied by small pits as seen in **Figure 1.7(b)**. These pits are likely a result of the removal of $MgZn_2$ precipitates during the etching process.

The evolution of microstructure as a result of the dissimilar joining of Ti-6Al-4V and AA7075 is shown in **Figure 1.8(a)**. An interlayer of Ag was used to modify the composition of the alloy during the welding process and reduce susceptibility to cracking. As seen in **Figure 1.8(b)**, the partly melted Ti-6Al-4V region near the fusion zone exhibits notable differences in microstructure and properties. This difference is referred to as macrosegregation rather than microsegregation. The macrosegregation process is associated with the liquidus temperature of the base materials and the weld pool. In the case that the liquidus temperature of the weld pool is lower than that of the base material, it might result in partial melting of the base material and the development of macrosegregation (Oliveira et al., 2017). In the present investigation, the laser beam was directed toward the Ti-6Al-4V base alloy. As a result of the significant energy density of the laser, a section of the Ti-6Al-4V base alloy experienced heating to a semi-solid or even liquid state. This heated region then migrated toward the melt pool due to the convection flow derived from the Marangoni effect(Oliveira et al., 2017). Upon entering the melt pool, the Ti-6Al-4V alloy underwent fast cooling within a short period, resulting in a semi-solid or even liquid state. However, due to

insufficient mixing with the liquidous Al alloy present in the melt pool, the Ti-6Al-4V alloy eventually solidified, forming partly melted islands of Ti-6Al-4V. Moreover, higher cooling after the welding process results in the creation of a distinct crystalline structure known as modified α towards the Ti-6Al-4V side, which has a needle-like morphology. A further increase in the cooling rate results in the development of fine acicular α, which is often regarded as needle-like martensite which is formed in HAZ of the Ti-6Al-4V side. The presence of the IMC layer and dendrites at the Al/Ti contact can be seen in **Figure 1.8**. During the cooling stage, Ti atoms diffuse into developing IMC dendrites and solidify on their surface, leading to the formation of Ti IMC dendrites enriched with Ti. In **Figure 1.8(c)**, the presence of IMCs can also be seen inside the FZ region, as shown by the grey colour. Due to the convective movement of the melt pool, IMCs originated from disrupted columnar dendritic structures. During rapid solidification, Si-segregation near grain boundaries causes dark lines in the Al-Si eutectics. The microstructure of α-Al reveals the presence of numerous small black Mg-Zn particles at the grain boundary, as shown in **Figure 1.8(d)**. These particles contribute to the increase of the mechanical properties of the AA7075 alloy owing to the precipitation strengthening phenomenon. The thermal cycle temperature during laser welding dissolves the precipitated phase in the HAZ into the aluminium alloy matrix, as shown in **Figure 1.8(d)**.

Elemental composition analysis was performed to examine variations across all weld zones by selecting different points. The cross-sectional views of the weldment are shown in **Figure 1.9**, **Figure 1.10,** and **Figure 1.11**. The first region, situated at the interface between Ti-6Al-4V and HAZ, is followed by a subsequent region inside the FZ. The microstructures that are relevant to the topic are shown in **Figure 1.8(a), (b), (c), and (d).** The results are represented in **Table 1.3**. **Figure 1.9** depicts the element composition variation at the interface of Ti-6Al4V and HAZ. Al and Ti compositions are observed to change abruptly at the interface between the Ti-6Al-4V and HAZ-containing IMC layer as shown in **Table 1.4**. However, the compositions are stable throughout the weldment, except for where titanium aluminides and Al-Si eutectic exist. Based on the obtained results, it can be inferred that the particles exhibiting a lighter shade of grey are composed of Ti, Al, and Si components. The

presence of Al-Si eutectics can be seen inside the FZ in certain areas characterized by a lower proportion of aluminium and a larger percentage of silicon. **Figure 1.10** illustrates the IMC layer at the interface between the Ti-6Al-4V and FZ. The IMC dendrites exhibit extension from the IMC layer to the fusion zone. Numerous pieces of IMCs, characterized by their lighter grey appearance, were detected scattered throughout IMC dendrites. These fragments are likely to have originated from broken dendrite arms, which may be attributed to the strong convective flow that occurs during the process of the welding process. The EDS technique was used to ascertain the compositions of the spots located on both the IMC layer and the IMC segments. The results are shown in **Table 1.3** as points 3 and 4. The atomic ratio at point 3 from **Table 1.3** shows the presence of high aluminium content as compared to Ti, indicating that the composition of the IMC layer can be Al_3Ti instead of $AlTi_3$ and AlTi. It is also evident from the thermodynamic viewpoint, that the formation of Al_3Ti is easier than the formation of $AlTi_3$ and TiAl. This is owing to the fact that Al_3Ti exhibits a comparatively lower Gibbs standard free energy of formation compared to the other three (Sujata et al., 1997). The observations made at point 4 in the FZ next to the Ti-6Al-4V side, point 5 in the HAZ of the AA7075 side, and point 6 in the FZ adjacent to the AA7075 side indicate that the main component in these areas is aluminum. Points 5 and 6 display minimum quantities of Ti Si and Ag, whereas point 4 is anticipated to have an aluminium-silicon (Al-Si) eutectic along with trace amounts of Ti and V. As discussed, the Ti/Al interface reaction resulted in the formation of Al_3Ti particles, and the Al_3Ti particles were either carried by the molten pool or extruded by nearby Al_3Ti grains in the interfacial IMCs. Although increasing the Al_3Ti particles can enhance the strength of the weld joint, it is important to note that this can also intensify the Ti/Al contact reaction. As a result, the Al_3Ti IMCs layer becomes abnormally thick, leading to joint failure. Therefore, it is crucial to control the Ti/Al contact reaction to a reasonable degree.

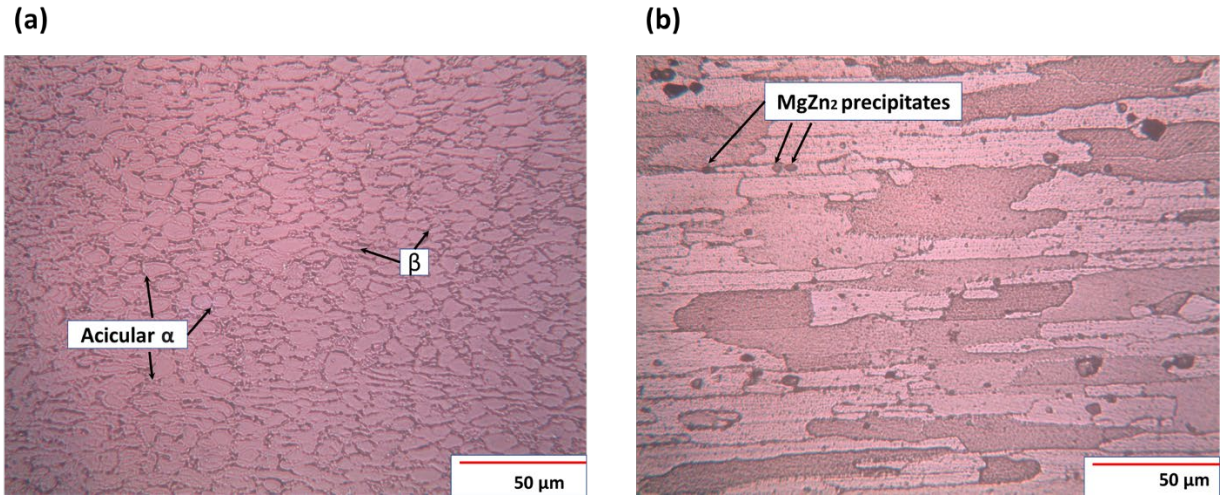

Figure 1.7 (a) Base alloy Ti-6Al-4V and (b) Base alloy AA7075

Moreover, as the temperature rises, a more consistent and gradual formation of intermetallic compounds occurs in the interface area, potentially leading to an enhancement in the material's overall hardness (as discussed below). In low-temperature conditions, the limited contact surface area results in minimal atomic diffusion. This might result in a lower hardness. As presented earlier, the presence of Ag between the AA7075 and Ti-6Al-4V reduces the formation of more brittle IMCs. However, it might lead to the development of $AgTi_3$ towards the Ti-6Al-4V side. It has been observed that the embrittlement impact of Ti-Ag base intermetallics is less than that of Al-Ti intermetallics, which results in decreasing the bond strength in FZ. This is because Ti-Ag base intermetallic has a lower bond strength. In addition, owing to the formation of $AgTi_3$ IMCs towards the Ti-6Al-4V side also led to a lowering in the overall porosity in the FZ as evident from **Figure 1.8**. Hence, incorporating Ag as an interlayer improves joint quality by reducing the formation of brittle IMCs and minimizing void formation within the weldment.

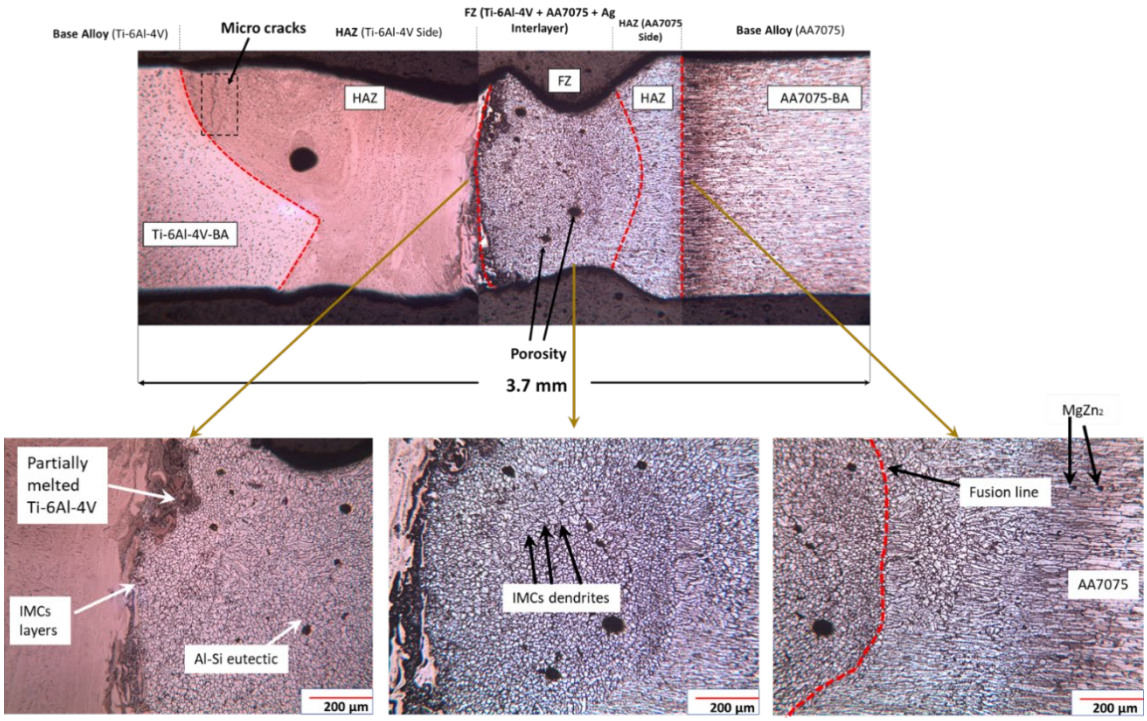

Figure 1.8 (a) Overall view of all the welding zones, (b) Ti-6Al-4V side, (c) FZ, and (d) AA7075 side

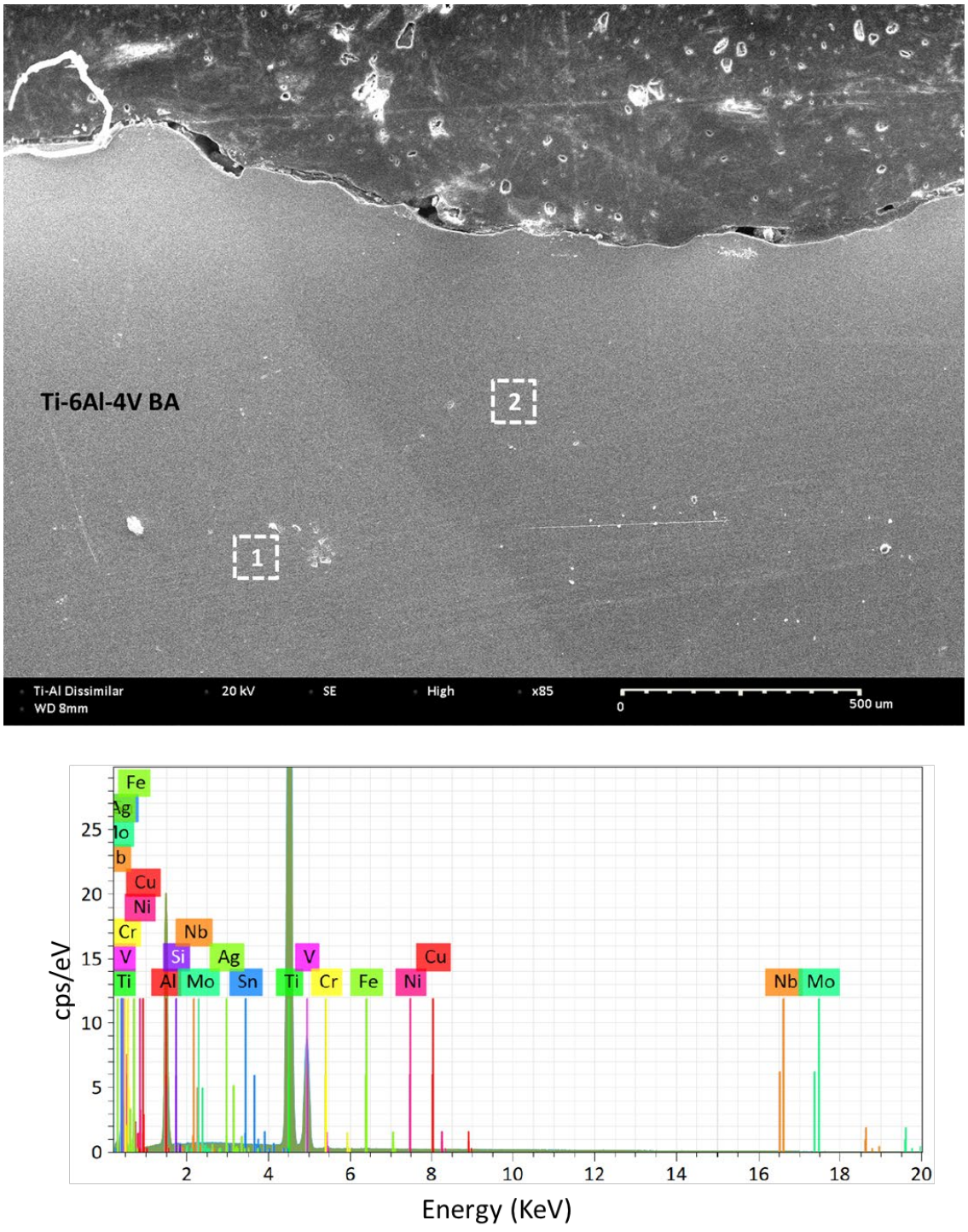

Figure 1.9 SEM image of Ti-6Al-4V side of weldment indicating EDS points along with EDS spectrum

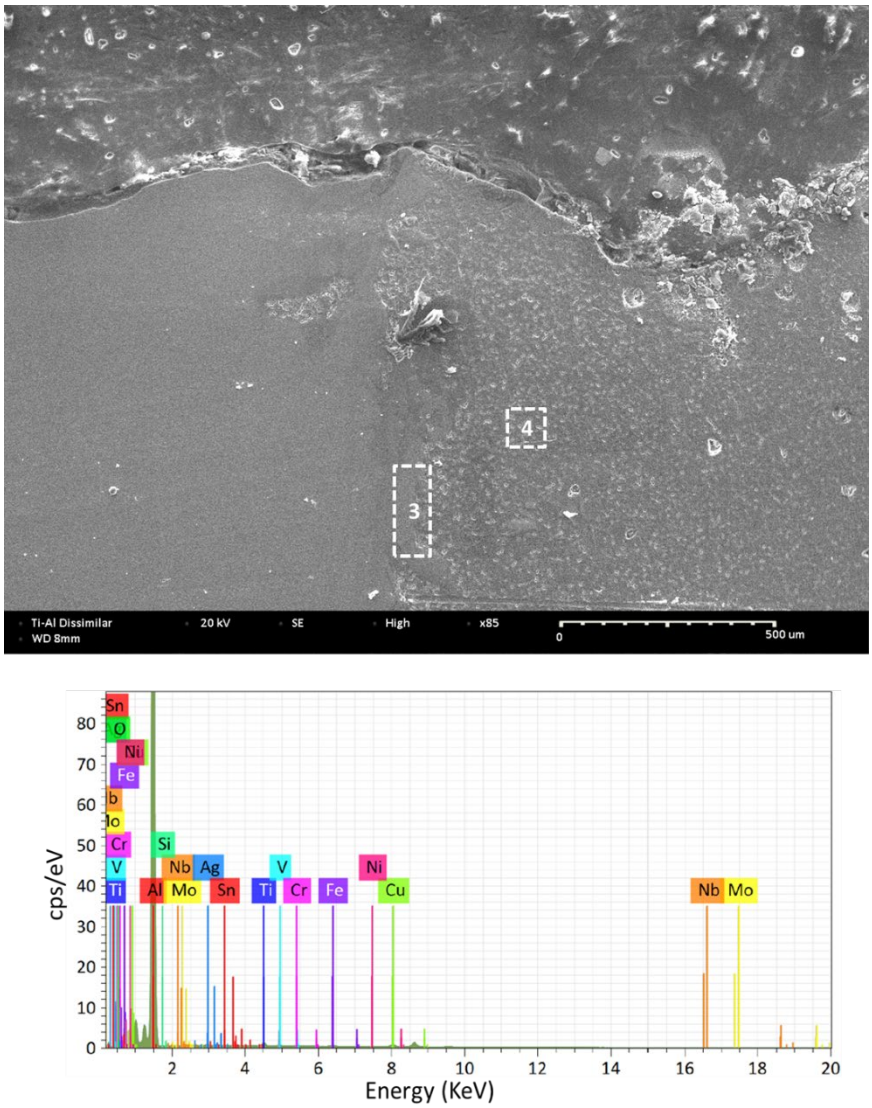

Figure 1.10 SEM image of weldment indicating EDS points along with EDS spectrum

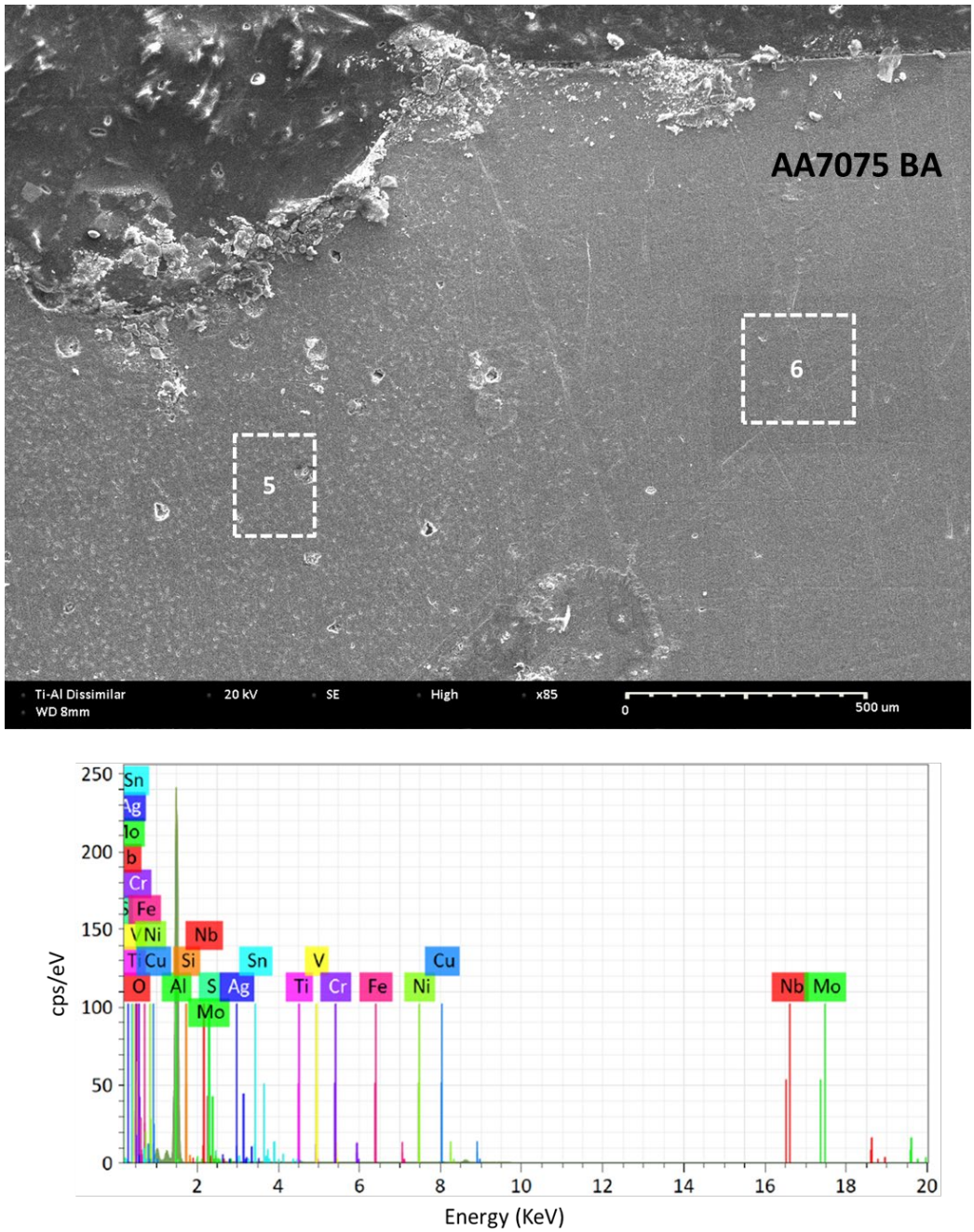

Figure 1.11 SEM image of AA7075 side of weldment indicating EDS points along with EDS spectrum

Tableau 1.3 Elemental compositional analysis as measured by EDS (wt. %)

Spectrum no.	Al	Si	Ti	V	Cr	Fe	Ni	Cu	Mg	Ag	Sn	Possible phases
1	5.60	0.01	90.66	3.40	0.00	0.19	0.06	0.01	0.05	0.00	0.00	Ti
2	10.38	0.07	76.25	2.87	0.00	0.18	0.01	0.18	0.04	5.01	0.00	$AgTi_3$
3	95.20	0.04	1.40	0.05	0.20	0.59	0.03	1.29	0.13	4.97	0.09	Al_3Ti
4	95.65	0.03	1.18	0.03	0.22	0.66	0.04	1.33	0.01	5.79	0.05	Ag_2Al, Al3Ti
5	93.14	0.06	1.47	0.05	0.21	0.60	0.06	0.95	2.31	1.05	0.07	Al (Mg enriched)
6	97.25	0.08	0.01	0.01	0.23	0.27	0.08	0.48	0.21	1.21	0.17	Al

1.3.2 Tensile testing

Figure 1.12 presents a comparison of tensile test properties of AA7075 BA and Ti-6Al-4V BA and AA7075/Ti-6Al-4V weldment with Ag interlayer. For the aluminum alloy AA7075, the material exhibits a high tensile strength, as indicated by the high peak on the curve; however, it also shows a relatively abrupt failure. In contrast, the Ti-6Al-4V demonstrates a different type of mechanical response: it gradually deforms with increasing stress and doesn't abruptly fail. When these two materials are joined together using a silver interlayer, the resultant joint shows a decrease in tensile strength compared to the base alloys, which suggests that the joint is less able to carry load compared to the individual base materials. However, the addition of an Ag interlayer significantly enhanced the ductility of the joint.

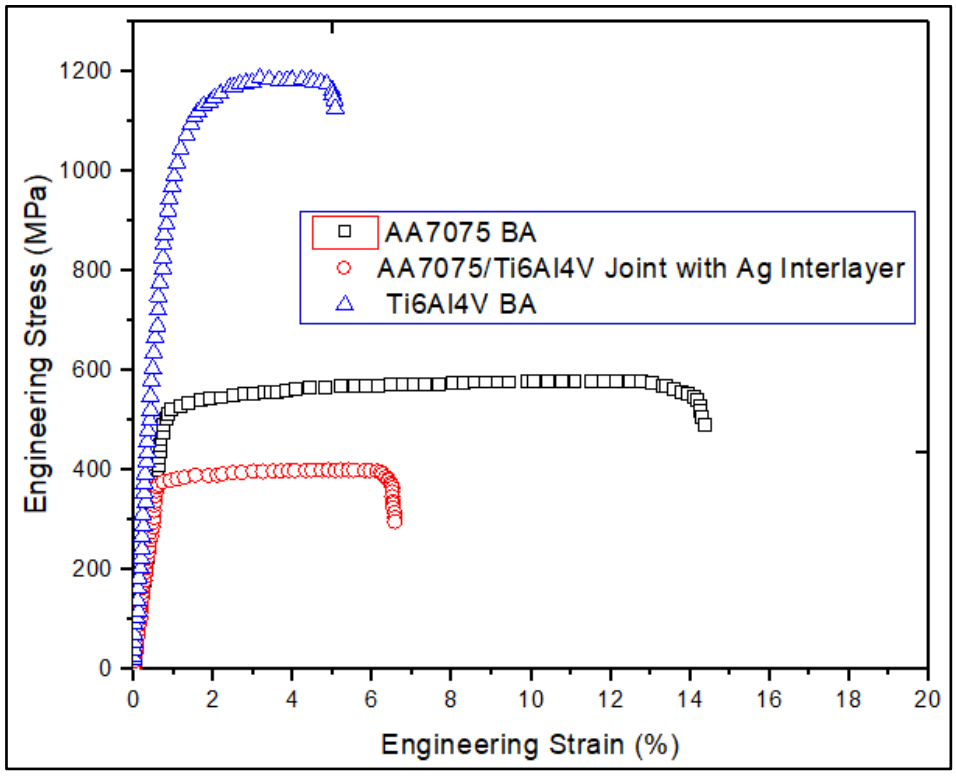

Figure 1.12 Stress-strain curves of tensile test results of AA7075 BA, Ti6Al4V BA, and AA7075/Ti6Al4V joint with Ag interlayer

1.3.3 Nanoindentation analysis

While nanoindentation is a valuable technique for evaluating the properties of thin film coatings on a microscale level, it has been a focal point of numerous prior studies primarily directed at characterizing bulk weldments. The nanohardness, normalized pile up/sink in, and residual stresses of friction stir welded AA6082-T6 and AA5083-H111 aluminum alloys of 10 mm thickness were investigated by Chariditis et al. (Charitidis et al., 2012c) using nanoindentation. For dissimilar FSW aluminum weldments 5 mm thick, Peng et al. (Peng et al., 2018) employed nanoindentation load-depth curves to determine nanohardness. It is worth mentioning, nanoindentation proves valuable in assessing the localized features of weldments, especially in situations where notable microstructural gradients exist throughout

the weld joint (Vitek & Babu, 2011). Hence, by combining nanoindentation with AFM, it becomes feasible to assess the properties of multiple phases present within a specific region.

Nanoindentation experiments were performed using a grid pattern of 2x2 for BA and both HAZs and while 3x3 array for FZ. These indents were strategically positioned inside 5 distinct regions of the weldment, namely the two BAs on both sides of FZ, and two HAZs around FZ and FZ as shown in **Figure 1.13**. The nano hardness test was performed using the Oliver and Pharr methodology, AFM analysis, and Work of Indentation in each zone. The calculations employed the load-depth curves depicted in **Figure 1.14**. Nanoindentation tests were carried out with a constant maximum load of 200 mN and maximum indentation depths of approx. 2000–2500 nm were recorded for BAs and HAZs. However, in the case of FZ, higher variation was monitored as the indentation depths were observed to be in the range of approx. 2500–4500 nm. Within the nanoindentation process, the material around the indents underwent notable deformation, resulting in the accumulation of material in the form of pile-ups. **Figure 1.15** shows the three-dimensional pile-ups viewed using AFM. AFM imaging enables quantifying deformation by measuring accumulated pile-up around indents.

Figure 1.16 presents the nanohardness values of the BA as determined by three different methods: the Oliver and Pharr technique (OP method), AFM analysis (AFM method), and the work of indentation (Total work and Plastic work). The variation in nanohardness concerning penetration depth can be observed. In comparison to other methods, the OP hardness demonstrates higher levels of hardness. It can be attributed to the fact that the OP approach does not consider the area of pile-ups, resulting in an overestimation of hardness (Tuck et al., 2001d). In the OP approach, the contact area is determined using the area function, which relates the area to the penetration depth through Equation 3. The values of the constants used in this equation are determined through a curve fitting methodology, where the initial constant in Equation 3 represents an ideal tip, while the remaining constants account for the tip's divergence from its original form caused by wear or imprecise assembly (Oliver & Pharr, 2004b). As a result, the nanohardness in the OP approach is overstated due to the removal of the region around the pileups. Kese et al. (Kese

et al., 2004b) proposed a solution to this problem by including the estimated pile-up area from AFM imaging into the area function of the OP technique. Furthermore, **Figure 1.14** demonstrates that the nanohardness value is at its lowest when considering the pile-up area, as determined using AFM analysis. The overestimation of pile-up regions, as seen by the load-depth curves in **Figure 1.14**, may be owed to the phenomenon of elastic recovery. Nanohardness values determined using the total work technique and the plastic work approach are very close to one another. As can be seen in **Figure 1.14**, the material recovers elastically during the unloading stage, and the steepness of the unloading curve results in a limited region under the curve and, thus, less elastic work. As a result, the pile-ups increased after unloading, as shown by AFM (**Figure 1.15**) in the area that had recovered elastically.

Figure 1.17, **Figure 1.18**, **Figure 1.19**, and **Figure 1.20** shows a similar pattern of variation in nanohardness in both HAZs and FZ and Ti-6Al-4V BA. The OP approach was found to provide higher estimates, whilst the AFM analysis revealed lower estimates, of nano hardness values in the BAs, HAZs, and FZ when compared to the equivalent microhardness values. The estimated nanohardness values obtained using the work of indentation methodology lie within the range between the nanohardness values obtained using the OP method and AFM analysis. Furthermore, these calculated nanohardness values of work of indentation (total and plastic) are notably closer to the microhardness values as evident in **Table 1.4**. Moreover, the similarity between nanohardness values obtained from both the total work and plastic work approaches can be attributed to their direct calculation using load-depth curves, making them independent of the pile-up area of indents. It is worth mentioning that the values are shown in **Table 1.4** for comparison. The experimentally determined effective elastic modulus for all five regions is showcased in **Figure 1.21** and **Figure 1.22**.

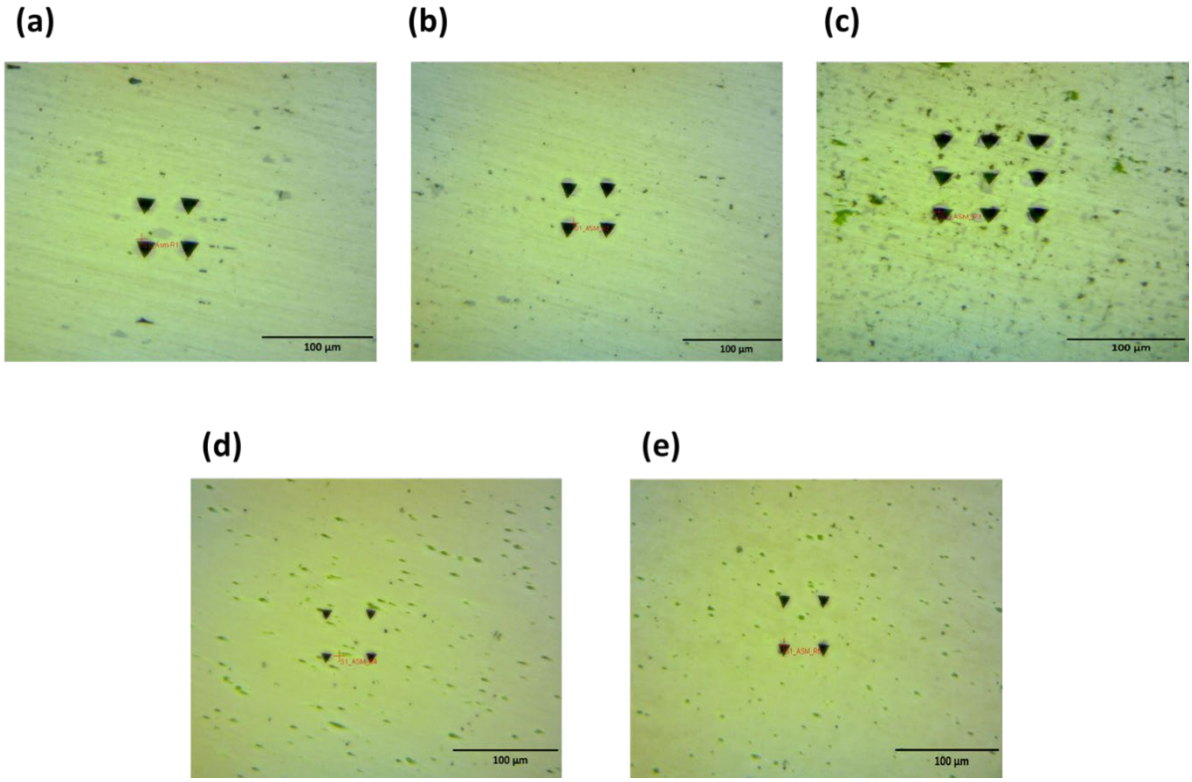

Figure 1.13 2-D images after nanoindentation at a constant load of ~ 200 mN (a) AA7075 BA, (b) HAZ on AA7075 side, (c) FZ, (d) HAZ on Ti-6Al-4V side and (e) Ti-6Al-4V BA

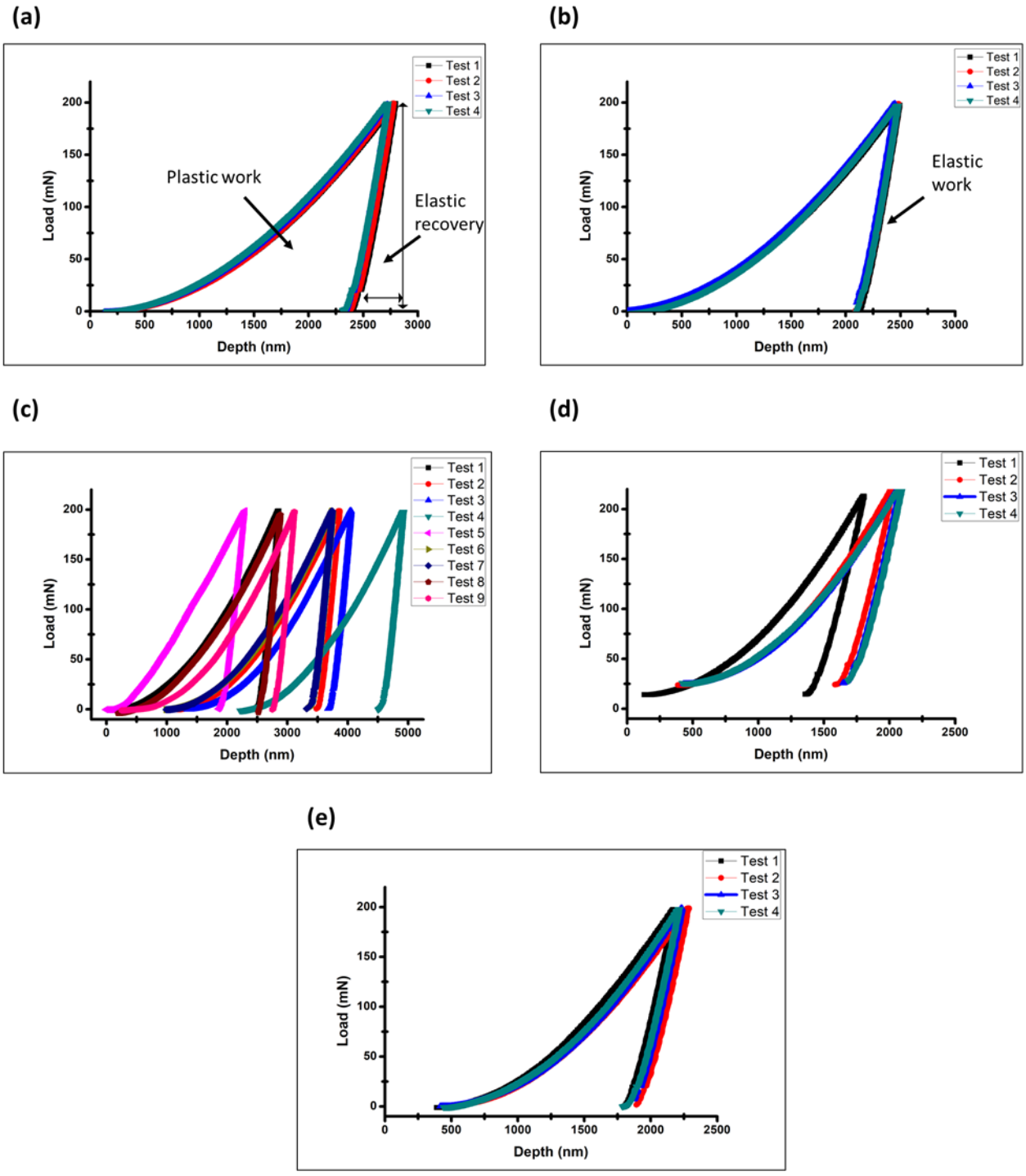

Figure 1.14 Load-depth curves after nanoindentation, (a) AA7075 BA, (b) HAZ on AA7075 side, (c) FZ, (d) HAZ on Ti-6Al-4V side and (e) Ti-6Al-4V BA

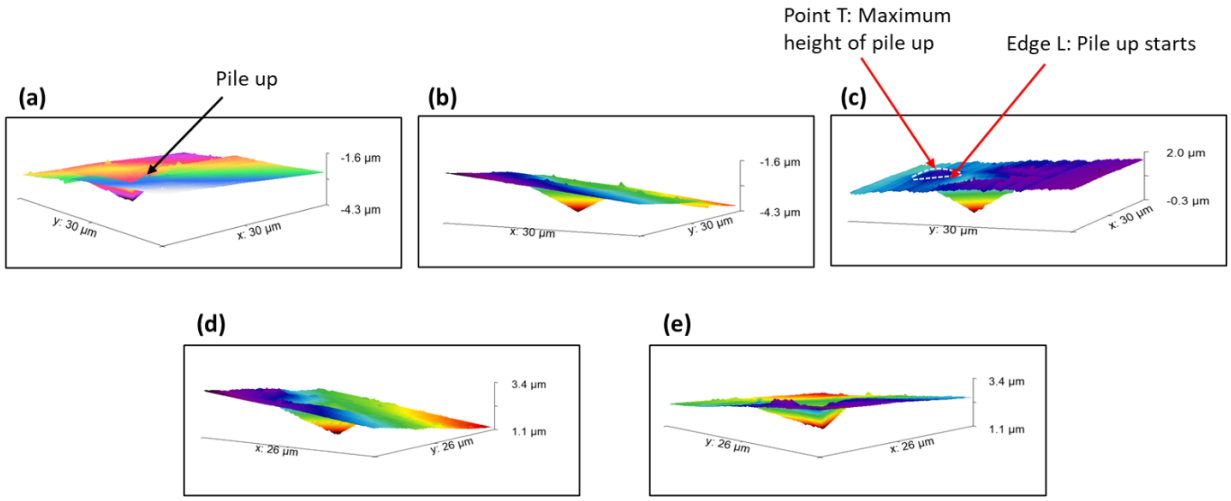

Figure 1.15 3-D side view of the surface after nanoindentation using AFM, (a) AA7075 BA, (b) HAZ on AA7075 side, (c) FZ, (d) HAZ on Ti-6Al-4V side, (e) Ti-6Al-4V BA

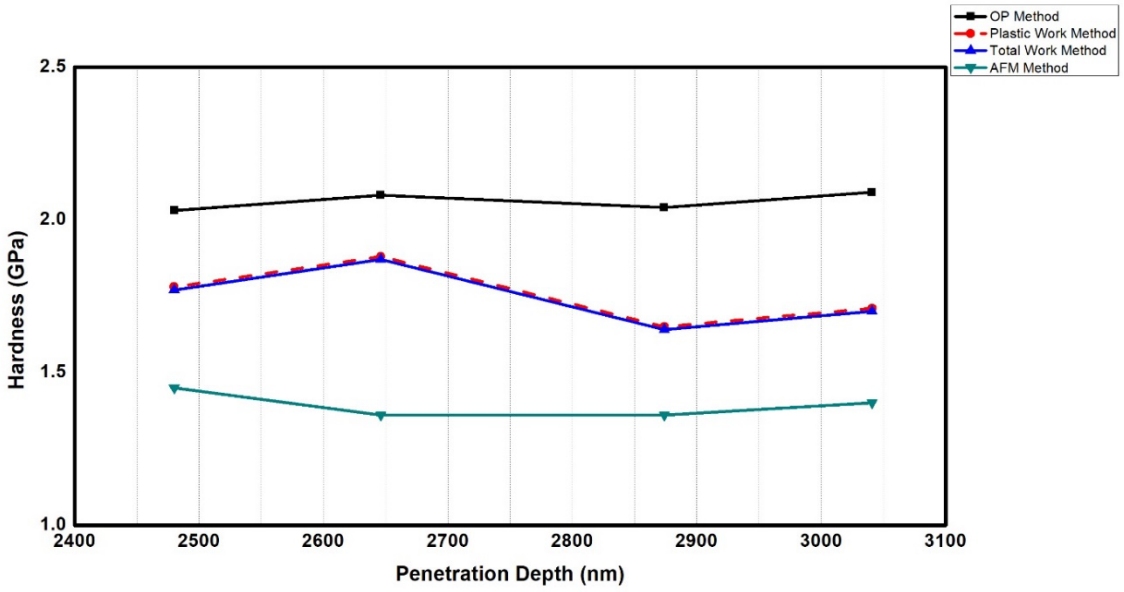

Figure 1.16 Nanohardness values measured in AA7075 base alloy using various approaches

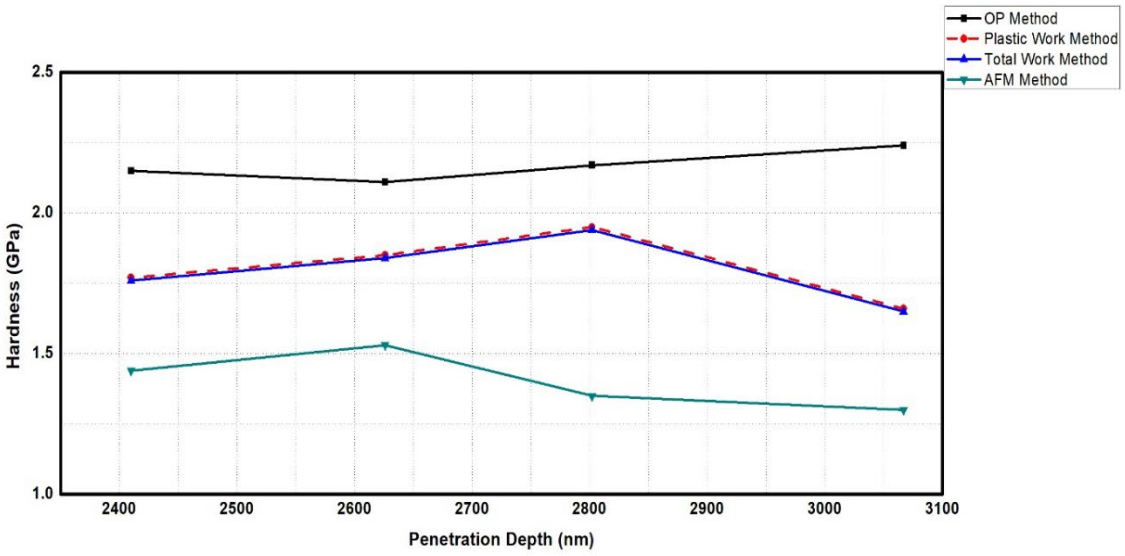

Figure 1.17 Nanohardness values measured in HAZ of AA7075 base alloy side using various approaches

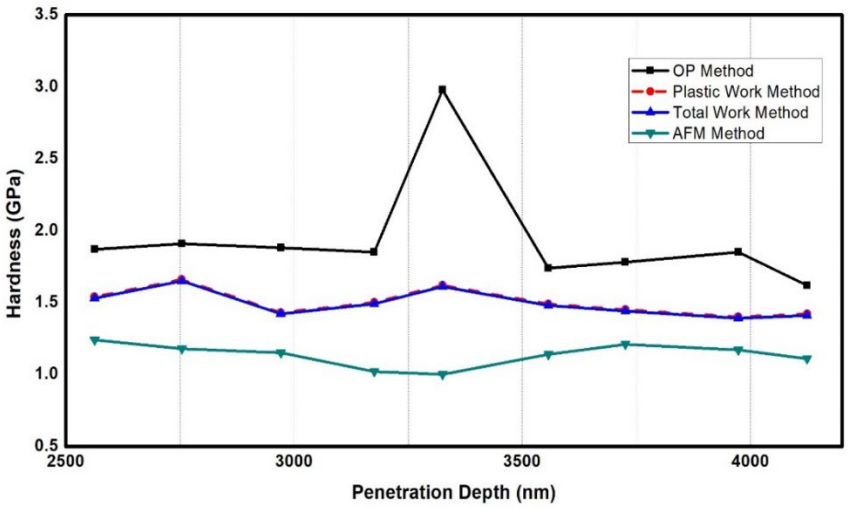

Figure 1.18 Nanohardness values measured in FZ using various approaches

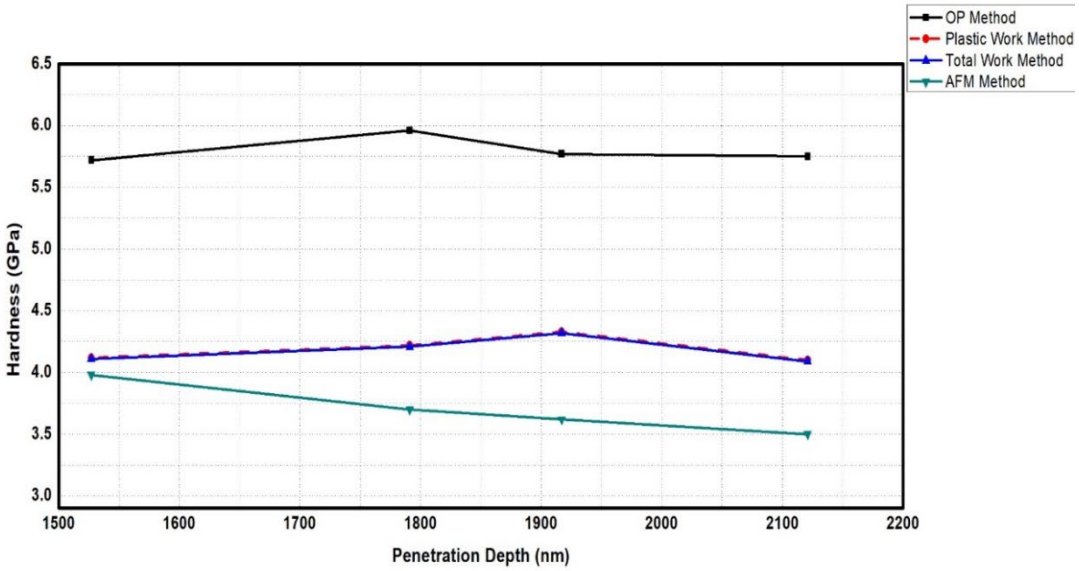

Figure 1.19 Nanohardness values measured in HAZ of Ti-6Al-4V base alloy side using various approaches

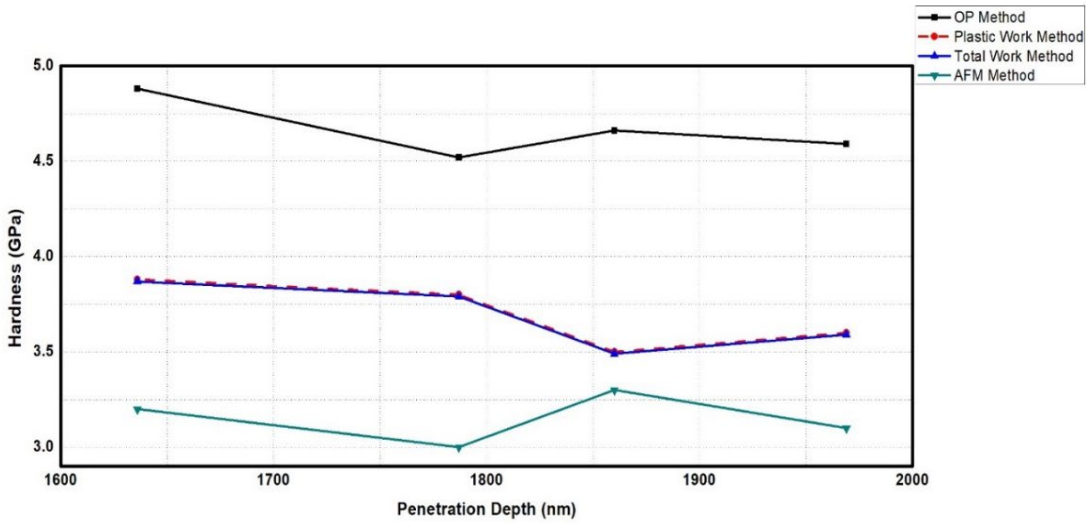

Figure 1.20 Nanohardness values measured in Ti-6Al-4V base alloy using various approaches

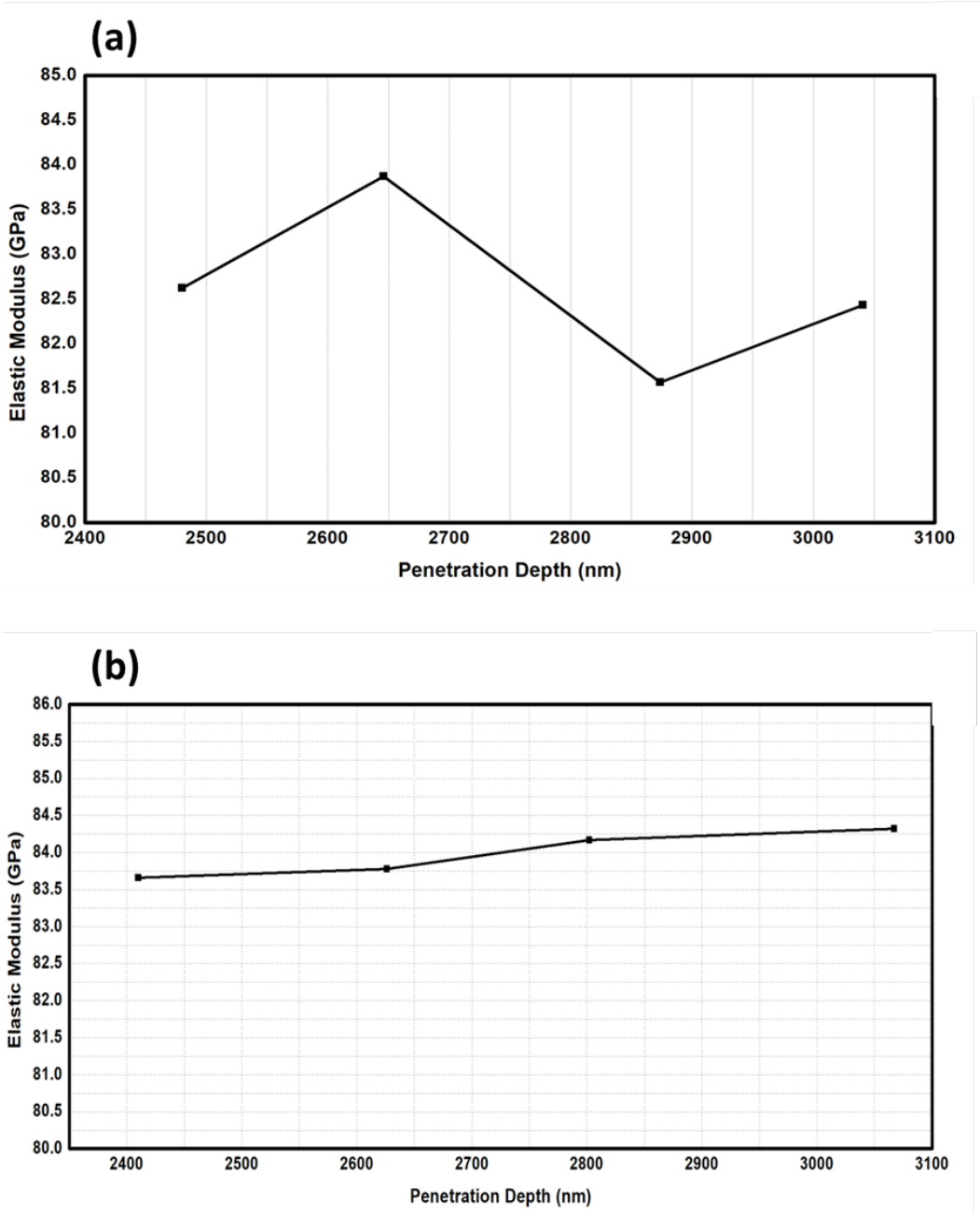

Figure 1.21 Nanoindentation-based determination of the effective elastic modulus of (a) AA7075 BA and (b) AA7075 side HAZ

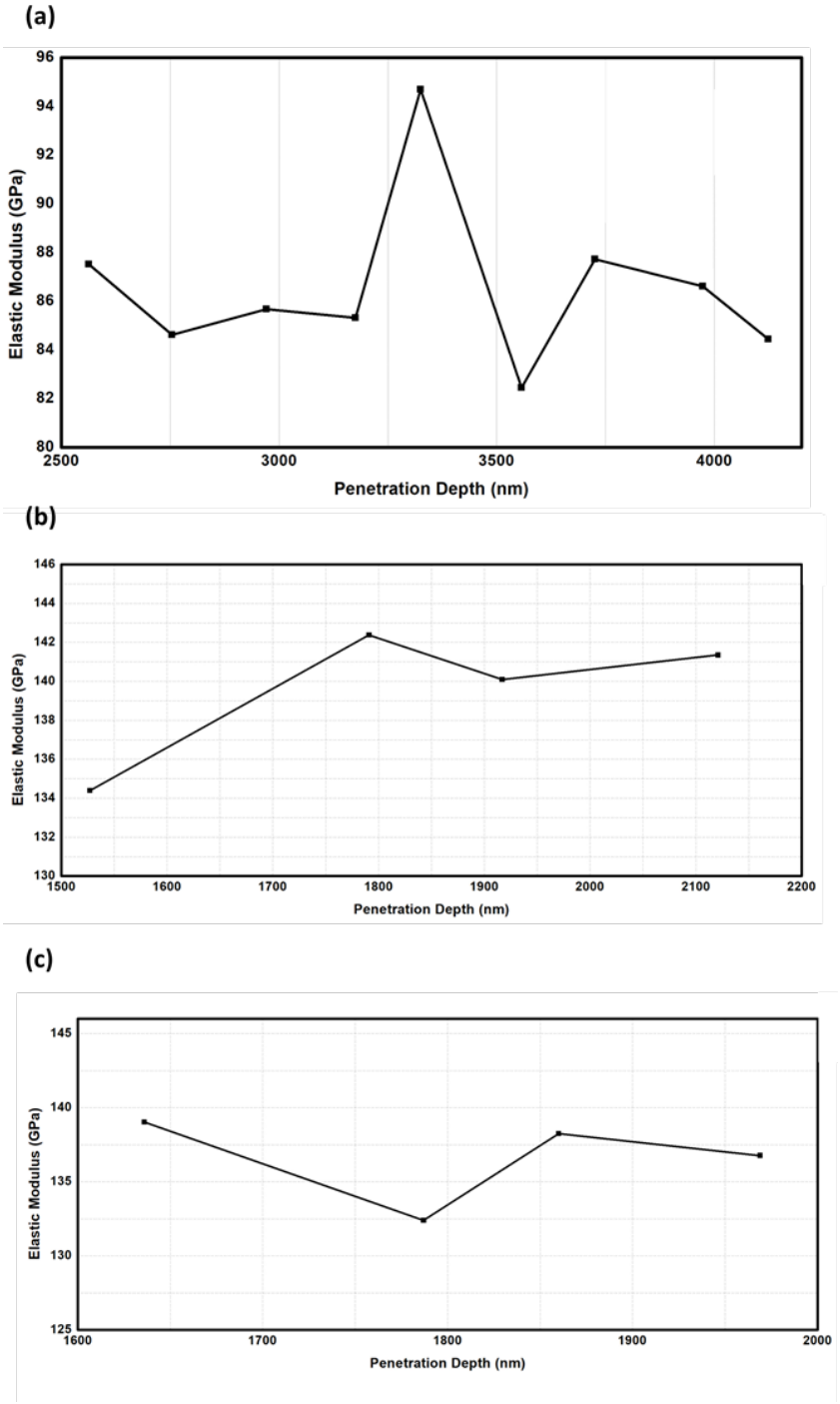

Figure 1.22 Nanoindentation-based determination of the effective elastic modulus of (a) FZ, (b) Ti-6Al-4V side HAZ and (c) Ti-6Al-4V BA

Nanoindentation pile behavior was studied further by plotting normalized hardness (H/E_r) and normalized pile up/sink in height (h_c/h_m) as shown in **Figure 1.23**, **Figure 1.24**, **Figure 1.25**, **Figure 1.26,** and **Figure 1.27**. Nanoindents in soft materials with low H/Er values are known to display pile-up phenomena when the ratio of contact depth to maximum depth (h_c/h_m) approaches unity ((‘A Theoretical Study of the Brinell Hardness Test’, 1989; Biwa & Storåkers, 1995)). Similarly, as h_c/h_m approaches zero, sink-in behavior may be seen around indents made in hard materials with a high H/E_r value. The calculated values of h_c/h_m for AA7075 BA, AA7075 side HAZ, and FZ are 0.9-1 and H/E_r are in the range of 0.08-0.032. These values are indicative of pile up around the nanoindents. Furthermore, piles up around the indentations are indicated by the fact that the values of (h_c/h_m) for AA7075 BA, AA7075 side HAZ, and FZ are all quite near to unity which is also evident from **Figure 1.15**. Therefore, pile-up predominates over other deformation mechanisms over the AA7075 BA, AA7075 side HAZ, and FZ as stated by Biwa et al. and Hill et al. (‘A Theoretical Study of the Brinell Hardness Test’, 1989; Biwa & Storåkers, 1995). The maximum value of H/E_r is discovered to be ~0.032 in the FZ, ~28% lower than the comparable highest value of H/E_r in the HAZ area of Ti-6Al-4V side as shown in **Figure 1.25** and **Figure 1.26** (one of the five zones in the weldment). It is also evident from **Figure 1.26** and **Figure 1.27** that Ti-6Al-4V side HAZ and BA have a proportionately lower value of h_c/h_m ratio while having higher H/E_r values as compared to AA7075 BA, AA7075 side HAZ and FZ. This could be owing to the formation of needle-like α’ martensite in Ti-6Al-4V side HAZ during the solidification phase after the welding process as discussed in the microstructure section. Additionally, the presence of tensile residual stresses owing to the formation of intermetallic compounds may also be responsible for this apparent softness in the FZ. The average nanohardness values across all of the methods are shown in **Table 1.4**. Using various methods, it is clear from **Table 1.4** that the BA AA7075 along with the HAZ on its side and FZ have the lowest and greatest converted microhardness, respectively, whereas the converse is true for nano hardness. This is because nanohardness is very sensitive to the state of residual stresses and the presence of IMCs. According to Charitidis et al. (Charitidis et al., 2012d), nanohardness decreases with increasing tensile residual stresses, however, microhardness is not

substantially affected by the stress condition, as stated by Jae-il Jang (Jang, 2009). The resulting decrease in FZ nano hardness from AA7075 BA was roughly ~6% for the OP technique, 18% for AFM analysis, and 14% for both the Total work approach and the plastic work methodology. The microhardness of the FZ was found to be 14% greater than that of the BA AA7075. According to the findings of Rossini et al. (Rossini et al., 2012), this type of stress profile is indicative of a weld in which the shrinkage phenomena is dominant. Furthermore, due to the formation of hard phases (acicular α and α martensite) in Ti-6al-4V side HAZ, following the rapid cooling cycle that occurs during solidification, it showed higher microhardness and nanohardness as shown in **Table 1.5**. Moreover, the Oliver and Pharr method and AFM analysis were also used to determine the elastic modulus and the values are shown in **Table 1.5**. It is also evident that the elastic moduli values calculated using the AFM approach are higher than the OP method for all the weldment zones.

Tableau 1.4 The nanohardness values of the dissimilar laser welded AA7075-Ti-6Al-4V alloys in different zones namely in the BAs, HAZs, and FZ, were calculated using several methodologies

Zone/Region	Microhardness (GPa)	OP method (GPa)	Total work method (GPa)	Plastic work method (GPa)	AFM method (GPa)
AA7075 BA	1.47	2.06	1.75	1.74	1.40
AA7075 side HAZ	1.67	2.16	1.81	1.80	1.41
FZ	1.71	1.94	1.50	1.50	1.14
Ti-6Al-4V side HAZ	4.08	5.80	4.20	4.18	3.70
Ti-6Al-4V BA	3.65	4.66	3.70	3.68	3.15

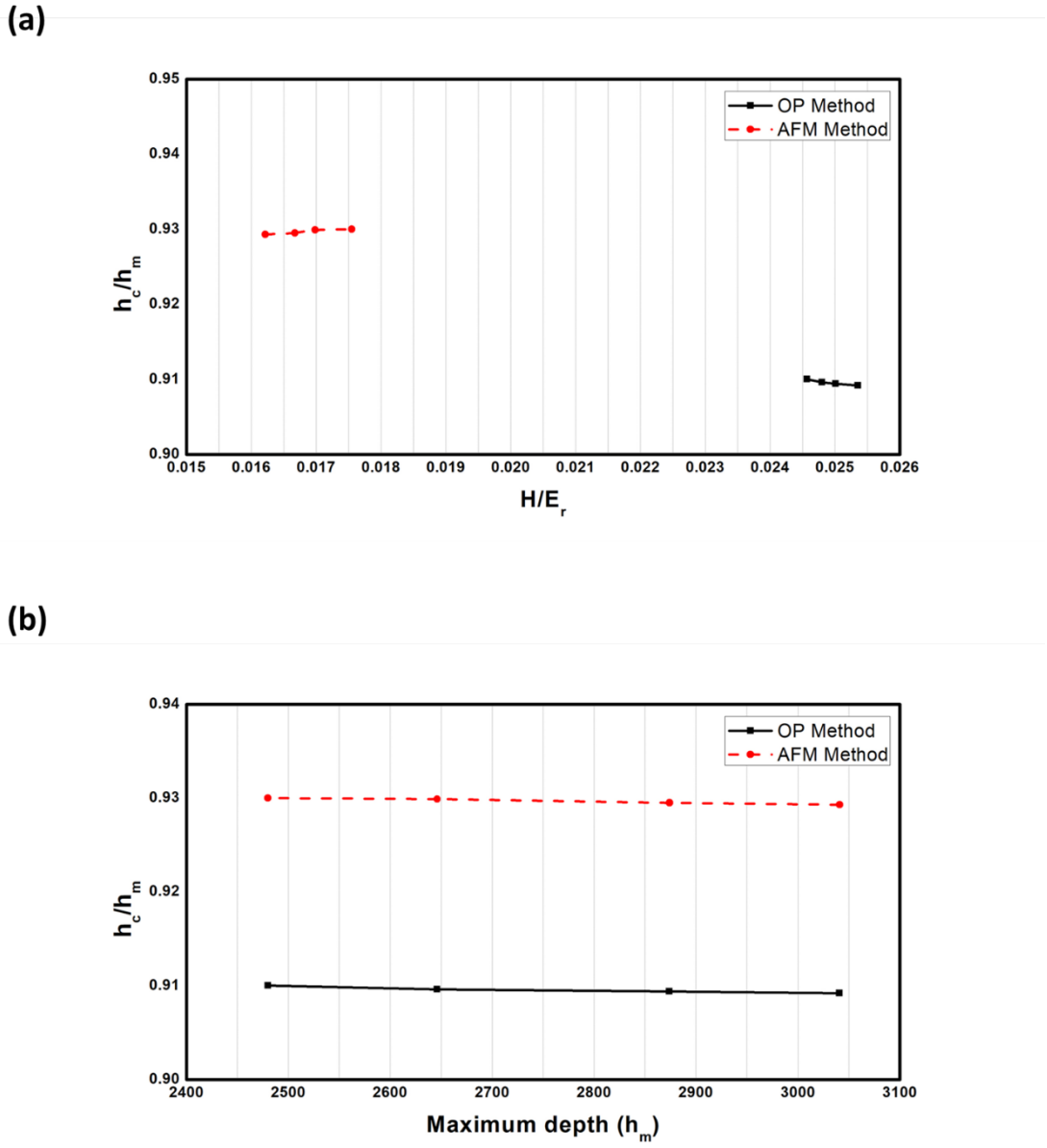

Figure 1.23 Plots of AA7075 BA showing pile up/sink in relative to (a) Normalized hardness and (b) Maximum depth

(a)

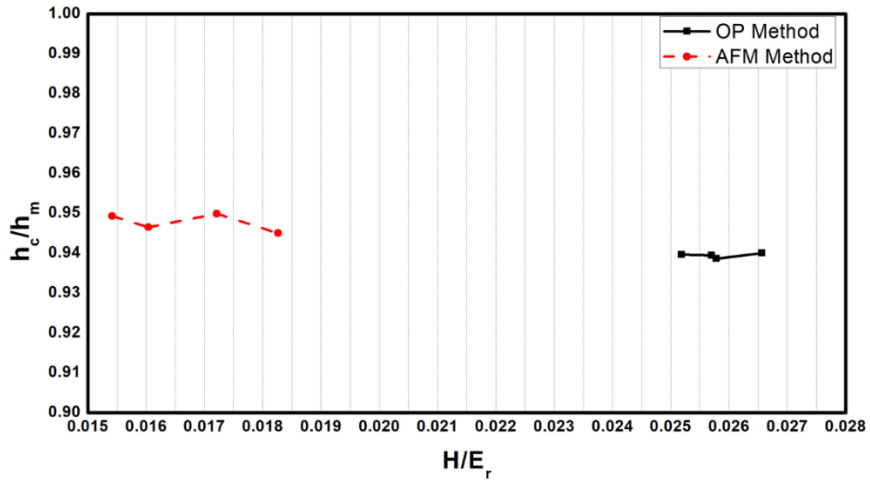

(b)

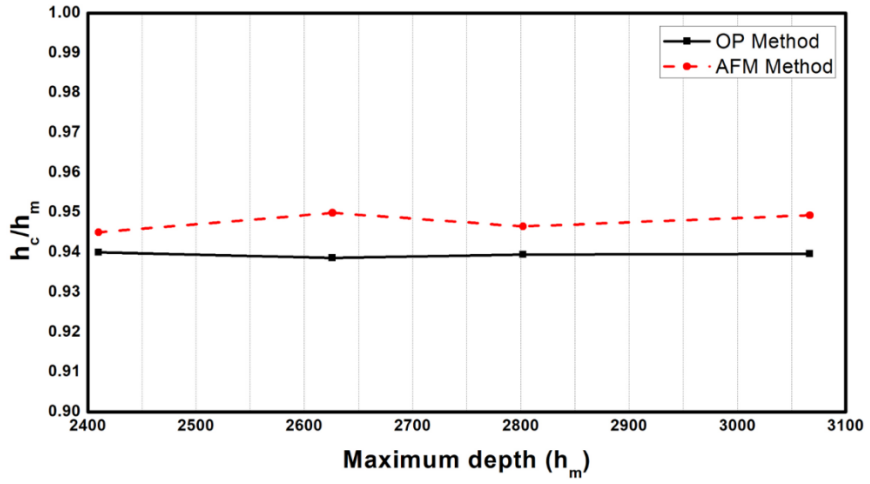

Figure 1.24 Plots of AA7075 side HAZ showing pile up/sink in relative to (a) Normalized hardness and (b) Maximum depth

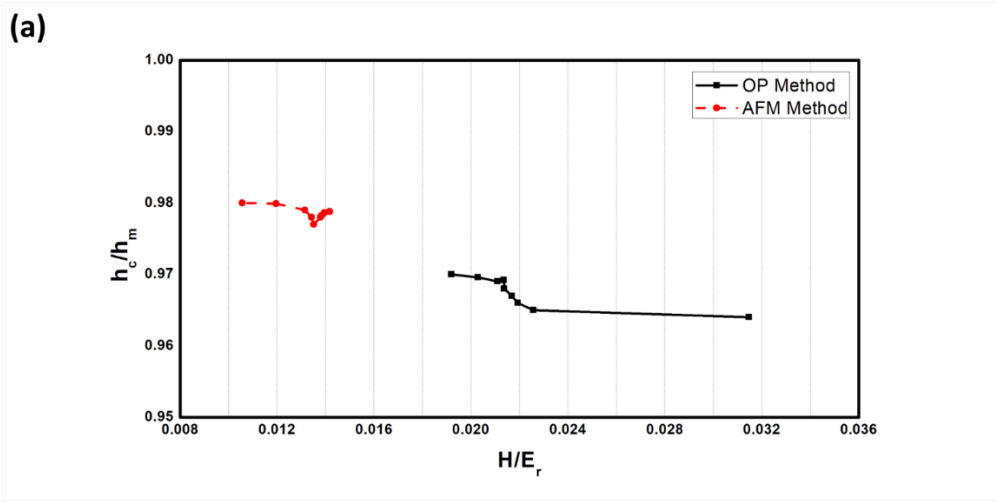

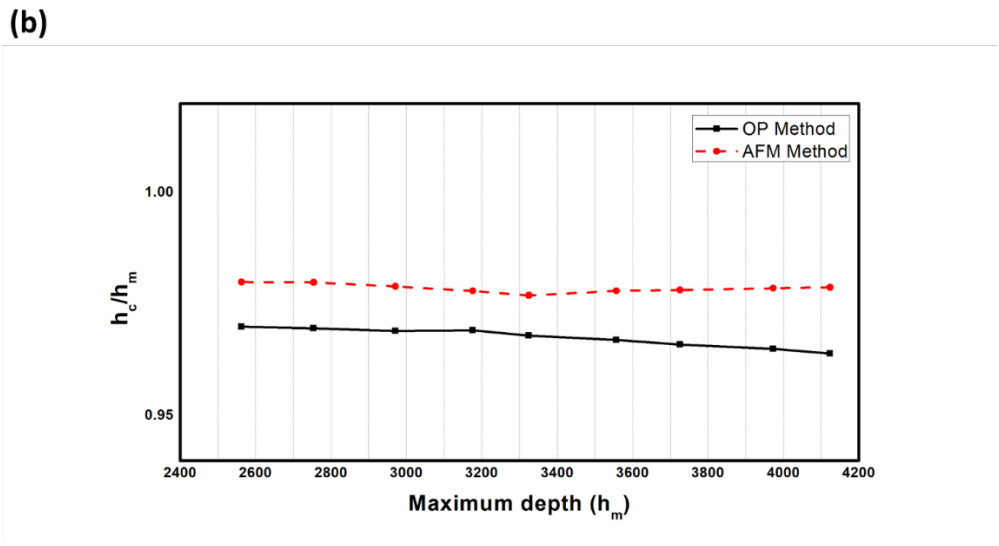

Figure 1.25 Plots of FZ showing pile up/sink in relative to (a) Normalized hardness and (b) Maximum depth

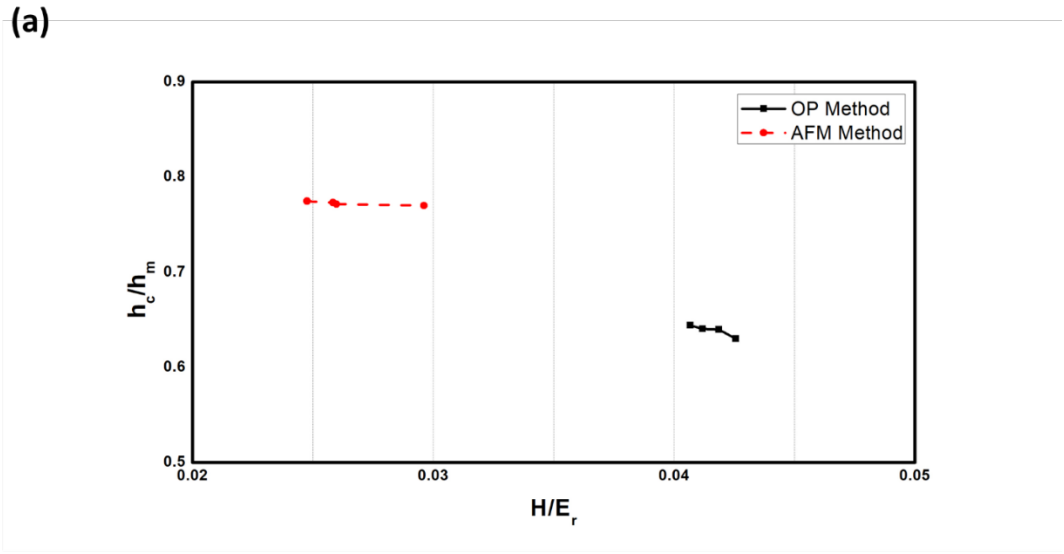

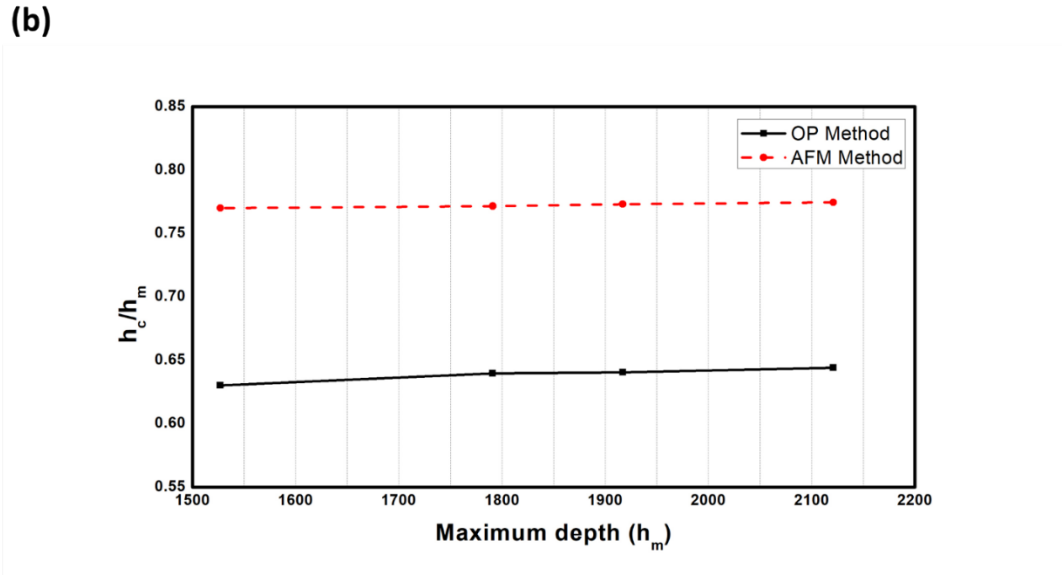

Figure 1.26 Plots of Ti-6Al-4V side HAZ showing pile up /sink in relative to (a) Normalized hardness and (b) Maximum depth

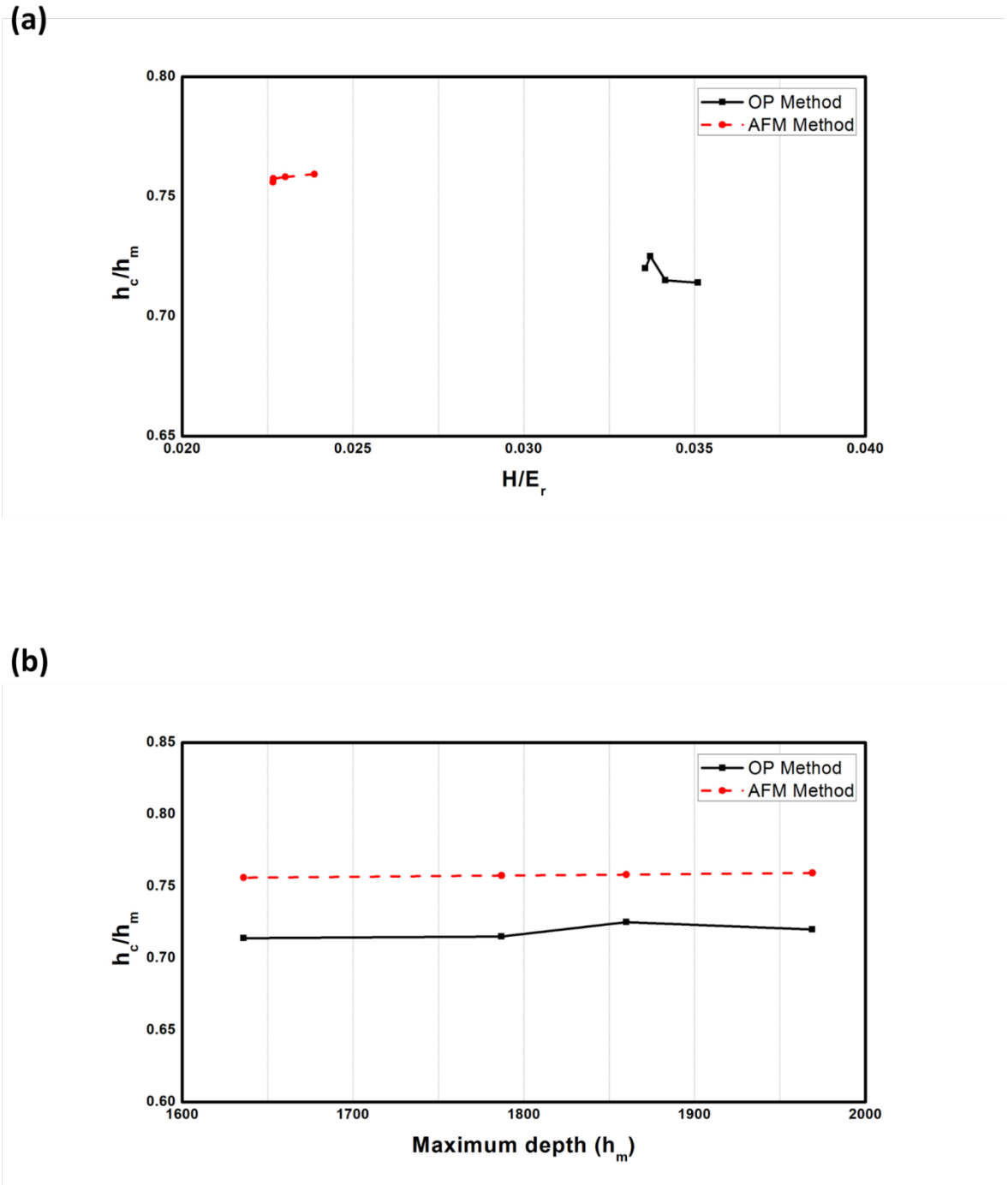

Figure 1.27 Plots of Ti-6Al-4V BA showing pile up/sink in relative to (a) Normalized hardness and (b) Maximum depth

Tableau 1.5 Effective elastic modulus values of OP and AFM methodologies

Zone/Region	OP method (GPa)	AFM method (GPa)
AA7075 BA	82.62	108.21
AA7075 side HAZ	83.98	110.76
FZ	86.55	120.35
Ti-6Al-4V side HAZ	139.55	162.13
Ti-6Al-4V BA	139.61	164.47

1.4 CONCLUSIONS

In the present study, dissimilar joints of laser-welded AA7075-Ti-6Al-4V with an Ag interlayer were prepared and the weldments were evaluated in terms of microstructure evolution and various nanoindentation methodologies. The following conclusions can be drawn based on the analyzed results as below:

- The insertion of Ag as an interlayer between AA7075-Ti-6Al-4V suppressed the formation of more brittle IMCs such as $AlTi_3$ and AlTi and improved the overall quality of the joint by reducing the interaction of Ti and Al.
- The OP method tends to overestimate the nanohardness nano hardness values due to its inability to account for pile-up areas, resulting in higher values.
- AFM analysis yields nanohardness nano hardness values that are relatively lower than microhardness values, while the work of indentation (total and plastic) values are much closer to the microhardness values.
- Due to the sensitive nature of nanoindentation, which takes into account the presence of tensile residual stresses in FZ, the microhardness and nanohardness values in FZ were inverse to one another.
- The work of the indentation method provides nanohardness values close to microhardness, suggesting its suitability for characterizing AA7075-Ti-6Al-4V

dissimilar weldments with an Ag interlayer, as it yields values similar to the microhardness results.

- The Ti-6Al-4V side HAZ exhibited higher microhardness and nanohardness values as compared to AA7075 BA, AA7075 side HAZ, and FZ due to the formation of hard phases (acicular α and α martensite).
- The nanoindentation results indicate that the nanohardness values are influenced by the depth of indentation, emphasizing its significance in assessing the material properties in these dissimilar weldments.

CHAPITRE 2
SOUDAGE BOUT A BOUT AU LASER DE L'ALLIAGE D'ALUMINIUM AA7075 ET DE L'ALLIAGE DE TITANE TI6AL4V EN UTILISANT UNE INTERCOUCHE DE CUIVRE

Titre en français du deuxième article :

Soudage bout a bout au laser de l'alliage d'aluminium AA7075 et de l'alliage de titane Ti6Al4V en utilisant une intercouche de cuivre.

Titre original (en anglais) :

Laser butt welding of AA7075 aluminum alloy and Ti6Al4V titanium alloy using a Cu interlayer.

Auteurs et affiliation :

Asim Iltaf : Étudiant au doctorat, Département de mathématiques, d'informatique et de génie, Université du Québec à Rimouski, Québec, Canada.
Shayan Dehghan : Chercheur post-doctoral, Département de mathématiques, d'informatique et de génie, Université du Québec à Rimouski, Québec, Canada.
Noureddine Barka : Professeur, Département de mathématiques, d'informatique et de génie, Université du Québec à Rimouski, Québec, Canada.
Claude Belzile : Assistant de recherche, Institut des Sciences de la Mer de Rimouski (ISMER), Université du Québec à Rimouski, Québec, Canada.

État de l'article :

Publié.

Revue :

Materials science and technology

Référence :

https://doi.org/10.1177/026708362412358

Résumé en français du deuxième article

Le soudage laser des alliages AA7075 et Ti6Al4V, deux alliages aérospatiaux très différents, a été réalisé avec un intercouche en cuivre pour éviter les intermétalliques fragiles Ti-Al. Le joint a été formé grâce à la diffusion du cuivre dans l'alliage AA7075 et à une diffusion limitée dans l'alliage Ti6Al4V, suivie de la formation d'un eutectique à l'interface AA7075/cuivre. L'analyse microstructurale et la spectroscopie à dispersion d'énergie de la zone de soudure ont révélé la présence de phases eutectiques aux joints de grains à l'intérieur de la zone fondue de l'AA7075. Une phase interfaciale Cu_3Ti_2 s'est formée à l'interface à l'état solide Ti6Al4V/ cuivre. Un joint robuste et solide a été obtenu grâce à l'utilisation efficace du cuivre en tant qu'intercouche.

Laser butt welding of AA7075 aluminum alloy and Ti6Al4V titanium alloy using a Cu interlayer

Asim Iltaf [a, *], Shayan Dehghan [a, *], Noureddine Barka [a], Claude Belzile [b]

[a] Department of Mathematics, Computer Science and Engineering, University of Quebec at Rimouski, Rimouski, QC G5L 3A1, Quebec, Canada.

[b] Institute of Marine Sciences of Rimouski, University of Quebec at Rimouski, Rimouski, QC G5L 3A1, Quebec, Canada.

[*]Corresponding authors (Asim Iltaf, Shayan Dehghan): Department of Mathematics, Computer Science and Engineering, University of Quebec at Rimouski, Rimouski, QC G5L 3A1, Quebec, Canada.

E-mail address: asim.iltaf@uqar.ca, shayan.dehghan@uqar.ca

Abstract

Laser welding of AA7075 and Ti6Al4V, two very different aerospace alloys, was performed with a copper (Cu) interlayer to avoid the brittle Ti-Al intermetallics. The joint was formed owing to the diffusion of Cu into the AA7075 alloy and limited diffusion in Ti6Al4V alloy, followed by eutectic formation at the AA7075/Cu interface. Microstructural and energy dispersive spectroscopy (EDS) analysis of the joint area revealed the presence of eutectic phases at grain boundaries inside the AA7075 fusion zone (FZ). An interfacial Cu_3Ti_2 phase formed at the solid-state Ti6Al4V/Cu interface. A robust and sound joint was achieved through the effective utilization of Cu as an interlayer.

***Keywords*:** Dissimilar joint, Microstructure, Tensile strength, EDS, Microhardness, Interlayer

2.1 INTRODUCTION

Lightweight, but most importantly durable materials are the key to reaching the goals, of hybrid structures, in terms of energy and fuel consumption for various industries such as automotive, and aerospace (S. Liu et al., 2022b). Using lightweight dissimilar structures can significantly reduce the total weight of the structures and pollutant emissions (Gagliardi et al., 2019). Aluminium (Al) and titanium (Ti) are ideal for manufacturing lightweight vehicle structures, reducing fuel consumption, and improving safety (Anchev et al., 2023; Fernandes et al., 2023). The aerospace industry benefits from their synergistic combination. The formation of brittle intermetallic compounds (IMCs) makes it difficult to weld Al-Ti and develop high-performance composite structures (Dak & Pandey, 2020). Few studies have investigated the laser welding of titanium alloys with 7000 series aluminum alloys (X. Chen et al., 2021; Kuryntsev, 2019a; S. Liu et al., 2022b).

Utilizing an interlayer in welding effectively reduces IMC formation, improving joint performance as shown by Teshome et al. (Teshome et al., 2023a). Common interlayers encompass Ni, Cu, Mg, V, and Ag/Ti-based filler metals (Y. Zhang et al., 2020). Forming a solid solution with metals like Nb, V, Zr, and Ta helps prevent brittle intermetallics. Additionally, substituting brittle Ti-Fe intermetallics with other types further improves joint performance(J. Li et al., 2020).

Laser welding is crucial for its ability to provide high precision, controlled welding with minimal heat input, resulting in strong, high-quality joints with less distortion. It's also versatile, and capable of joining a wide range of materials, even those considered difficult to weld using traditional methods [11,12]. In this study, laser welding in butt configuration was used to join AA7075 and Ti6Al4V alloys, with a Cu interlayer. Notably, there has been limited research on the utilization of a copper interlayer for laser welding of these alloys previously. The results of this investigation are expected to improve the understanding of laser welding of Al and Ti alloys and make way for more widespread use of dissimilar material welding in the industry(Ke et al., 2023; Zheng et al., 2023).

2.2 EXPERIMENTAL PROCEDURE

The present study used AA7075 aluminium alloy and Ti6Al4V titanium alloy sheets (80 mm × 50 mm × 1.6 mm). A Cu interlayer (99.95% purity) of 0.4 mm thickness was inserted between the two alloys to reduce the formation of IMCs. The oxide coating and greasy dirt on the surface of both alloys were cleaned off using SiC sandpaper and acetone before welding. Weld parameters were optimized with the Cu interlayer before the experiment was carried out. Consequently, AA7075 alloy and Ti6Al4V alloy were joined using an optimized set of process parameters, which included a laser power of 3 kW, a scanning speed of 40 mm/s, and a laser spot size of 1.5 mm. The welding was performed in butt configuration using a fiber laser equipped with an IPG Photonics Ytterbium Laser Systems source model (YLS-3000-ST2) and the laser was pointed toward the weld centerline as shown in **Fig. 2.1 (a)**. The resultant weldment was etched by Kroll solution (6% HNO3 and 2% HF by volume in distilled water) to reveal the microstructure. The etching time was reduced for the dissimilar joint to avoid over-etching/over-corrosion as compared to the etching of base alloys. The etching time for base alloys was approx. 25-30 sec while for the joint area it was around 10-15 sec. The joint area was protected with hot glue while etching the base alloys. The nanoindentation test was performed in load control mode having a peak load of 200 mN using the Nanoindenter (iMicro from Nanomechanics, Inc.) with a Berkovich indenter tip. SEM (SNE-4500M Plus, SEC) equipped with an EDS detector (Esprit, Bruker) was used to study fractography and chemical composition of the joint and fractured surface.

2.3 RESULTS AND DISCUSSION

Fig. 2.1 shows the cross-sectional microstructure of the dissimilar butt joint of AA7075 and Ti6Al4V made by laser welding using Cu as an interlayer. The joint consists of three regions of interest: AA7075 FZ, mix zone, and Ti6Al4V/Cu interface. There is minimal melting phenomena of the titanium alloy, and the joint interface is flat (Moon et al., 2024). Minimizing the melting of titanium during welding is crucial as it reduces the mixing of titanium atoms with aluminum atoms, thereby significantly lowering the likelihood of

forming a brittle Ti/Al intermetallic compound. This preservation of the base materials' properties results in a stronger, more ductile weld joint, maintaining the integrity and performance of the base materials. Therefore, the interaction between the AA7075 and Cu and Ti6Al4V and Cu was the focus of the present investigation. The joint was mainly formed at the AA7075/Cu and Ti6Al4V/Cu interface owing to the eutectic liquid forming and limited diffusion of Cu into Ti6Al4V, respectively. Cu diffused into the AA7075 alloy, resulting in the formation of a large diffusion zone inside the AA7075 alloy and adjacent to the mix zone, **Fig. (2.1b-I, II)**. Some discontinuous minor cracks can be observed inside the AA7075 FZ. **Fig. (2.1b-II)**. The minimal effect of the current process on the Ti6Al4V can also be observed in **Fig. 2.1 (b-III).** In laser beam welding (LBW), a rapid cooling rate results in significant local undercooling (Sonar et al., 2021). This phenomenon promotes faster nucleation and development of fine grains and dendrites as shown in **Fig. (2.1b-IV, V)**. The mix zone mainly consists of AA7075, Ti6Al4V, and Cu, **Fig. (2.1b-VI)**. In the mix zone, a Vanadium solid solution was formed and this led to a more robust joint. Vanadium solid solution contributes to strengthening mechanisms in several ways. Firstly, it can create a size mismatch due to its distinct atomic size, which generates lattice distortions and thus impedes the movement of dislocations in the material. This resistance to dislocation motion enhances the strength of the alloy. Additionally, the presence of Vanadium can also lead to the formation of secondary phases or precipitates which can further obstruct dislocation movement, contributing to the overall strengthening effect. These mechanisms make Vanadium a valuable element in alloy design for improved mechanical properties.

Fig. 2.1(b) also shows the presence of porosity in the joint. Pore formation is a significant issue in LBW of 7xxx series alloys. This occurs due to a small amount of gas getting into the laser-melted zone, leading to gas porosity. Hydrogen (H_2), which has a high solubility in molten aluminum, is the primary cause of pore formation in this alloy. The hydrogen originates from oxides or impurities in the filler and base materials, which then dissolve into the bulk material (Khalil et al., 2019). On the other hand, porosity in LBW occurs in various forms, including necking, swelling, and collapsing. The primary cause of

porosities is the inconsistent vaporization of volatile alloying elements like Zn and Mg, which have varying vapor pressures (Khalil et al., 2019).

SEM images of the unetched joint along with some points in AA7075 FZ for EDS analysis are presented in **Fig. 2.2(a-I, II).** EDS mapping showed a higher concentration for Cu in the the AA7075 FZ interface, indicating the slow diffusion of Cu out of the mix zone, **Fig. (2.2a-III)**. The initial stage of the joining procedure was the process of diffusion, Cu was diffused into the AA7075. Afterward, the eutectic liquid is formed consisting of Al and Cu at the bonding temperature, as determined by the AA7075-Cu phase diagram (Yan et al., 2001). Grain coarsening can also be observed near the AA7075/Cu interface. There were three primary eutectic phases present at the interface of the joint in AA707/5 FZ; Al_2Cu, $Al_{13}Fe$, and $Al_2Mg_3Zn_3$, **Fig. (2.2a-IV, V)**. The Al-Cu phase diagram also allows for the prediction of the formation of Al_2Cu and $Al_{13}Fe$ at the interface region of the weldment (Yan et al., 2001). Whereas, $Al_2Mg_3Zn_3$ is potentially formed by the solidification of the eutectic liquid during the cooling process (referred to **Table 2.1**). As the Al_2Cu phase excluded Mg and Zn throughout its growth, it led to the formation of $Al_2Mg_3Zn_3$ near the Al_2Cu phase in the AA7075 FZ.

The EDS analysis presented in **Table 2.1** reveals the absence of Ti in the eutectic phases located at the AA7075 FZ i.e., Al_2Cu, $Al_{13}Fe$, and $Al_2Mg_3Zn_3$. The concentration of Cu, Mg, and Zn is significantly higher in AA7075 FZ as compared to Ti6Al4V. However, the EDS analysis also showed the diffusion of Cu into the Ti6Al4V. The Cu mapping in **Fig. 2.2(a-III)**, obtained from the joint, exhibits a prominent Cu concentration towards the Ti6Al4V interface as well. The presence of Cu at the Ti6Al4V/Cu interface indicates the formation of the Cu_3Ti_2 phase. Consequently, a solid-state bond was formed at the Ti6Al4V/Cu interface owing to Cu_3Ti_2. **Fig. 2.2(b)** shows the microhardness profile over the joint region. Hardness values were found to increase from AA7075 FZ to the mix zone and Ti6Al4V. Owing to the formation of the Cu_3Ti_2 phase at the Ti6Al4V/Cu, higher hardness is indicated at this interface. While the formation of the Cu_3Ti_2 interfacial phase can enhance joint strength, it can also introduce brittleness. Intermetallic compounds are often more brittle

than base materials, which can lead to cracking under stress or impact, especially in applications where the weld is subject to dynamic loading or thermal cycling. Therefore, the formation of the Cu_3Ti_2 phase resulted in high-strength Ti6Al4V/Cu interface while reducing the ductility and toughness of the weld joint, making it less able to absorb energy and more susceptible to brittle fracture.

The weld's tensile strength was measured and the results are shown in **Fig. 2.3(a)**. Three tensile specimens were tested to ensure the repeatability and reliability of the results. Three samples were used to confirm that the observed mechanical properties are consistent and not an anomaly of a single specimen. The UTS was observed to be at 240 MPa. The test was repeated thrice, every sample examined fractured at the Ti6Al4V/Cu alloy interface, suggesting that the Ti/Cu alloy interface was the weakest point in the weldment. Following the tensile test, the fractured surface was analyzed as shown in **Fig. 2.3(b, c)** which exhibits a brittle cleavage fracture mechanism. **Fig. 2.3(c)** shows the cleavage plane, as well as the steps and black blocky substances. Moreover, **Fig. 2.3(c)** demonstrates that the fracture surface is lumpy and uneven due to the extraction of several second phases. EDS spectra of the fractured surface indicate prominent peaks of Ti and Cu signifying the presence of Cu_3Ti_2 IMCs as shown in **Fig. 2.3(d)** and **Table 2.2**. Stress concentrations due to the formation of Cu_3Ti_2 near the Ti6Al4V/Cu interface are primarily responsible for the joint's fracture, **Fig. 2.3(e)**. The Cu_3Ti_2 near the weld toe probably interacted with the stress concentrations to cause the fracture. Furthermore, nanoindentation was conducted in a 3x3 grid across the AA7075FZ, mix zone, and Ti6Al4V/Cu interface, and the load-displacement (P-h) curves of the various zones are shown in **Fig. 2.3(f).** The nanoindentation results were consistent with the EDS analysis and microhardness results above. Ti6Al4V/Cu interface showed lower penetration depth (Test 9) among all the regions validating the presence of brittle Cu_3Ti_2.

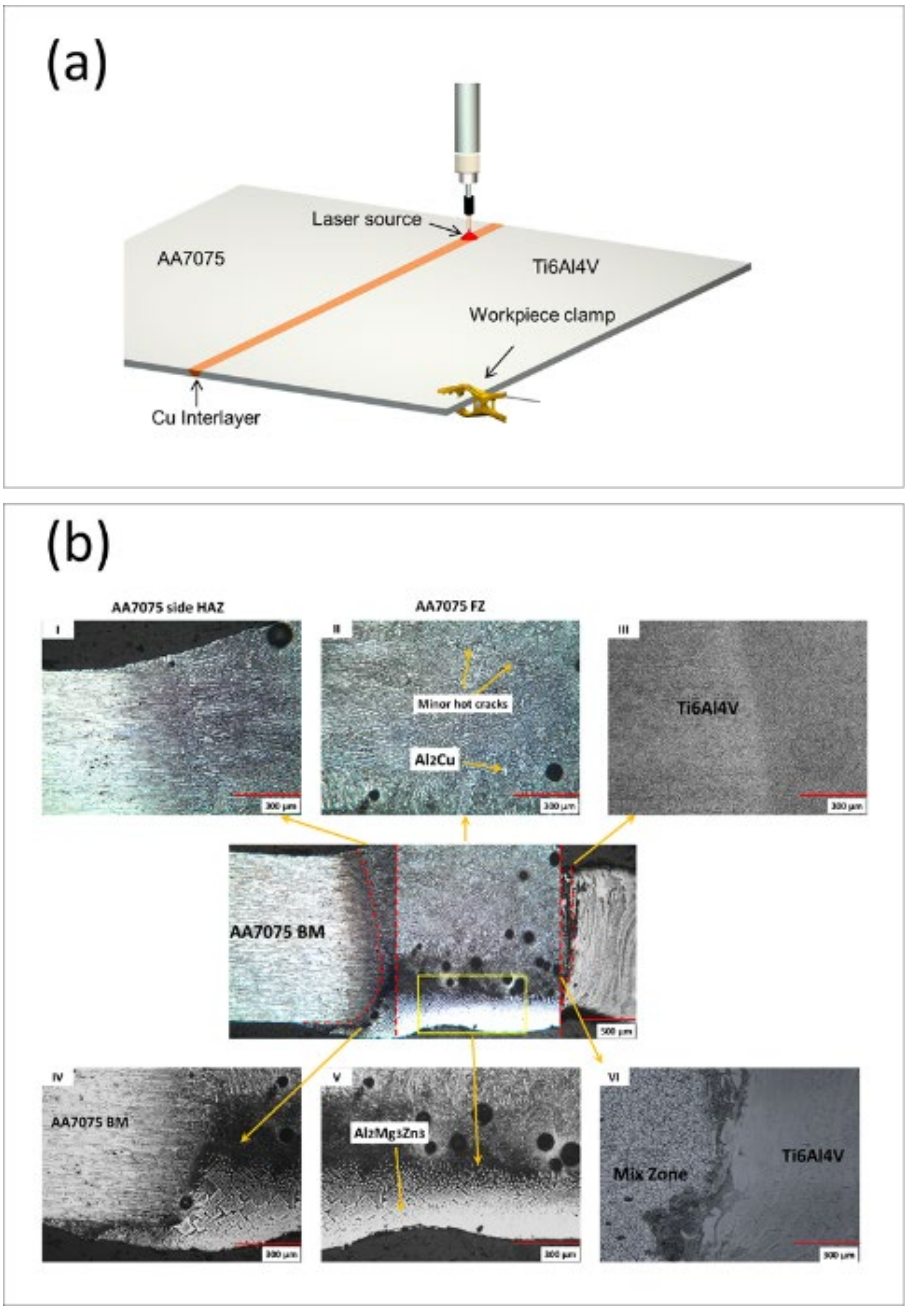

Figure 2.1 (a) Schematic diagram of laser welding in butt configuration; (b) Microstructural evolution of dissimilar joint of AA7075-Ti6Al4V with Cu interlayer.

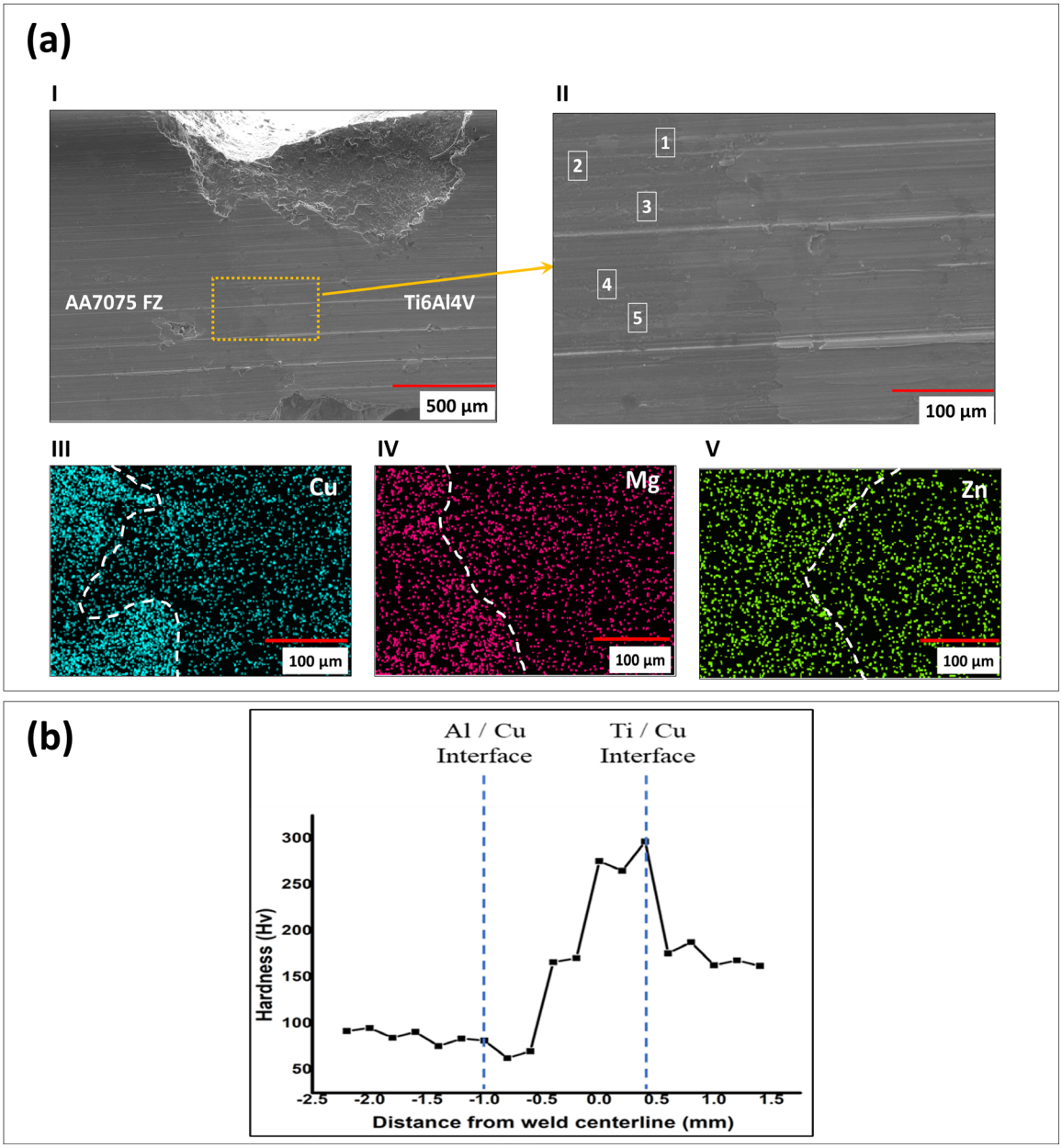

Figure 2.2 (a-I) SEM image of the joint without etching; (a-II) Selected points of interest for EDS and the results are shown in Table 1; (a-III, IV, and V) Elemental mapping of Cu, Mg and Zn; (b) Microhardness profile.

Tableau 2.1 Chemical composition of the different regions (Fig. 3.2) as measured by EDS (at. %).

Spectrum no.	Al	Ti	Zn	V	Fe	Ni	Cu	Mg	Sn	Potential phases
1	Bal.	1.03	0.58	1.20	0.51	0.04	30.24	0.37	0.33	Al_2Cu
2	Bal.	0.06	0.41	0.38	7.68	0.03	25.84	0.16	0.09	$Al_{13}Fe$+L
3	Bal.	0.30	1.18	0.03	0.66	0.04	41.33	0.01	0.05	Al_2Cu
4	Bal.	0.08	8.37	0.01	0.27	0.08	18.30	0.21	0.01	$Al_2Mg_3Zn_3$
5	Bal.	0.60	1.47	0.05	0.60	0.06	43.26	2.31	0.07	Al_2Cu

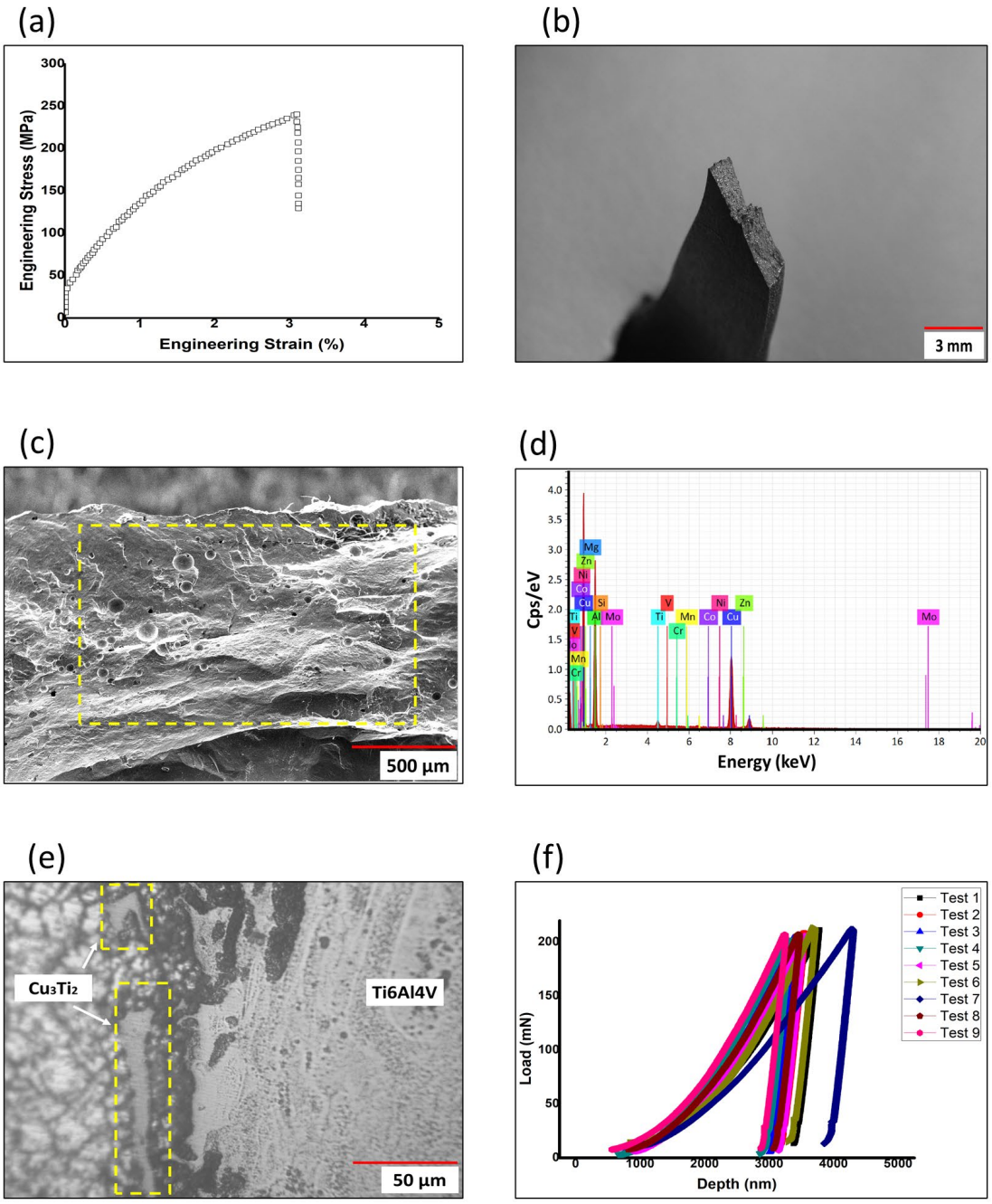

Figure 2.3 (a) Tensile test curve; (b) Physical appearance of the fractured tensile specimen; (c) SEM image of fractured surface; (d) EDS spectra of fractured surface; (e) Fracture location; (f) P-h curves across AA7075 FZ, mix zone, and Ti6Al4V/Cu interface.

Tableau 2.2 Chemical composition of the fractured surface (Fig. 3.3c) as measured by EDS (at. %).

Spectrum no.	Ti	Al	V	Fe	Zn	Mg	Ni	Cu	Potential phases
1	42.47	2.25	0.44	0.95	0.84	0.13	0.67	Bal.	Cu_3Ti_2

2.4 CONCLUSIONS

This research explored the use of Cu as an interlayer for laser welding AA7075 and Ti6Al4V alloys. Following conclusions are drawn from this study:

1) Utilizing Copper as an interlayer in laser welding led to successful dissimilar joining between AA7075 and Ti6Al4V alloys.
2) Owing to the formation of eutectic phases such as Al_2Cu, $Al_2Mg_3Zn_3$, and $Al_{13}Fe$ in the FZ of AA7075, the brittleness of the joint was reduced. On the other hand, diffusion of Cu into Ti6Al4V resulted in a brittle Cu_3Ti_2 IMC at the Ti6Al4V/Cu interface.
3) Tensile test result showed that the joint achieved an approximate tensile strength of 240 MPa.
4) EDS analysis of the fractured tensile specimens indicated that the fracture occurred due to the formation of Cu_3Ti_2 at the Ti6Al4V/Cu interface.
5) The microhardness and nanoindentation tests further validated the EDS analysis, confirming the observations.

CHAPITRE 3
EFFET DE L'INTERCOUCHE EN ARGENT SUR LES PROPRIETES MICROSTRUCTURALES ET LE COMPORTEMENT EN NANOFLUAGE DES SOUDURES DISSEMBLABLES TI6AL4V/AA7075 REALISEES PAR SOUDAGE LASER

Titre en français du troisième article :

Effet de l'intercouche en argent sur les propriétés microstructurales et le comportement en nanofluage des soudures dissemblables Ti6Al4V/AA7075 réalisées par soudage laser.

Titre original (en anglais) :

Effect of Ag interlayer on the microstructural properties and nanocreep behaviour of Ti6Al4V/AA7075 dissimilar laser weldments.

Auteurs et affiliation :

Asim Iltaf : Étudiant au doctorat, Département de mathématiques, d'informatique et de génie, Université du Québec à Rimouski, Québec, Canada.
Noureddine Barka : Professeur, Département de mathématiques, d'informatique et de génie, Université du Québec à Rimouski, Québec, Canada.
Shayan Dehghan : Chercheur post-doctoral, Département de mathématiques, d'informatique et de génie, Université du Québec à Rimouski, Québec, Canada.

État de l'article :

Publié.

Revue :

The Proceedings of the Institution of Mechanical Engineers, Part L: Journal of Materials: Design and Applications

Référence :

https://doi.org/10.1177/146442072412433.

Résumé en français du troisième article

La rupture par fluage constitue un risque potentiel dans les joints soudés dissemblables entre les alliages d'aluminium et de titane, pouvant compromettre l'intégrité du joint. Cette étude utilise le soudage par faisceau laser pour réaliser l'assemblage dissemblable de l'AA7075 et du Ti6Al4V en incorporant un intercouche en argent. Le rôle de l'intercouche en argent pour l'assemblage dissemblable des alliages AA7075 et Ti6Al4V et son impact sur la microstructure et le comportement en nanofluage des joints sont examinés. Les résultats ont montré que l'utilisation de l'argent réduisait considérablement l'interaction entre le titane et l'aluminium, ce qui a conduit à une diminution de la formation de composés intermétalliques fragiles. Les résultats de nanodureté et de microscopie à force atomique ont indiqué que la zone affectée thermiquement du Ti6Al4V présentait la plus grande dureté et la moindre déformation plastique, en raison de la formation de martensite α'. L'analyse du fluage par nanoindentation a révélé la valeur la plus élevée de l'exposant de contrainte dans la zone affectée thermiquement du Ti6Al4V, indiquant un mécanisme de fluage par ascension des dislocations. De plus, les résultats suggèrent également que le mécanisme de fluage observé pourrait être attribué à la fois au fluage diffusif et à l'ascension des dislocations dans d'autres zones.

Effect of Ag interlayer on the microstructural properties and nanocreep behaviour of Ti6Al4V/AA7075 dissimilar laser weldments

Asim Iltaf [a, *], Noureddine Barka [a], Shayan Dehghan [a, *]

[a] Department of Mathematics, Computer Science and Engineering, University of Quebec at Rimouski, Rimouski, QC G5L 3A1, Quebec, Canada.

[*]Corresponding authors (Asim Iltaf, Shayan Dehghan): Department of Mathematics, Computer Science and Engineering, University of Quebec at Rimouski, Rimouski, QC G5L 3A1, Quebec, Canada.

E-mail address: asim.iltaf@uqar.ca, shayan.dehghan@uqar.ca

Abstract

Creep failure poses a potential risk in dissimilar welded joints between aluminium and titanium alloys, potentially compromising the joint's integrity. This study utilizes laser beam welding to achieve dissimilar joining of AA7075 and Ti6Al4V by incorporating an Ag interlayer. The role of Ag interlayer for dissimilar joining of AA7075 and Ti6Al4V alloys and its impact on the microstructure and nanocreep behavior of joints is examined. The findings showed that the use of Ag decreased the interaction of Ti/Al considerably with each other which led to a reduction in the formation of brittle intermetallic compounds (IMCs). The nanohardness and atomic force microscopy (AFM) results indicated that the Ti6Al4V HAZ exhibited the highest hardness and least plastic deformation, owing to the formation of α' martensite. The nanoindentation creep analysis revealed the highest stress exponent value in Ti6Al4V HAZ, pointing to a dislocation climb creep mechanism. Additionally, the results also suggested that the observed creep mechanism might be attributed to both diffusional creep and dislocation climb for other zones.

***Keywords*:** Laser Welding, Interlayer, Nanoindentation, Nanocreep, EDS, AFM

3.1 INTRODUCTION

The current industrial trend is moving towards the manufacturing of multifunctional components through the integration of various similar and dissimilar materials (González et al., 2017; Iltaf, Dehghan, et al., 2024; Iltaf et al., 2023; Ramezani et al., 2023). This has brought a significant focus on the welding and joining of dissimilar alloys, which is essential in the fabrication of hybrid structures(Nagarajan & Manoharan, 2023; J. Yang et al., 2022). These attributes make the combination of titanium- and aluminum (Ti/Al)-based dissimilar alloy joints particularly advantageous in various industrial applications (Cooke & Atieh, 2020; Kumar et al., 2022; Raja Kumar et al., 2020, 2022; Ribeiro et al., 2021; N. Singh et al., 2020; Y. Zhang et al., 2021). For example, in the design of aero-engine compressors, using a transition joint between titanium alloys and aluminum alloys is a strategy to reduce overall engine weight (Blakey-Milner et al., 2021; Gialanella & Malandruccolo, 2020; Williams & Boyer, 2020). These joints utilize the strengths of both alloys to enhance equipment performance, save material costs, and improve design efficiency. However, a general challenge arises from the formation of brittle Al/Ti intermetallic compounds (IMCs) when directly joining these two alloys (Bunaziv et al., 2021; Gadakh et al., 2021; Kar et al., 2023; Manjunath et al., 2023). This issue can be addressed by selecting an appropriate welding process, adjusting the input process parameters, and incorporating a suitable metallic interlayer between the base alloys (Oliveira et al., 2020; Selvamani, 2022; Tey et al., 2020).

Failures in dissimilar alloy joints during service are common and can be attributed to various factors. Differences in microstructural and mechanical characteristics at the weld joint, combined with varying coefficients of thermal expansion (CTE) between the alloys, can lead to creep at the interface. Additionally, the presence of significant residual stresses, arising from disparities in chemical composition, thermal conductivity, and melting points, as well as metallurgical incompatibility, can adversely affect the creep behavior of these joints (Hepworth,

1984). Creep resistance is critical for the proper performance of a structure; if creep deformation surpasses the critical failure deformation outlined in the design specifications, the component may no longer operate safely (McKeen, 2009). Therefore, it is of utmost importance to conduct thorough investigations into the creep deformation behavior of dissimilar welded joints. Creep refers to the deformation of a material that occurs over time when it is subjected to a constant stress, which is below its yield strength, and maintained at a steady temperature. Li et al. (W. B. Li et al., 1991b) observed that during nanoindentation tests, a phenomenon known as indentation creep can occur. This type of creep is noted to happen at temperatures ranging from room temperature up to half the melting point of the metallic materials, denoted as 0.5 T_m.

The nano-indentation experiment is a widely recognized non-destructive testing method used to measure the mechanical properties of various materials, including bulk materials, coatings, thin films, and others. A notable application of this technique is in performing indentation creep testing (Schuh, 2006b). Unlike traditional macroscopic creep deformation tests, which typically involve uniaxial compression or tension, nanoindentation creep testing is considered a quick, reliable, convenient, and non-destructive method for examining the micro- and nanomechanical properties of different materials (Hu et al., 2015b; Ma et al., 2008b). In these tests, the creep properties of a small volume of material near the indenter tip are analyzed. The loading rate in nanoindentation is significantly faster than micro and macro indentation, typically two to three orders of magnitude, and the stress experienced beneath the indenter is much more complex compared to that in conventional creep tests (W. B. Li et al., 1991b).

The mechanical strength of welds is closely linked to the diverse microstructures that develop across various metallurgical and welding zones. To explore the creep resistance of welded alloys, where the microstructural variations are more distinct, the nanoindentation technique has been employed. Nguyen et al. (Nguyen et al., 2019b, 2019e) utilized the rate-jump method in their study of the strain rate sensitivity in welded joints of SM 490 and SS 400 structural steels. They conducted this study

through nanoindentation under low-cycle fatigue loading conditions. Their findings indicated that an increase in strain rate during indentation correlates with an increase in both yield strength and indentation hardness. In a separate study, Gao et al. (Zengliang et al., 2020b) examined the creep behavior of P92 steel weld joints after creep–fatigue loading using nanoindentation. They observed that the fine-grained heat-affected zone exhibited lower hardness and creep resistance compared to other areas of the weld joint. Similarly, Song et al. (Y. Song et al., 2020b) applied nanoindentation to assess creep deformation in various zones of SA508Gr3steel-welded joints. Notably, the application of nanoindentation to study weldments of titanium and aluminium-based alloys has yet to be explored.

In the current study, nanoindentation is applied to the weld joint consisting of AA7075 BA (base alloy) and Ti6Al4V BA with a Silver (Ag) interlayer, to reveal the complex metallurgical reactions occurring. Using Ag as an interlayer in the laser welding of Ti6Al4V and AA7075, instead of other metals, offers specific advantages due to its unique properties. The exceptional thermal conductivity of Ag ensures efficient heat distribution, reducing thermal gradients that can cause weld defects. Unlike other metals that might react unfavorably with either Ti or Al, Ag minimizes the formation of brittle intermetallic compounds, enhancing weld quality. Its relatively low melting point allows for better welding process control, facilitating the formation of a robust joint without excessive heat input that could degrade the base materials. Additionally, the good electrical conductivity and corrosion resistance of Ag are beneficial in applications where these properties are critical. In comparison, other metals might not offer this balanced combination of thermal properties, compatibility, and performance, making Ag a preferred choice for achieving high-quality welds between Ti6Al4V and AA7075. This study involves conducting nanohardness line scans and creating nanohardness maps, along with measuring the creep behavior in these specific regions through nanoindentation. This approach is designed to provide

detailed insights into the localized mechanical properties and creep resistance of the materials in the vicinity of the weld joint.

3.2 MATERIALS AND METHODS

AA7075 and Ti-6Al-4V annealed sheets were joined through the laser beam welding (LBW) technique. These sheets had dimensions of 80 x 50 x 1.6 mm. A silver (Ag) foil interlayer, approximately 380 μm thick, was utilized between the sheets of AA7075 and Ti-6Al-4V. The chemical compositions of these alloys, determined by EDS, are displayed in **Table 3.1** and **Table 3.2**. **Figure 3.1** illustrates that the welding was performed in a butt configuration. For this study, the optimal parameters for the laser welding process were established through initial experiments, and the optimized parameters are shown in **Table 3.3**. For reproducibility and reliability of the findings,

three specimens were manufactured. These samples were used in order to validate the consistency of the mechanical properties.

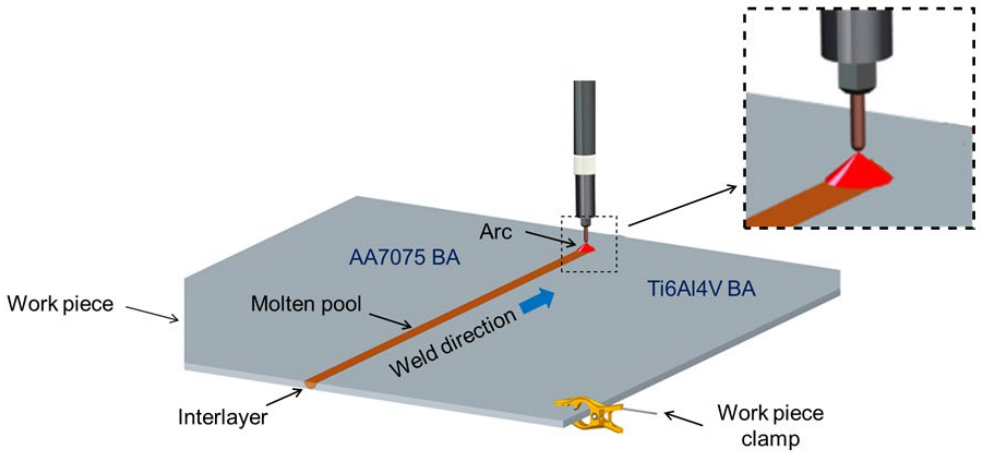

Figure 3.1. Schematic diagram of laser welding of AA7075 BA and Ti6Al4V with Ag interlayer

Tableau 3.1 Electrochemical dispersive spectroscopy (EDS) chemical analysis of AA7075 BA (at. %)

Zn	Si	Fe	Mg	Mn	Cu	Cr	Al
5.24	0.65	0.23	0.76	0.13	0.21	0.058	Bal.

Tableau 3.2 EDS chemical analysis of Ti6Al4V BA (at. %)

Al	Sn	Fe	Zr	V	Si	Nb	C	Ti
5.87	0.076	0.17	0.021	4.12	0.028	0.04	0.352	Bal.

Tableau 3.3 Optimized laser welding parameters

Laser power (kW)	Welding speed (mm/sec)	Working distance (mm)	Focal length (mm)	Focal spot diameter (mm)
3	50	150	310	0.92

The welding was conducted using a fiber laser, specifically the IPG Photonics Ytterbium Laser Systems model YLS-3000-ST2. This class 4 laser can produce 3 kW of peak power. It functions by producing continuous wave emissions at a wavelength of 1070 nm. The connection between the laser source and the BIMO HIGHYAG laser head is established through advanced optical fibers with a 600 µm diameter. The laser head is equipped with a lens of 310 mm fixed focal length and includes a focusing module with a M_{foc} value of 1.50, along with an adjustable zoom collimator. This setup results in a circular laser focus, varying in diameter from 0.3 to 1.53 mm, based on the interaction of the focusing module, collimation module, and the fiber's diameter. This interrelation is quantitatively explained in Equation Eq. (1).

$$\phi_{focus} = M_{col.}.M_{foc}.\phi_{fiber} \quad (1)$$

The variable ϕ signifies the laser spot's diameter at its focal point. The collimation factor, labeled as M_{col}, is fixed at 1.022. The focusing capacity is represented by the focalization modulus, M_{foc}, set at 1.5. The experiment used a fiber with a diameter, ϕ_{fiber}, of 600 µm. With the collimator set to its minimum, the diameter of the focused spot reached 0.92 mm. The laser head connects to a FANUC M-710iC robot, featuring a 6-axis articulated arm for precise, pre-set movements in multiple directions, as depicted in **Figure 3.2**. This robotic unit can handle payloads up to 70 kg, operates at a manual linear speed of 250 mm/s, and achieves an automated angular speed between 175 and 355 °/s.

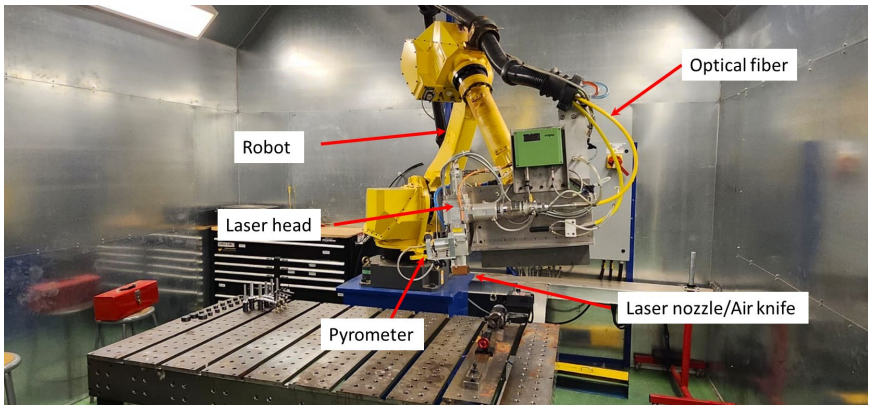

Figure 3.2 Laser unit (3000W: Model YLS-3000-ST2) installed on a six-axis FANUC robotic arm

Wire electrical discharge machining (EDM) was employed for preparing samples for microhardness testing, nanoindentation, and metallography study. The weldments for microstructural examination and nanoindentation assessments were mounted, then subsequently abraded using SiC paper ranging from 220 to 4000 grit sizes. A final polish was achieved using 0.25 mm diamond paste on a microcloth. These prepared samples were then analyzed using an Olympus BH2-UMA optical microscope to assess grain morphology in the microstructure. Microhardness profiles were recorded using a Tukon-300 microhardness tester, applying a 200 gf load and a 10 s dwell time.

Room temperature nanoindentation tests were conducted using a nanoindenter in a load-controlled mode. The specimens' elastic moduli and nano-hardness were determined by applying a 200 mN constant load with a Berkovich tip, with the maximum load and strain rate set at 200 mN and 0.1 s^{-1}, respectively. To assess creep depth changes over time, the indentation tip was held in place for 200 s. Drift velocity was then monitored by decreasing the load to 90% and shortening the hold time to 40 s. After unloading the indenter from the sample surface, nanohardness and elastic modulus values were calculated using the established (Oliver & Pharr, 1992d). Additionally, the nanoindentation strain rate was determined following the approach outlined by (Oliver & Fabes, 1995) as expressed in Eq. (2).

$$Creep\ strain\ rate\ (\varepsilon') = \frac{Rate\ of\ indentation\ depth}{Indentation\ depth} = \frac{h'}{h} = \left(\frac{1}{h}\right) \times \left(\frac{dh}{dt}\right) \quad (2)$$

The empirical creep model, as depicted in Equation Eq. (3), was used to curve fit the indentation depth rate data with the experimentally observed creep rate, post calculation of the creep strain rate (X. Liu et al., 2016). The formula is:

$$h = h_i + a(t - t_i)^{(1/2)} + b(t - t_i)^{(1/4)} + c(t - t_i)^{(1/8)} \quad (3)$$

In this equation, 't' denotes the time allocated for creep, h represents the depth of indentation by the indenter, and the remaining terms are the optimal fit parameters. Following the application of this empirical model, the creep stress during the indentation holding stage was calculated using Eq. (4). This equation is derived from a range of published sources including (Hu et al., 2015c; Lucas & Oliver, 1999; Nguyen et al., 2019c; Oliver & Pharr, 1992d; Y. Song et al., 2020c; Su et al., 2013a; Zengliang et al., 2020c)

$$\sigma = \left(\frac{H}{3}\right)\left(\frac{h_{max}}{h}\right) \quad (4)$$

In Eq. (4), h_{max} denotes the maximum loading depth, h is the instantaneous depth, and σ represents the indentation creep stress.

The power-law relationship is employed specifically for estimating the creep stress exponent during the stable or secondary creep phase. This relationship between stress and creep strain rate is documented in the literature as an effective method for analyzing creep behavior at room temperature. The expression for the power-law relationship is given in Equation Eq. (5) as detailed by (Su et al., 2013b):

$$\varepsilon' = k\sigma^n \quad (5)$$

Here, the stress exponent (n) is determined by measuring the slope in the plotted graph of the creep strain rate (ε') against indentation creep stress (s), as described by

Eq. (5). Additionally, atomic force microscopy (AFM) was utilized to examine the indent depth and the surface morphology of the weldments.

3.3 RESULTS AND DISCUSSION

3.3.1 Physical appearance of weldment

Figure 3.3 displays a representative image of the top and bottom surface of the weld bead, revealing that the weld bead was free from contamination and had a bright appearance. Titanium and aluminium alloys are known for their tendency to react with atmospheric oxygen at high temperatures during welding, leading to oxide formation that can degrade weld joint quality, as referenced in the literature (Baruah & Bag, 2016b, 2016a, 2017). The degree of oxidation in the weld pool can be inferred from the bead's color (Baruah & Bag, 2017). The bright silvery appearance of the weld bead in **Figure 3.3**, in contrast to blue and purple, indicates minimal contamination in the weld pool (Lathabai et al., 2001; X. Li et al., 2005)

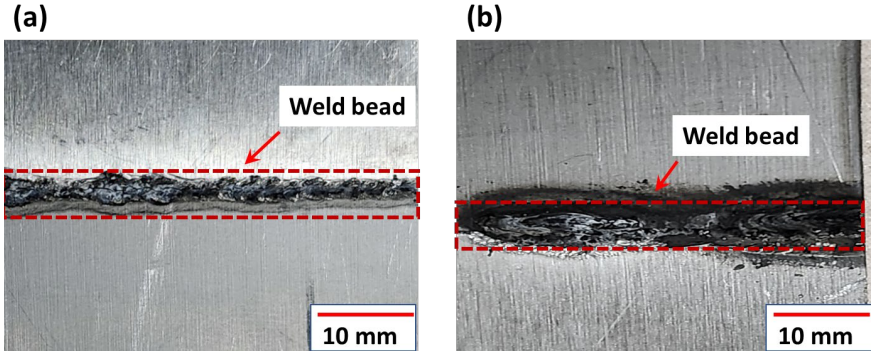

Figure 3.3. Surface appearance, (a) Top surface of the weldment and (b) Bottom surface of the weldment

3.3.2 Microstructural analysis

In this study, 1.6 mm thick Ti-6Al-4V and AA7075 aluminum alloy sheets were welded, incorporating a 380 µm thick Ag interlayer. The AA7075 alloy's microstructure is predominantly a globular aluminum cubic (fcc) phase with minor pits,

likely from $MgZn_2$ precipitate removal during etching, as seen in **Figure 3.4(a)**. **Figure 3.4 (a)** shows a micrograph of AA7075 BA, and as indicated by the label "Precipitates," it is meant to show areas where precipitates are present within the metal's matrix. As mentioned earlier, the aluminum alloy showed minor pits from precipitate removal, suggesting that during the preparation or etching of the sample for microscopy, some precipitates may have been dislodged, leaving behind small pits or voids. **Figure 3.4 (a)**, therefore, shows the actual precipitates rather than the pits left by any removed ones. This indicates that there are both intact precipitates within the material as well as areas where precipitates have been removed, although only the former is labeled in **Figure 3.4(a).** The Ti-6Al-4V alloy primarily consists of equiaxed hexagonal close-packed (hcp) α-phase grains with some intergranular cubic body-centered cubic (bcc) β-phase, as illustrated in **Figure 3.4(b)**. **Figure 3.5** shows the overall microstructural changes due to the dissimilar welding of Ti-6Al-4V and AA7075. Using Ag as an interlayer modified the alloy composition during welding, minimizing crack susceptibility. The partly melted Ti-6Al-4V area near the fusion zone, depicted in **Figure 3.6(a)**, shows distinct microstructural and property differences, termed macrosegregation. This phenomenon relates to the base materials' liquidus temperature and the weld pool. The laser beam's high energy density partially melts the Ti-6Al-4V, causing it to flow towards the melt pool due to Marangoni effect-driven convection, solidifying into partly melted Ti-6Al-4V islands. After welding, rapid cooling forms a modified α-phase with needle-like morphology on the Ti-6Al-4V side. Rapid cooling also produces fine acicular α, resembling needle-like martensite in the Ti-6Al-4V's heat-affected zone (HAZ). **Figure 3.6(b)** shows IMC layers and dendrites at the Al/Ti interface. During cooling, Ti atoms solidify on the dendrite surfaces, forming Ti-enriched IMC dendrites. **Figure 3.6(b)** displays IMCs in the fusion zone (FZ), likely from disrupted columnar dendritic IMCs in the melt pool. Si-segregation near grain boundaries forms Al-Si eutectics, seen as dark lines in **Figure 3.6(c)**, where small black Mg-Zn particles along α-Al grain boundaries enhance AA7075's mechanical properties

through precipitation strengthening. The weld's thermal cycle dissolves precipitated phases in the HAZ into the aluminium alloy matrix, as observed in **Figure 3.6(c)**.

Elemental composition analysis of specific points across weld zones is revealed as shown in **Figure 3.7**. The Ti-6Al-4V/HAZ interface and subsequent FZ regions show microstructural relevance as detailed in **Table 3.4**. The chemical composition of specific points is shown in **Table 3.4** as discussed in chapter 1. **Table 3.4** indicates abrupt Al and Ti composition changes at this interface, but stability elsewhere, except near titanium aluminides and Al-Si eutectics. Lighter grey particles, composed of Ti, Al, and Si, and Al-Si eutectics with less Al and more Si, are present in the FZ. **Figure 3.6** shows the IMC layer at the Ti-6Al-4V/FZ interface, with IMC dendrites extending into the FZ. EDS identified IMC layer and segment compositions (**Table 3.4**, points 3 and 4). The Al_3Ti IMC layer's high aluminium content suggests its formation over $AlTi_3$ and TiAl due to lower Gibbs free energy. Al predominates in regions near the Ti-6Al-4V and AA7075 sides and the HAZ of AA7075 (points 4-6). Al_3Ti particles, formed at the Ti/Al interface, either flow with the molten pool or are extruded by nearby grains, increasing weld joint strength. However, excessive Ti/Al reaction can thicken the Al_3Ti IMC layer, risking joint failure. Controlled Ti/Al interaction is therefore very crucial.

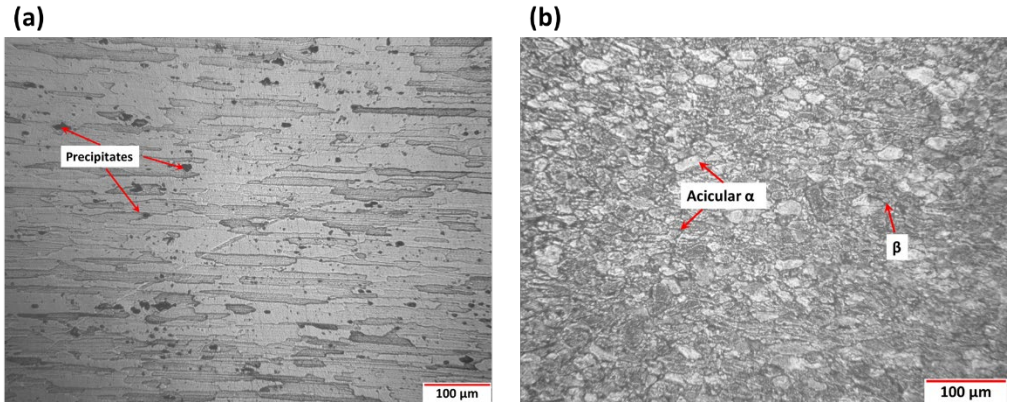

Figure 3.4 (a) Microstructure of AA7075 BA, (b) Microstructure of Ti6Al4V BA

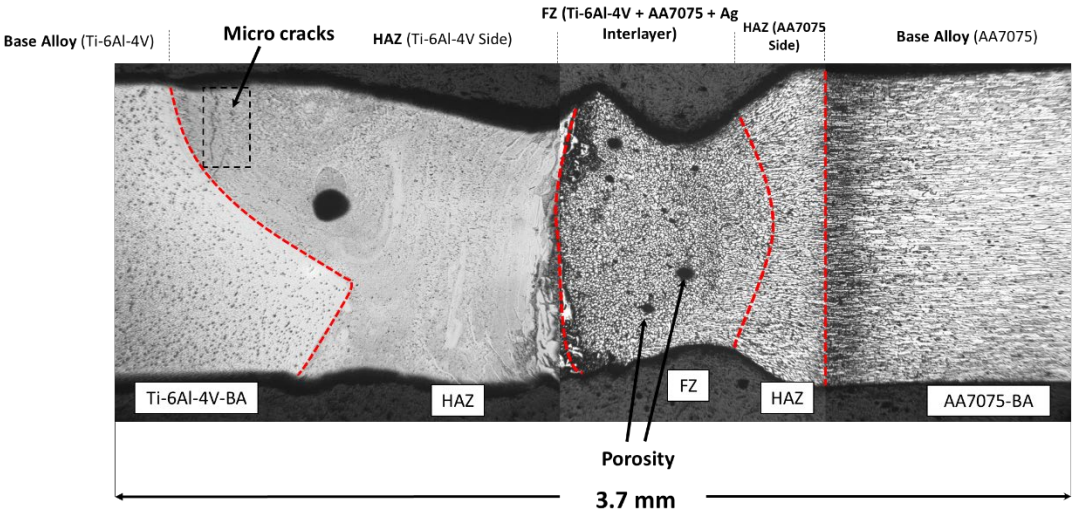

Figure 3.5 An overall view of the weldment showing all the zones in the joint

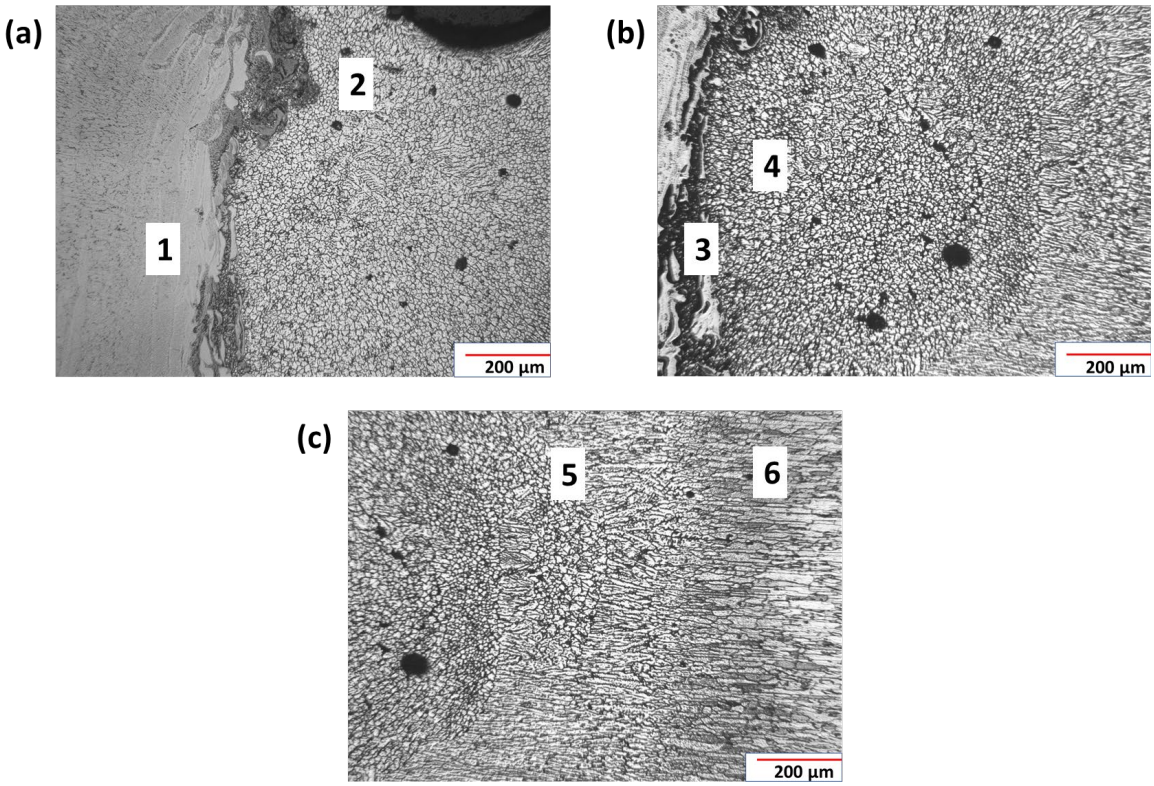

Figure 3.6 (a) Ti6Al4V side microstructure including HAZ, (b) FZ containing AA7075+Ti6Al4V+Ag, and (c) AA7075 side microstructure including HAZ

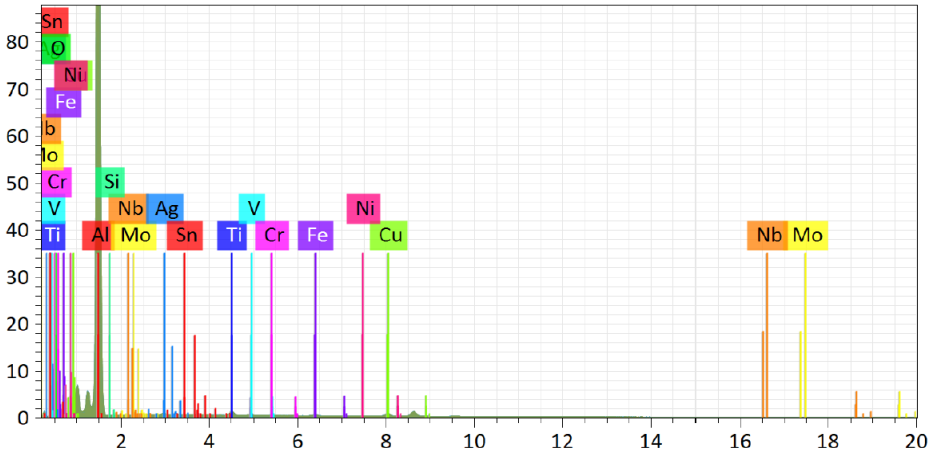

Figure 3.7 EDS spectra result of point analysis

Tableau 3.4 EDS point analysis result (Iltaf, Barka, et al., 2024).

Spectrum no.	Al	Si	Ti	V	Cr	Fe	Ni	Cu	Mg	Ag	Sn	Potential phases
1	5.60	0.01	90.66	3.40	0.00	0.19	0.06	0.01	0.05	0.00	0.00	Ti
2	10.38	0.07	76.25	1.87	0.00	0.28	0.01	0.18	0.04	5.01	0.00	$AgTi_3$
3	95.20	0.04	1.40	0.05	0.20	0.59	0.03	1.29	0.13	4.97	0.09	Al_3Ti
4	95.65	0.03	1.18	0.03	0.22	0.66	0.04	1.33	0.01	5.79	0.05	Ag_2Al, Al_3Ti
5	93.14	0.06	1.47	0.05	0.21	0.60	0.06	0.95	2.31	1.05	0.07	Al (Mg enriched)
6	97.25	0.08	0.01	0.01	0.23	0.27	0.08	0.48	0.21	1.21	0.17	Al

3.3.3 Microhardness analysis

As illustrated in **Figure 3.8**, the microhardness profiles of all weldment zones and BAs were measured, showing an increase in microhardness within the fusion zone as compared to AA7075. The FZ exhibited higher microhardness, approximately 55% greater than that of the AA7075 base alloy. The lowest microhardness was observed in the AA7075 BA. The temperature influences intermetallic compound formation at the interface, affecting material hardness. High temperatures promote consistent, gradual IMC formation, enhancing hardness, while low temperatures limit atomic diffusion and lower hardness. Ag interlayer use reduces brittle IMC formation but may lead to $AgTi_3$ formation on the Ti-6Al-4V side. Ti-Ag intermetallics have a lower embrittlement impact than Al-Ti intermetallics, decreasing FZ bond strength. $AgTi_3$ IMC formation also reduces FZ porosity, as evident in **Figure 3.5**. Ag use thus improves joint quality by mitigating brittle IMC and void formation. The Ti-6Al-4V HAZ on the side showed

greater microhardness measurement compared to AA7075 BA, AA7075 side HAZ, and FZ. This is attributed to the presence of hard phases; acicular α and α martensite.

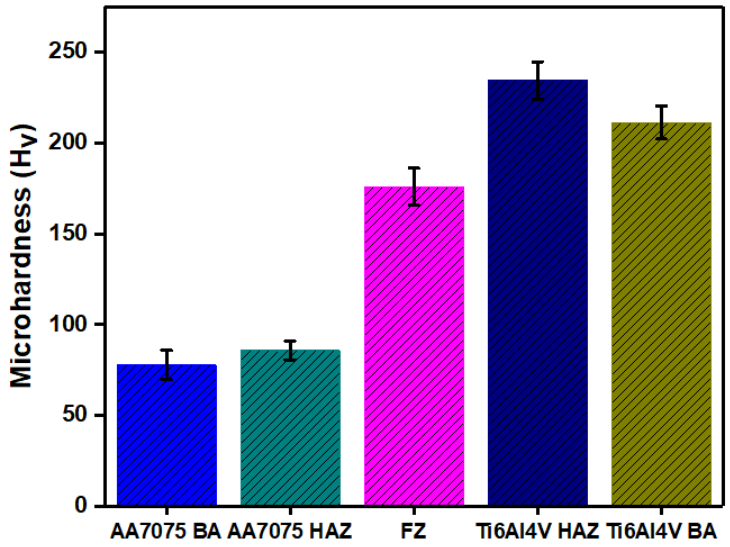

Figure 3.8 Microhardness profile of the joint zones including base alloys

3.3.4 Nanoindentation characterization

The nanomechanical properties of all the joint zones and BAs were evaluated using nanoindentation at room temperature. **Figure 3.9** illustrates the load-displacement (P-h) curves under a constant load of 200 mN, showing the nanohardness and elastic modulus of the weldments. The load-displacement loading curve is influenced by both elastic and plastic deformation, as per Kick's law ($P = Ch^2$, where C is a constant), as explained by Hainsworth et al. (Hainsworth et al., 1996). The indentation process results in a combination of elastic-plastic loading and purely elastic unloading deformations, with variations in penetration depth likely due to microstructural changes during the solidification in the laser beam welding (LBW) process (Hainsworth et al., 1996).

From the P-h curves in **Figure 3.9(a)**, the AA7075 BA and AA7075 HAZ showed the highest penetration displacement, approximately 2726 nm, and 2491 nm, respectively. Among all the zones and both BAs, the maximum displacement was noted

at AA7075 BA (~2726 nm), whereas the minimum penetration occurred at Ti6Al4V HAZ (~1674 nm). This difference in penetration depth may be linked to the indentation effect at the grain boundary microstructure variation as explained in section 3.2.

Figure 3.9(b) presents the nanohardness and elastic modulus data, calculated using the Oliver and Pharr method. Moving from AA7075 BA towards the Ti6Al4V BA led to a rise in nanohardness from 2.06 GPa to 5.80 GPa in the Ti6Al4V HAZ. The lowest values were observed in FZ (1.94 GPa) owing to the use of an Ag interlayer as it reduces brittle IMC formation but can form $AgTi_3$ on the Ti6Al4V side. Ti-Ag IMCs are less embrittling than Al-Ti. Furthermore, an increase in indentation depth at constant load implied lower nanohardness due to reduced dislocation density, as per Gale and Achuthan (Gale & Achuthan, 2014)

Regarding elastic modulus, as shown in **Figure 3.9(b)**, an increase from 82.62 GPa to 139.55 GPa was observed from AA7075 BA to Ti6Al4V HAZ. However, there was a slight increase from AA7075 BA (82.62 GPa) to 86.55 for the FZ. This reduction might be attributed to the formation of less brittle $AgTi_3$ IMCs as evident from **Table 3.4**. This fluctuation in the elastic modulus values can be linked to the varying microstructural variations influenced by the use of Ag interlayer, which affects the material's response to indentation forces.

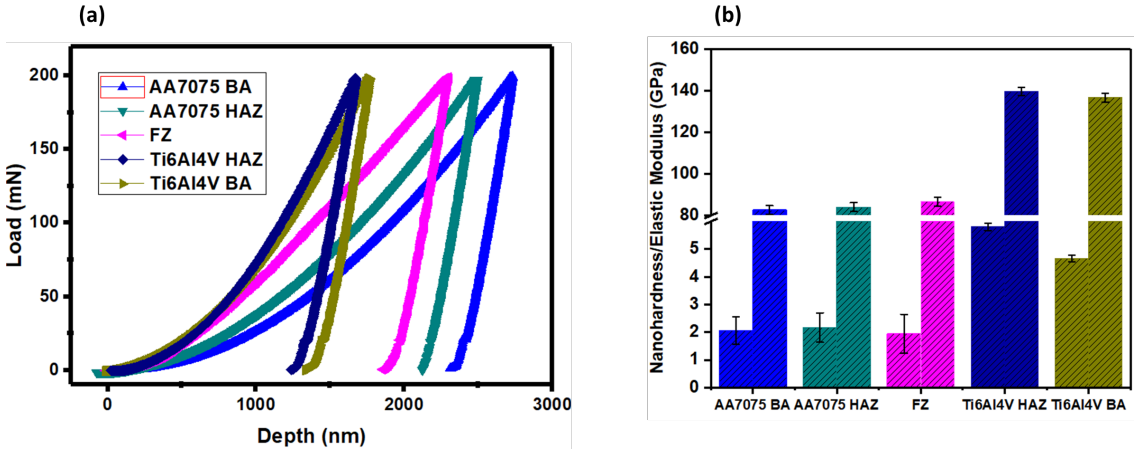

Figure 3.9 (a) Load-displacement (P-h) curves, and (b) Nanohardness and elastic modulus measurements for all the zones, including the base alloys

3.3.4.1 Nanocreep evaluation

Figure 3.10(a) presents the load-displacement curves for all the zones, including both base alloys. It shows an increase in indenter penetration depth from approximately 1512.71 nm in the Ti6Al4V HAZ to around 1775.87 nm in the FZ. **Figure 3.10(b)** displays the depth-time (h-t) curves, using nanoindentation data gathered during a 200 s holding period for all the weldment zones and both alloys. These curves show an initial rapid increase in penetration depth as the maximum load of 200 mN is reached in about 40 s, followed by a decrease in penetration depth after reaching this maximum load.

Throughout the 200 s holding period, significant depth plateaus were observed in each zone and the base alloys. Creep displacement versus time (h-t) curves, derived from these plateaus, are shown in **Figure 3.10(b)**.

The depth plateaus during the holding stage (200 s) as shown in **Figure 3.10(b)**, suggest an initial increase in penetration depth before reaching maximum load (200 mN). The initial increase in penetration depth is illustrated in **Figure 3.11**. **Figure 3.11** displays the depth versus time (h-t) curves of all weld zones along with the base alloy from **Figure 3.10(b)**. The maximum creep displacement was found to be about 184.35

nm in the FZ, while the minimum, approximately 145.64 nm, was observed in the Ti6Al4V HAZ. The creep displacements in Ti6Al4V BA, AA7075 BA, AA7075 HAZ, and 400 W were about 155.11 nm, 165.30 nm, and 175 nm, respectively, indicating that they were lower than the FZ by 15.86%, 10.33%, and 5.07%.

Using Equation (3), the fitted curves were plotted (represented by a red line), while the black line indicate the experimental data, as seen in **Figure 3.12**. These fitted curves closely match the experimental results for all zones and both base alloys. During the primary creep stage, as shown in **Figure 3.12**, indentation depth increased rapidly withholding time for each weldment zone and the base alloys. During the secondary creep stage, the penetration depth increased linearly over the 200 s holding time. Tertiary creep, commonly observed in conventional creep tests, does not occur in indentation creep, as the hardness test is a compression test, and the specimen does not fracture (Mahmudi et al., 2013).

In a creep test, elastic deformation refers to the initial, reversible strain a material undergoes when stress is applied, which is instantaneous and follows Hooke's Law, governed by the material's elastic modulus. This phase is typically short-lived and does not permanently alter the material. On the other hand, plastic deformation is the subsequent, irreversible strain that occurs under sustained stress, leading to permanent changes in the material's structure. Initially, plastic deformation causes an increase in strain rate due to dislocation movement, but over time, it reaches a steady state where strain hardening, where the material becomes stronger and more resistant to deformation and recovery processes where the material's structure rearranges to relieve stress occur simultaneously, stabilizing the strain rate. The creep strain rate of all weld beads and the base alloy was calculated using Equation (2), as shown in **Figure 3.13**. The results indicate a sharp decrease in creep strain rate at a constant load for each weldment zone and both base alloys, attributable to strain hardening caused by plastic deformation. Following this initial decrease, as observed in **Figure 3.13**, the creep strain rate gradually declined and stabilized, characteristic of secondary or steady-state

creep, due to strain hardening and simultaneous recovery within the joint and base alloys (Oliver & Pharr, 1992e).

Figure 3.14(a) illustrates the relationship between stress and creep strain rate in indentation for the base alloys and all weldment zones. The slope of the linear fit in this graph represents the creep stress exponent, which provides insights into the material's creep resistance and the creep phenomena. Higher values of the creep stress exponent, as noted in **Table 3.5** indicate better resistance to creep, following the findings of Van Swygenhoven and Derlet (Van Swygenhoven & Derlet, 2001).

It was found that the diffusional creep mechanism was predominant only in the FZ and AA7075 HAZ as shown in **Figure 3.14(b)**. Additionally, the grain boundary sliding mechanism was observed in the AA7075 base alloy. In contrast, the dislocation creep mechanism was evident in the Ti6Al4V BA and Ti6Al4V HAZ, as their stress exponent values were slightly higher than 3(**Table 3.5**). This higher stress exponent implies an increased generation and involvement of dislocations in the deformation process during the 200 s holding time under constant load, as explained by Zhang et al. (W. D. Zhang et al., 2016). The generation of dislocations during loading is proportional to the applied load or indentation depth, and these dislocations form in the plastically deformed region beneath the indenter, as discussed by Almasri and Voyiadjis (Almasri & Voyiadjis, 2007).

The Ti6Al4V HAZ, owing to the formation of the martensitic α phase, resulted in a high dislocation density beneath the indenter. Consequently, this bead exhibited a higher stress exponent compared to the other weld beads. This finding emphasizes the intricate relationship between microstructural characteristics (phase transformation in Ti6Al4V HAZ and formation of less brittle IMCs) and the mechanical properties, like nanohardness and creep behavior, in dissimilar weldments of AA7075/Ti6Al4V with Ag interlayer.

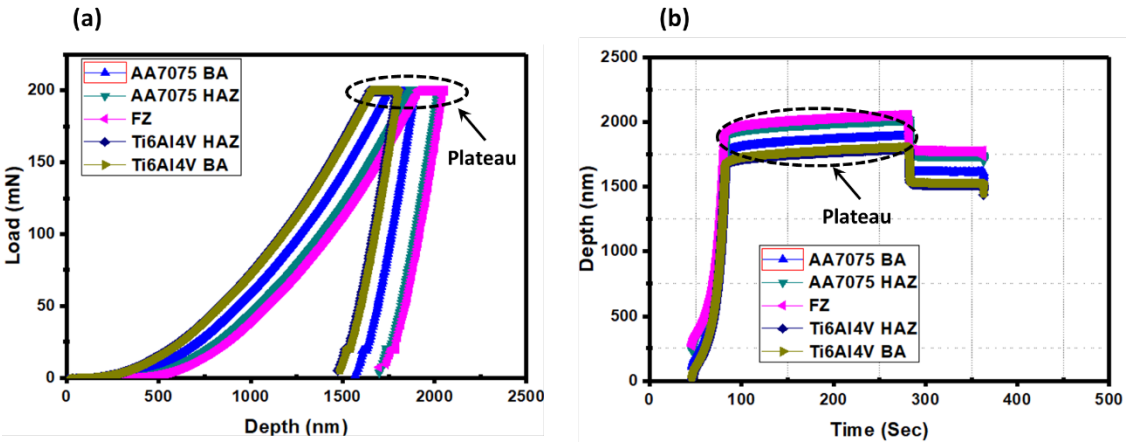

Figure 3.10 (a) Load-displacement curves from nanoindentation, and (b) Depth-time curves for each zone including base alloys

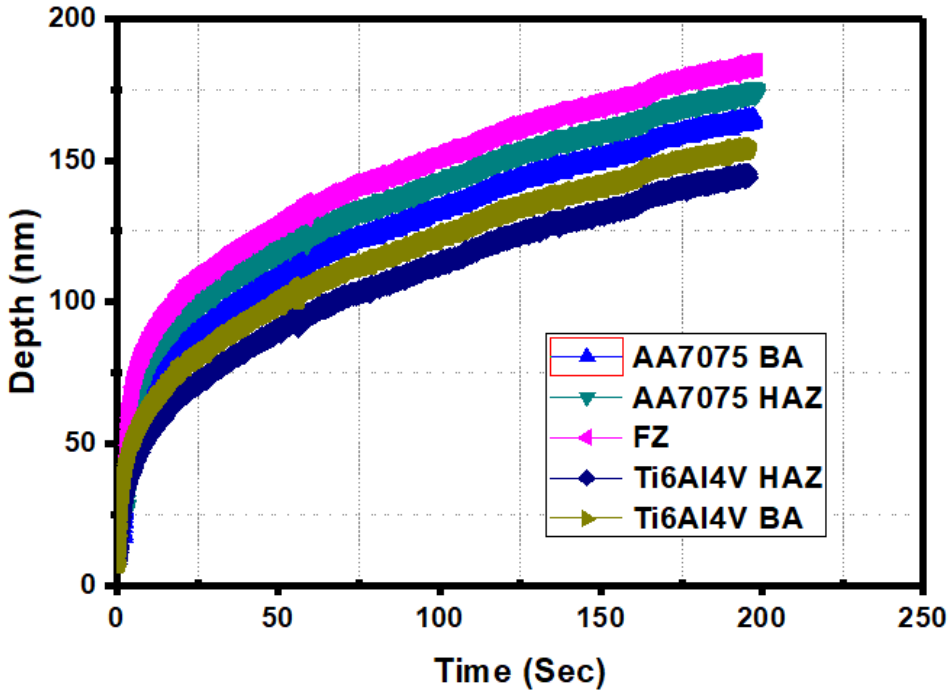

Figure 3.11 Curves representing the depth penetration for each zone and the base alloys

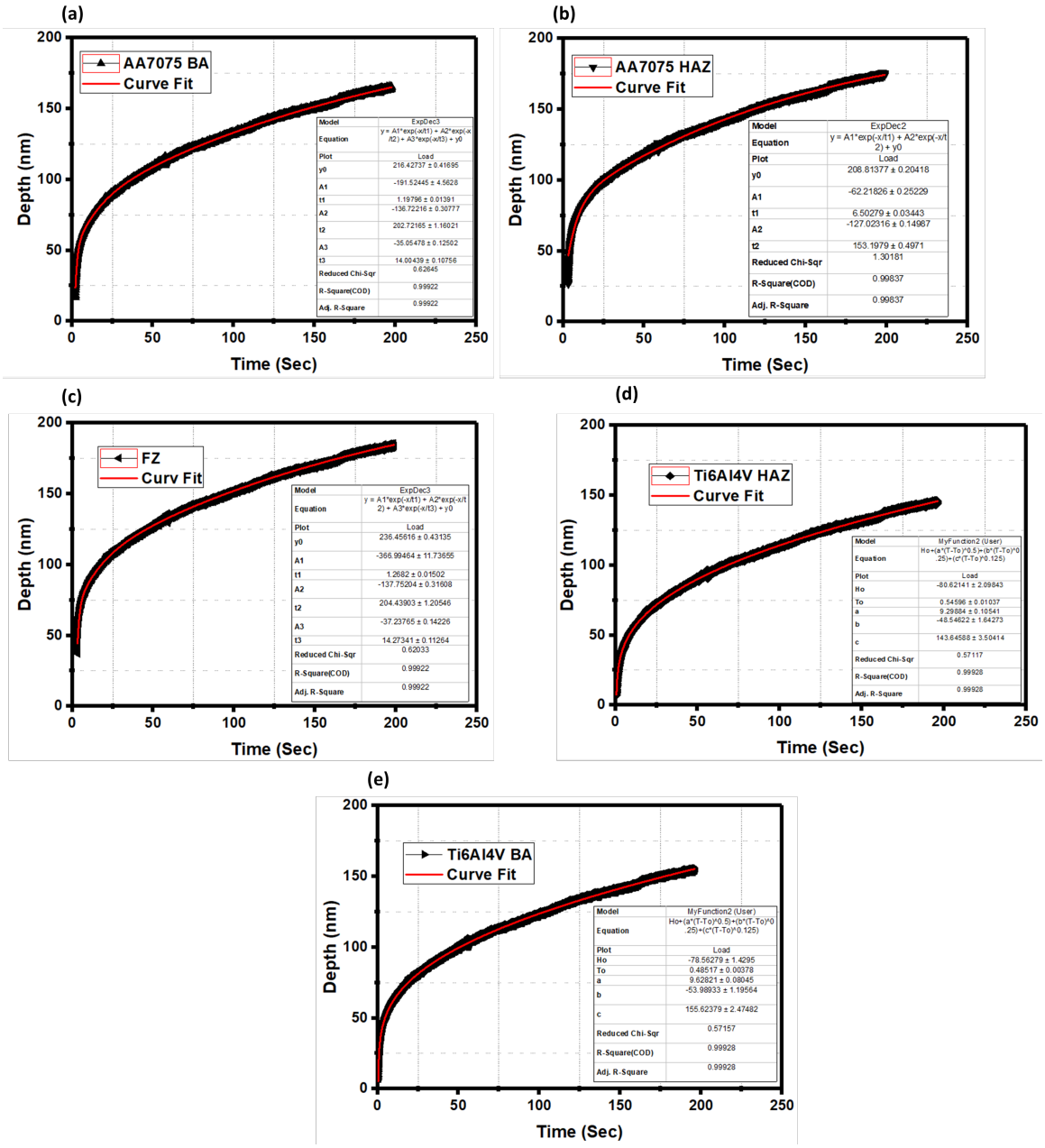

Figure 3.12 Comparative data showing fitted (red line) and experimental (black line) results for, (a) AA7075 BA, (b) AA7075 HAZ, (c) FZ, (d) Ti6Al4V HAZ, and (e) Ti6Al4V BA

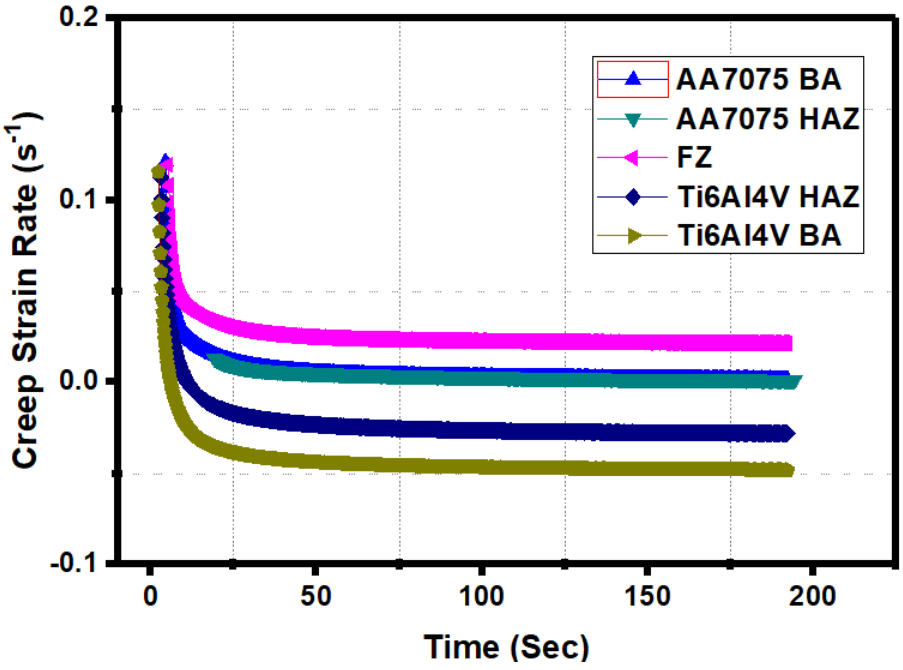

Figure 3.13 Graphs depicting the relationship between creep strain rate and time for all the weldment zones including base alloys

Tableau 3.5 Creep stress exponent values correlated with creep mechanisms, as per Van Swygenhoven and Derlet (Van Swygenhoven & Derlet, 2001)

S.No.	Creep stress exponent	Nanocreep mechanism
1	1-2	Diffusion creep
2	2-3	Grain boundary sliding
3	3-4	Viscous motion of dislocation
4	>4	Dislocation climb mechanism

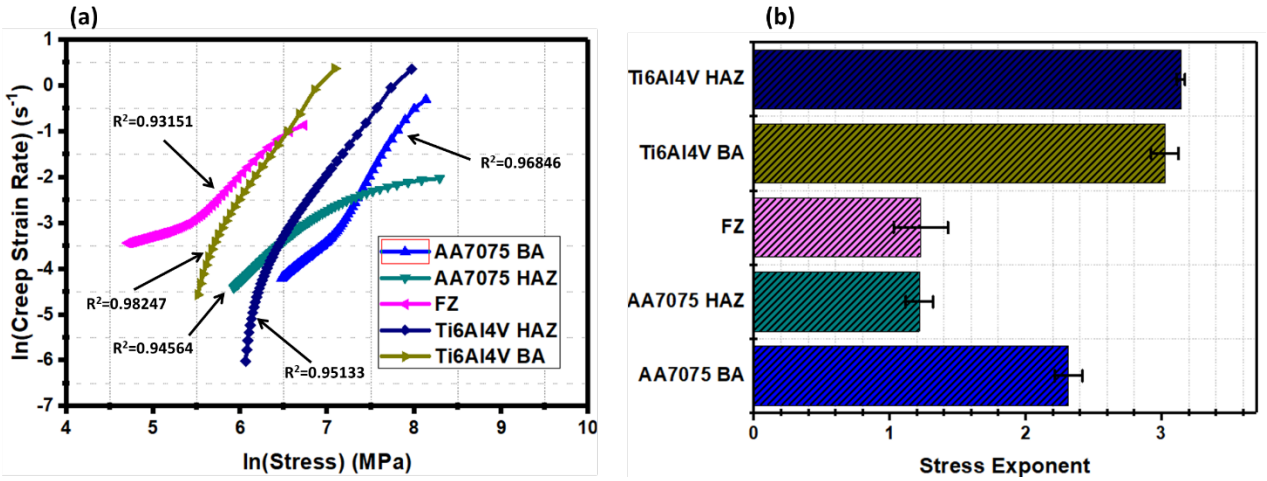

Figure 3.14. (a) Curves showing the creep strain rate versus stress, and (b) Creep stress exponent values for each zone including base alloys

3.3.4.2 Atomic Force Microscopy (AFM) analysis

During nanoindentation, material displacement occurs, creating a pile-up around the indent's edges. This phenomenon for AA7075 BA, FZ, and Ti6Al4V BA, through Atomic Force Microscopy (AFM) analysis, is shown in **Figure 3.15**, **Figure 3.16**, and **Figure 3.17**. The 2-D AFM images of the along with their corresponding line surface profiles are also depicted in **Figure 3.15**, **Figure 3.16**, and **Figure 3.17**. Insets in these figures provide side-view 3D mappings. This is a color-coded topographical map produced by an AFM after performing nanoindentation on a material. The indent is the central feature, shown by a change in color that indicates a variation in height due to the indentation process. The varied colors surrounding the indent suggest a gradient in topography, with red and yellow areas indicating higher regions—these are the pile-ups. The gradient of colors from red to blue illustrates the transition from the raised pile-up area back to the baseline surface level. The uniform background suggests that the surface outside the immediate indentation area is relatively flat and unaltered. The right image with 3-D insets in **Figure 3.15**, **Figure 3.16**, and **Figure 3.17** is a cross-sectional analysis of the indentation. The lines represent profiles taken at different

points across the indent. The deepest point corresponds to the maximum penetration of the indenter, and the surrounding raised lines show the height of the material that has piled up around it. The Gwyddion software was used to measure the depth of the indent and the height of the pile-up, providing quantitative data on the material's response to indentation. The indentation depth in the FZ (**Figure 3.16**) is notably deeper than that in the AA7075 BA and Ti6Al4V BA (**Figure 3.15** and **Figure 3.17**), indicating a higher degree of plastic deformation in the former.

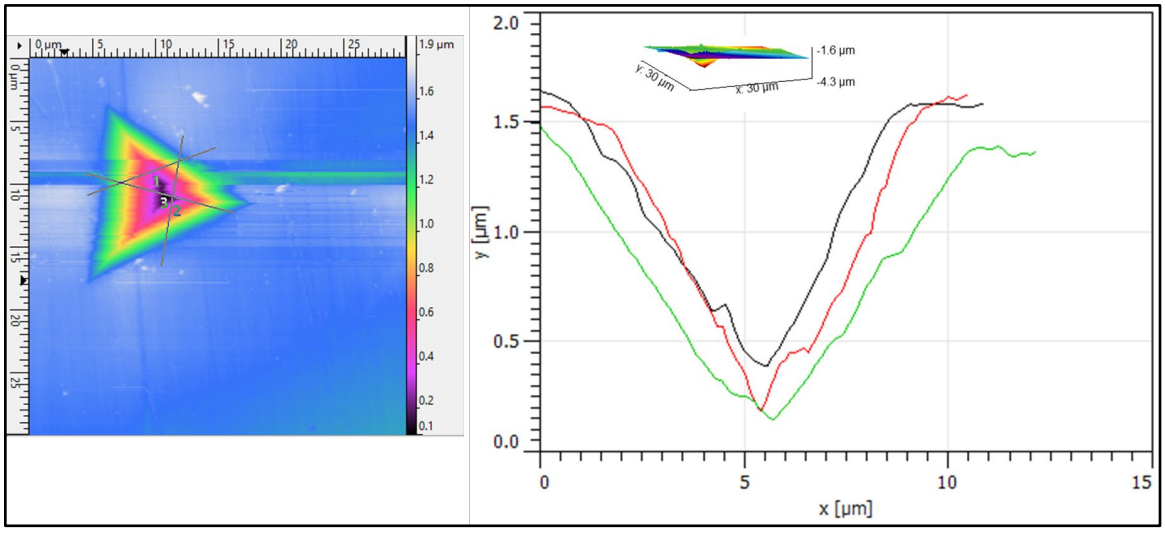

Figure 3.15. 2-D (Left image) and 3-D images (Inset in right image) of nanoindentation along with depth measurement profiles of AA7075 BA

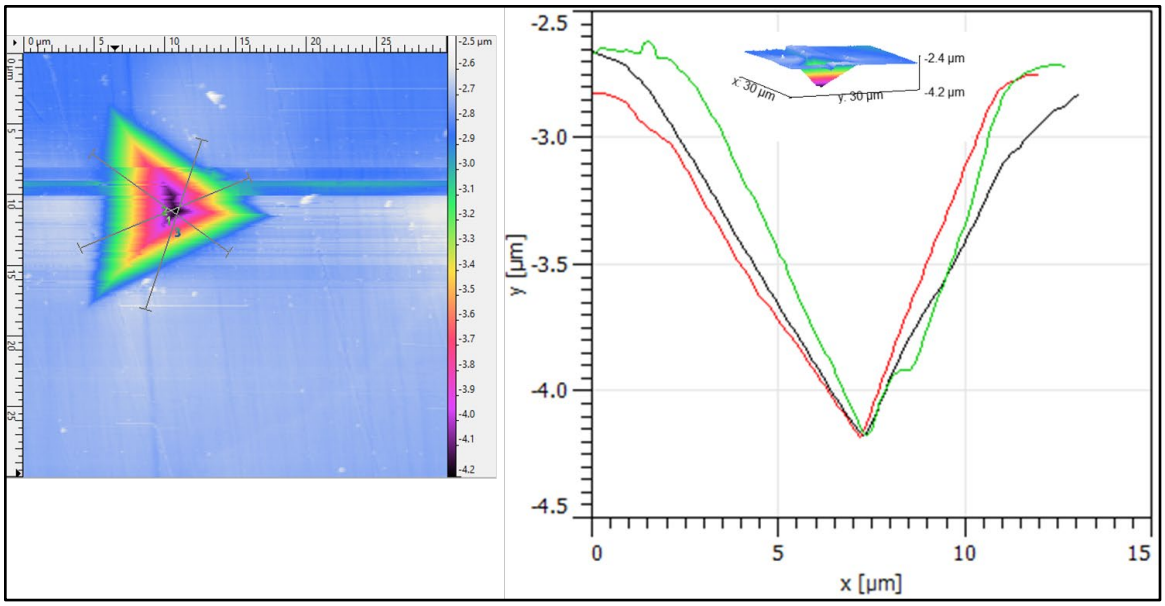

Figure 3.16. 2-D and 3-D images of nanoindentation along with depth measurement profiles of FZ

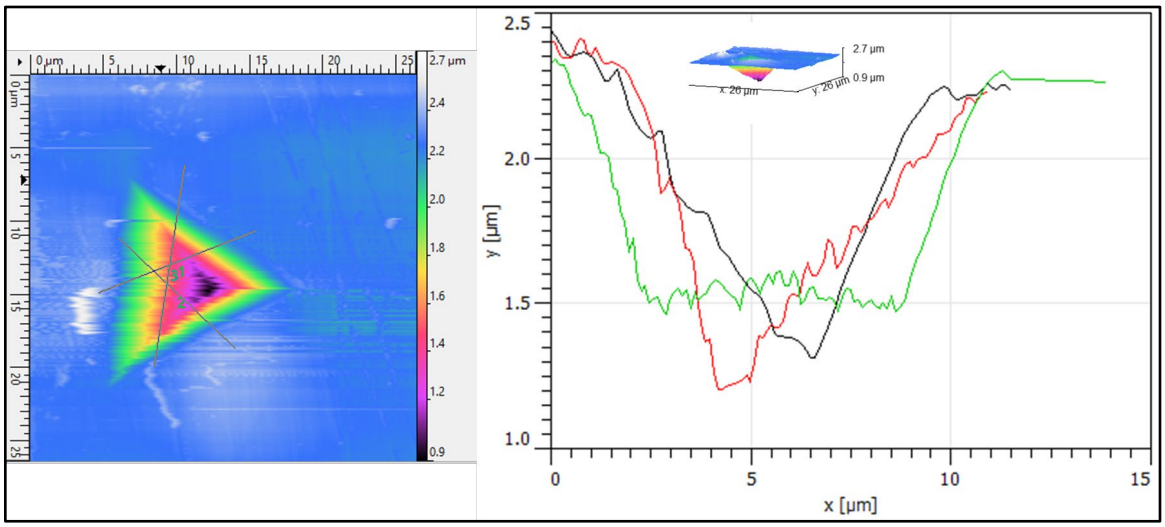

Figure 3.17. 2-D and 3-D images of nanoindentation along with depth measurement profiles of Ti6Al4V BA

3.4 CONCLUSIONS

The study investigated a laser-welded joint between AA7075 and Ti6Al4V with an Ag interlayer, focusing on the changes in microstructure and using nanoindentation and nanocreep analysis. The findings led to these conclusions:

- Incorporating Ag as an interlayer in the AA7075/Ti6Al4V joint inhibited the development of brittle intermetallic compounds (IMCs) like $AlTi_3$ and AlTi, enhancing the joint's quality by minimizing the interaction between Ti and Al.
- The microhardness results revealed that the FZ had greater values than the AA7075 HAZ and AA7075 BA due to the formation of Ag_2Al and Al_3Ti phases.
- Nanoindentation P-h curves revealed that the Fusion Zone (FZ) had lower displacement depth and greater nanohardness compared to the HAZ and AA7075 BA.
- Nanoindentation and nanocreep analysis indicated different deformation mechanisms in the base alloys and different zones of the joint. The FZ and AA7075 HAZ showed diffusional creep (lowest stress exponent), the AA7075 BA exhibited grain boundary sliding creep (stress exponent between 2-3), and the Ti6Al4V HAZ along with Ti6Al4V BA demonstrated dislocation climb creep mechanism (highest stress exponent).
- Comparing the joint with Ag interlayer and without Ag interlayer, it can be inferred that the interlayer enhanced the diffusion process in the FZ and HAZ of AA7075, resulting in increasing its creep resistance due to an altered microstructure with fewer IMCs.
- Atomic Force Microscopy (AFM) revealed higher average plastic deformation in the FZ compared to the AA7075 BA and Ti6Al4V BA, owing to fewer dislocations.

The present study examined the microstructure and nanomechanical properties of dissimilar joints with Ag interlayer. Future investigations are needed to understand how an Ag interlayer influences the corrosion resistance of the joint.

CHAPITRE 4
UNE ÉTUDE SUR LE SOUDAGE LASER DE JOINTS DISSEMBLABLES DE TI6AL4V ET AA7075 UTILISANT UN INTERCOUCHE EN CUIVRE : PROPRIÉTÉS MÉCANIQUES ET COMPORTEMENT À LA CORROSION

Titre en français du quatrième article :

Une étude sur le soudage laser de joints dissemblables de Ti6Al4V et AA7075 utilisant un intercouche en cuivre : Propriétés mécaniques et comportement à la corrosion.

Titre original (en anglais) :

A study on laser welding of dissimilar joints of Ti6Al4V and AA7075 using a Cu Interlayer: Mechanical properties and corrosion behaviour.

Auteurs et affiliation :

Asim Iltaf : Étudiant au doctorat, Département de mathématiques, d'informatique et de génie, Université du Québec à Rimouski, Québec, Canada.
Narges Ghafouri Varnosfaderani : Étudiant au doctorat, Department of Materials Engineering, Isfahan University of Technology, 84156-83111, Isfahan, Iran.
Noureddine Barka : Professeur, Département de mathématiques, d'informatique et de génie, Université du Québec à Rimouski, Québec, Canada.
Shayan Dehghan : Chercheur post-doctoral, Département de mathématiques, d'informatique et de génie, Université du Québec à Rimouski, Québec, Canada.

État de l'article :

Révisions majeures soumises.

Revue :

The Proceedings of the Institution of Mechanical Engineers, Part L: Journal of Materials: Design and Applications

Résumé en français du quatrième article

Cette étude explore l'utilisation d'un intercouche en cuivre dans le soudage laser dissemblable entre les alliages AA7075 et Ti6Al4V. L'objectif principal de l'intercouche en cuivre est de réduire la formation de composés intermétalliques fragiles, connus pour compromettre l'intégrité mécanique des joints soudés. Des évaluations détaillées ont été menées pour analyser la morphologie du joint, les propriétés mécaniques dans les différentes zones, la fractographie et le comportement à la corrosion des joints soudés. Le comportement à la corrosion a été évalué à l'aide de tests de polarisation potentiodynamique et de spectroscopie d'impédance électrochimique. Les résultats expérimentaux indiquent que l'introduction de l'intercouche en cuivre améliore de manière significative la fusion entre les alliages dissemblables, conduisant à des joints avec une résistance mécanique et une résistance à la corrosion accrues. En contrôlant efficacement la formation et la distribution des composés intermétalliques, l'intercouche renforce le joint et confère également une plus grande durabilité face à la dégradation environnementale. L'utilisation de l'intercouche en cuivre montre des perspectives prometteuses pour améliorer la fiabilité et les performances des structures soudées à partir de matériaux dissemblables.

A study on laser welding of dissimilar joints of Ti6Al4V and AA7075 using a Cu Interlayer: Mechanical properties and corrosion behaviour

Asim Iltaf [a, *], Narges Ghafouri Varnosfaderani [b], Noureddine Barka [a], Shayan Dehghan [a], Claude Belzile [c]

[a] Department of Mathematics, Computer Science and Engineering, University of Quebec at Rimouski, Rimouski, QC G5L 3A1, Quebec, Canada.

[b] Department of Materials Engineering, Isfahan University of Technology, 84156-83111, Isfahan, Iran.

[c] Institute of Marine Sciences of Rimouski, University of Quebec at Rimouski, Rimouski, QC G5L 3A1, Quebec, Canada.

[*]Corresponding author (Asim Iltaf): Department of Mathematics, Computer Science and Engineering, University of Quebec at Rimouski, Rimouski, QC G5L 3A1, Quebec, Canada.

E-mail address: asim.iltaf@uqar.ca

Abstract

This study explores the approach of using a copper (Cu) interlayer in dissimilar laser welding between AA7075 and Ti6Al4V alloys. The primary goal of the Cu interlayer is to mitigate the formation of brittle intermetallic compounds (IMCs), which are known to compromise the mechanical integrity of welded joints. Detailed evaluations were conducted to assess the morphology of the joint, mechanical properties across different zones, fractography, and the corrosion behavior of the welded joints. Corrosion behavior was assessed through potentiodynamic polarization and electrochemical impedance spectroscopy (EIS) tests. The experimental results indicate that the introduction of the Cu interlayer significantly improves fusion between

dissimilar alloys, leading to joints with enhanced mechanical strength and corrosion resistance.By effectively controlling the formation and distribution of IMCs, the interlayer strengthens the joint and also imparts greater durability against environmental degradation. The use of the Cu interlayer shows promising implications for improving the reliability and performance of welded structures made from dissimilar materials.

***Keywords*:** Laser welding, Dissimilar joint, mechanical properties, pitting, corrosion behaviour

4.1 INTRODUCTION

For vehicle weight reduction, the aerospace and automotive industries are increasingly employing lightweight structural materials, particularly titanium and aluminum alloys, for component fabrication. These materials enhance fuel efficiency along with contributing to environmental sustainability. Furthermore, there is a prominent trend towards integrating the advantageous properties of titanium and aluminum alloys within singular vehicle structures. However, the fusion of titanium alloys with other metals poses significant challenges in conventional welding due to the formation of a strong t-oxide layer on titanium surfaces and its minimal solubility in other metals. Consequently, mechanical fastening techniques such as riveting and bolting are predominantly utilized, as these methods prevent the complexities associated with metallurgical bonding. In response to these challenges, research and development efforts are being directed toward new dissimilar metal welding technologies, leveraging processes such as friction stir welding, explosive welding, laser welding, electron beam welding, and diffusion bonding, to enable the effective joining of these materials (Baqer et al., 2018; Esmaeili et al., 2019; Fan et al., 2017; Fang et al., 2019; H. Wang & Wang, 2019).

Joining Al/Ti alloys is challenging due to their differing physical properties and the formation of intermetallic compounds (IMCs) that cause cracking upon cooling and

solidification (Quazi et al., 2020; Z. Wang et al., 2020a; XUE et al., 2021). For successful aluminum-to-titanium bonding, it is essential to minimize the IMC layer at the interface and reduce IMC particles in the fusion zone. While IMCs in the Ti-Al combination offer high-temperature strength, their presence limits deformation possibilities and leads to increased strength but decreased ductility and fracture toughness (Malikov et al., 2020).

Laser welding is an effective method for joining Al/Ti alloys, offering precision in weld pool size and location due to the narrow focus of the laser beam. This technique allows variations in chemical composition and intermetallic layer thickness. Several studies have addressed laser welding challenges with significant advancements. Kreimeyer et al. (Kreimeyer et al., 2005) found that the thickness of intermetallic layers in welded Ti-6Al-4V and AA6016 T4 alloys slightly varied with heat input. Peyre et al. (Peyre et al., 2014)demonstrated that variation in laser welding-brazing, energy parameters had minimal impact on the strength of welded T40 titanium and AA5754 aluminum alloys, regardless of using Al_5Si filler wire. Failures in tensile tests consistently occurred at the aluminum alloy fusion zone's interfacial layer, containing $TiAl_3$. Jiang et al. (Jiang & Chen, 2019) identified that the interface of laser-welded dissimilar 5083 Al-Mg and Ti-6Al-4V alloys had multiple intermetallic phases, indicating that increased IMC concentration weakened the joint. Chen et al. (S. Chen, Li, Chen, Dai, et al., 2011b) modified the laser beam's power distribution to enhance the uniformity of the metal at the Ti-Al intermetallic layer, improving the mechanical properties of the dissimilar welds. Previous research on high-speed keyhole Yb: YAG laser welding of Ti-6Al-4V and AA5754 alloys revealed three interface types with varying intermetallic phases, including TiAl, Al_3Ti, and Ti_3Al, which are influenced by welding parameters(Tomashchuk et al., 2015c). Tomashchuk et al. (Tomashchuk et al., 2017b) examined how filler wire composition and edge shapes affect welded-brazed laser joint properties between T40 titanium and AA5754 aluminum alloys. The results showed that tensile strength is influenced by the reaction zone's development at the interface, with 2–25 μm wide interlayers of Ti_5Si_3, τ_2 ($Al_{21}Si_{46}Ti_{33}$), and $Ti(Al, Si)_3$

IMCs enhancing the strength. Kuryntsev et al. (Kuryntsev, 2019b) explored CP Ti and AA2024 overlapped laser welds, achieving tensile strengths of 80–120 MPa based on energy input.

The metallurgical reactions at the Ti/Al interface significantly affected the formation and growth rate of the Ti-Al IMC layer. It was suggested that Al_3Ti forms through crystallization during the cooling phase of the welding-brazing process (Z. Zhang et al., 2022). Introducing elements into the Ti/Al interface reaction could alter the formation of Ti-Al IMCs. In the case of Ti/Al joints using Al12Si filler metal, a $Ti_7Al_5Si_{12}$ layer was observed to initially develop at the Ti/Al boundary, which is controlled by the dissolution of Ti and the segregation of Si at the interface. This formation subsequently prevented the growth of the Al_3Ti layer due to the $Ti_7Al_5Si_{12}$ layer acting as a barrier to Ti dissolution, ultimately reducing the brittleness of the Ti/Al joints (S. Chen, Li, Chen, & Huang, 2011b; P. Li, Lei, Zhang, & Chen, 2020b).

Various studies suggest that using an interlayer is often seen as an efficient method to enhance the strength of dissimilar joints (J. Li et al., 2022; Meng et al., 2022). The interlayer should exhibit high solid solubility with the base metals (Teshome et al., 2023b). Thus, the ideal interfacial joint is achieved with fully diffusion, resulting in the interfacial compounds being solid solutions. Consequently, introducing an interlayer is anticipated to help prevent the creation of IMCs at the interface. Several interlayers such as silver (Ag) (Xiong et al., 2018), nickel (Ni) (Vijayan et al., 2022), copper (Cu) (H. Sun et al., 2023), and titanium (Ti) (X. Lv et al., 2022) have been widely utilized in the joining of dissimilar materials.

In this study, an innovative approach for manufacturing dissimilar welds of AA7075 and Ti6Al4V alloys is introduced, using a Cu interlayer. The study investigates the effects of the Cu interlayer on the joint morphology. It also evaluates the mechanical characteristics of different zones and phases in the Ti6Al4V/AA7075 joints. The tensile strength and fractography of these dissimilar joints are analyzed and compared to the base alloys. Furthermore, corrosion analysis is included to assess the

durability of the welded joints in harsh environments. These promising results offer valuable insights for designing and improving dissimilar metal composites.

4.2 METHODOLOGY

4.2.1 Laser beam welding (LBW) and sample description

Full penetration Bead-on-Plate (BoP) welding was conducted on AA7075 and Ti6Al4V sheets measuring 100 × 80 × 1.6 mm in their as-received condition, using fiber laser welding as shown in **Figure 4.1**. The chemical composition of the base alloys is detailed in **Table 4.1** and **Table 4.2**. **Figure 4.1** shows the schematic representations of the laser beam welding (LBW) process. **Table 4.3** indicates the optimized welding parameters used for the current study to achieve better joints. Leyens and Peters ('Titanium and Titanium Alloys', 2003) observed that for sheet thicknesses below 3 mm, neither joint preparation prior to welding nor the addition of filler materials is necessary.

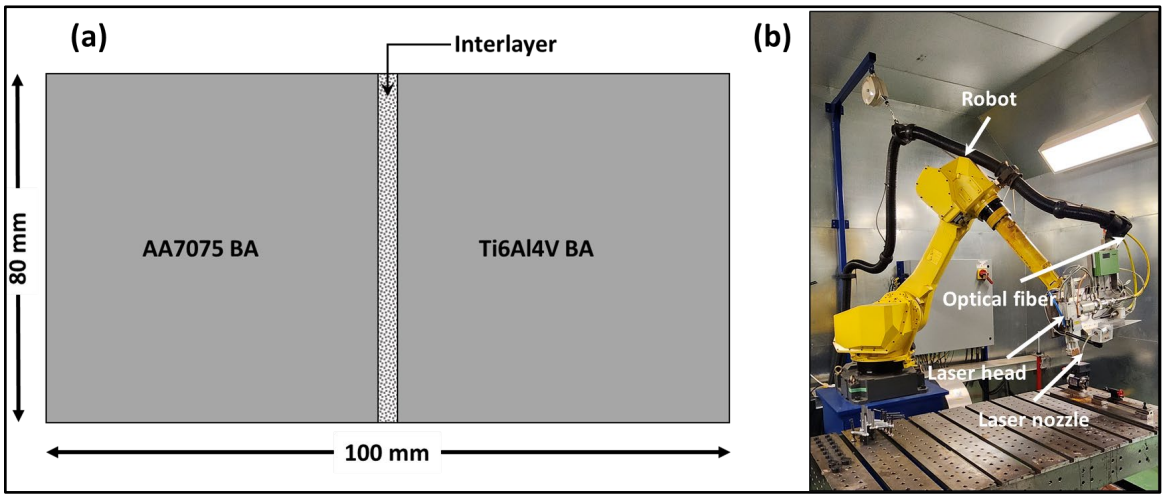

Figure 4.1 (a) Schematic of dissimilar welding configuration with an interlayer, (b) Laser welding setup (Model: YLS-3000-ST2)

The welding was conducted using a fiber laser from IPG Photonics, specifically the Ytterbium Laser Systems model YLS-3000-ST2. This laser is categorized as a class 4 device, having a maximum power capacity of 3 kW. It functions by generating continuous wave output at a wavelength of 1070 nanometers. The system integrates the laser source with a BIMO HIGHYAG laser head via high-performance optical fibers that are 100 µm and 600 µm in diameter. The laser head features a lens with a fixed 310 mm focal length, a focusing module marked M_{foc} = 1.50 and an adjustable zoom collimator. The process results in a circular focal point, with a diameter ranging from 0.3 to 1.53 mm depending on the focusing module, collimation module, and the fiber diameter.

Tableau 4.1 Electrochemical dispersive spectroscopy (EDS) chemical analysis of AA7075 BA (wt. %)

Al	Zn	Si	Mg	Fe	Cu	Mn	Cr
Bal.	4.33	0.71	0.63	0.34	0.25	0.21	0.07

Tableau 4.2 EDS chemical analysis of Ti6Al4V BA (wt. %)

Ti	Al	V	Fe	Sn	Nb	C	Zr	Si
Bal.	5.65	4.37	0.18	0.06	0.03	0.25	0.02	0.03

Tableau 4.3 Optimized laser welding parameters used for laser welding of AA7075/Ti6Al4V dissimilar joint with Cu interlayer

Laser power (kW)	3
Welding speed (mm/sec)	40
Working distance (mm)	150

Focal length (mm)	310
Focal spot diameter (mm)	1.50

4.2.2 Microstructural and fractography analysis

The metallographic and tensile samples were extracted from the welded plate through electric discharge machining (EDM), as depicted in **Figure 4.2**. To analyze the microstructure of the welded sections, metallographic specimens were initially ground with abrasive paper up to 4000 grits, then mechanically polished with 1μm diamond suspension paste. Moreover, these samples were etched with Kroll's solution (6% HNO3 and 2% HF by volume in distilled water). The microstructure was observed using an Olympus BH2-UMA optical microscope (OM) equipped with a sensitive tint filter. Fractography analyses were made using an SEC SNE-4500M scanning electron microscope (SEM) equipped with a Bruker Esprit EDS sensor.

4.2.3 Mechanical behavior characterization

The micro-hardness profiles across the weld area were evaluated using a CLEMEX CTM Vickers hardness tester, applying a force of 200 gf and a holding period of 10 seconds. For microhardness testing, samples shown in **Figure 4.2** prepared for microstructure analysis were used. Additionally, ASTM standard E8M-04 was followed for preparing tensile test specimens with a gauge length of 25 mm. The tensile tests were performed on a 100 kN MTS machine at a strain rate of 2.5 mm/min. Moreover, the impact testing was performed as per ASTM Standard E23-12c.

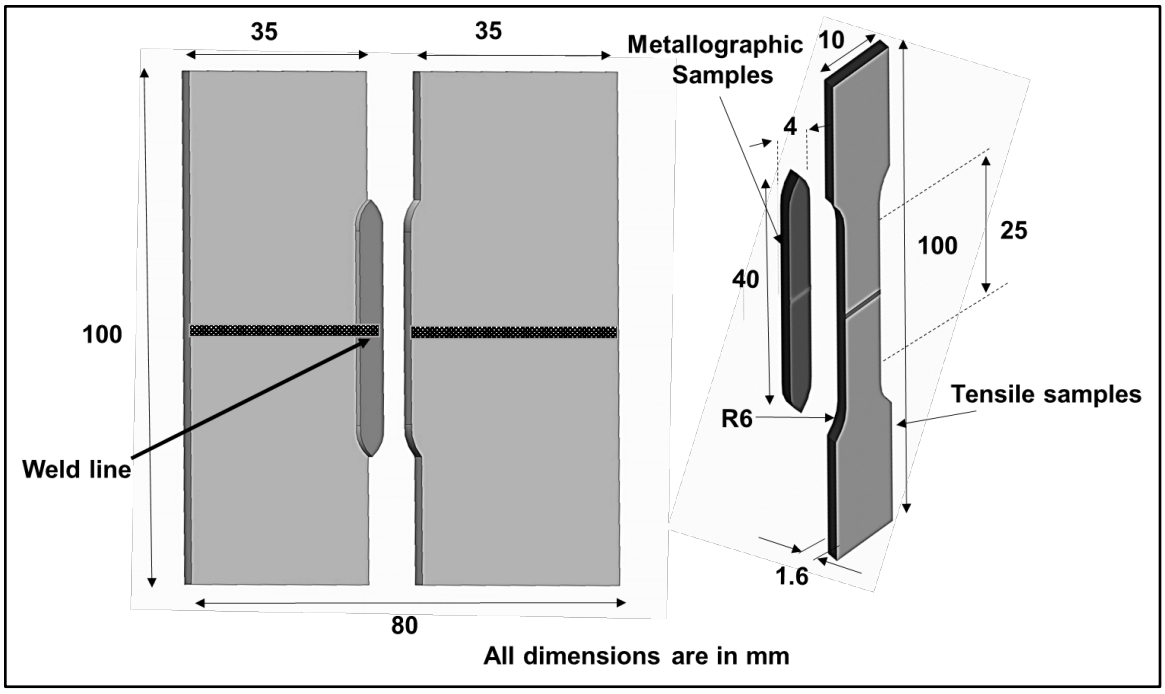

Figure 4.2 Schematic illustration of the metallographic and tensile specimens

4.2.4 Corrosion testing

In order to assess the corrosion performance of the samples, three specimens were prepared: Ti6Al4V BA, AA7075 BA, and the joining area of Ti6Al4V / AA7075 (including fusion zone and heat-affected zone regions). These were machined to a 0.5 cm^2 area, and their surfaces were abraded using SiC sandpaper and cleaned with deionized water and ethanol. Corrosion tests were conducted using a Potentiostat device (Gamry Reference-3000) in a three-electrode cell, with an Ag/AgCl electrode as the reference, a platinum electrode as the counter, and the prepared specimens as the working electrode, all in a 3.5% NaCl solution. To stabilize the specimens in the test solution, an open circuit potential (OCP) test was conducted for 1 hour. Potentiodynamic polarization and cyclic polarization tests were then performed within a potential range of -1 to 1.5 V vs OCP at a scan rate of 1 mV/s. Analysis of the potentiodynamic polarization and cyclic polarization curves was performed using the Gamry Echem Analyst™ software. The potentials were standardized based on

reversible hydrogen potential (RHE) using Equation 1. Finally, electrochemical impedance spectroscopy (EIS) tests were conducted at a voltage amplitude of 10 mV and a frequency range of 10 mHz to 100 kHz to assess the specimens' resistance to corrosion. The Z_{view} software was used to fit the EIS data and find the equivalent circuit model.

$$E_{RHE} = E_{Ag/AgCl} + 0.059\,pH + E^{\circ}_{Ag/AgCl} \left(E^{\circ}_{Ag/AgCl} = 0.1967V \quad at \quad 25^{\circ}C\right) \tag{1}$$

4.3 RESULTS AND DISCUSSION

4.3.1 Microstructural characterization

In this research, sheets of Ti-6Al-4V and AA7075 aluminum alloy, each 1.6 mm in thickness, were joined using a welding method that included a 0.4 mm Cu interlayer. The microstructure of the AA7075 alloy is mainly characterized by spherical aluminum cubic (fcc) phase structures with some small pits, which are likely due to the removal of $MgZn_2$ precipitates during the etching process, as depicted in **Figure 4.3(a)**. On the other hand, the Ti-6Al-4V alloy is composed predominantly of rounded hexagonal close-packed (hcp) α-phase grains, accompanied by a minor presence of intergranular cubic body-centered cubic (bcc) β-phase, as shown in **Figure 4.3(b)**. **Figure 4.4** depicts the cross-sectional microstructure of a dissimilar butt joint between AA7075 and Ti6Al4V, manufactured using laser welding with a Cu interlayer. The joint shows the Ti6Al4V/Cu interface, with minimal melting of the titanium alloy and a flat joint interface. The limited melting of titanium is key as it prevents extensive mixing with aluminum, significantly reducing the risk of brittle Ti/Al intermetallic formations and thus preserving the base materials' properties, which ensures a stronger, more ductile weld joint. The investigation primarily focused on the interfaces between AA7075/Cu and Ti6Al4V/Cu, where the joint formation is attributed to eutectic liquid formation and constrained Cu diffusion into Ti6Al4V, respectively. Cu diffusion into AA7075 leads to a pronounced diffusion zone with some sporadic minor cracks visible in the

AA7075 fusion zone as shown in **Figure 4.5**. In LBW, rapid cooling rates cause considerable local undercooling (Sonar et al., 2021), resulting in rapid nucleation and the growth of fine grains and dendrites as depicted in **Figure 4.5**. The FZ predominantly consists of AA7075, Ti6Al4V, and Cu with the formation of a Vanadium-solid solution enhancing joint robustness. Vanadium aids in strengthening by creating lattice distortions that hinder dislocation movement and potentially forming secondary phases that further impede dislocations, enhancing material strength(Vafaeenezhad & Shahverdi, 2024). **Figure 4.4** and **Figure 4.5** also highlight porosity which is typical in LBW of 7xxx series Al alloys. The porosity arises from entrapped gases like hydrogen, which is highly soluble in molten aluminum and primarily originates from oxides or impurities in the filler or base materials, dissolving into the material (Khalil et al., 2019). Porosity exists in various forms such as necking, swelling, and collapsing (**Figure 4.4** and **Figure 4.5**), often due to inconsistent vaporization of volatile elements like Zn and Mg, which exhibit different vapor pressures (Khalil et al., 2019).

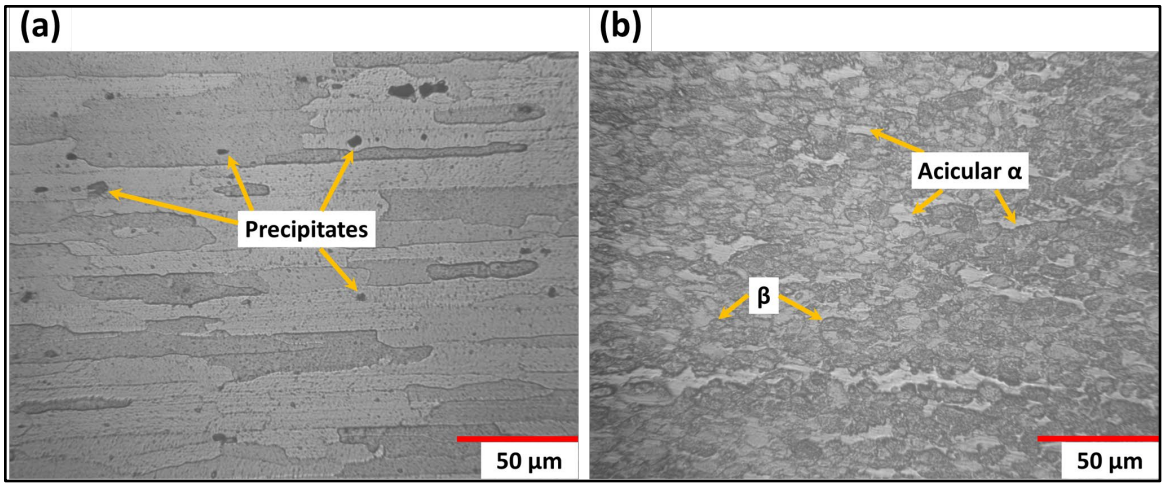

Figure 4.3 (a) AA7075 base alloy, **(b)** Ti6Al4V base alloy

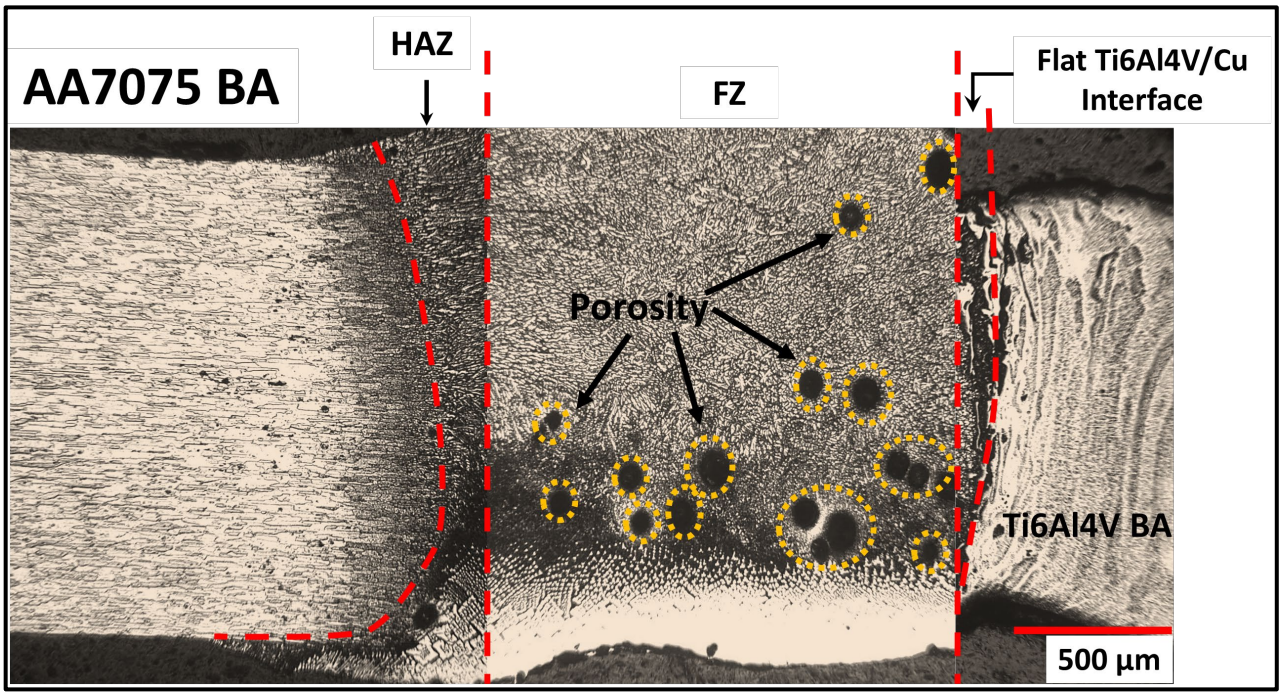

Figure 4.4 Microstructural evolution in dissimilar AA7075/Ti6Al4V joint depicting zones/interfaces depicting fusion zone (FZ), heat affected zone (HAZ), and base alloys (BAs) (Iltaf, Dehghan, et al., 2024)

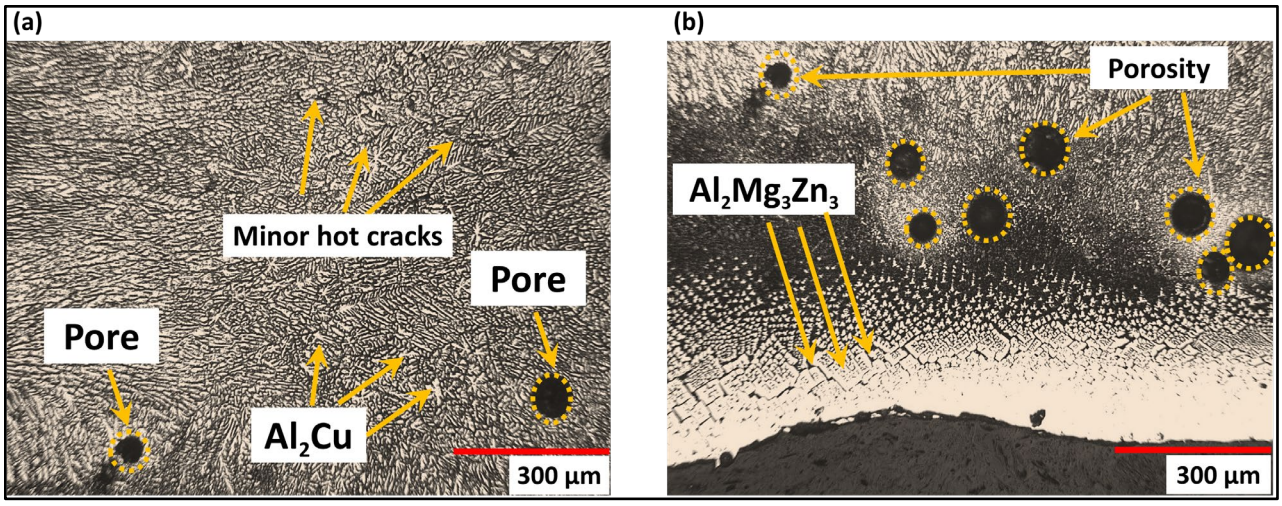

Figure 4.5 (a) Middle of FZ of the joint, and (b) Bottom image of FZ of the joint

4.3.2 Mechanical properties

4.3.2.1 Tensile tests

Figure 4.6 shows the stress-strain results for three different materials: AA7075 BA, Ti6Al4V BA, and a joint composed of AA7075/Ti6Al4V with a Cu interlayer. The AA7075 BA material, shows a significant increase in stress with strain up to a point of peak stress, after which it rapidly fails, indicating a brittle failure after the elastic limit. The Ti6Al4V BA, shows a more gradual increase in stress with increasing strain, indicating a more ductile material with a higher strain at failure compared to the AA7075 BA. The joint material (AA7075/Ti6Al4V with Cu interlayer) exhibits a significant stress-strain response. Initially, it follows a similar pattern to the Ti6Al4V BA, suggesting that the joint's behavior is largely influenced by the Ti alloy. However, the stress peaks at a lower value than either of the base materials before it drops, indicating the joint's maximum stress capacity is lower than that of the individual alloys, and it may be the weakest link in terms of mechanical strength. This graph is useful for comparing the mechanical properties of the materials and understanding how they would behave under tensile loads.

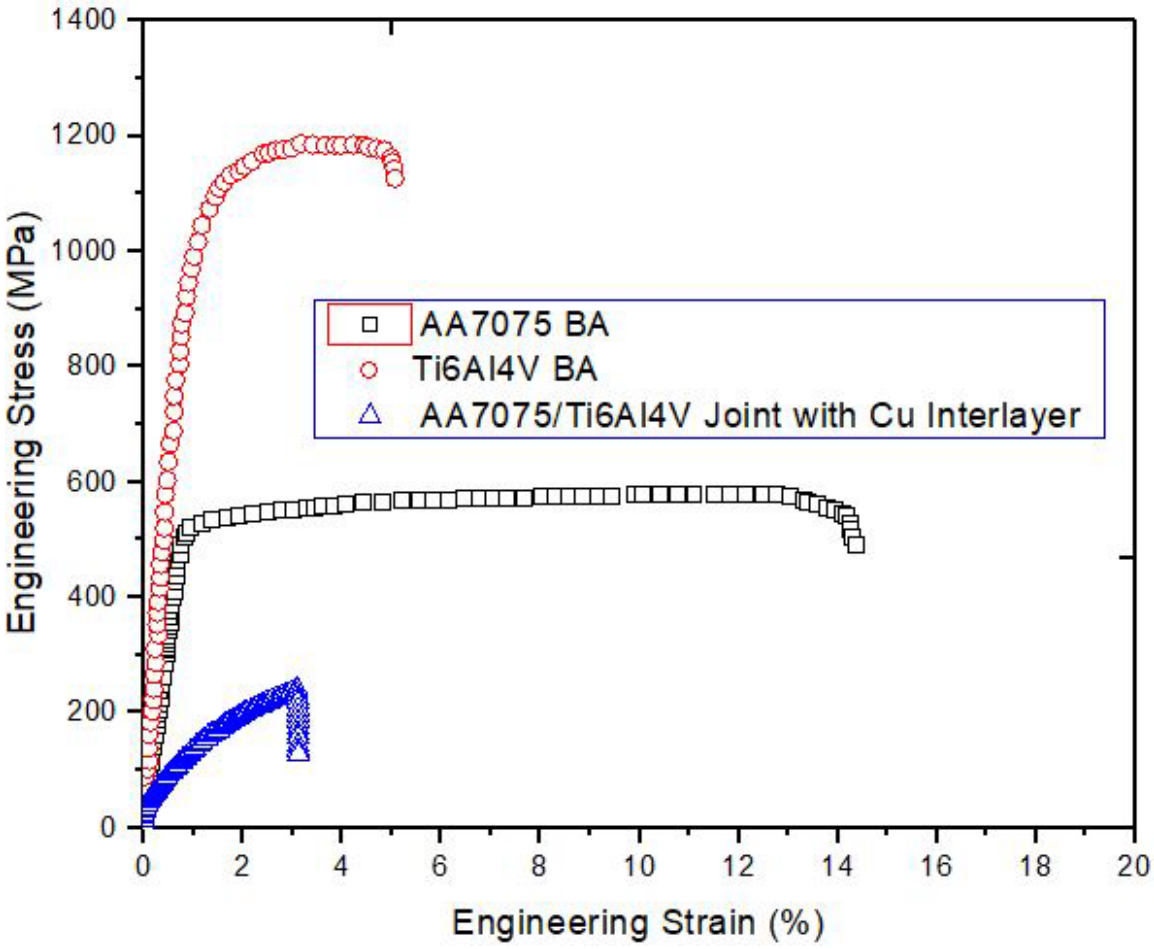

Figure 4.6 Engineering stress-strain result of the AA7075 BA, Ti6Al4V BA, and their joint with Cu interlayer (Iltaf, Dehghan, et al., 2024)\

4.3.2.2 Microhardness tests

Figure 4.7 presents the microhardness values, for different zones in a dissimilar joint between AA7075 and Ti6Al4V with a Cu interlayer. Microhardness is a measure of a material's resistance to local deformation, typically indentation. From left to right, the graph displays the microhardness values for the base material of AA7075 BA, the HAZ of AA7075, the fusion zone (FZ, where the actual joining occurs), the HAZ of

Ti6Al4V, and the Ti6Al4V BA. The AA7075 alloy has a relatively low hardness compared to the other zones, with the HAZ of AA7075 showing a slight increase in hardness. The FZ exhibits the highest microhardness value, which could be due to the presence of the Cu interlayer and the formation of new phases during the welding process. Following the fusion zone, the HAZ of Ti6Al4V has a microhardness value that is lower than the FZ but higher than the base materials. Finally, the Ti6Al4V base material shows a substantial hardness, though not as high as the fusion zone, which indicates it's inherently a harder material compared to AA7075 but may not resist deformation as well as the weld zone with the Cu interlayer. This graph is essential for evaluating the consistency and quality of the joint between the dissimilar AA7705/Ti6Al4V materials.

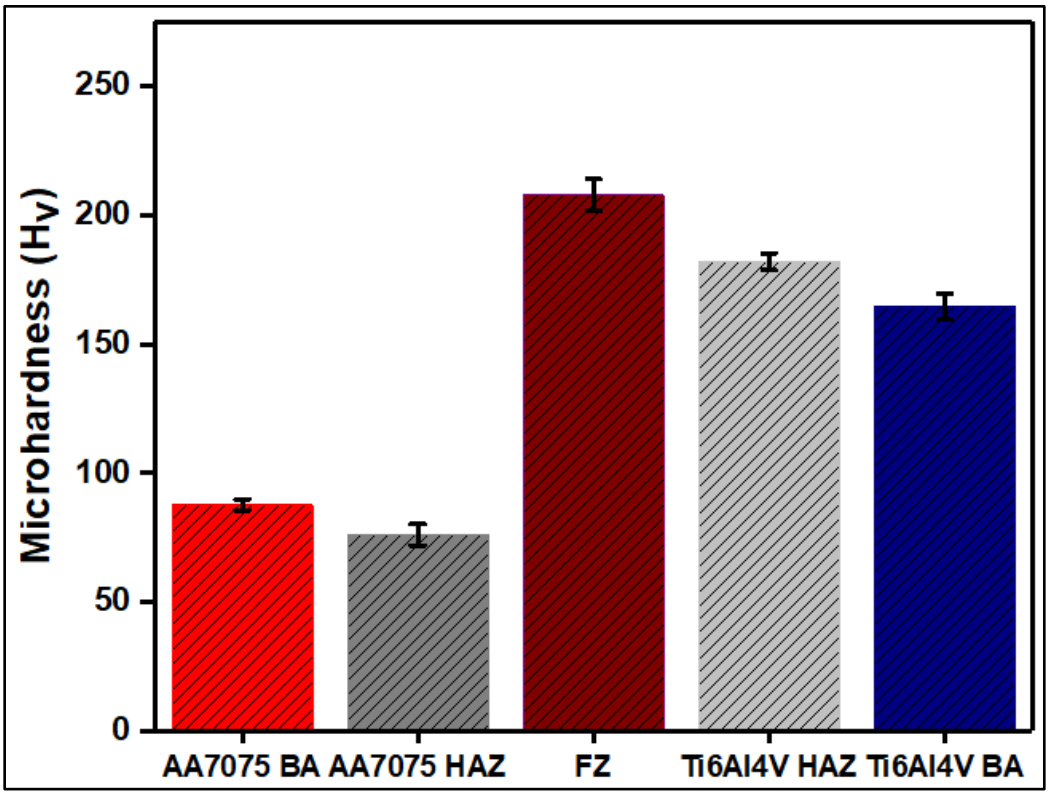

Figure 4.7 Microhardness values of all the zones in AA7075/Ti6Al4V dissimilar joint with Cu interlayer. Error bars indicate standard deviation on three measurements

4.3.2.3 Impact testing

Table 4.4 presents the impact testing results for AA7075 BA, the FZ, and Ti6Al4V alloy, focusing on the energy absorbed during testing, which is indicative of the material's toughness. For the AA7075 BA, the energy absorbed was recorded at 28.3 Joules with a standard deviation of ±2.5, suggesting relatively high toughness compared to the other samples. The joint with FZ, which includes the Cu interlayer, showed a lower energy absorption of 12.7 J with a standard deviation of ±1.4, indicating a reduction in toughness in this area. The Ti6Al4V sample absorbed an energy of 15.2 Joules with a standard deviation of ±1.7, highlighting its lower toughness relative to the AA7075 BA. The impact testing results are consistent with the results shown in section 3.2.1.

Tableau 4.4 Impact testing results for AA7075 BA, Ti6Al4V BA and AA7075/Ti6Al4V dissimilar joint with Cu interlayer

Alloy/Zone	Energy absorbed (J)
AA7075 BA	28.3±2.5
Joint	12.7±1.4
Ti6Al4V BA	15.2±1.7

4.3.2.4 Fractography analysis

Figure 4.8 shows the physical appearance of fractured samples after tensile testing. **Figure 4.9** is an overview of the fracture surface. The yellow dashed box indicates a specific area of interest that will be examined in greater detail in subsequent images. This kind of overview is critical for understanding the general fracture pattern, which can provide initial features about the fracture mechanism (e.g., fatigue, overload, stress corrosion cracking). In the next image, finer details of the fracture surface can be seen. The features observed can be interpreted as dimples or pits, which are indicative of a ductile fracture mechanism. Ductile fractures occur when a material undergoes plastic deformation before failure, leading to the formation of these characteristic dimples as voids in the material nucleate, grow, and coalesce. Consistent dimple patterns across the surface support the conclusion of a ductile fracture mechanism, whereas variations might suggest different mechanisms or material inconsistencies. In all these images, the appearance of dimples suggests that the material has undergone considerable plastic deformation, which is a characteristic of ductile failure. Brittle fractures, in contrast, would show flat facets and ridges corresponding to specific crystallographic planes. The presence of pits, as mentioned in section 3.1, can be associated with the presence of inclusions or precipitates in the material that were

pulled out or detached from the matrix during the fracture. This can be particularly common in alloys where secondary phase particles are present.

Figure 4.8 Physical appearance of fractured tensile specimens (a) AA7075/Ti6Al4V joint, (b) AA7075 BA and (c) Ti6Al4V BA

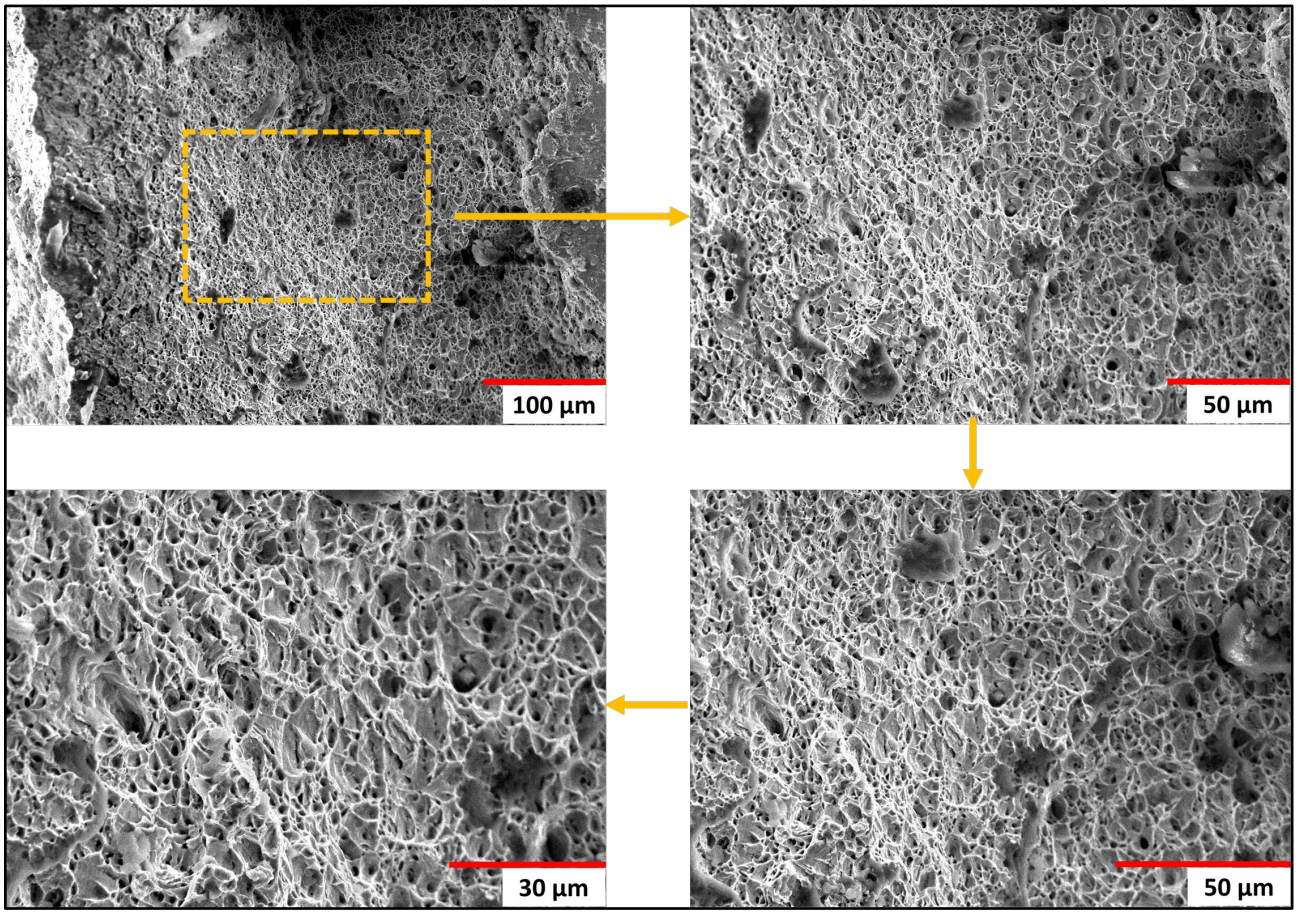

Figure 4.9. SEM fractography images of AA7075 BA tensile test fractured specimen

Figure 4.10 shows a broad overview of the fracture surface of AA7075/Ti6Al4V joint. In this case, the rough and jagged texture with a tangled appearance suggests a highly deformed area, which is characteristic of a partially ductile fracture. This indicates that the material experienced significant plastic deformation before failure. Further magnification provides an even closer look at the fracture surface. The appearance of dimpled rupture, with many small, rounded features (dimples), is a hallmark of ductile fracture. Furthermore, the last image shows similar rough and irregular features, indicating the ductile nature of the fracture. The consistency of this ductile texture across different areas of the surface reinforces the conclusion that the material has undergone significant plastic deformation.

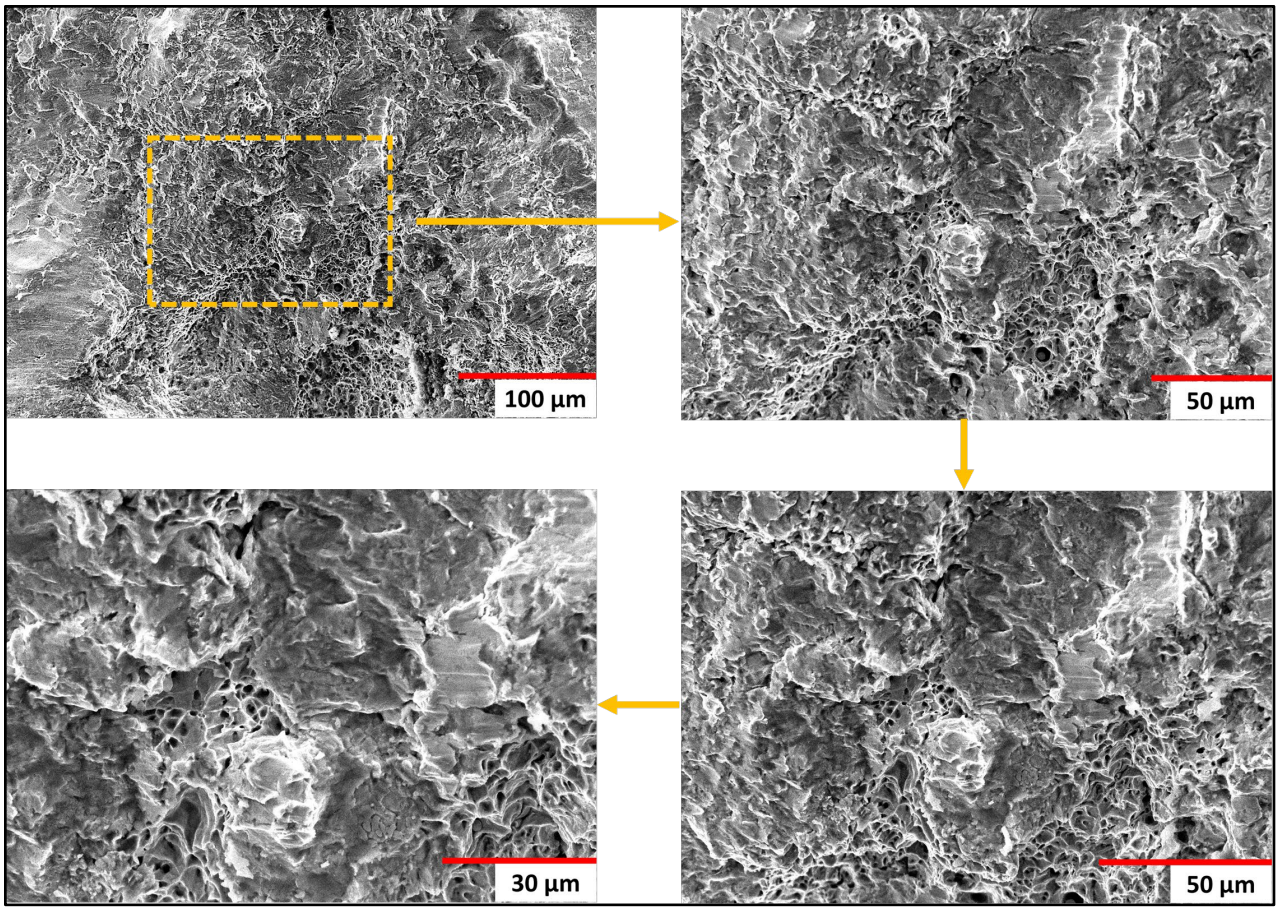

Figure 4.10 SEM fractography images of AA7075/Ti6Al4V joint tensile test fractured specimen

Figure 4.11 shows a broad overview of the fracture surface of the Ti6Al4V BA. The surface is rough and irregular, which is consistent with a ductile fracture. The presence of many small voids and dimples indicates that the joint underwent significant plastic deformation before failure. The dimples are formed by the growth and coalescence of microvoids within the material as it was deformed plastically under tensile stresses. The shape and size of the dimples and the consistency of the ductile fracture features across different regions suggest that the material failed under similar stress conditions throughout the fracture surface. The rough and torn appearance supports the conclusion that the fracture occurred through ductile mechanisms.

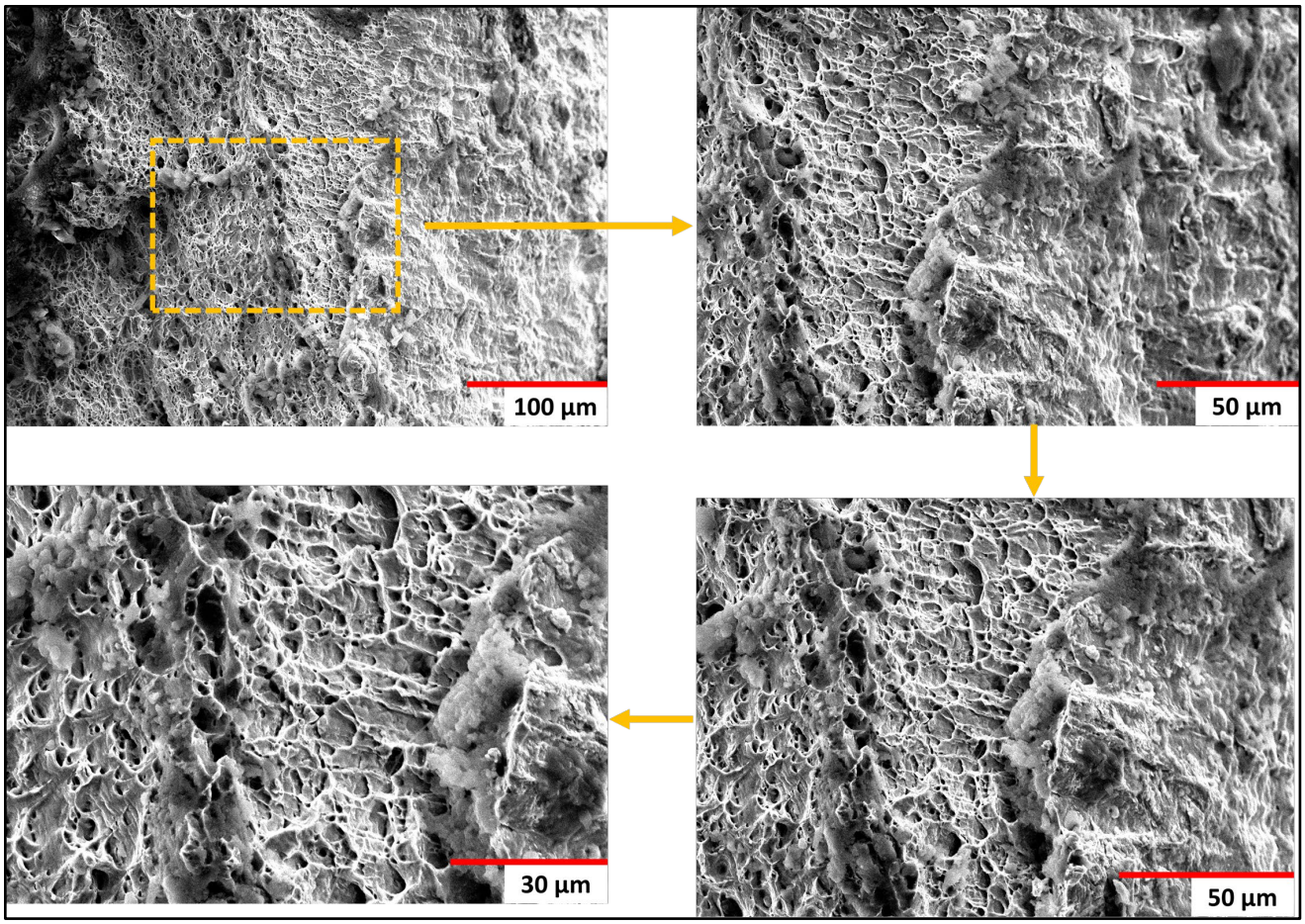

Figure 4.11 SEM fractography images of Ti6Al4V BA tensile test fractured specimen

4.3.3 Evaluation of corrosion behavior

4.3.3.1 Potentiodynamic polarization test (Tafel test)

The potentiodynamic polarization test was employed to estimate corrosion potential (E_{Corr}) and corrosion current density (i_{Corr}). **Figure 4.12** illustrates the potentiodynamic polarization curves of samples AA7075 BA, Ti6Al4V BA, and the joining area of Ti6Al4V/AA7075 in a 3.5% NaCl solution. Using the Tafel

extrapolation method, the E_{Corr} and i_{Corr} of the specimens were determined. Additionally, polarization resistance (R_p) is calculated using equation 2, where β_a, β_c, and i_{Corr} show the anodic Tafel slope, the cathodic Tafel slope, and the corrosion current density, respectively (Ehsan et al., 2024; Rzaij et al., 2022; Z. Song & Tegus, 2023; S. Zhao et al., 2024). The results obtained from the potentiodynamic polarization test are presented in **Table 4.5**.

$$R_P = \frac{\beta_a \beta_c}{2.303(\beta_a + \beta_c) i_{corr}} \quad (2)$$

The E_{Corr} signifies the thermodynamic tendency for corrosion reactions, while the i_{Corr} reflects the kinetics of corrosion reactions and the corrosion rate. A more positive E_{Corr} and lower i_{Corr} correspond to greater resistance against corrosion (T. Li et al., 2024). Sample Ti6Al4V BA demonstrates superior corrosion resistance with the most positive E_{Corr} (0.2663 V vs RHE), the least i_{Corr} (6.7903×10^{-7} A.cm^{-2}), and a relatively stable passive region when compared to other samples, as indicated by Figure 12. Conversely, the Sample AA7075 BA, exhibits a more negative E_{Corr} and a higher i_{Corr}, implying it is more susceptible to corrosion. The Ti6Al4V/AA7075 joint sample exhibits an E_{Corr} of -0.0555 V vs RHE and an i_{Corr} of 1.0297×10^{-5} A.cm$^{-2,}$ indicating intermediate corrosion resistance between the two base materials. The corrosion rate and polarization resistance (R_p) values have an inverse relationship. This confirms the findings that the sample of Ti6Al4V BA with the lowest i_{Corr} has the highest R_p value, while the sample of AA7075 BA with the highest i_{Corr} has the lowest R_p. The joining area exhibits intermediate values for both i_{Corr} and R_p, indicating its position between the two base materials in terms of corrosion resistance.

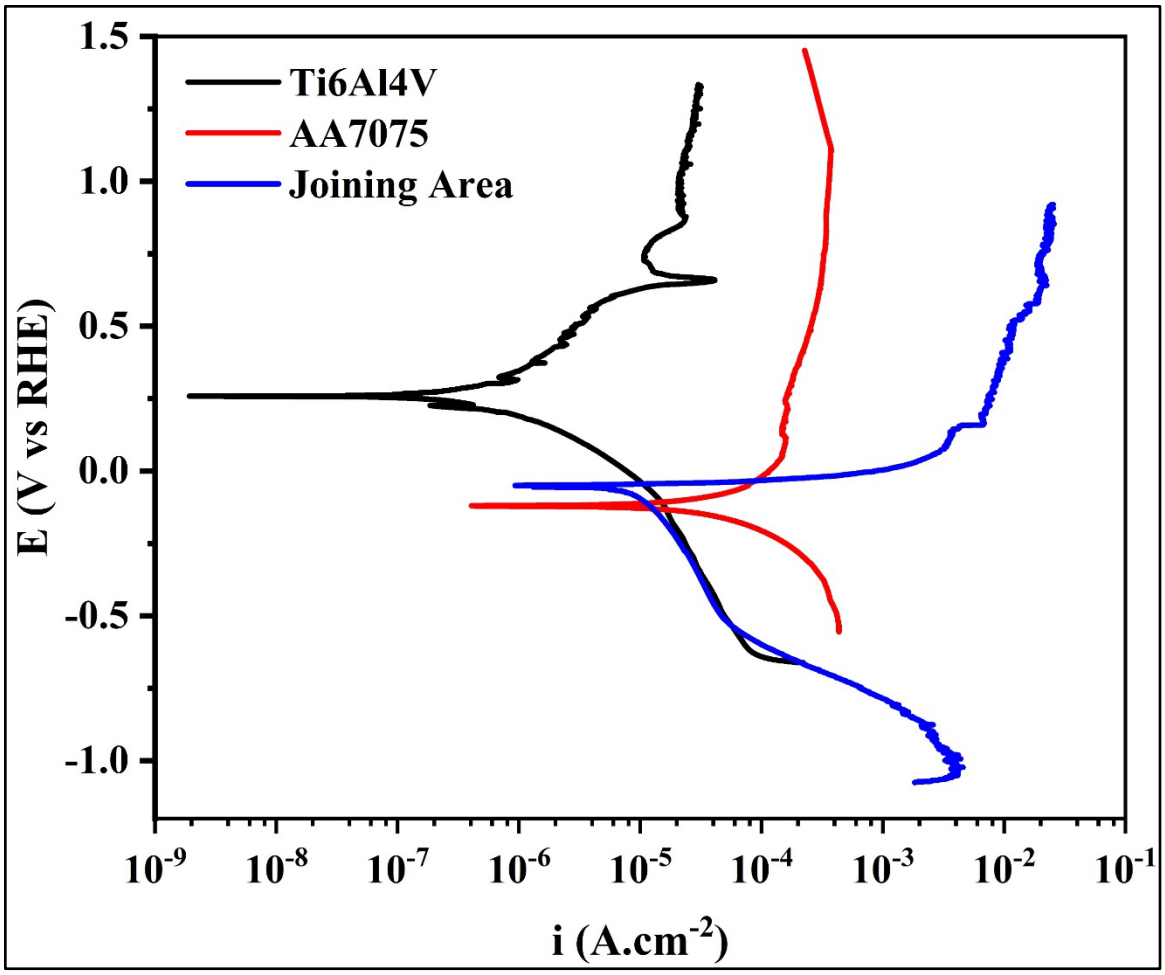

Figure 4.12. Potentiodynamic polarization plots of Ti6Al4V, AA7075, and Joining area in 3.5 wt.% NaCl solution at a pH of 7

Tableau 4.5 Electrochemical parameters extracted from the potentiodynamic polarization plots in **Figure 4.12**.

Sample	E_{corr}	i_{corr}	β_a	$-\beta_c$	R_p
	V	$A.cm^{-2}$	V/dec	V/dec	$K\ \Omega.cm^2$
Ti6Al4V	0.2663	6.7903×10^{-7}	0.37879	0.25204	96.777
AA7075	-0.1181	5.7763×10^{-5}	0.40918	0.32365	1.358

Joining Area	-0.0555	1.0297×10^{-5}	0.08284	0.60286	3.071

4.3.3.2 Electrochemical impedance spectroscopy (EIS) test

To evaluate corrosion behavior more accurately, the specimen underwent electrochemical impedance spectroscopy (EIS) after 24 hours of immersion in a 3.5% NaCl aerated solution. **Figure 4.13** displays Nyquist and Bode plots for Ti6Al4V BA, AA7075 BA, and the joining area. A larger semi-circle diameter in the Nyquist plot (**Figure 4.13a**) indicates higher corrosion resistance. In the Bode plot (**Figure 4.13b**), corrosion resistance can also be determined by the impedance value at 0.01 Hz ($|Z|_{0.01Hz}$) (J. Wang et al., 2023). The $|Z|_{0.01Hz}$ values for Ti6Al4V BA, AA7075 BA, and the joining area are 37169, 8435.5, and 309.6 $\Omega.cm^2$, respectively. This means that the corrosion resistance follows this order: Ti6Al4V BA > AA7075 BA > Joining area.
Based on the Bode phase diagrams (**Figure 4.13c**), all three samples, Ti6Al4V BA, AA7075 BA, and the Joining area, exhibit two-time constants and thus two capacitive loops in their equivalent circuits as shown in **Figure 4.14**. In the Nyquist plot, two semi-circles are also observed, where the first semi-circle at high frequencies corresponds to the oxide film and the second semi-circle at low frequencies corresponds to electric double-layer capacitances. The parameters of various circuit elements for the samples of Ti6Al4V, AA7075, and Joining area are listed in **Table 4.6**. In all samples, R_s, R_{film}, CPE_{film}, R_{ct}, and CPE_{dl} are the solution resistance, the oxide film resistance, the oxide film constant-phase element, the double-layer charge transfer resistance, and the double-layer constant-phase element, respectively. The constant-phase element (CPE) is used as a non-ideal capacitance. In the Joining area sample, an inductive loop was observed at low frequencies, in which L and R_L were the inductor and the inductor resistance, respectively. In this case, the discharge reactions are mainly controlled by the electrochemical polarization. R_s represents the solution resistance, and since the solution is uniform across all tests, its value remains

approximately constant in all samples. The R_{film} value is higher in the Ti6Al4V BA sample compared to the other two samples, indicating the formation of a passive and corrosion-resistant oxide layer. The oxide layer in the AA7075 BA sample, with a lower R_{film} compared to the Ti6Al4V BA sample, exhibits less resistance to corrosion due to the formation of an unstable oxide layer. Considering that the R_{ct} value in the Ti6Al4V BA sample is higher than in the other samples, the charge transfer from the alloy to the corrosive solution occurs less frequently. In the Joining area sample, the lower R_{film} and R_{ct} values compared to the base metal samples could be attributed to the formation of intermetallic compounds and the creation of galvanic couples resulting from the connection of dissimilar metals. This has been exacerbated by the presence of Cu as an interlayer. The additional inductive resistance (R_L) in the Joining area sample suggests localized micro-galvanic interactions within the joint area (W. Wang et al., 2024) There are distinct differences in the corrosion characteristics of the joint compared to the parent metals., likely due to microstructural changes and the presence of the Cu interlayer, affecting the overall corrosion resistance and electrochemical behavior.

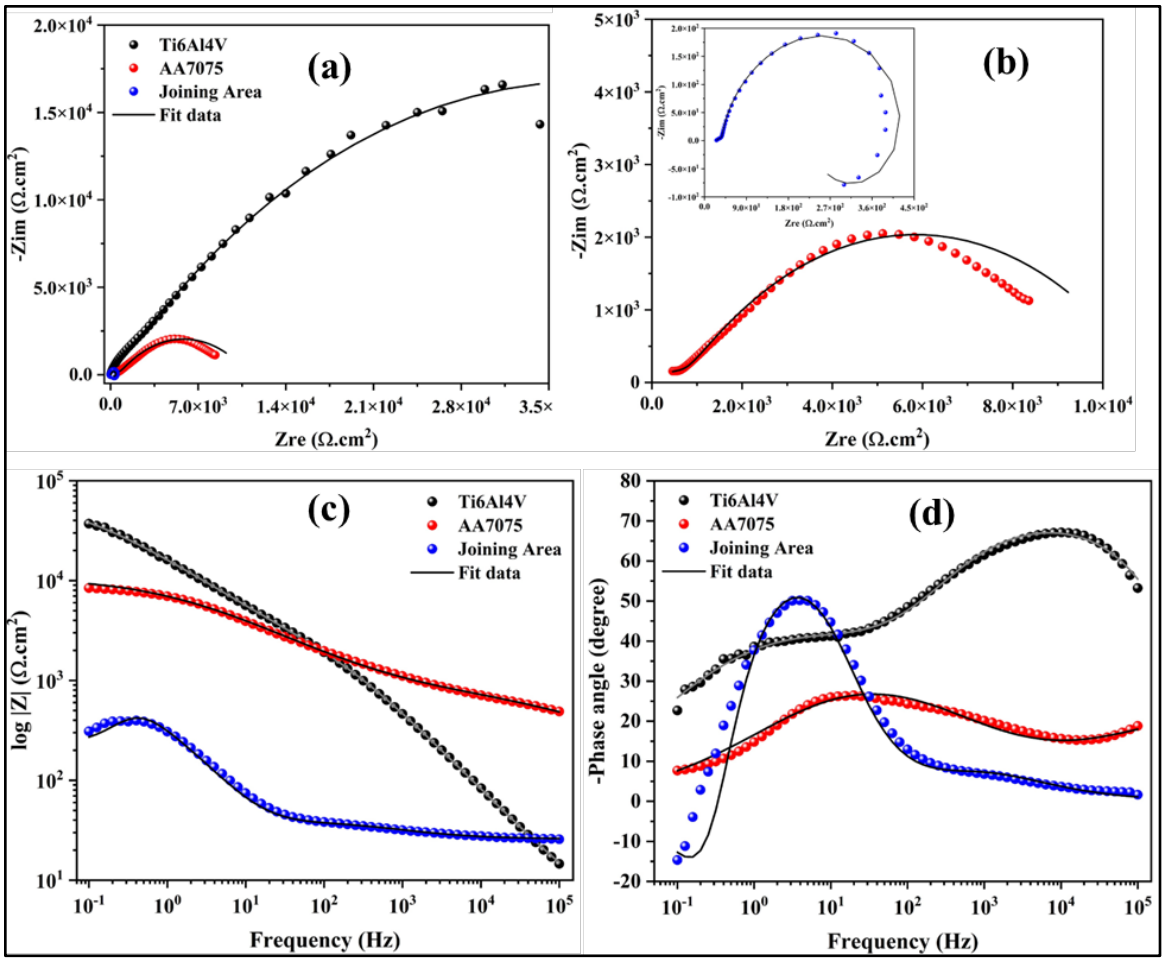

Figure 4.13. (a, b) Nyquist, (c) Bode Z, and (d) Bode-phase plots for Ti6Al4V, AA7075, and Joining area samples in 3.5 wt.% NaCl solution at a pH of 7

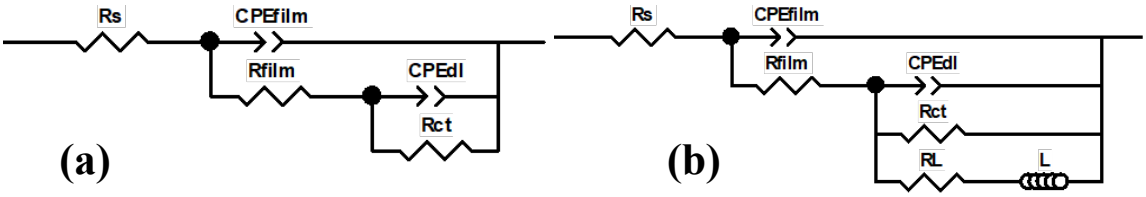

Figure 4.14 Electrical equivalent circuits are used to fit the electrochemical impedance data of samples. (a) Ti6Al4V and AA7075 BA (Lu et al., 2023; H. Zhang et al., 2022), (b) Joining area (Lin & Lin, 2021; Y. Xu et al., 2021)

Tableau 4.6 Electrical parameters extracted from the fitting plot of the EIS tests for Ti6Al4V, AA7075, and Joining area samples

Sample	R_s ($\Omega.cm^2$)	CPE_{film} ($F.cm^{-2}\ s^{n-1}$)	n_{film}	R_{film} ($\Omega.cm^2$)	CPE_{dl} ($F.cm^{-2}\ s^{n-1}$)	n_{dl}	R_{ct} ($\Omega.cm^2$)	R_L ($\Omega.cm^2$)	L ($\Omega.s.cm^2$)
Ti6Al4V	24.29	6.2×10^{-8}	0.79	2365	9.38×10^{-10}	0.52	73844	-	-
AA7075	27.4	8.04×10^{-13}	0.45	721.4	3.19×10^{-10}	0.48	10200	-	-
Joining Area	25.8	3.3×10^{-6}	0.62	15.5	1.85×10^{-4}	0.95	575	330	360

4.3.3.3 Cyclic polarization test

Cyclic polarization is a widely utilized method for assessing the pitting corrosion resistance of welded joints (Iltaf, Karim, et al., 2021). Pitting corrosion is characterized by severe localized damage in the form of deep pits, making it more destructive than general corrosion, and is particularly concerning for structures in marine environments (Kuphasuk et al., 2001). **Figure 4.15** shows the cyclic polarization plots for Ti6Al4V, AA7075, and Joining area samples in 3.5 wt.% NaCl solution at a pH of 7. These plots

are instrumental in understanding the corrosion behavior of these materials. The graph for Ti6Al4V indicates that the material has a passive behavior over a wide range of potentials, as seen by the broad, flat region in the anodic branch. This flat region signifies stable passivity and resistance to localized corrosion. However, there is a breakdown potential (E_b) after which the current increases sharply, indicating the initiation of pitting corrosion. The reverse scan from the transpassive region shows a hysteresis loop, which is typical for materials that undergo repassivation of pits. For AA7075, the curve is characterized by a more pronounced active-passive transition. The absence of a pronounced passive region suggests this alloy is more prone to continuous corrosion in the test environment. The pitting potential (E_{pit}) is marked, beyond which the current increases rapidly due to the onset of pitting. The return path of the loop indicates that the pits might repassivate as the potential decreases, suggesting some self-healing properties of the oxide film. The Joining Area, representing the interface between Ti6Al4V and AA7075 using a Cu interlayer, exhibits a different corrosion mechanism. The plot shows a shift towards more negative potentials for both the pitting potential (Epit) and the repassivation potential (Eprot), indicating a lower resistance to the initiation and growth of corrosion pits compared to the base metals. This could be due to microgalvanic corrosion processes occurring between the dissimilar metals and the Cu interlayer, or due to the presence of intermetallic compounds that are more reactive in the corrosive environment. The presence of a broad hysteresis loop on the reverse scan suggests that once corrosion initiates, it is more difficult for the material in the Joining Area to repassivate, leading to more severe localized corrosion. The cyclic polarization plots demonstrate the varying resistance to corrosion of the two base materials and their joining area. Ti6Al4V shows superior corrosion resistance with a broad passivity range, while AA7075 is more susceptible to corrosion, as seen by the absence of a wide passive region and a more negative pitting potential. The joining area shows the most negative pitting potential and a wide hysteresis loop, highlighting the challenges in maintaining corrosion resistance in welded joints of dissimilar alloys.

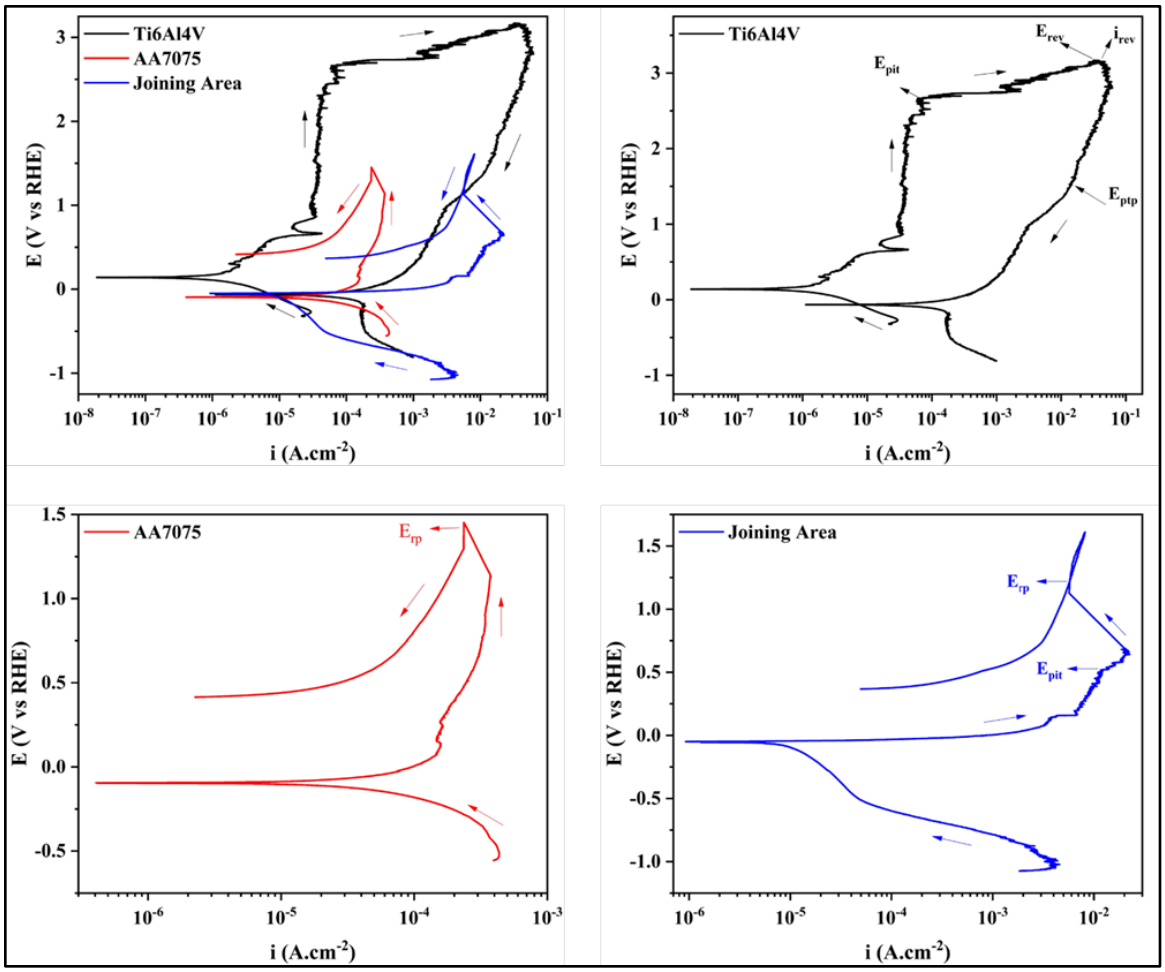

Figure 4.15 Cyclic polarization plots for Ti6Al4V, AA7075, and Joining area samples in 3.5 wt.% NaCl solution at a pH of 7

4.3.3.4 SEM analysis after Corrosion testing

In the SEM micrographs and corresponding EDS analyses provided in **Figure 4.16**, **Figure 4.17**, and **Figure 4.18**, the oxygen content revealed in the EDS spectra offers insights into the oxide layer formation on the surface of each material following corrosion tests. The EDS analysis of the joining area (**Figure 4.16**) indicates a higher oxygen content, suggesting extensive oxide layer formation which is a result of the aggressive corrosion process facilitated by the interaction of the Cu interlayer with the dissimilar metals. This oxide layer is typically non-uniform and signifies potential

weak spots where corrosion could penetrate deeper into the material as explained in section 3.4.2. For the Ti6Al4V alloy (**Figure 4.17**), the EDS spectra show a moderate increase in oxygen content, reflecting a more passive and protective oxide layer that contributes to the alloy's superior corrosion resistance. The oxide layer is more uniform and stable, offering effective protection against the corrosive environment. Meanwhile, the AA7075 alloy (**Figure 4.18**) exhibits significant oxygen presence in the EDS analysis, indicating a thick but potentially porous and less protective oxide layer. This aligns with the observed extensive surface roughness and suggests that the oxide layer on AA7075 does not effectively prevent the underlying metal from further corrosion, especially compared to the more resilient oxide film on Ti6Al4V BA.

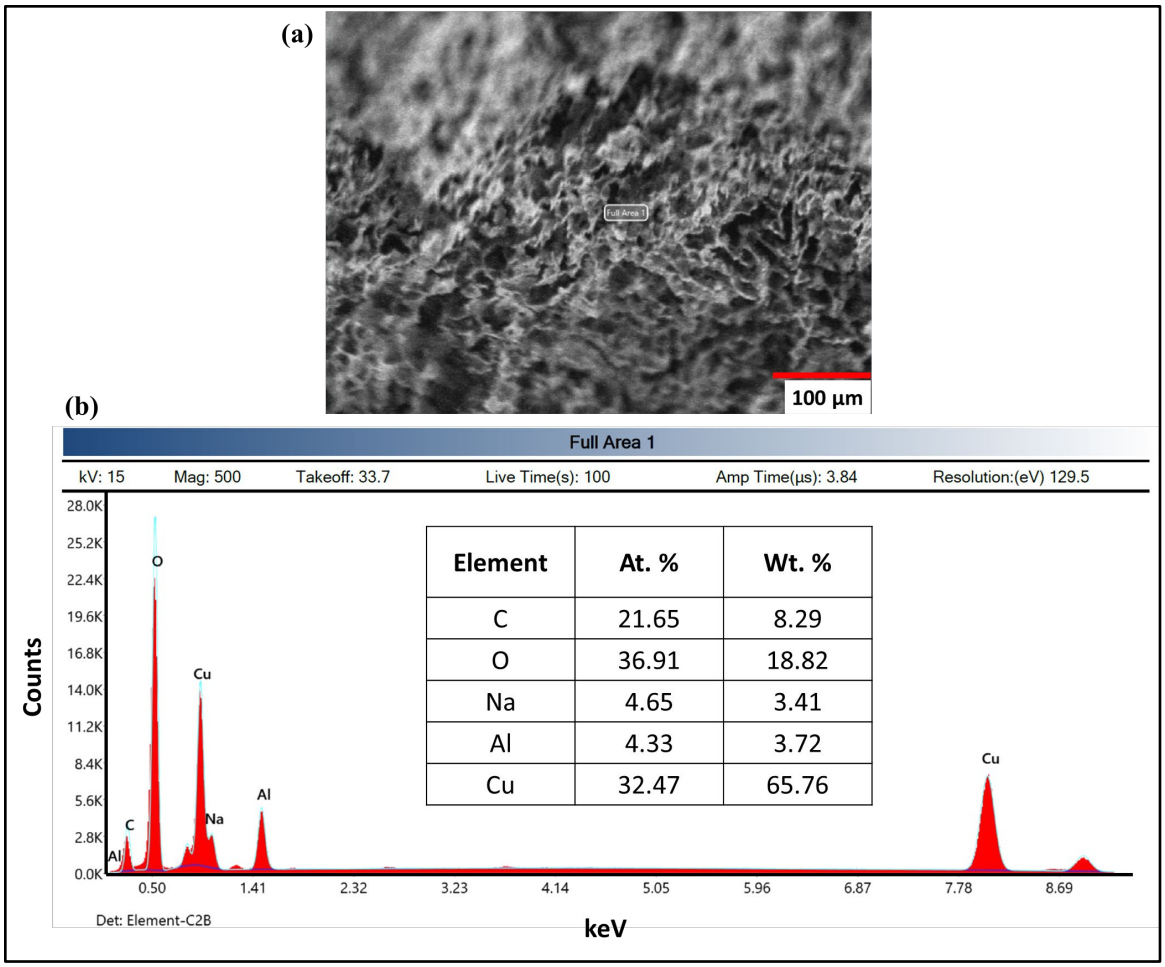

Element	At. %	Wt. %
C	21.65	8.29
O	36.91	18.82
Na	4.65	3.41
Al	4.33	3.72
Cu	32.47	65.76

Figure 4.16 (a) SEM micrograph after corrosion analysis of joining area (b) EDS spectra of joining area after corrosion tests

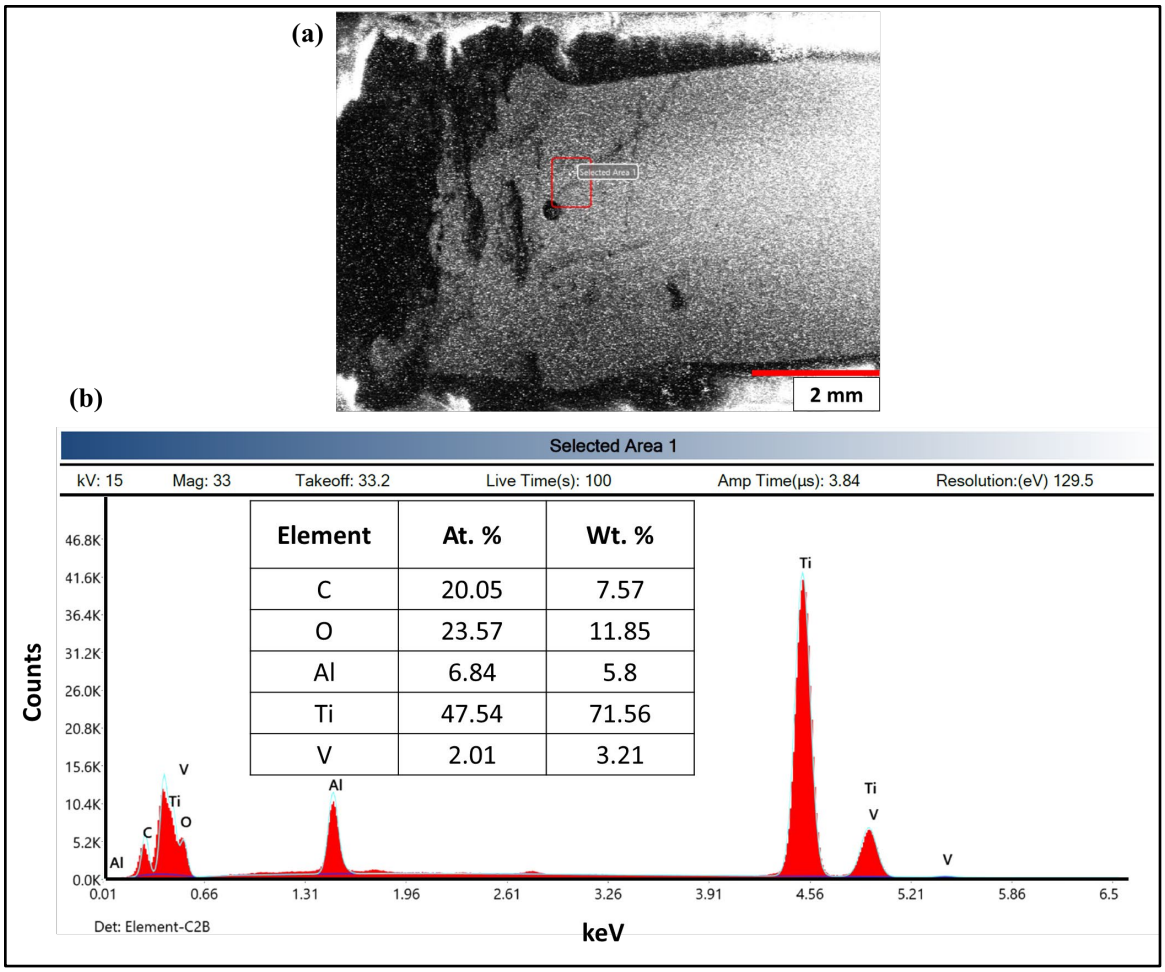

Figure 4.17 (a) SEM micrograph after corrosion analysis of Ti6Al4V BA (b) EDS spectra of Ti6Al4V BA after corrosion tests

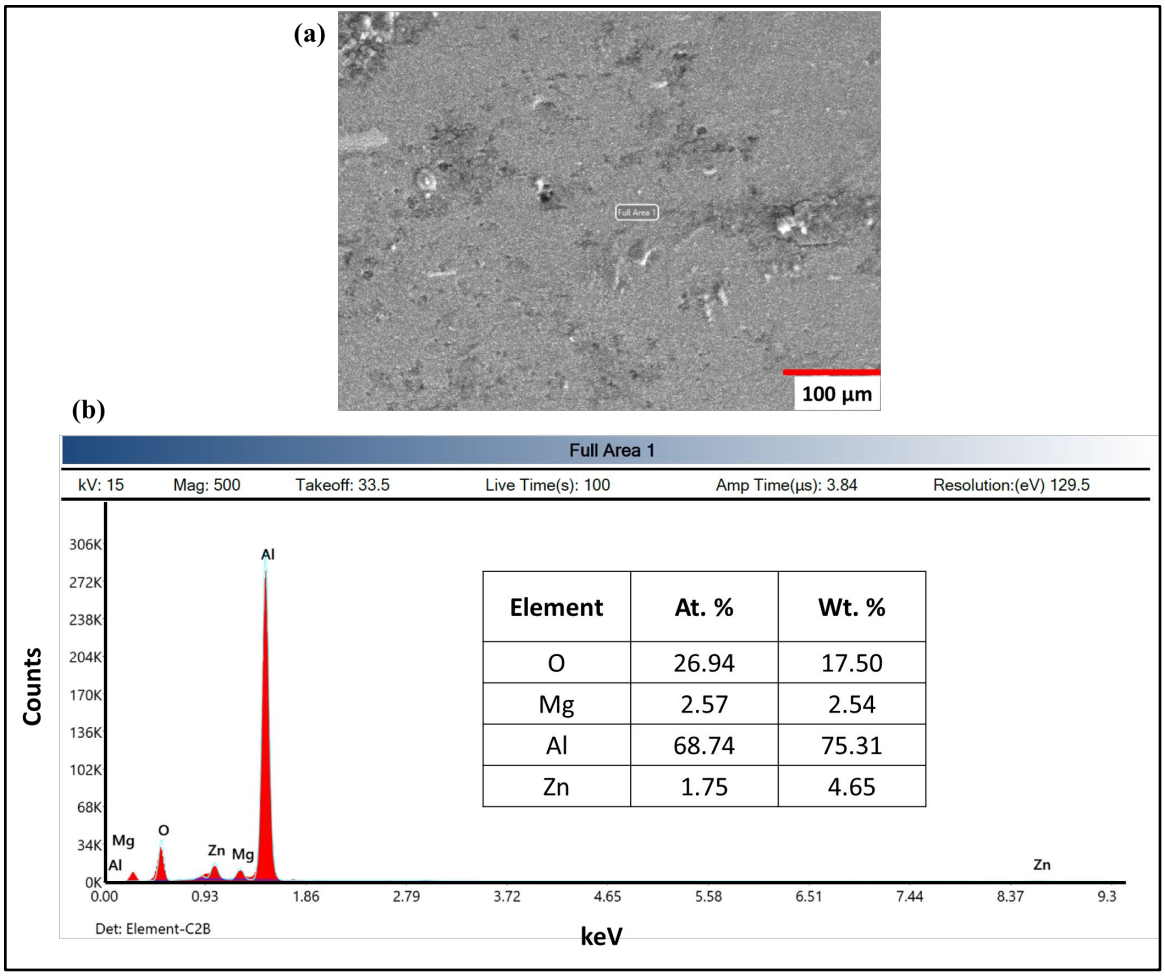

Figure 4.18 (a) SEM micrograph after corrosion analysis of AA7075 BA (b) EDS spectra of AA7075 BA after corrosion tests

4.4 CONCLUSIONS

This study conclusively demonstrates that using a Cu interlayer in laser welding of AA7075 and Ti6Al4V alloys significantly enhances the mechanical and corrosion properties of the joint. Based on the detailed analysis of the current study, following key conclusions can be drawn:

1. The microstructural examination revealed a well-bonded interface with minimal defects, indicating that the Cu interlayer effectively mitigates the challenges typically associated with welding dissimilar materials AA7075 and Ti6Al4V.
2. The joint exhibited a notable increase in microhardness within the fusion zone, with values peaking significantly higher than those of the base alloys along with improved toughness, indicating enhanced joint robustness.
3. The introduction of a Cu interlayer in laser welding between AA7075 and Ti6Al4V alloys resulted in improved mechanical properties. The tensile strength for the joint with the Cu interlayer was found to be enhanced.
4. The use of a Cu interlayer significantly controlled the thickness and composition of the intermetallic layer at the welding interface, which is crucial for reducing brittleness and enhancing joint ductility.
5. The Potentiodynamic polarization test (Tafel test) of the joint area showed a corrosion potential (E_{corr}) of -0.0555 V versus Reversible Hydrogen Electrode (RHE) and a corrosion current density (i_{corr}) of 1.0297×10-5 A/cm², indicating intermediate corrosion resistance between the two base alloys.

CHAPITRE 5
AMÉLIORATION DE LA RÉSISTANCE À LA CORROSION ET DE L'INTÉGRITÉ MÉCANIQUE DES JOINTS SOUDÉS AU LASER TI6AL4V/AA7075 : UNE ÉTUDE COMPARATIVE DES INTERCOUCHES EN ARGENT ET CUIVRE

Titre en français du cinquième article :

Amélioration de la résistance à la corrosion et de l'intégrité mécanique des joints soudés au laser Ti6Al4V/AA7075 : Une étude comparative des intercouches en argent et cuivre.

Titre original (en anglais) :

Enhancing Corrosion Resistance and Mechanical Integrity of Laser-Welded Ti6Al4V/AA7075 Joints: A Comparative Study of Ag and Cu Interlayers.

Auteurs et affiliation :

Asim Iltaf : Étudiant au doctorat, Département de mathématiques, d'informatique et de génie, Université du Québec à Rimouski, Québec, Canada.
Narges Ghafouri Varnosfaderani : Étudiant au doctorat, Department of Materials Engineering, Isfahan University of Technology, 84156-83111, Isfahan, Iran.
Noureddine Barka : Professeur, Département de mathématiques, d'informatique et de génie, Université du Québec à Rimouski, Québec, Canada.
Shayan Dehghan : Chercheur post-doctoral, Département de mathématiques, d'informatique et de génie, Université du Québec à Rimouski, Québec, Canada.

État de l'article :

Soumis.

Revue :

Metals and Materials International

Résumé en français du cinquième article

Dans cette étude, la résistance à la corrosion et les caractéristiques des contraintes résiduelles des joints dissemblables soudés au laser entre les alliages Ti6Al4V et AA7075 ont été largement examinées en utilisant des intercouches en argent et cuivre. La recherche a utilisé la polarisation potentiodynamique et la spectroscopie d'impédance électrochimique pour évaluer le comportement électrochimique des joints. L'intercouche en Ag a montré une résistance à la corrosion supérieure dans la zone fondue, avec un potentiel de corrosion (E_{corr}) de 0,260 V et une faible densité de courant de corrosion (i_{corr}) de $4,55 \times 10^{-6}$ A/cm². Cela indique un taux de corrosion plus lent par rapport à l'intercouche en cuivre, qui a montré des propriétés électrochimiques moins favorables. De plus, l'intercouche en Ag a présenté une résistance à la polarisation (R_p) plus élevée, soit 7,079 kΩ·cm², ce qui suggère une meilleure capacité de protection contre les environnements corrosifs. Les mesures des contraintes résiduelles ont fourni des informations supplémentaires sur les performances mécaniques des joints. L'intercouche en argent a induit des contraintes compressives des deux côtés, à savoir AA7075 et Ti6Al4V, ce qui est bénéfique pour améliorer la résistance à la corrosion et l'intégrité structurelle. Les contraintes compressives aident à réduire l'initiation et la propagation des fissures, renforçant ainsi la durabilité du joint. En revanche, l'intercouche en cuivre a introduit des contraintes de traction, ce qui peut accélérer la corrosion localisée et réduire la durée de vie du joint en raison d'une sensibilité accrue à la formation de fissures.

Enhancing Corrosion Resistance and Mechanical Integrity of Laser-Welded Ti6Al4V/AA7075 Joints: A Comparative Study of Ag and Cu Interlayers

Asim Iltaf [a, *], Narges Ghafouri Varnosfaderani [b], Noureddine Barka [a], Shayan Dehghan [a]

[a] Department of Mathematics, Computer Science and Engineering, University of Quebec at Rimouski, Rimouski, QC G5L 3A1, Quebec, Canada.

[b] Department of Materials Engineering, Isfahan University of Technology, 84156-83111, Isfahan, Iran.

[*]Corresponding author (Asim Iltaf): Department of Mathematics, Computer Science and Engineering, University of Quebec at Rimouski, Rimouski, QC G5L 3A1, Quebec, Canada.

E-mail address: asim.iltaf@uqar.ca

Abstract

In this study, the corrosion resistance and residual stress characteristics of laser-welded dissimilar joints between Ti6Al4V and AA7075 alloys were extensively investigated using Ag and Cu interlayers. The research employed potentiodynamic polarization and electrochemical impedance spectroscopy (EIS) to evaluate the electrochemical behavior of the joints. The Ag interlayer demonstrated superior corrosion resistance in the fusion zone (FZ), with a corrosion potential (Ecorr) of 0.260 V and a low corrosion current density (icorr) of 4.55×10^{-6} A/cm². This indicates a

slower rate of corrosion compared to the Cu interlayer, which showed less favorable electrochemical properties. Additionally, the Ag interlayer exhibited a higher polarization resistance (Rp) of 7.079 kΩ·cm², suggesting enhanced protective capabilities against corrosive environments. Residual stress measurements provided further insights into the mechanical performance of the joints. The Ag interlayer induced compressive stresses on both the AA7075 and Ti6Al4V sides, which is beneficial for improving corrosion resistance and structural integrity. Compressive stresses help in mitigating crack initiation and propagation, thereby enhancing the durability of the joint. On the other hand, the Cu interlayer introduced tensile stresses, which can accelerate localized corrosion and reduce the lifespan of the joint due to increased susceptibility to crack formation.

***Keywords*:** Dissimilar weldments, Interlayers, Residual stresses, corrosion resistance, EIS

5.1 INTRODUCTION

Over the past two decades, there has been a growing demand for joining dissimilar materials in industrial applications. This trend is driven by several benefits, such as reducing operational and material costs, increasing design flexibility, and seeking products with enhanced mechanical and thermal properties (Kah & Jukka Martikainen, 2014; Raj & Biswas, 2022). Extensive research has focused on joining Aluminum (Al) and Titanium (Ti) alloys because they possess superior properties. However, traditional fusion welding methods—such as diffusion welding, explosive welding, electron beam welding, and laser welding—encounter significant challenges when used to join these materials. The primary reason is the substantial mismatch in their physical and thermal properties (Ohnuma et al., 2000b). Unlike traditional welding methods, laser welding is widely used for joining dissimilar metals because it offers high thermal density, concentrated heat, rapid processing speeds, minimal thermal deformation, and a reduced environmental impact (Casalino et al., 2017b; P.

Wang et al., 2016). Several modifications have been implemented to optimize processing parameters, addressing challenges associated with localized melting and distortion (Casalino et al., 2017b; Leo et al., 2018b). These challenges lead to complications during the fusion welding of Al and Ti joints, such as limited mutual solubility, the formation of porosity, and solidification cracking (Cross, 2005). Moreover, during the fusion welding process, intermetallic compounds (IMCs) like Al_3Ti, AlTi, and Ti_3Al were found to form continuously and develop substantial thickness. If these IMCs are not evenly distributed, their formation can lead to brittleness and negatively affect the weld's properties. However, when the IMCs are uniformly distributed at the weld interface, they can act as dispersoids and enhance the mechanical strength and corrosion resistance of the weld (Z. Li et al., 2022). Therefore, to achieve a strong bond between Al and Ti, it is essential to control the formation of IMCs and ensure they are uniformly distributed at the joint interface.

Chen et al. (Y. Chen et al., 2008) utilized a rectangular spot laser welding-brazing technique to create butt joints between 5A06Al alloy and Ti6Al4V, using AlSi12 flux-cored wire as a filler. By adjusting the heat input, the thickness and morphology of the intermetallic compound (IMC) at the interface were altered. When a low-heat input was applied, a continuous serrated TiAl3 reaction layer formed at the interface, and the joint fractured within the fusion zone, displaying a high tensile strength of 290 MPa. Peyre [16] successfully applied laser-induced reactive wetting to join T40 alloy with A5754 alloy in a lap configuration. A 2.4 mm diameter laser beam was used to melt the aluminum alloy, allowing it to spread across the titanium alloy surface. At the interface between the liquid Al and solid Ti, a serrated $TiAl_3$ IMC primarily formed, with a thickness ranging from 0.5 μm to 2.4 μm. Although flux was used to enhance the wetting of the molten aluminum, the wetting width remained limited, potentially reducing the mechanical strength of the joints. A maximum linear resistance strength of approximately 300 N/mm was achieved in an AA5754/T40 joint without the use of filler metal. In the single-beam laser fusion brazing process of Al and Ti alloys, when the molten Al spread beyond the laser-irradiated area and interacted with the cooler Ti

alloy, the melt pool temperature decreased rapidly, limiting the spread length. The dual-beam laser technique, considered a more advanced welding method, has been employed for joining dissimilar alloys because it allows for flexible adjustment of energy distribution, beam spacing, and spot size (S. Deng et al., 2020; P. Li et al., 2020; P. Li, Lei, Zhang, & Chen, 2020c; Tomashchuk et al., 2017c). Tomashchuk et al. (Tomashchuk et al., 2017c) investigated the laser welding-brazing of 3 mm thick AA5754 alloy to T40 alloy using a defocused tandem laser spot. Si-rich structures were observed in the upper and middle sections of the joints, while very thin (<0.5 μm) Si-rich interfaces, with a maximum length of 2100 μm, formed at the bottom of the 45° groove, which was insufficient for establishing a strong joint connection. Under optimal welding conditions, the length of these extremely thin Si-rich interfaces could be reduced to under 300 μm, achieving a joint efficiency of up to 90%. Li et al. (P. Li et al., 2020) produced Al/Ti butt joints using a dual-spot laser welding-brazing method with Al-12Si filler wire. At a laser power of 1900 W, high-quality joints with a serrated IMC layer, approximately 0.45 ± 0.15 μm thick, exhibited the best tensile strength, reaching 241 MPa. Deng et al. (S. Deng et al., 2020) utilized both single-spot and twin-spot beams for laser welding-brazing of DP590 steel to AA7075-T5 aluminum alloy. Both experimental and simulation results demonstrated that the contact angle was significantly reduced, and the spreading length increased compared to the single-spot laser beam method. The preheating effect from the second auxiliary laser beam enhanced the spreading of the molten Al alloy. Vacchi et al. (Vacchi et al., 2017) studied lap joints of AA6181-T4 aluminum alloy and Ti-6Al-4V titanium alloy, examining their surface corrosion behavior. They reported that the Al side was highly susceptible to corrosion, exhibiting numerous preferential sites for pitting corrosion. They also suggested that the intensity of corrosion attack decreased in the weld nugget region due to the presence of small precipitates. A similar behavior was observed by Gharavi et al. (Gharavi et al., 2014) when they evaluated the corrosion behavior of lap joints made from the AA6061-T6 alloy. According to these reports, Al/Ti joints resulted in significant formation of intermetallic constituent particles. This extensive

formation further intensified galvanic corrosion coupling and decreased the corrosion resistance of the material. However, it is important to note that in the aforementioned studies, the Al/Ti joints were produced using randomly selected parameters. Therefore, it is crucial to investigate the corrosion behavior of Al/Ti LBW joints and identify the optimal LBW parameters for this system to ensure optimal overall service performance.

Generally, corrosion occurs more readily on the Al side of an Al/Ti joint because Al has a corrosion potential of -0.5 V, which is approximately 60% lower than that of Ti, around -0.2 V. Since Al has a relatively lower corrosion potential, the joint strength of Al/Ti can be adversely affected, potentially leading to joint failure. Therefore, it is essential to control the corrosion behavior of Al/Ti LBW joints to ensure optimal overall service performance. Given the limited research available on this topic, the aim of this study was to investigate the use of silver (Ag) as interlayer in joining the Ti6Al4V and AA7075 alloys using LBW process. Residual stresses characterization of the optimized weldments was conducted to understand the distrivbution of the stresses across the join. The study also focused on assessing the corrosion behavior of the welded joint, which is crucial for ensuring its reliability and performance in service. Finally, the results of Ag interlayer weldment are compared with the copper (Cu) interlayer weldment. The findings from this investigation provide valuable insights for developing Al/Ti joints with improved mechanical strength and corrosion resistance, potentially benefiting industries such as aerospace, automotive, and marine.

5.2 MATERIALS AND METHODS

A full penetration Bead-on-Plate (BoP) welding was performed on AA7075 and Ti6Al4V sheets, each measuring 100×80×1.6 mm in their original condition, using fiber laser welding. The chemical compositions of the base materials and the optimized LBW process parameters have been reported in our previous study (Iltaf, Barka, et al., 2024). Leyens and Peters (‘Titanium and Titanium Alloys’, 2003) noted that for sheet

thicknesses under 3 mm, joint preparation before welding and the use of filler materials are unnecessary.

To evaluate the corrosion performance of the samples, three types of specimens were prepared: Ti6Al4V BA, AA7075 BA, and the joint area of Ti6Al4V/AA7075 with Ag interlayer, which includes both the fusion zone and heat-affected zone regions. Each specimen was machined to an area of 0.5 cm^2 and had its surface abraded with silicon carbide (SiC) sandpaper before being cleaned with deionized water and ethanol.

5.2.1 Residual stresses measurement

The residual stresses present in the weldment were evaluated using the hole-drilling strain measurement method (HDSM). Strain gauges was installed 5 mm and 10 mm away from the weld centerline, and a hole was drilled at the center of this gauge, as illustrated in **Figure 5.1**. Strain data were collected through a multi-channel data acquisition system connected to the drilled strain gauge. Measurements were taken continuously, increasing the hole depth incrementally by 0.4 mm starting from the surface. After collecting the data, the transverse (perpendicular to the welding direction) and longitudinal (parallel to the welding direction) residual stresses were calculated using H-drill software.

Figure 5.1 HDSM apparatus setup.

5.2.2 Corrosion tests

Corrosion tests were conducted using a Gamry Reference-3000 Potentiostat in a three-electrode cell configuration. An Ag/AgCl electrode served as the reference electrode, a platinum electrode as the counter electrode, and the prepared specimens acted as the working electrode, all immersed in a 3.5% NaCl solution. To stabilize the specimens within the test solution, an open circuit potential (OCP) test was performed for one hour.

Subsequently, potentiodynamic polarization and cyclic polarization tests were carried out over a potential range from -1 to 1.5 V relative to the OCP at a scan rate of 1 mV/s. The resulting curves from these tests were analyzed using Gamry Echem Analyst™ software. Finally, electrochemical impedance spectroscopy (EIS) tests were conducted to assess the corrosion resistance of the specimens. These tests were performed at a voltage amplitude of 10 mV across a frequency range of 10 mHz to 100 kHz. The EIS data were fitted, and the equivalent circuit model was determined using Zview software.

5.3 RESULTS AND DISCUSSION

5.3.1 Residual stresses analysis

Figure 5.2 provides a graphical representation of the percentage of residual strains in relation to the normalized hole depth at various distances from the weld centerline for both materials. This figure illustrates how the residual stresses vary not only with depth beneath the surface but also with the lateral distance from the weld. The analysis depicted in **Figure 5.2** is crucial for understanding the distribution of residual stresses throughout the welded joint. By examining how these stresses change with both depth and distance from the weld, valuable insight into the mechanical behavior of the weldment can be estimated.

A comprehensive examination of the longitudinal residual stresses (**Table 5.1**) in the Ag interlayer weldment revealed that both the AA7075 side and the Ti6Al4V titanium alloy side exhibit significant compressive residual stresses, especially in areas close to the weld centerline. Detailed measurements presented in **Table 5.1** show that on the AA7075 side, the compressive residual stress was measured at -579 MPa at a distance of 5 mm from the weld centerline. This stress value decreases to -261 MPa when the distance from the centerline increases to 10 mm. Similarly, the Ti6Al4V side shows a compressive residual stress of -647 MPa at 5 mm from the centerline, which reduces to -131 MPa at a 10 mm distance. The transverse residual stresses display a comparable trend, with higher compressive stresses detected nearer to the weld centerline, as outlined in **Table 5.2**. On the AA7075 side, the transverse residual stress is -472 MPa at a 5 mm distance from the weld centerline and decreases to -312 MPa at 10 mm away. The Ti6Al4V side exhibits even higher compressive stresses, -647 MPa at 5 mm from the centerline and decreasing to -160 MPa at a 10 mm distance. The above mentioned understanding the variation of residual stresses is essential for assessing the overall structural integrity and performance of the welded joint.

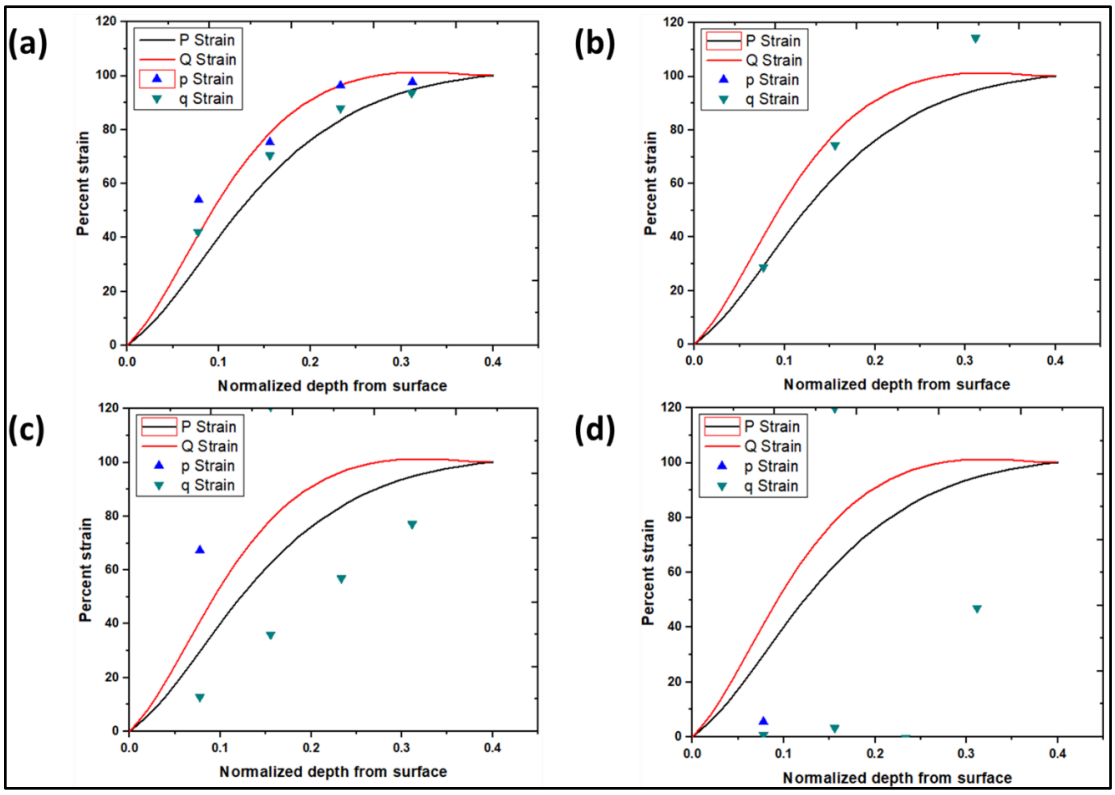

Figure 5.2 Analysis on the percentage of residual strains relative to the normalized hole depth for the Ag interlayer weldment at various distances from the weld centerline: (a) 5 mm towards Ti6Al4V, (b) 10 mm towards Ti6Al4V, (c) 5 mm towards AA7075, and (d) 10 mm towards AA7075.

Tableau 5.1 The longitudinal residual stress values determined for weldment with silver Ag interlayer.

Sample	AA7075 side	Ti6Al4V side

Distance from weld centerline (mm)	5	10	5	10
Ag interlayer weldment (MPa)	-579	-261	-647	-131

Tableau 5.2 The transverse residual stress values determined for weldment with silver Ag interlayer.

Sample	**AA7075 side**		**Ti6Al4V side**	
Distance from weld centerline (mm)	5	10	5	10
Ag interlayer weldment (MPa)	-472	-312	-647	-160

5.3.2 Corrosion tests analysis

5.3.2.1 Potentiodynamic polarization test (Tafel test)

A potentiodynamic polarization diagram was used to estimate corrosion potential and corrosion current density as shown in **Figure 5.3**. In addition, by using this diagram and equation 1, the polarization resistance is extracted, where β_a, β_c, and i_{corr} show the anodic Tafel slope, the cathodic Tafel slope, and the corrosion current density, respectively.

Polarization resistance: $$R_P = \frac{\beta_a \beta_c}{2.303(\beta_a + \beta_c) i_{corr}} \quad (1)$$

The potentials were standardized based on reversible hydrogen potential (RHE) using formula 2.

$$E_{RHE} = E_{Ag/AgCl} + 0.059\,pH + E^{\circ}_{Ag/AgCl} \left(E^{\circ}_{Ag/AgCl} = 0.1967V \quad at \quad 25^{\circ}C\right) \tag{2}$$

The data provided in **Table 5.3** show distinct differences in the corrosion behavior of the three areas tested. Ti6Al4V exhibited a relatively high corrosion potential of 0.266 V, indicating that it is less likely to undergo corrosion under the tested conditions compared to the other samples. Additionally, the corrosion current density for Ti6Al4V was 6.79×10^{-7} A.cm^{-2}, which is very low, signifying a slow rate of corrosion. The polarization resistance for Ti6Al4V was the highest among the samples, measuring 96.777 KΩ.cm^2. A high polarization resistance typically correlates with strong resistance to corrosion, as it reflects the material's ability to form and maintain a protective oxide layer on its surface, reducing the overall corrosion rate.

In contrast, AA7075, a commonly used high-strength Al alloy, displayed significantly lower corrosion resistance. Its corrosion potential was -0.118 V, much lower than that of Ti6Al4V, indicating a higher tendency to corrode. The corrosion current density for AA7075 was also notably higher, at 5.78×10^{-5} A.cm^{-2}, pointing to a faster rate of material degradation in the NaCl solution. The polarization resistance for AA7075 was 1.358 KΩ.cm^2, much lower than that of Ti6Al4V, which suggests that AA7075 lacks a robust protective oxide layer, making it more susceptible to corrosion in chloride-rich environment. The fusion zone (FZ) area, which represents the region where Ti6Al4V and AA7075 with Ag interlayer were welded together, exhibited intermediate corrosion behavior. The corrosion potential of the FZ was 0.260 V, slightly lower than Ti6Al4V but still significantly higher than AA7075. The corrosion current density in the FZ was 4.55×10^{-6} A.cm^{-2}, higher than Ti6Al4V but much lower than AA7075, suggesting that the FZ offers better corrosion resistance than AA7075, though not as much as Ti6Al4V. The polarization resistance for the FZ was 7.079 KΩ.cm^2, indicating that the welded region offers moderate protection against

corrosion, likely due to the combined properties of both base materials and the Ag interlayer.

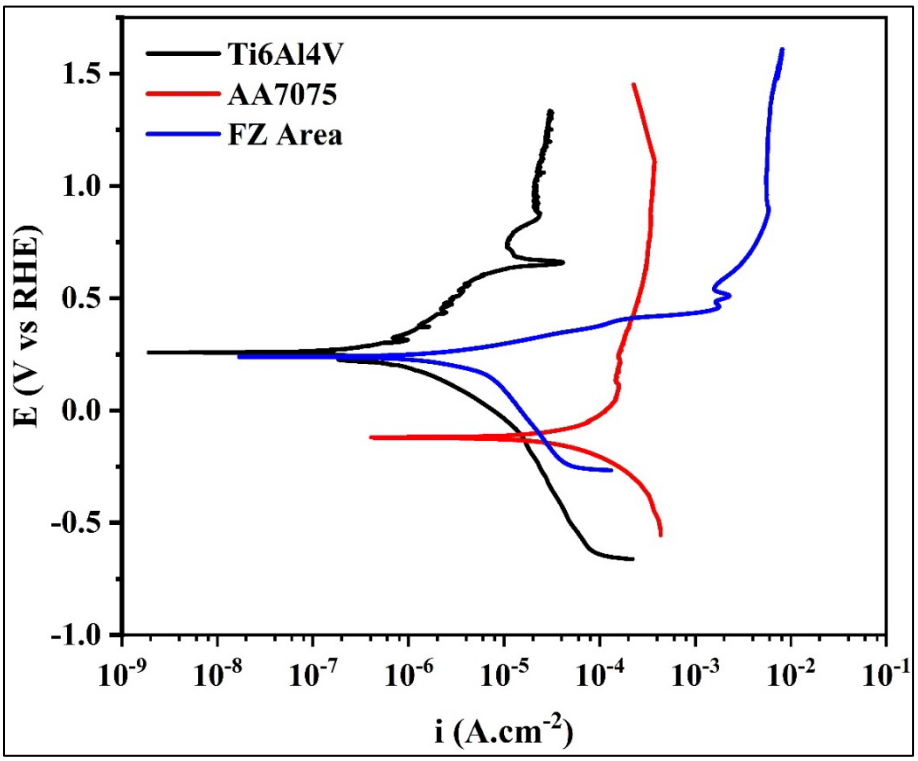

Figure 5.3 Potentiodynamic polarization plots of Ti6Al4V, AA7075, and FZ Area in 3.5 wt.% NaCl solution at a pH of 7.

Tableau 5.3 Electrochemical parameters extracted from the potentiodynamic polarization plots in **Figure 5.3.**

Sample	E_{corr} V	i_{corr} A.cm^{-2}	B_a V/dec	$-B_c$ V/dec	R_p K Ω.cm^2
Ti6Al4V	0.266	6.79×10^{-7}	0.37879	0.25204	96.777
AA7075	-0.118	5.78×10^{-5}	0.40918	0.32365	1.358
FZ Area	0.260	4.55×10^{-6}	0.08771	0.5199	7.079

5.3.2.2 Electrochemical impedance spectroscopy (EIS) test

The EIS results for the base alloys and the FZ are shown in **Figure 5.4**. Z_{view} software was used to fit the EIS data and find the best equivalent circuit model (**Figure 5.5)**. In all samples, R_s, R_{film}, CPE_{film}, R_{ct}, and CPE_{dl} are the solution resistance, the oxide film resistance, the oxide film constant-phase element, the double-layer charge transfer resistance, and the double-layer constant-phase element, respectively.

The results are summarized in **Table 5.4**. Ti6Al4V showed superior performance in terms of its electrochemical properties. Its charge transfer resistance (Rct) was 73,844 Ω.cm², the highest among the samples, indicating a strong resistance to the flow of electrons from the metal surface into the electrolyte, which translates to better protection against corrosion. The oxide film resistance (R_{film}) for Ti6Al4V was also high, measuring 2,365 Ω.cm², signifying the presence of a stable and protective oxide layer on the surface of the material. The constant-phase elements (CPE) also suggested favorable conditions for Ti6Al4V, with a CPEfilm of 6.2×10^{-8} $F.cm^{-2}.s^{n-1}$ and a double layer CPE_{dl} of 9.38×10^{-10} $F.cm^{-2}.s^{n-1}$, both indicating good surface stability and corrosion resistance.

On the other hand, AA7075 showed significantly lower resistance to corrosion. Its charge transfer resistance was only 10,200 Ω.cm², highlighting the alloy's higher susceptibility to corrosion compared to Ti6Al4V. The oxide film resistance was also lower, at 721.4 Ω.cm², which is consistent with the results from the potentiodynamic polarization test, indicating a less protective oxide layer on AA7075. The CPE values for AA7075 also reflected its poorer performance, with a CPEfilm of 8.04×10^{-13} $F.cm^{-2}.s^{n-1}$ and a CPEdl of 3.19×10^{-10} $F.cm^{-2}.s^{n-1}$.

The FZ area once again displayed intermediate results, with a charge transfer resistance of 37,137 Ω.cm² and an oxide film resistance of 632.1 Ω.cm². While these

values are lower than those for Ti6Al4V, they are still better than AA7075, suggesting that the welding process has improved the corrosion resistance of the FZ area. The CPE values for the FZ were 1.08×10^{-9} F.cm^{-2}.s^{n-1} for the film and 9.62×10^{-6} F.cm^{-2}.s^{n-1} for the double layer, which are consistent with the FZ's moderate corrosion behavior.

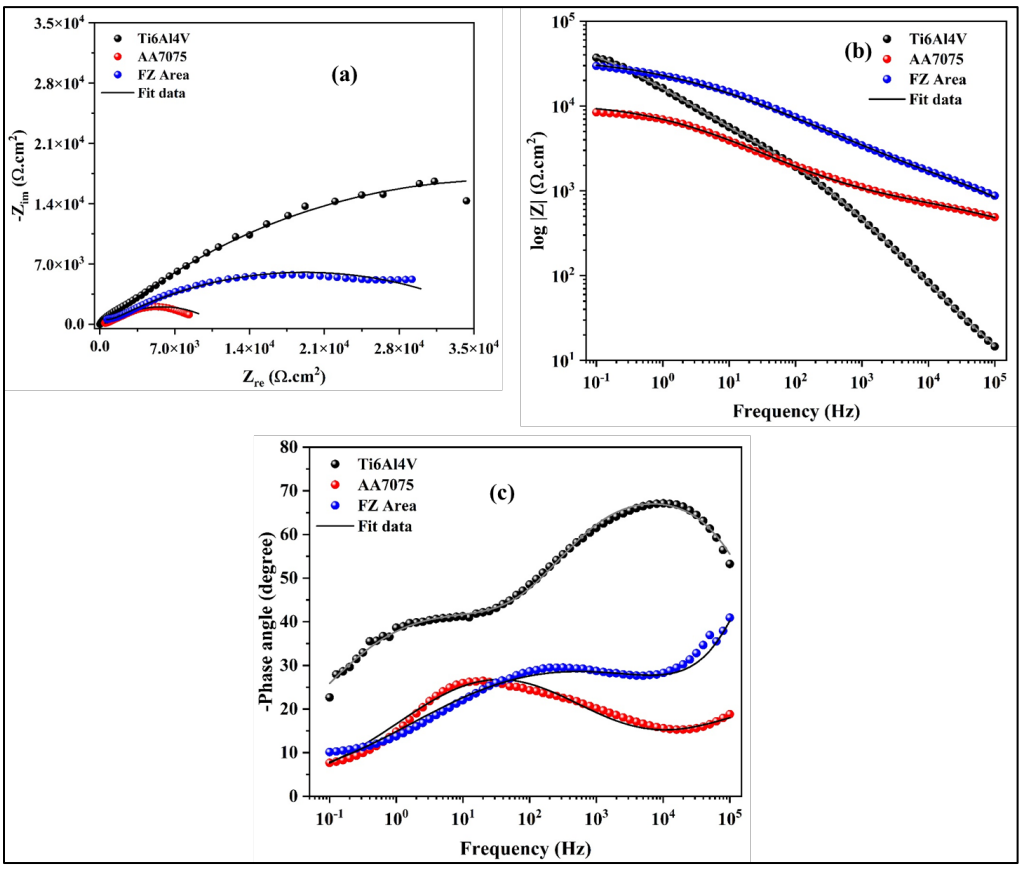

Figure 5.4 (a) Nyquist, (b) Bode Z, and (c) Bode-phase plots for Ti6Al4V, AA7075, and FZ Area samples in 3.5 wt.% NaCl solution at a pH of 7.

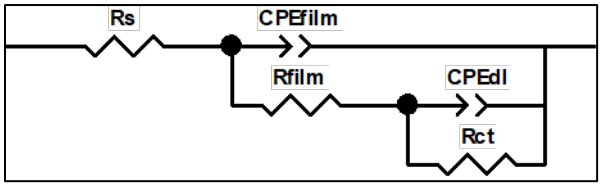

Figure 5.5 Electrical equivalent circuit used to fit the electrochemical impedance data of samples: Ti6Al4V, AA7075 and FZ Area.

Tableau 5.4 Electrical parameters extracted from the fitting plot of the EIS tests for Ti6Al4V, AA7075, and FZ Area samples

Sample	R_s ($\Omega.cm^2$)	CPE_{film} ($F.cm^{-2}\ s^{n-1}$)	n_{film}	R_{film} ($\Omega.cm^2$)	CPE_{dl} ($F.cm^{-2}\ s^{n-1}$)	n_{dl}	R_{ct} ($\Omega.cm^2$)
Ti6Al4V	24.29	6.2×10^{-8}	0.79	2365	9.38×10^{-10}	0.52	73844
AA7075	27.4	8.04×10^{-13}	0.45	721.4	3.19×10^{-10}	0.48	10200
FZ Area	20.6	1.08×10^{-9}	0.98	632.1	9.62×10^{-6}	0.4	37137

5.3.2.3 Cyclic polarization test

In the cyclic polarization test, the samples were subjected to cyclic voltage scans to assess their susceptibility to localized forms of corrosion, such as pitting or crevice corrosion. This test is particularly useful for identifying the potential at which localized corrosion initiates and whether the material can repassivate after such events. The

cyclic polarization curves shown in **Figure 5.6**, reveals key differences. Ti6Al4V display a relatively flat cyclic polarization curve with minimal hysteresis, indicating that it has excellent resistance to pitting and can easily repassivate if localized corrosion initiates. This is consistent with the high corrosion resistance observed in the previous tests. However, AA7075 showed a much larger hysteresis loop in its cyclic polarization curve, suggesting that it is more prone to pitting corrosion. Once corrosion initiates in AA7075, it is harder for the material to repassivate, which is a major drawback for applications in chloride-rich environments. The FZ area, similar to the previous tests, displayed intermediate behavior. While it showed some susceptibility to pitting corrosion, the hysteresis loop was smaller than that of AA7075, suggesting that the welding process has improved its resistance to localized forms of corrosion, although not to the same extent as Ti6Al4V. The results of these tests clearly show that Ti6Al4V possesses superior corrosion resistance compared to AA7075 and the FZ area. The fusion zone, while not as resistant as Ti6Al4V, demonstrates improved properties over AA7075, likely due to the influence of the Ag interlayer in the FZ.

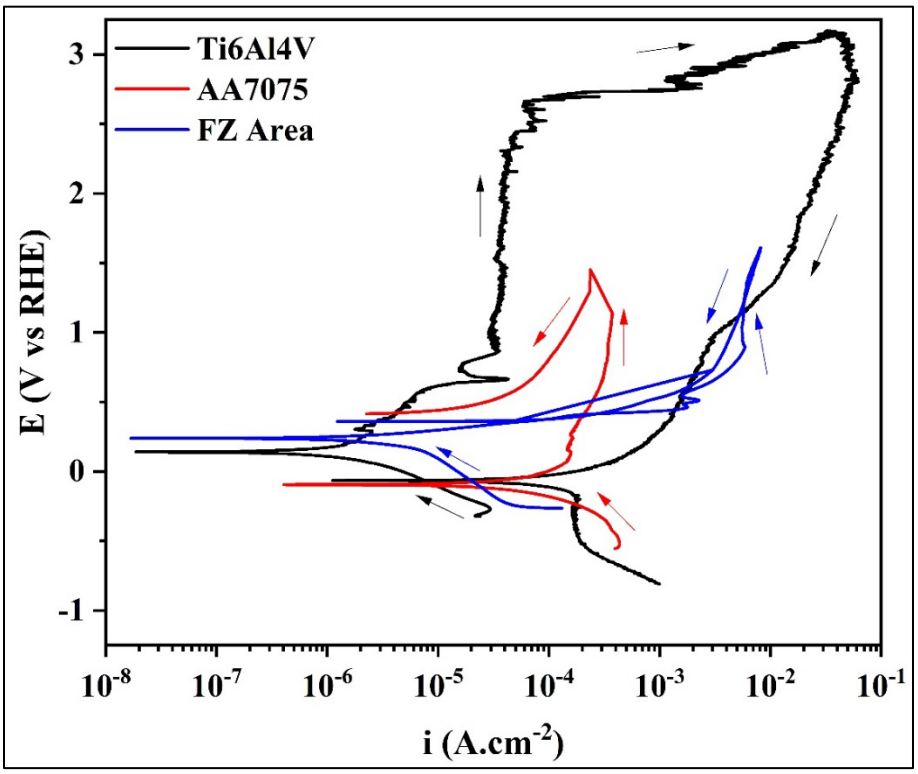

Figure 5.6 Cyclic polarization plots for Ti6Al4V, AA7075, and FZ Area samples in 3.5 wt.% NaCl solution at a pH of 7.

5.3.2.4 Scanning electron microscopy (SEM) after corrosion testing

The SEM analysis conducted after the corrosion testing provided crucial insights into the surface morphology and elemental distribution across the joint area. After exposing the welded specimens to a corrosive 3.5% NaCl solution, significant changes in the surface characteristics were observed.

The SEM image shown in **Figure 5.7(a)**, revealed distinct areas of corrosion damage, primarily concentrated in the Al-rich FZ. These pits were characterized by deep cavities, a known feature in Al alloys when subjected to Cl- environments. This aligns with the electrochemical test results, where AA7075 demonstrated significantly poorer corrosion resistance than Ti6Al4V. Elemental analysis using energy-dispersive X-ray spectroscopy (EDS) as shown in **Figure 5.7(b)** revealed the formation of Al_2O_3

occurs, but it is not as protective or stable as the TiO_2 layer, especially when exposed to aggressive environments like the NaCl solution used in the tests. This difference in oxidation behavior further explains the superior surface stability and corrosion resistance observed in Ti6Al4V compared to FZ during the corrosion testing.

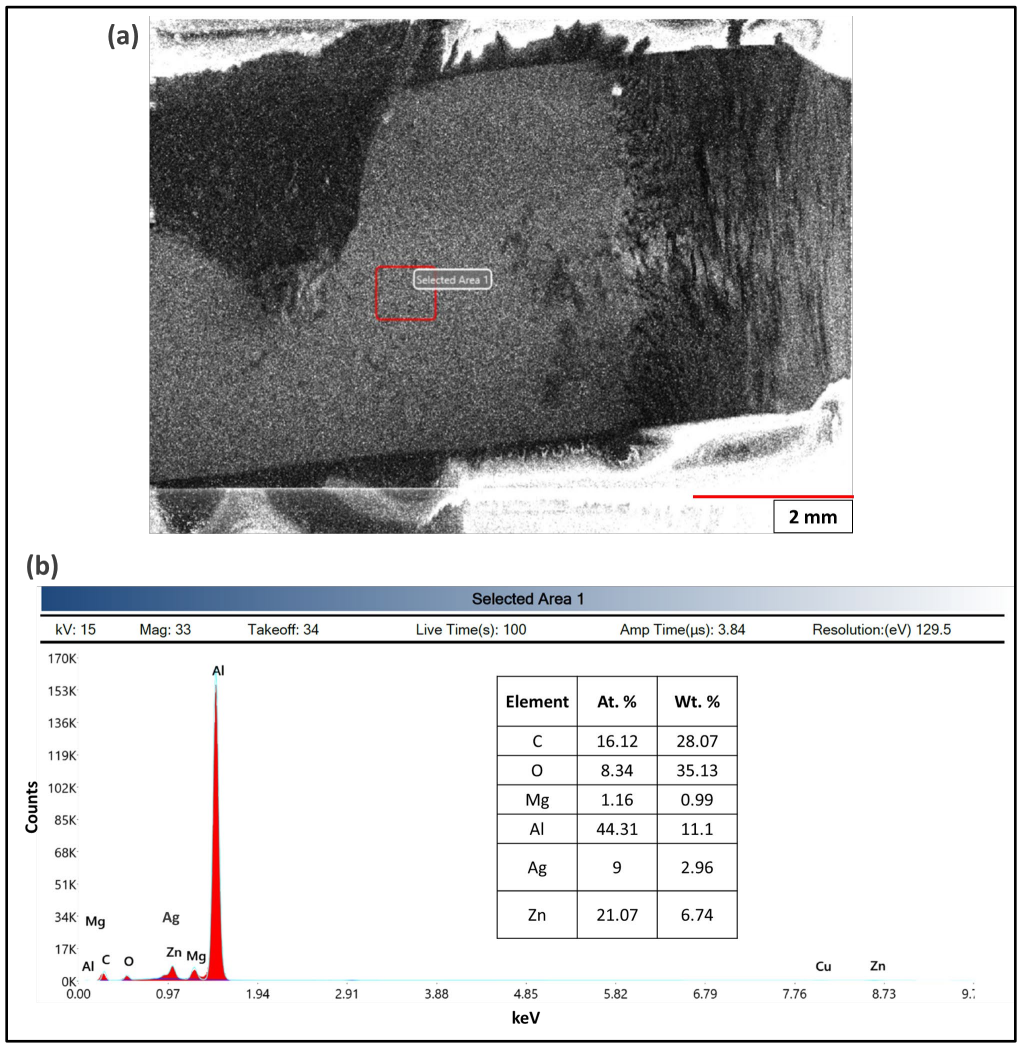

Figure 5.7 SEM along with EDS result of the joint area after the corrosion testing

5.4 COMPARISON OF AG AND CU WELDMENTS

The residual stresses result for the Cu weldment have been discussed above. Here, the results for the Ag weldment are also shown in **Figure 5.8** along with summarized values for both weldments in **Table 5.5** and **Table 5.6**. As mentioned previously, the residual stresses in weldments with Ag and Cu interlayers were analyzed using the hole-drill strain measurement method. The Ag interlayer weldment displayed significant compressive stresses on the AA7075 side and Ti6Al4V side. Conversely, the Cu interlayer weldment exhibited tensile stresses on both sides, indicating that the type of interlayer influences the distribution and magnitude of residual stresses. The Ag interlayer resulted in higher compressive stresses on both side of the joint, while the Cu interlayer weldment maintained tensile stresses on both sides with a notable decrease at greater distances from the weld centerline.

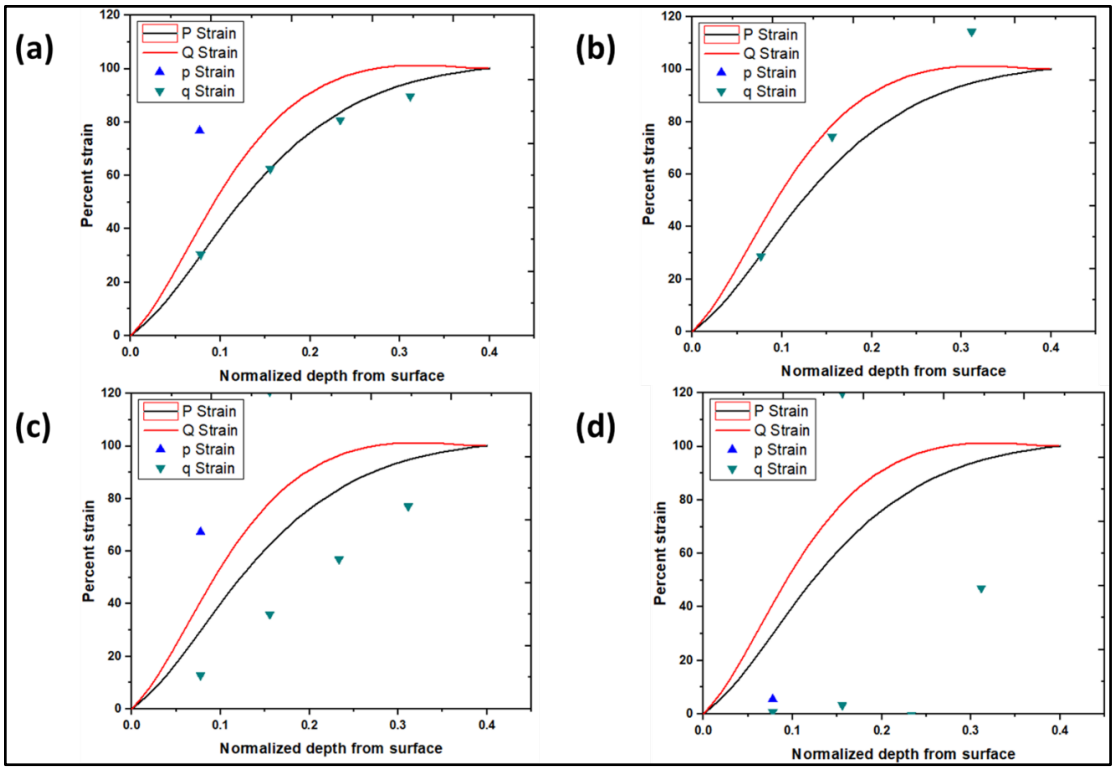

Figure 5.8 Analysis on the percentage of residual strains relative to the normalized hole depth for the Cu interlayer weldment at various distances from the weld centerline: (a) 5 mm towards Ti6Al4V, (b) 10 mm towards Ti6Al4V, (c) 5 mm towards AA7075, and (d) 10 mm towards AA7075.

Tableau 5.5 The longitudinal residual stress values determined for weldments with silver Ag and Cu interlayers.

Sample	**AA7075 side**		**Ti6Al4V side**	
Distance from weld centerline (mm)	5	10	5	10

Ag interlayer weldment (MPa)	-579	-261	-647	-131
Cu interlayer weldment (MPa)	507	384	275	-363

Tableau 5.6 The transverse residual stress values determined for weldments with silver Ag and Cu interlayers.

Sample	***AA7075 side***		***Ti6Al4V side***	
Distance from weld centerline (mm)	5	10	5	10
Ag interlayer weldment (MPa)	-472	-312	-647	-160
Cu interlayer weldment (MPa)	388	292	345	251

The corrosion results and residual stress values reveal distinct behaviors between the dissimilar joints of Ti6Al4V and AA7075, when comparing joints with Ag and Cu interlayer weldments. The comparison between the corrosion resistance of the Ag and Cu interlayer weldments clearly shows that the Ag interlayer offers superior protection. The weldments with the Ag interlayer exhibited a higher E_{corr} and a lower corrosion i_{corr}, indicating better resistance to corrosion initiation and a slower corrosion rate. In contrast, the Cu interlayer weldments had a more negative corrosion potential and a higher corrosion current density, suggesting faster degradation in the corrosive environment. Additionally, the EIS results further indicated the enhanced performance of the Ag interlayer, showing higher Rp, which correlates with better corrosion resistance. The residual stress analysis also favors the Ag interlayer, as it induced

compressive stresses that further improve corrosion resistance, while the Cu interlayer resulted in tensile stresses, which can accelerate localized corrosion.

5.5 CONCLUSIONS

This study investigated the corrosion resistance and mechanical performance of laser-welded Ti6Al4V/AA7075 joints using Ag and Cu interlayers. Following conclusions can be drawn from this study:

- The Ag interlayer demonstrated better corrosion resistance than the Cu interlayer. The corrosion potential (Ecorr) of the Ag interlayer weldment was higher, and the corrosion current density (icorr) was lower, indicating reduced susceptibility to corrosion. The EIS results further showed that the Ag interlayer exhibited a higher charge transfer resistance (Rct) and oxide film resistance (Rfilm), contributing to its superior performance.
- The residual stress measurements revealed that the Ag interlayer induced significant compressive stresses on both the AA7075 and Ti6Al4V sides, which are beneficial in enhancing the joint's mechanical strength and corrosion resistance. In contrast, the Cu interlayer weldments exhibited tensile stresses, which can promote crack formation and accelerate corrosion processes.
- The Ag interlayer proved to be the better choice for dissimilar laser welding of Ti6Al4V and AA7075 alloys. It not only improved corrosion resistance, with a Rp of 7.079 $k\Omega \cdot cm^2$, but also exhibited compressive residual stresses that further protected the joint against environmental degradation.

CHAPITRE 6
ÉTUDE DES PROPRIÉTÉS NANOMÉCANIQUES ET DE LA RÉSISTANCE AU FLUAGE DES SOUDURES DISSEMBLABLES AA7075/TI-6AL-4V EN UTILISANT UN INTERCOUCHE EN CUIVRE DANS LE SOUDAGE AU FAISCEAU LASER

Titre en français du sixième article :

Étude des propriétés nanomécaniques et de la résistance au fluage des soudures dissemblables AA7075/Ti-6Al-4V en utilisant un intercouche en cuivre dans le soudage au faisceau laser.

Titre original (en anglais) :

Studying the nano-mechanical Properties and Creep Resistance of Dissimilar AA7075/Ti-6Al-4V Weldments Using a Cu Interlayer in Laser Beam Welding.

Auteurs et affiliation :

Asim Iltaf : Étudiant au doctorat, Département de mathématiques, d'informatique et de génie, Université du Québec à Rimouski, Québec, Canada.
Noureddine Barka : Professeur, Département de mathématiques, d'informatique et de génie, Université du Québec à Rimouski, Québec, Canada.
Shayan Dehghan : Chercheur post-doctoral, Département de mathématiques, d'informatique et de génie, Université du Québec à Rimouski, Québec, Canada.

État de l'article :

Soumis.

Revue :

The Journal of Materials Engineering and Performance

Résumé en français du sixième article

Cette recherche étudie le soudage au faisceau laser des alliages dissemblables AA7075 et Ti6Al4V en utilisant un intercouche en cuivre, en se concentrant sur les propriétés nanomécaniques et le comportement au fluage du joint soudé. L'étude vise à évaluer l'efficacité de l'intercouche en cuivre pour minimiser la formation de composés intermétalliques fragiles et améliorer les propriétés mécaniques du joint. Des tests de nanoindentation ont été réalisés pour mesurer la nanodureté, le module d'élasticité et le déplacement de fluage dans différentes régions de la soudure, y compris les zones affectées thermiquement, les zones fondues et l'interface cuivre/Ti6Al4V. L'analyse du nanofluage a révélé des différences significatives de déplacement à travers le joint, avec un déplacement maximal dans la zones affectées thermiquement de l'AA7075 (~176 nm) et un déplacement minimal à l'interface cuivre/Ti6Al4V (~121 nm). Le taux de déformation de fluage a été évalué à l'aide d'un modèle en loi de puissance, démontrant que le fluage diffusif dominait dans la zone mixte, tandis que le glissement des joints de grains et le fluage par dislocation étaient observés dans les régions de l'AA7075. La microscopie à force atomique a confirmé des variations dans la profondeur d'indentation et la morphologie de surface, mettant en évidence le rôle de l'intercouche en cuivre dans l'influence du comportement mécanique de la soudure. Dans l'ensemble, cette étude démontre le potentiel de l'utilisation d'un intercouche en Cu pour améliorer la résistance, la résistance au fluage et la performance globale des joints dissemblables entre les alliages AA7075 et Ti-6Al-4V.

Studying the nano-mechanical Properties and Creep Resistance of Dissimilar AA7075/Ti-6Al-4V Weldments Using a Cu Interlayer in Laser Beam Welding

Asim Iltaf [a, *], Noureddine Barka [a], Shayan Dehghan [a]

[a] Department of Mathematics, Computer Science and Engineering, University of Quebec at Rimouski, Rimouski, QC G5L 3A1, Quebec, Canada.

[*]Corresponding author (Asim Iltaf): Department of Mathematics, Computer Science and Engineering, University of Quebec at Rimouski, Rimouski, QC G5L 3A1, Quebec, Canada.

E-mail address: asim.iltaf@uqar.ca

Abstract

This research investigates the laser beam welding (LBW) of dissimilar AA7075 and Ti6Al4V alloys using a copper (Cu) interlayer, focusing on the nanomechanical properties and creep behavior of the welded joint. The study aims to evaluate the effectiveness of the Cu interlayer in minimizing the formation of brittle intermetallic compounds (IMCs) and enhancing the joint's mechanical properties. Nanoindentation testing was conducted to measure nanohardness, elastic modulus, and creep displacement in various regions of the weld, including the heat-affected zones (HAZ), fusion zones (FZ), and the Cu/Ti6Al4V interface. Nanocreep analysis revealed significant differences in displacement across the joint, with maximum displacement occurring in the AA7075 HAZ (~176 nm) and minimum displacement in the Cu/Ti6Al4V interface (~121 nm). The creep strain rate was evaluated using a power-law model, demonstrating that diffusional creep dominated in the mix zone, while grain boundary sliding, and dislocation creep were observed in the AA7075 regions. Atomic force microscopy (AFM) confirmed variations in the indentation depth and surface morphology, highlighting the role of the Cu interlayer in influencing the weld's

mechanical behavior. Overall, this study demonstrates the potential of using a Cu interlayer to enhance the strength, creep resistance, and overall performance of dissimilar joints between AA7075 and Ti-6Al-4V alloys.

***Keywords*:** Dissimilar laser welding, microstructure, nanoindentation, nanomodules, nanocreep

6.1 INTRODUCTION

Recent scientific and technological advancements in material joining techniques have revolutionized the approach engineers and designers take to combine different materials. This progress has led to the exploration of new structural design concepts that leverage the unique properties of various components, rather than depending solely on similar materials. As a result, it's now possible to create components and structures with improved mechanical performance while simultaneously reducing their weight. This marks a significant advancement in the development of more sustainable mechanical systems. Industries such as automotive and aerospace, which are dedicated to reducing vehicle weight, have increasingly adopted lightweight materials like fiber-reinforced polymers, aluminum, and titanium alloys. These materials are key to producing lighter, safer, and more environmentally friendly vehicles, contributing to a more sustainable transportation industry through the continuous enhancement of product efficiency (A et al., 2022; Batistão et al., 2020; Correia et al., 2021).

However, the differences between the materials being joined have introduced additional challenges. The growing use of multi-material combinations for lightweight designs has created a need for technologies that can reliably join these dissimilar materials. Due to the physical and chemical differences between these materials, their compatibility and weldability often decrease, which can compromise their ability to be successfully joined (Jandaghi et al., 2020, 2021).

Traditionally, mechanical fastening, adhesive bonding, or a combination of these methods have been used to join dissimilar materials (Amancio-Filho & Dos Santos,

2009). However, these techniques come with certain drawbacks, such as requiring multiple processing steps, which increases both time and assembly costs. Additionally, they often necessitate pre- or post-treatment of the workpieces and can introduce stress concentration areas around fastening holes, making these joining methods less advantageous. Additionally, Conventional welding processes are often impractical for joining dissimilar metal alloys, primarily due to metallurgical differences that result in the formation of brittle intermetallic phases, which weaken the mechanical performance of the joints. Therefore, there is a need to utilize alternative technologies. Among the various joining methods, laser fusion welding has gained widespread attention due to its distinct advantages, including higher energy density, minimal material wear in non-contact processing, and greater precision (S. Chen, Li, Chen, & Huang, 2011a; Z. Wang et al., 2020b).

Zhang et al. (J. Zhang et al., 2022) employed dual laser-beam bilateral synchronous welding-brazing to achieve Ti/Al butt joints, reporting that the welding heat input and heat distribution determined the morphology, composition, and thickness of the intermetallic compounds (IMCs). Liu et al. (S. Liu et al., 2022c) used AA4047 filler in YAG pulse laser welding for Ti-6Al-4V and AA7075 alloys, observing the formation of two IMC layers: TiAl adjacent to the Ti-6Al-4V and $TiAl_3$ next to the fusion zone. Li et al. (P. Li, Lei, Zhang, & Chen, 2020d) studied the impact of Si content in solder filler on interfacial reactions and mechanical properties of laser welded-brazed Ti/Al joints, finding that adding Si to the filler metal increased joint strength. Gu et al. (Gu et al., 2021b) utilized an Nb plate in laser welding of TC4 Ti alloy and 6082 Al alloy by offsetting the pulsed laser beam, noting that two types of metallurgical joining interfaces were formed with the appropriate offset distance and laser heat input. Zhang et al. (Z. Zhang et al., 2021) added a W mesh plate in the laser welding-brazing of Ti6Al4V to A6061, identifying second-phase $Al_5(W)$ and $Al_{18}Mg_3W_2$ in the Al weld, with $Al_3(Ti,W)$ and $(Al,Si)_3Ti$ layers at the Ti/Al interface, which improved joint performance. However, despite being a green manufacturing process, laser beam generation consumes significant energy, as the electro-optical

conversion efficiency of the laser source is typically around 30% (C. Li et al., 2010). Reducing the energy consumption of laser processing for energy-saving production is therefore crucial. Wei et al. (Wei et al., 2015) conducted butt welding of DP800 galvanized steel using preheated filler wire, achieving a 16% energy savings. Zhou et al. (J. Zhou et al., 2021) applied a magnetic field to assist magnesium/aluminum laser welding, finding that it improved heat and mass transfer during welding, thereby enhancing the thermal efficiency of laser energy. Despite these effective approaches, their application is limited due to the complexity and poor process flexibility of these measures.

Additionally, significant residual stresses caused by differences in chemical composition, thermal conductivity, melting points, and metallurgical incompatibility can all impact the creep performance of the dissimilar joints (Klueh et al., 1983). Since microstructural features like interfaces and the fusion zone (FZ) are typically only a few microns in size, conventional creep testing cannot effectively measure the creep deformation in individual zones. Therefore, a nanoindentation method has been employed to assess the creep deformation behavior of these weldments. Song et al. (Y. Song et al., 2020a) utilized nanoindentation to explore the creep mechanisms in different zones of SA508Gr3 steel weldments, finding that dislocation activity could play a major role in the creep deformation based on strain rate sensitivity measurements. Similarly, Gao et al. (Zengliang et al., 2020d) observed that P92 steel joints, particularly in the fine-grained heat-affected zones, exhibited lower hardness and reduced creep resistance compared to other joint regions under creep–fatigue loading. However, nanoindentation has yet to be used to investigate the creep deformation mechanisms in Ti and Ni weldments.

In this study, the nanoindentation technique was applied to determine the creep mechanism in different zones of a laser welded AA7075/Cu/Ti6Al4V joint. Additionally, nanohardness (H) and elastic modulus (E) mappings were conducted to investigate the diffusion of Cu into AA7075 and Ti6Al4V.

6.2 EXPERIMENTAL PROCEDURE

AA7075 and Ti-6Al-4V annealed sheets, each measuring 80 x 50 x 1.6 mm, were joined using the laser beam welding (LBW) method. An Ag interlayer was placed between the AA7075 and Ti-6Al-4V sheets. Optimal laser welding parameters were identified through preliminary experiments and are detailed in **Table 6.1**. The chemical compositions of these alloys, as analyzed by EDS, are provided in **Table 6.2** and **Table 6.3**. To ensure the reproducibility and reliability of the results, three specimens were produced, and these samples were used to confirm the consistency of the mechanical properties. Wire electrical discharge machining (EDM) was utilized to prepare samples for nanoindentation and metallographic analysis. The welded specimens for microstructural and nanoindentation evaluations were mounted and polished with SiC paper, progressing from 220 to 4000 grit sizes. A final polishing was performed using 0.25 mm diamond paste on a microcloth. The polished samples were then examined with an Olympus BH2-UMA optical microscope to evaluate the grain morphology in the microstructure.

Tableau 6.1 Optimal laser welding parameters for joining AA7075 and Ti6Al4V dissimilar alloys with a Cu interlayer.

Laser power (kW)	Welding speed (mm/sec)	Focal length (mm)	Focal spot diameter (mm)
3	40	310	150

Tableau 6.2 Chemical analysis of AA7075 BA alloy (wt. %) using Energy Dispersive X-ray Spectroscopy (EDS).

Zn	Si	Mg	Fe	Cu	Mn	Cr	Al

4.21	0.71	0.62	0.37	0.21	0.22	0.06	Bal.

Table 6.3 Chemical composition analysis of Ti6Al4V BA alloy (wt. %) using EDS.

Al	**V**	**Fe**	**Sn**	**Nb**	**C**	**Zr**	**Si**	**Ti**
5.63	4.35	0.18	0.05	0.03	0.25	0.03	0.05	Bal.

Nanoindentation tests at room temperature were performed using a nanoindenter in load-controlled mode. The elastic modulus and nanohardness of the specimens were measured by applying a constant load of 200 mN with a Berkovich tip, with maximum load and strain rate set to 200 mN and 0.1 s^{-1}, respectively. To evaluate changes in creep depth over time, the indentation tip was held in position for 200 seconds. Drift velocity was monitored by reducing the load to 90% and decreasing the hold time to 40 seconds. After the indenter was unloaded from the sample surface, the nanohardness and elastic modulus values were calculated using established methods (Oliver & Pharr, 1992d). Furthermore, the nanoindentation strain rate was calculated using the method as indicated in Equation (1)(Oliver & Fabes, 1995).

$$Creep\ strain\ rate\ (\varepsilon') = \frac{Rate\ of\ indentation\ depth}{Indentation\ depth} = \frac{h'}{h} = \left(\frac{1}{h}\right) \times \left(\frac{dh}{dt}\right) \quad (1)$$

After determining the creep strain rate as outlined in reference (X. Liu et al., 2016), the empirical creep model presented in Equation (2) was employed to fit the indentation depth rate data to the experimentally observed creep rate. The corresponding formula is:

$$h = h_i + a(t - t_i)^{(1/2)} + b(t - t_i)^{(1/4)} + c(t - t_i)^{(1/8)} \quad (2)$$

In this formula, 't' represents the duration allocated for creep, 'h' indicates the depth of indentation made by the indenter, and the remaining variables are the

parameters optimized for the best fit. After applying this empirical model, the creep stress during the indentation holding phase was calculated using Equation (3). This equation is derived from various published sources (Hu et al., 2015c; Lucas & Oliver, 1999; Nguyen et al., 2019c; Oliver & Pharr, 1992d; Y. Song et al., 2020c; Su et al., 2013a; Zengliang et al., 2020c).

$$\sigma = \left(\frac{H}{3}\right)\left(\frac{h_{max}}{h}\right) \quad (3)$$

In Equation (3), h_{max} represents the maximum loading depth, h is the instantaneous indentation depth, and σ denotes the indentation creep stress. The power-law relationship is specifically used to estimate the creep stress exponent during the steady or secondary creep phase. This correlation between stress and creep strain rate is well-established in the literature as an effective method for analyzing creep behavior at room temperature. The expression for this power-law relationship is provided in Equation (4) as detailed by reference (Su et al., 2013b):

$$\varepsilon' = k\sigma^n \quad (4)$$

In this context, the stress exponent 'n' is determined by measuring the slope of the plotted graph of the creep strain rate ε'against the indentation creep stress σ, as described in Equation (4). Additionally, atomic force microscopy (AFM) was employed to examine the indentation depth and surface morphology of the weldments.

6.3 RESULTS AND DISCUSSION

6.3.1 Visual representation of the joints

Figure 6.1 presents representative images of the weld bead's top and bottom surfaces, showing that the weld bead was free of contamination and had a bright appearance. It is well-known that titanium and aluminum alloys tend to react with

atmospheric oxygen at high temperatures during welding, leading to oxide formation that can deteriorate weld joint quality, as referenced in studies (Baruah & Bag, 2016b, 2016a, 2017). The degree of oxidation in the weld pool can be inferred from the color of the bead. The bright, silvery appearance of the weld bead in **Figure 1**, as opposed to blue or purple hues, suggests minimal contamination in the weld pool (Lathabai et al., 2001; X. Li et al., 2005).

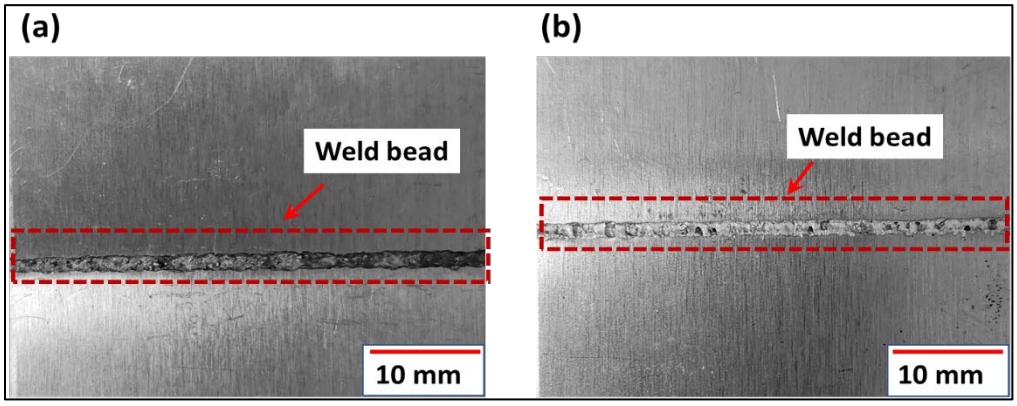

Figure 6.1 Visual appearance of the weldment with a Cu interlayer: (a) the top surface of the weldment, and (b) the bottom surface of the weldment.

6.3.2 Microstructure evaluation

As explained in our previously published study (Iltaf, Dehghan, et al., 2024) — which is necessary for understanding the nanocreep analysis discussed later in this paper—**Figure 6.2** illustrates the cross-sectional microstructure of a dissimilar butt joint between AA7075 and Ti6Al4V, using laser welding with a Cu interlayer. The joint comprises three key regions: the AA7075 FZ, the mix zone, and the Ti6Al4V/Cu interface. There is minimal melting of the titanium alloy, resulting in a flat joint interface (Moon et al., 2024). Minimizing the melting of titanium during welding is crucial because it reduces the mixing of titanium and aluminum atoms, thereby significantly lowering the likelihood of forming brittle Ti/Al intermetallic compounds. Maintaining the properties of the base materials leads to a stronger and more ductile

weld joint, maintaining the integrity and performance of the original materials. Therefore, the current investigation focused on the interactions between AA7075 and Cu, as well as Ti6Al4V and Cu. The joint formation primarily occurs at the AA7075/Cu and Ti6Al4V/Cu interfaces due to the formation of a eutectic liquid and the limited diffusion of Cu into Ti6Al4V, respectively. Copper diffuses into the AA7075 alloy, creating a significant diffusion zone within the AA7075 and adjacent to the mix zone (**Figure 6.2**(b)-I, II). Some minor discontinuous cracks are observed within the AA7075 FZ (**Figure 6.2** (b)-II). The minimal impact of the current process on Ti6Al4V is also evident in **Figure 6.2** (b)-III. In LBW, rapid cooling rates lead to substantial local undercooling (Sonar et al., 2021). This phenomenon promotes faster nucleation and the development of fine grains and dendrites, as shown in **Figure 6.2** (b)-IV and V. The mix zone mainly consists of AA7075, Ti6Al4V, and Cu (**Figure 6.2** (b)-VI). Within this zone, a vanadium solid solution forms, contributing to a more robust joint. The vanadium solid solution enhances the joint's strength through several mechanisms. First, vanadium's distinct atomic size creates a size mismatch, causing lattice distortions that impede the movement of dislocations within the material. This resistance to dislocation motion increases the alloy's strength. Additionally, the presence of vanadium can lead to the formation of secondary phases or precipitates, which further obstruct dislocation movement and contribute to the overall strengthening effect. These mechanisms make vanadium a valuable element in alloy design for improved mechanical properties. **Figure 6.2** (b) also reveals the presence of porosity in the joint. Pore formation is a significant issue in LBW of 7xxx series alloys. This occurs due to small amounts of gas entering the laser-melted zone, leading to gas porosity. Hydrogen (H_2), which has high solubility in molten aluminum, is the primary cause of pore formation in this alloy. The H_2 originates from oxides or impurities in the filler and base materials, which then dissolve into the bulk material (Khalil et al., 2019). Porosity in LBW can manifest in various forms, including necking, swelling, and collapsing. The main cause of porosity is the inconsistent vaporization of volatile alloying elements like Zn and Mg, which have different vapor pressures.

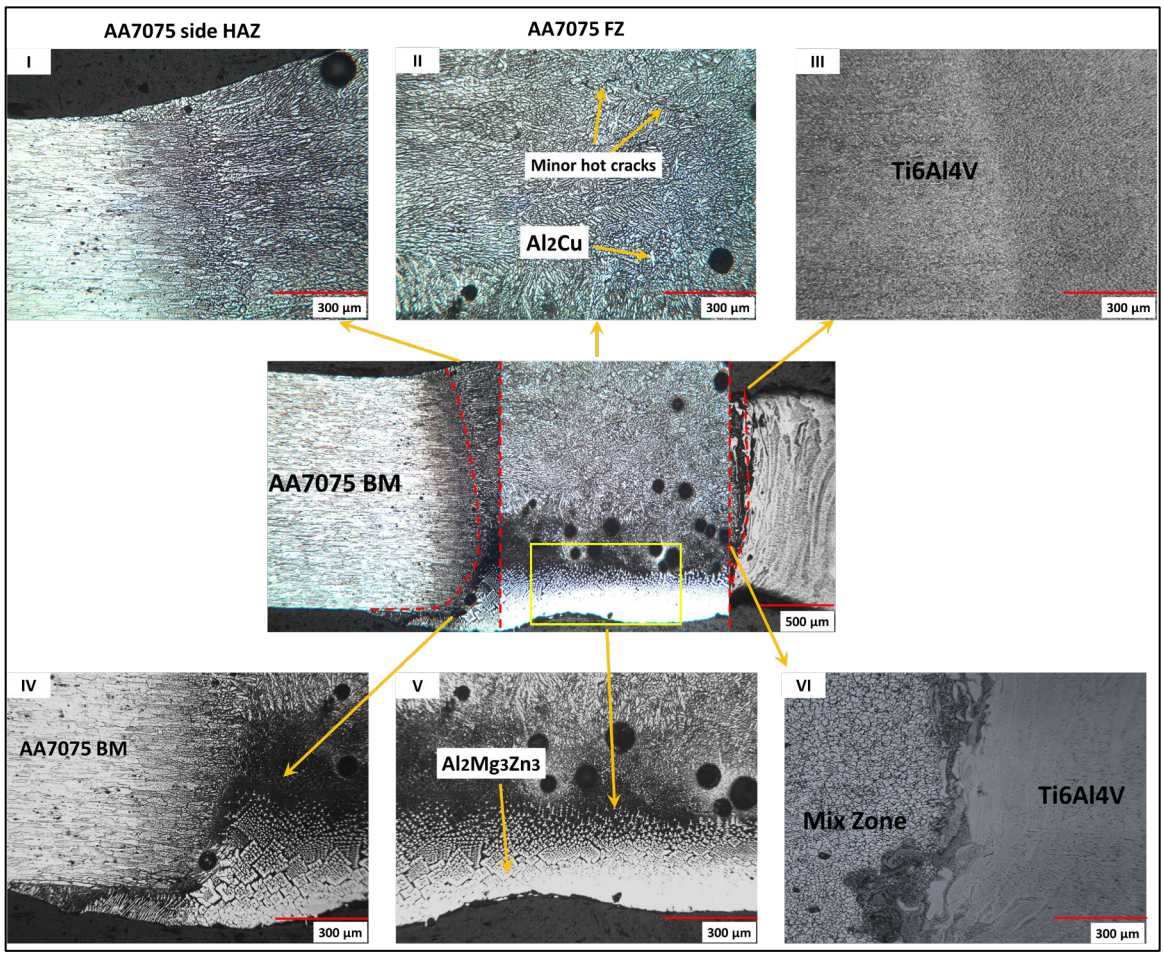

Figure 6.2 Optical images of microstructure of dissimilar joint of AA7075-Ti6Al4V with Cu interlayer (Iltaf, Dehghan, et al., 2024).

6.3.3 Nanoindentation study

The nanomechanical properties of all joint regions were evaluated at room temperature using nanoindentation. **Figure 6.3** shows the (a) placement of nanoindentations, (b) load-displacement (P-h) curves under a constant load of 200 mN, and (c) the nanohardness and elastic modulus of the weldments. The load-displacement

curve reflects both elastic and plastic deformations, following Kick's law ($P = Ch^2$, where C is a constant), as described by Hainsworth et al. (Hainsworth et al., 1996). The indentation process results in a combination of elastic-plastic loading and purely elastic unloading deformations, with variations in penetration depth likely due to microstructural changes during the solidification process in LBW (Hainsworth et al., 1996). Based on the P-h curves in **Figure 6.3(b)**, the AA7075 side HAZ and mix zone exhibited the highest penetration displacements of approximately 2941 nm and 2375 nm, respectively. Among all the joint regions, the maximum displacement was recorded in the AA7075 side HAZ (~2941 nm), while the minimum penetration depth was observed in the Cu/Ti6Al4V interface (~1231 nm). This variation in penetration depth may be related to the indentation effect influenced by the microstructure evolution, as discussed in Section 3.2. Furthermore, **Figure 6.3(c)** presents the nanohardness and elastic modulus values, calculated using the Oliver and Pharr method. Moving from the AA7075 HAZ to the Cu/Ti6Al4V interface, nanohardness increased from 1.37 GPa to 5.81 GPa. The lowest nanohardness value was observed in the AA7075 HAZ at 1.37 GPa, which can be attributed to the use of a Cu interlayer. The Cu interlayer reduces the formation of brittle IMCs and lead to the formation of solid solutions as discussed in section 3.2. Additionally, an increase in indentation depth at a constant load indicates lower nanohardness, possibly due to reduced dislocation density, as explained by Gale and Achuthan (Gale & Achuthan, 2014).

Regarding the elastic modulus, as shown in **Figure 6.3(c)**, an increase from 64.13 GPa to 73.22 GPa was observed from the AA7075 HAZ to the Cu/Ti6Al4V interface. However, a slight increase was noted from the in the mix zone and AA7075 FZ from the AA7075 HAZ. These fluctuations in elastic modulus values are linked to microstructural variations influenced by the use of the Cu interlayer, which affects the material's response to indentation forces.

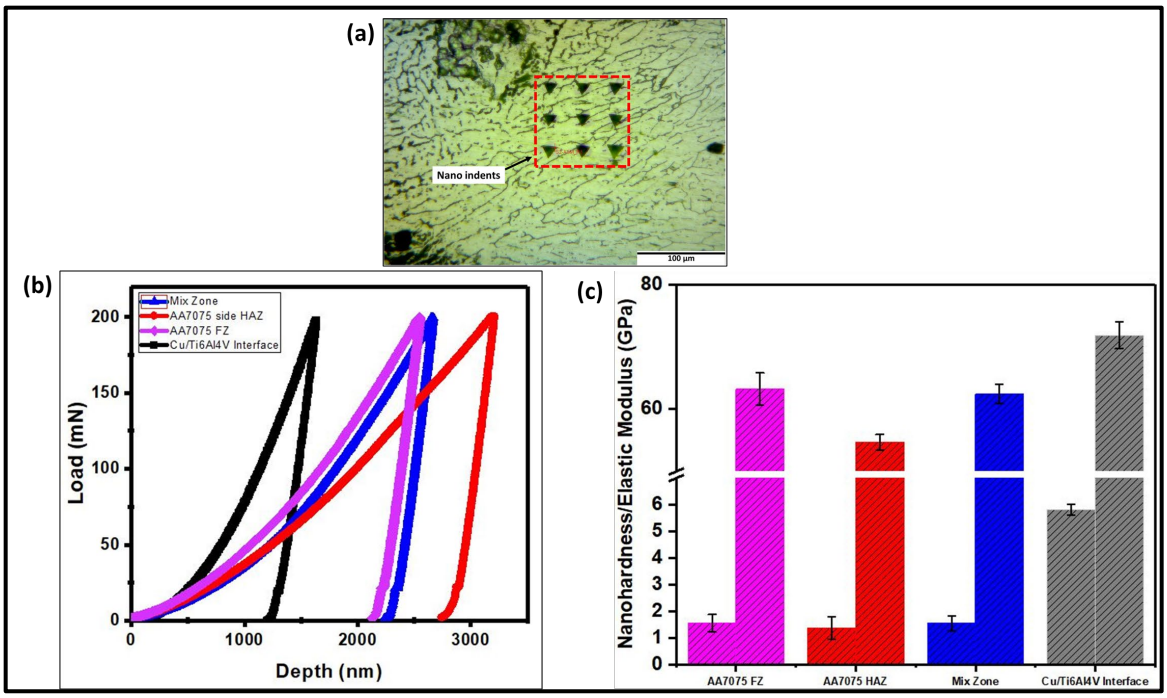

Figure 6.3. (a) Placement of nanoindentations, (b) Load-displacement (P-h) curves, and (c) nanohardness and elastic modulus measurements.

6.3.3.1 Nanocreep analysis

Figure 6.4(a) shows the load-displacement nanocreep curves for all weldment regions. The values indicate an increase in the indenter's penetration depth from approximately ~1631 nm in the Cu/Ti6Al4V interface to about ~2058 nm in the AA7075 HAZ. In **Figure 6.4**(b), depth-time (h-t) curves are presented based on nanoindentation data collected over a 200-second holding period for all weld zones and base alloys. These curves reveal an initial rapid increase in penetration depth as the maximum load of 200 mN is achieved within roughly 40 s, followed by a stabilization of the penetration depth upon reaching this peak load.

Throughout the 200 s holding period, notable depth plateaus were observed in each region and base alloy. The h-t curves derived from these plateaus are illustrated in **Figure 6.5**. The plateaus during the holding stage suggest an initial increase in

penetration depth before the maximum load is attained, as shown in **Figure 6.6**. This figure displays the modeled data (red line) alongside the experimental data (black line) for all weld zones. The maximum creep displacement was approximately ~176 nm in the AA7075 HAZ, while the minimum displacement was about ~121 nm in the Cu/Ti6Al4V interface. The creep displacements for mix zone and AA7075 FZ were approximately ~148 nm and ~141 nm, respectively. These values are lower than that of the AA7075 HAZ by 16% and 20%, respectively.

Moreover, using Equation (2), fitted curves (represented by the red line) were plotted against the experimental data (black line), as seen in **Figure 6.6**. These fitted curves closely align with the experimental results for all zones and base alloys. During the primary creep stage depicted in **Figure 6.6**, the indentation depth increased rapidly with holding time for each weldment zone. In the secondary creep stage, the penetration depth increased linearly over the 200 s holding time. Tertiary creep, which is common in conventional creep tests, does not occur in indentation creep because the hardness test is a compression test, and the specimen does not fracture (Mahmudi et al., 2013). In a creep test, elastic deformation refers to the initial, reversible strain a material experiences when stress is applied, following Hooke's Law and determined by the material's elastic modulus. This phase is typically brief and does not cause permanent changes to the material. In contrast, plastic deformation is the subsequent, irreversible strain under sustained stress, leading to permanent alterations in the material's structure. Initially, plastic deformation results in an increased strain rate due to dislocation movement. Over time, it reaches a steady state where strain hardening and recovery processes occur simultaneously, stabilizing the strain rate. The creep strain rate for all weld regions was calculated using Equation (1) and is presented in **Figure 6.7**. The results show a sharp decrease in creep strain rate at a constant load for each weldment zone, attributed to strain hardening from plastic deformation. After this initial decrease, the creep strain rate gradually declined and stabilized, characteristic of secondary or steady-state creep, due to simultaneous strain hardening and recovery within the joint (Oliver & Pharr, 1992e). **Figure 6.8** illustrates the relationship between stress and creep

strain rate during indentation for the all-weldment zones. The slope of the linear fit in this graph represents the creep stress exponent, providing insights into the material's creep resistance and behavior. Higher values of the creep stress exponent, as noted in **Table 6.4**, indicate better resistance to creep, consistent with the findings of Van Swygenhoven and Derlet (Van Swygenhoven & Derlet, 2001). Additionally, it was determined that the diffusional creep mechanism dominated only in the mix zone, as shown in **Figure 6.9**. Furthermore, grain boundary sliding was observed in the AA7075 HAZ. In contrast, the dislocation creep mechanism was evident in the AA7075 FZ, as their stress exponent values were slightly higher than 3 (**Table 6.4**). This higher stress exponent suggests increased dislocation generation and involvement in the deformation process during the 200 s holding time under constant load, as explained by Zhang et al. (W. D. Zhang et al., 2016). The generation of dislocations during loading is proportional to the applied load or indentation depth, and these dislocations form in the plastically deformed region beneath the indenter, as discussed by Almasri and Voyiadjis (Almasri & Voyiadjis, 2007). The AA7075 FZ exhibited a higher stress exponent compared to the other weld regions due to the formation of the solid solution and the suppression of formation of IMCs, which resulted in a high dislocation density beneath the indenter. This finding shows the complex relationship between microstructural evolution such as formation of solid solutions and less brittle IMCs and mechanical properties like creep behavior in dissimilar weldments of AA7075/Ti6Al4V with a Cu interlayer.

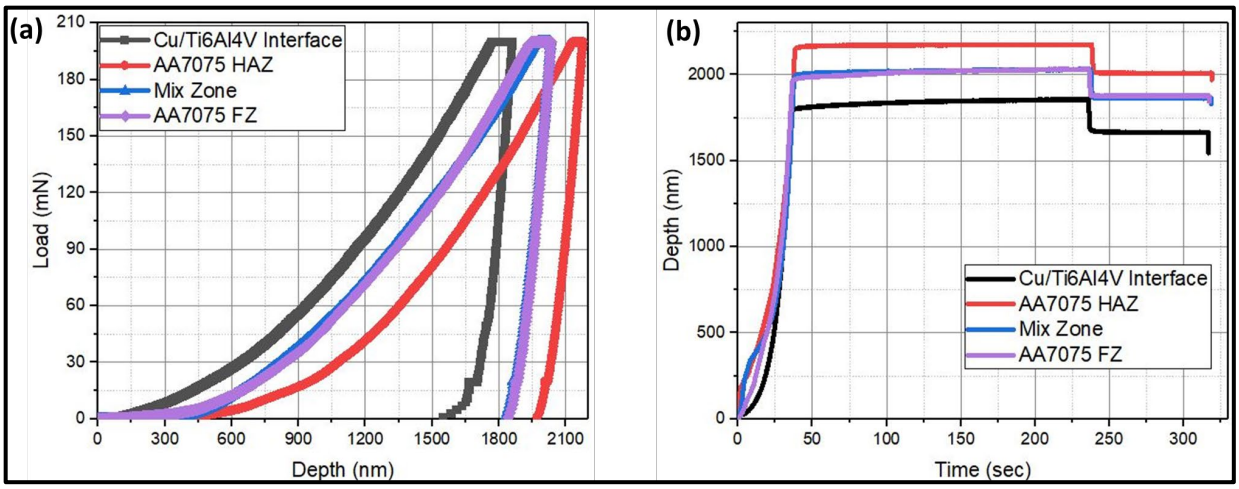

Figure 6.4 (a) Creep curves showing load versus displacement, and (b) Depth versus time graphs.

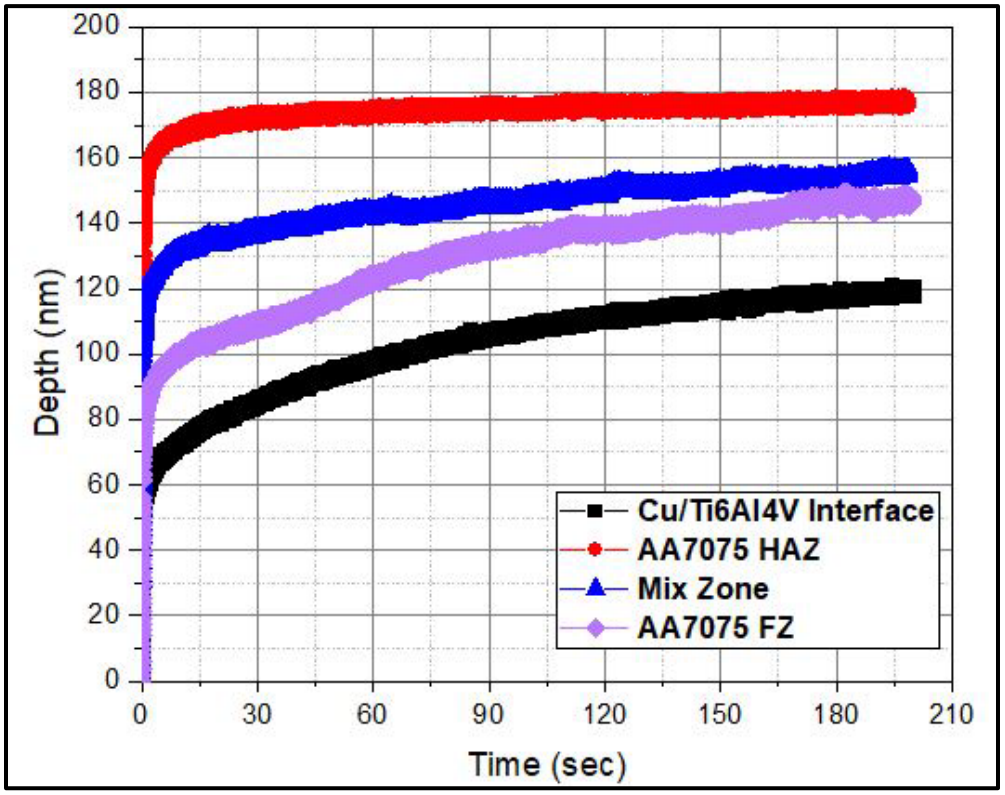

Figure 6.5 Displacement-time (h-t) curves for all the regions.

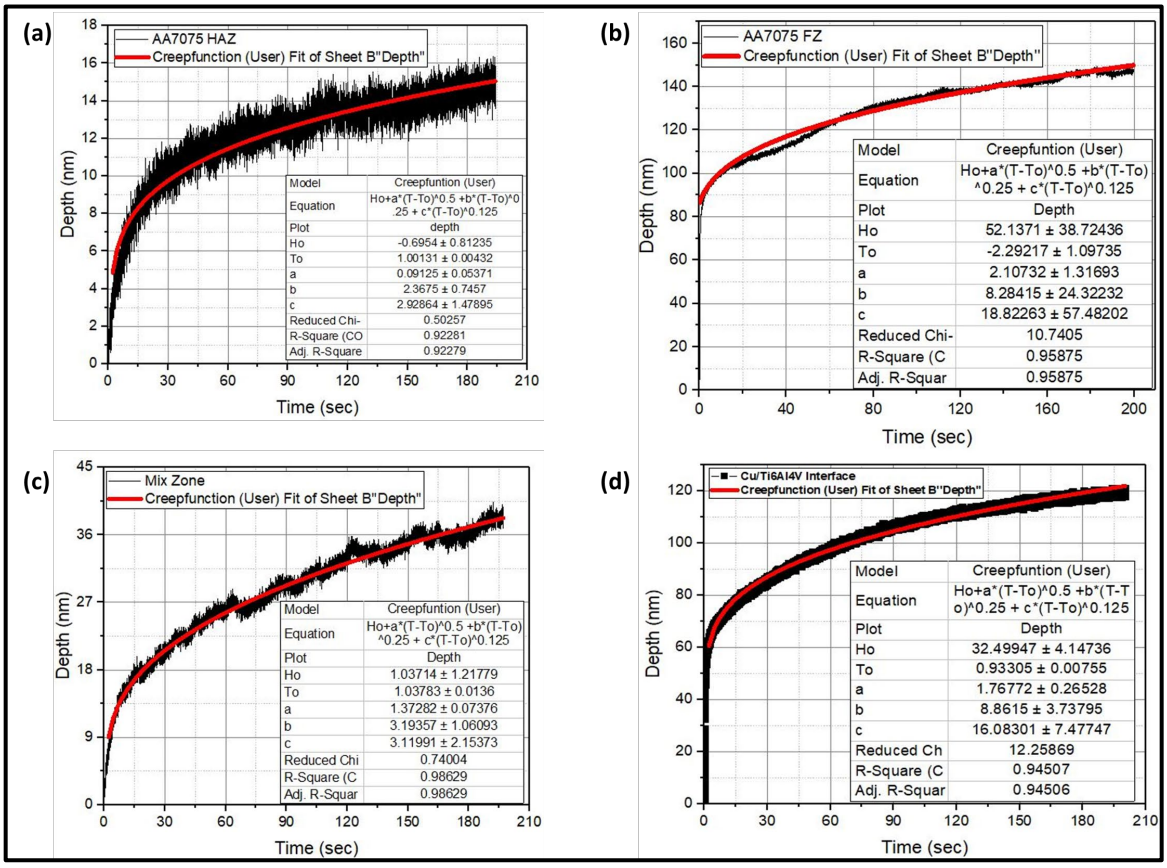

Figure 6.6 Modeled data (red line) alongside experimental data (black line), (a) AA7075 HAZ, (b) AA7075 FZ, (c) Mix zone and (d) Cu/Ti6Al4V interface.

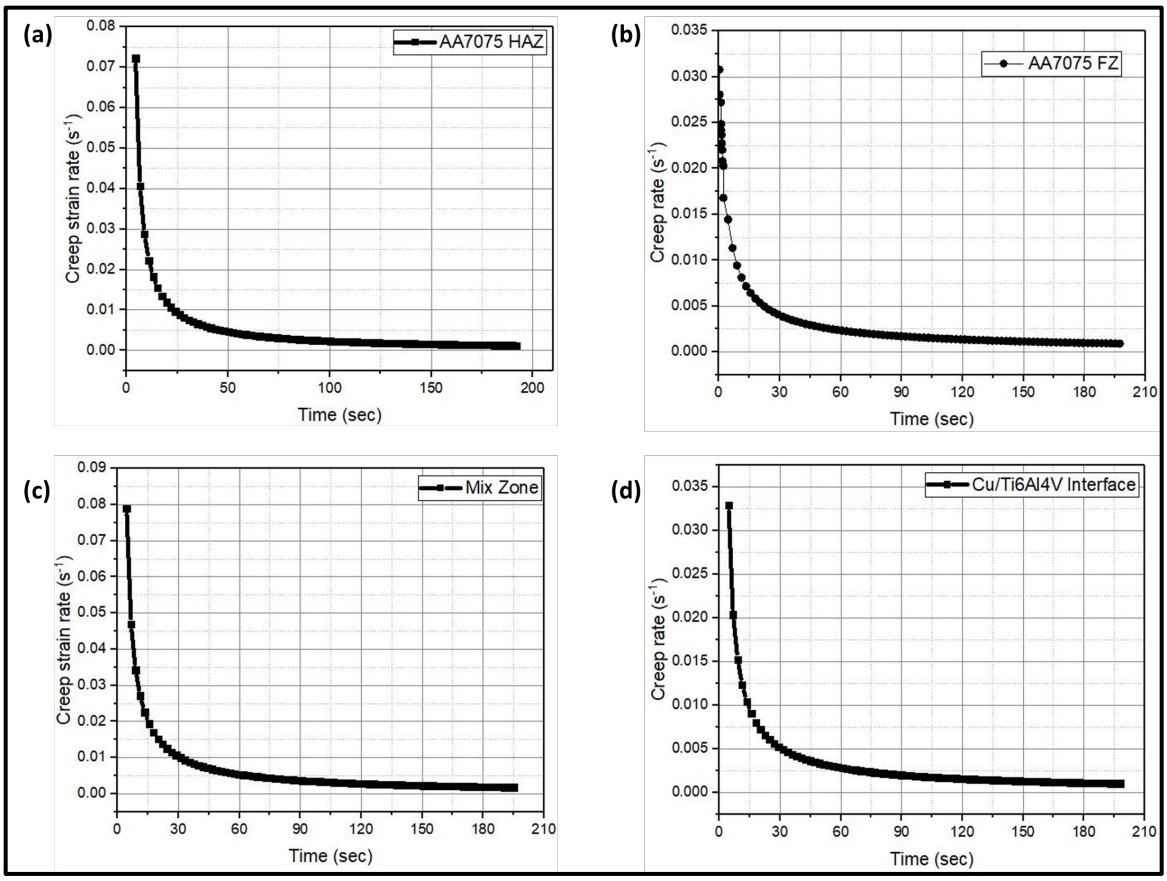

Figure 6.7 Curves showing the creep strain rate as a function of time for all regions of joint, (a) AA7075 HAZ, (b) AA7075 FZ, (c) Mix zone and (d) Cu/Ti6Al4V interface.

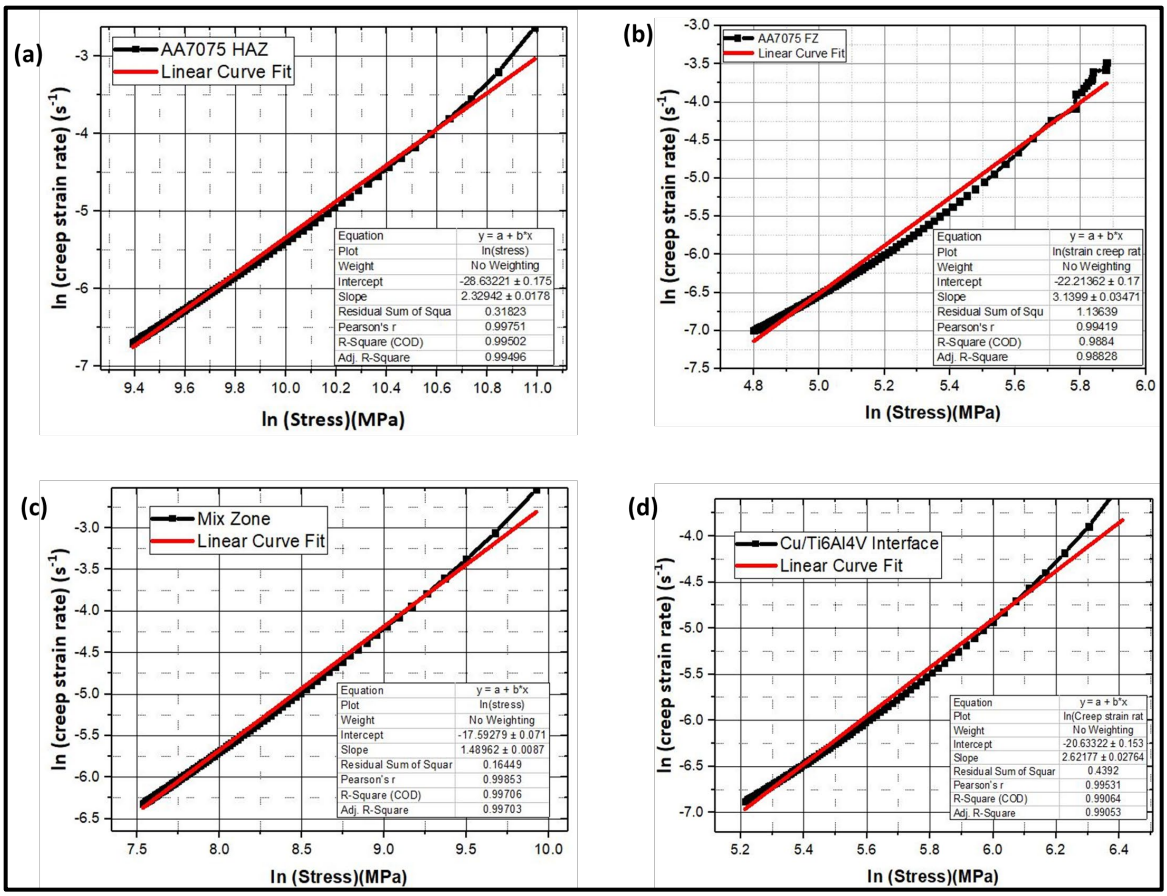

Figure 6.8 Modeled data (red line) alongside experimental data (black line) of curves depicting the relationship between creep strain rate and stress, (a) AA7075 HAZ, (b) AA7075 FZ, (c) Mix zone and (d) Cu/Ti6Al4V interface.

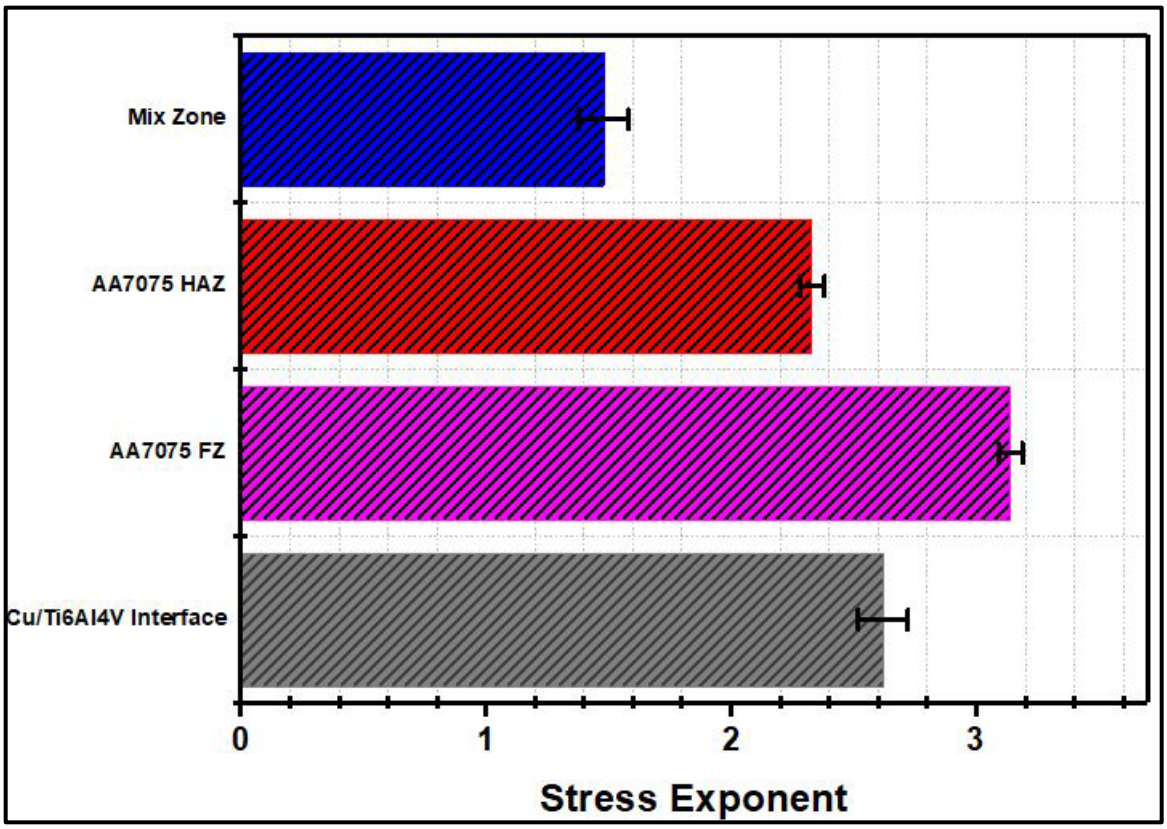

Figure 6.9 The creep stress exponent for each region of the joint.

Tableau 6.4 The creep stress exponent values are associated with creep mechanisms according to the findings of Van Swygenhoven and Derlet (Van Swygenhoven & Derlet, 2001).

S. No.	Creep stress exponent	Nanocreep mechanism
1	1-2	Diffusion creep
2	2-3	Grain boundary sliding
3	3-4	Viscous motion of dislocation

4	>4	Dislocation climb mechanism

6.3.3.2 Atomic force microscopy (AFM) analysis

When nanoindentation is performed, the material beneath the indenter displaces, causing pile-up and sink-in phenomena around the edges of the indent. This phenomenon is observed in AA7075 HAZ, mix zone, AA7075 FZ and Cu/Ti6Al4V interface through AFM analysis, as illustrated in **Figure 6.9**, **Figure 6.10**, **Figure 6.11** and **Figure 6.12**, respectively. These figures showcase 2-D AFM images alongside their corresponding line surface profiles, with side-view 3D mappings included as insets. The AFM images are color-coded topographical maps generated after nanoindentation. The central indent is highlighted by a color change, indicating variations in height due to the indentation. Surrounding the indent, a gradient of colors signifies changes in topography. The transition of colors illustrates the shift from the raised pile-up areas back to the original surface level. In **Figure 6.9(b)**, **Figure 6.10(b)**, **Figure 6.11(b)** and **Figure 6.12(b)**, the images with 3D insets provide a cross-sectional view of the indentation. Lines in these images represent profiles taken at various points across the indent. The deepest point corresponds to where the indenter penetrated the most, while the raised lines around it depict the height of the piled-up material. Using Gwyddion software, the depth of the indent and the height of the pile-up were measured to obtain quantitative data on how the material responds to indentation. Consequently, the indentation depth in the AA7705 HAZ region (**Figure 6.9**) is deeper compared to other regions of the weldment. This indicates that the AA7705 HAZ material undergoes a higher degree of plastic deformation during nanoindentation.

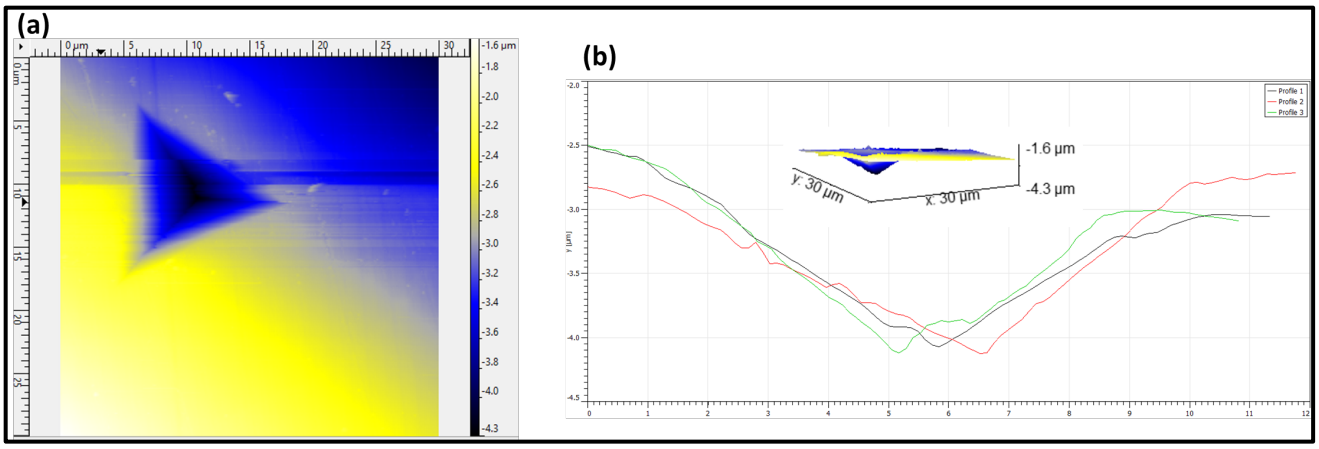

Figure 6.10 The 2-D image on the left and the 3-D images (shown in the inset on the right) illustrate the nanoindentation indent, along with the depth measurement profiles of AA7075 HAZ

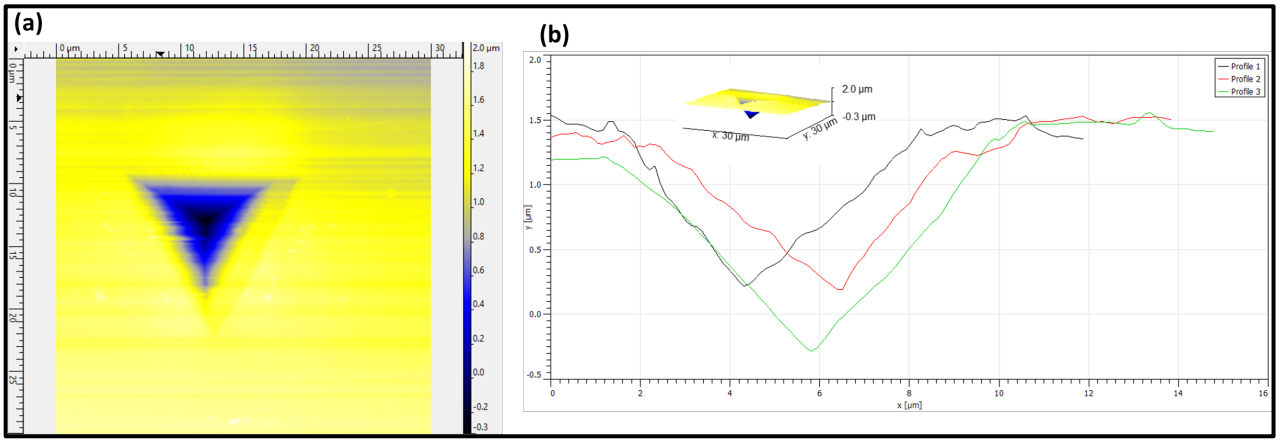

Figure 6.11 The 2-D image on the left and the 3-D images (shown in the inset on the right) illustrate the nanoindentation indent, along with the depth measurement profiles of mix zone

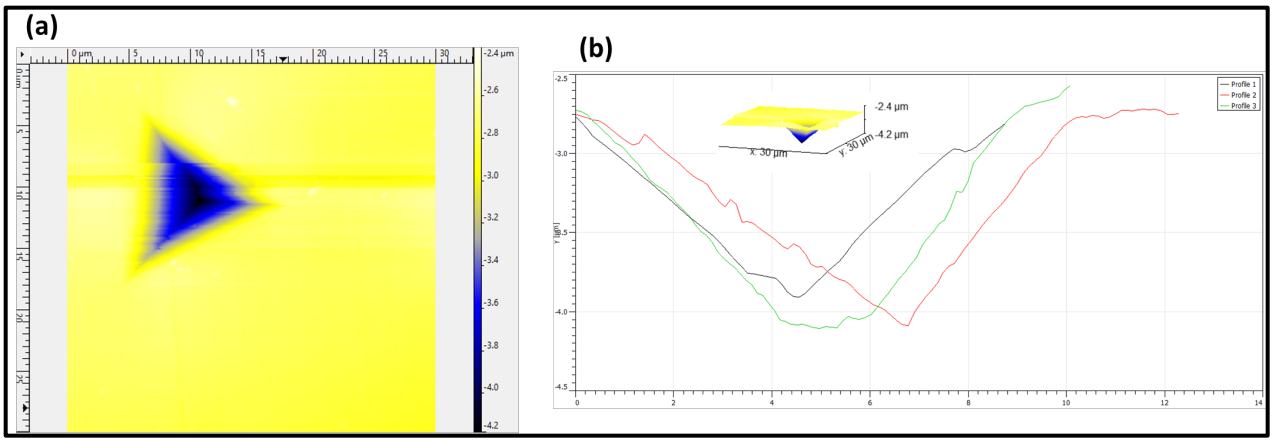

Figure 6.12 The 2-D image on the left and the 3-D images (shown in the inset on the right) illustrate the nanoindentation indent, along with the depth measurement profiles of AA7075 FZ

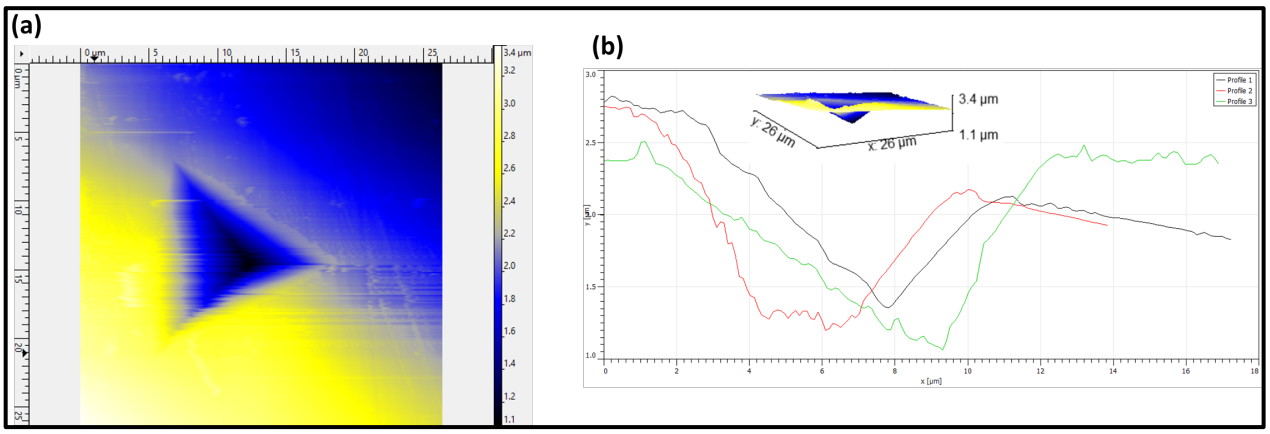

Figure 6.13 The 2-D image on the left and the 3-D images (shown in the inset on the right) illustrate the nanoindentation indent, along with the depth measurement profiles of Cu/Ti6Al4V interface

6.4 COMPARISON OF CU AND AG WELDMENTS

In our previous study, I explored the use of an Ag interlayer in dissimilar laser welding of AA7075 alloy and Ti6Al4V alloy(Iltaf, Barka, et al., 2024). The Ag

interlayer effectively minimized the formation of brittle IMCs between the AA7075 alloy and Ti6Al4V, enhancing weld quality through the formation of Ag_2Al and Al_3Ti phases. This led to increased microhardness and reduced creep displacement in the FZ. Additionally, the Ti6Al4V HAZ exhibited the highest hardness due to the formation of martensitic α-phase. Nanocreep analysis revealed that dislocation climb was the dominant creep mechanism in the Ti6Al4V regions, while diffusional creep prevailed in the AA7075 regions. Overall, the use of the Ag interlayer provided superior creep resistance in the FZ.

In the current study, I investigated the effect of a Cu interlayer on the same dissimilar weld joint. The Cu interlayer was successful in reducing Ti/Al interactions, thereby minimizing the formation of brittle IMCs and improving the mechanical properties of the weld. The highest hardness and elastic modulus were observed at the Cu/Ti6Al4V interface. Significant differences in nanocreep behavior were noted across various zones of the joint, including the AA7075 HAZ and the FZ. In conclusion, both Ag and Cu interlayers effectively mitigate the formation of brittle IMCs in dissimilar laser welding of AA7075 and Ti6Al4V alloys. However, the Ag interlayer offers overall better performance due to its superior creep resistance in the FZ. In contrast, the Cu interlayer provides improved creep resistance specifically at the Cu/Ti-6Al-4V interface. Therefore, the choice between Ag and Cu interlayers should be guided by the specific application requirements.

6.5 CONCLUSIONS

This study investigated the laser welding of dissimilar AA7075 and Ti6Al4V alloys using a Cu interlayer, focusing on the nanomechanical properties and creep behavior of the joint. Following conclusions are drawn from the current study:

1. The microstructure varied across the joint, with the Cu interlayer promoting solid solution formation in the AA7075 and minimizing melting on the Ti6Al4V side, preventing brittle intermetallics. The rapid cooling led to fine

grain structures, particularly in the mix zone, improving strength and creep resistance. The Cu interlayer effectively controlled diffusion, enhancing overall joint performance.

2. The nanohardness varied significantly across the joint, with the lowest value of 1.37 GPa in the AA7075 HAZ and the highest value of 5.81 GPa at the Cu/Ti6Al4V interface. This variation demonstrates the strengthening effect of the Cu interlayer, which reduced the formation of brittle intermetallic compounds (IMCs) and enhanced hardness at the interface.
3. The elastic modulus showed a similar trend, increasing from 64.13 GPa in the AA7075 HAZ to 73.22 GPa at the Cu/Ti6Al4V interface. This increase in stiffness indicates improved mechanical performance at the Cu/Ti interface, influenced by the interlayer's ability to control the diffusion of elements and microstructure.
4. Creep displacement was highest in the AA7075 HAZ (~176 nm) and lowest at the Cu/Ti6Al4V interface (~121 nm). The reduced displacement at the interface reflects the enhanced creep resistance provided by the Cu interlayer, while the HAZ exhibited more significant deformation under stress due to its lower hardness.
5. The creep stress exponent varied across the welded joint, with dislocation creep dominating in the AA7075 HAZ and FZ, while grain boundary sliding was prominent at the Cu/Ti6Al4V interface. The mix zone showed the lowest stress exponent, indicating diffusional creep. These variations demonstrate the Cu interlayer's role in enhancing creep resistance at the Ti6Al4V interface, while the AA7075 regions, particularly the HAZ, exhibited lower resistance to creep due to higher dislocation activity.
6. Atomic force microscopy (AFM) analysis revealed significant differences in indentation depth and surface morphology across the weld regions. The AA7075 HAZ exhibited the deepest indentations, indicating higher plastic deformation, while the Cu/Ti6Al4V interface showed minimal deformation.

These findings confirm the role of the Cu interlayer in enhancing the joint's resistance to plastic deformation and maintaining surface integrity across the weld.

CONCLUSION GÉNÉRALE

Cette recherche porte sur le soudage laser d'alliages dissemblables, en particulier l'alliage d'aluminium AA7075 et l'alliage de titane Ti6Al4V, en utilisant argent et le cuivre comme intercouches. L'étude évalue l'impact de ces intercouches sur les caractéristiques microstructurales, les performances mécaniques, la résistance à la corrosion et le comportement en fluage à l'échelle nanométrique. L'objectif principal est d'améliorer les propriétés de ces soudures, notamment dans des secteurs comme l'aérospatiale, où le rapport résistance/poids, la résistance à la corrosion et la stabilité mécanique à long terme sous contrainte sont essentiels. Le soudage laser, choisi pour sa précision, réduit les défauts et la formation de composés intermétalliques fragiles, qui représentent un défi majeur lors de l'assemblage de matériaux dissemblables tels que l'aluminium et le titane. Les résultats établissent un lien direct entre les matériaux d'intercouche et les performances globales des joints.

Propriétés mécaniques

L'un des principaux défis dans le soudage de ces matériaux est la formation de composés intermétalliques fragiles, notamment à l'interface des deux alliages, qui affaiblissent le joint. Le joint avec l'intercouche en argent s'est avéré très efficace pour minimiser la formation de composés intermétalliques indésirables tels que Al_3Ti et $TiAl_3$ dans la zone fondue. Ces phases sont généralement fragiles et peuvent affecter négativement les performances mécaniques du joint. En limitant la formation de ces phases, l'intercouche en argent a contribué à stabiliser la microstructure, ce qui a entraîné une augmentation globale des propriétés mécaniques, rendant le joint plus résistant à la déformation et à la rupture sous charge. Le joint avec l'intercouche en cuivre a également apporté des avantages en réduisant l'interaction titane/aluminium, mais il a favorisé la formation de composés intermétalliques à base de cuivre, en particulier Cu_3Ti_2 à l'interface Ti6Al4V/Cu. Ces composés intermétalliques à base de cuivre étaient moins fragiles que les phases Al_3Ti et $TiAl_3$, ce qui a amélioré les

propriétés mécaniques à l'interface. Cependant, cela a eu un coût : l'interface cuivre/Ti6Al4V a montré une fragilité légèrement supérieure à celle du joint avec l'intercouche en argent.

Analyse des contraintes résiduelles

L'analyse des contraintes résiduelles dans cette étude a montré une variation significative entre les intercouches argent et cuivre dans les joints soudés au laser des alliages AA7075 et Ti6Al4V. Les joints avec intercouche en argent ont induit des contraintes résiduelles compressives des deux côtés de la soudure, à savoir AA7075 et Ti6Al4V, ce qui est avantageux pour améliorer à la fois la résistance mécanique et la résistance à la corrosion. Plus précisément, les contraintes résiduelles compressives étaient les plus élevées près de la ligne médiane de la soudure, diminuant progressivement à mesure que l'on s'éloigne de la soudure. Cette nature compressive réduit le risque d'initiation et de propagation des fissures, contribuant ainsi à améliorer l'intégrité structurelle et à prolonger la durée de vie du joint. En revanche, les joints avec intercouche en cuivre ont généré des contraintes résiduelles en traction, ce qui est moins favorable, car les contraintes de traction peuvent favoriser la formation de fissures et la corrosion localisée, compromettant ainsi potentiellement la performance à long terme de la soudure.

Résistance à la corrosion

La résistance à la corrosion est un facteur crucial pour déterminer la fiabilité à long terme des joints soudés, notamment dans des secteurs comme l'aérospatiale, où l'exposition à des conditions environnementales sévères est courante. Le joint soudé avec intercouche en argent a montré une résistance à la corrosion supérieure, en particulier dans la zone fondue. Cette amélioration des performances est attribuée à la suppression des composés intermétalliques fragiles, qui sont souvent plus sujets à la corrosion. En minimisant la formation des composés intermétalliques, qui peuvent agir

comme des sites d'initiation de la corrosion, l'intercouche en argent a contribué à maintenir l'intégrité structurelle du joint dans des environnements corrosifs. Bien que l'intercouche en cuivre ait également amélioré la résistance à la corrosion, ses performances étaient légèrement inférieures à celles de l'intercouche en argent. La phase Cu_3Ti_2, bien que moins fragile que les composés intermétalliques titane/aluminium, n'offre pas le même niveau de résistance à la corrosion que les phases formées dans le joint avec intercouche en argent. Cette différence de performance en matière de corrosion met en évidence l'avantage de l'argent dans des environnements où la résistance à la corrosion est une priorité.

Comportement en nanofluage

Le nanofluage fait référence à la déformation des matériaux dépendante du temps sous contrainte à l'échelle nanométrique, ce qui est particulièrement pertinent dans les applications de haute performance où les matériaux sont soumis à des charges prolongées. Le joint avec intercouche en argent a montré une résistance supérieure au nanofluage, notamment dans la zone fondue. La suppression des composés intermétalliques fragiles a contribué à cette amélioration, car ces composés intermétalliques sont plus susceptibles à la déformation par fluage. Dans les joints avec intercouche en Ag, le mécanisme de fluage dominant dans les régions Ti6Al4V était l'ascension des dislocations, un processus qui permet une meilleure résistance au fluage sous des conditions de charge prolongée. L'étude des courbes profondeur-temps et des données de charge-déplacement a montré que l'intercouche en argent permettait un meilleur contrôle de la diffusion des éléments entre les deux alliages, en particulier dans les régions AA7075, où un fluage diffusif a été observé. Cette diffusion contrôlée réduit le risque de rupture induite par le fluage, rendant l'intercouche en argent plus efficace pour maintenir la stabilité à long terme du joint. L'intercouche en cuivre, bien qu'améliorant également la résistance au fluage, a montré de meilleures performances à l'interface cuivre/Ti6Al4V que dans la zone de fusion. Cela indique que, bien que l'intercouche en cuivre soit efficace dans des régions localisées, sa résistance globale

au fluage à travers tout le joint n'est pas aussi élevée que celle de l'intercouche en argent. La zone de fusion dans le joint avec intercouche en cuivre a montré une plus grande sensibilité à la déformation par fluage, probablement en raison de la formation d'composés intermétalliques à base de cuivre, qui ne fournissent pas le même niveau de résistance au fluage que la microstructure du joint avec intercouche en argent.

Comparaison des performances des intercouches

Lors de la comparaison des deux intercouches, l'argent s'est révélé être le matériau intercouche le plus efficace, offrant de meilleures performances sur plusieurs critères, notamment les propriétés mécaniques, la résistance à la corrosion et le comportement en nanofluage. L'intercouche en argent a constamment fourni des résultats supérieurs dans toutes les zones du joint soudé. Sa capacité à supprimer la formation d'composés intermétalliques fragiles, à améliorer la résistance mécanique, à renforcer la résistance à la corrosion et à offrir une excellente résistance au fluage en fait le choix privilégié pour les applications nécessitant des performances à long terme dans des conditions exigeantes. La recherche démontre que l'utilisation d'intercouches comme l'argent et le cuivre peut améliorer de manière significative les performances des joints soudés au laser entre métaux dissemblables. Les résultats de cette étude ont de fortes implications pour les industries qui nécessitent des joints à haute performance, légers et durables, en particulier les industries aérospatiale et automobile.

Travaux futurs

Les travaux futurs pourraient se concentrer sur l'examen de l'influence des procédés de soudage et de leurs paramètres sur les propriétés de fatigue des joints soudés. Dans les alliages de titane et d'aluminium, le développement de la texture joue un rôle crucial dans la détermination des propriétés mécaniques, et des techniques comme la diffraction d'électrons rétrodiffusés pourraient être utilisées pour approfondir cette aspect. De plus, l'effet de différents motifs de balayage du faisceau dans le soudage

laser pourrait être exploré afin d'évaluer leur impact sur les performances et les propriétés des soudures dissemblables. L'influence du traitement thermique après soudage sur les propriétés mécaniques et la microstructure des joints AA7075/Ti6Al4V représente également un domaine d'étude prometteur. En outre, une comparaison d'autres techniques de soudage industriel, pourrait fournir des informations précieuses sur les avantages relatifs de chaque méthode.

RÉFÉRENCES BIBLIOGRAPHIQUES

A, S. S., Kumar, A., & Mugada, K. K. (2022). Investigation of material flow, microstructure evolution, and texture development in dissimilar friction stir welding of Al6061 to Ti6Al4V. *Materials Today Communications*, *33*, 104424. https://doi.org/10.1016/J.MTCOMM.2022.104424

A theoretical study of the Brinell hardness test. (1989). *Proceedings of the Royal Society of London. A. Mathematical and Physical Sciences*, *423*(1865), 301–330. https://doi.org/10.1098/RSPA.1989.0056

Abdel-Hady Gepreel, M., & Niinomi, M. (2013). Biocompatibility of Ti-alloys for long-term implantation. *Journal of the Mechanical Behavior of Biomedical Materials*, *20*, 407–415. https://doi.org/10.1016/J.JMBBM.2012.11.014

Ahmed, W., Elhissi, A., Jackson, M. J., & Ahmed, E. (2012). Precision machining of medical devices. *The Design and Manufacture of Medical Devices*, 59–113. https://doi.org/10.1533/9781908818188.59

Akman, E., Demir, A., Canel, T., & Sinmazçelik, T. (2009). Laser welding of Ti6Al4V titanium alloys. *Journal of Materials Processing Technology*, *209*(8), 3705–3713. https://doi.org/10.1016/J.JMATPROTEC.2008.08.026

Almasri, A. H., & Voyiadjis, G. Z. (2007). Effect of Strain Rate on the Dynamic Hardness in Metals. *Journal of Engineering Materials and Technology*, *129*(4), 505–512. https://doi.org/10.1115/1.2744430

Amancio-Filho, S. T., & Dos Santos, J. F. (2009). Joining of polymers and polymer–metal hybrid structures: Recent developments and trends. *Polymer Engineering & Science*, *49*(8), 1461–1476. https://doi.org/10.1002/PEN.21424

Aminzadeh, A., Parvizi, A., & Moradi, M. (2020). Multi-objective topology optimization of deep drawing dissimilar tailor laser welded blanks; experimental and finite element investigation. *Optics & Laser Technology*, *125*, 106029. https://doi.org/10.1016/J.OPTLASTEC.2019.106029

Anchev, A., Kaisheva, D., Kotlarski, G., Dunchev, V., Stoyanov, B., Ormanova, M., Atanasova, M., Todorov, V., Daskalova, P., & Valkov, S. (2023). Welding of Ti6Al4V and Al6082-T6 Alloys by a Scanning Electron Beam. *Metals*, *13*(7), 1252.

Arifin, A. (n.d.). *Dissimilar metal welding using Shielded metal arc welding: A Review*.

Attar, H., Ehtemam-Haghighi, S., Kent, D., Okulov, I. V., Wendrock, H., Bönisch, M., Volegov, A. S., Calin, M., Eckert, J., & Dargusch, M. S. (2017). Nanoindentation and wear properties of Ti and Ti-TiB composite materials produced by selective laser melting. *Materials Science and Engineering: A*, *688*, 20–26. https://doi.org/10.1016/J.MSEA.2017.01.096

Babu, A., & Devanathan, C. (2013). *An Overview of Friction Stir Welding*.

Banerjee, D., & Williams, J. C. (2013a). Perspectives on titanium science and technology. *Acta Materialia*, *61*(3), 844–879. https://doi.org/10.1016/j.actamat.2012.10.043

Banerjee, D., & Williams, J. C. (2013b). Perspectives on Titanium Science and Technology. *Acta Materialia*, *61*(3), 844–879. https://doi.org/10.1016/J.ACTAMAT.2012.10.043

Baqer, Y. M., Ramesh, S., Yusof, F., & Manladan, S. M. (2018). Challenges and advances in laser welding of dissimilar light alloys: Al/Mg, Al/Ti, and Mg/Ti alloys. *International Journal of Advanced Manufacturing Technology*, *95*(9–12), 4353–4369. https://doi.org/10.1007/S00170-017-1565-6/METRICS

Baruah, M., & Bag, S. (2016a). Influence of heat input in microwelding of titanium alloy by micro plasma arc. *Journal of Materials Processing Technology*, *231*, 100–112. https://doi.org/10.1016/J.JMATPROTEC.2015.12.014

Baruah, M., & Bag, S. (2016b). Microstructural Influence on Mechanical Properties in Plasma Microwelding of Ti6Al4V Alloy. *Journal of Materials Engineering and Performance*, *25*(11), 4718–4728. https://doi.org/10.1007/S11665-016-2333-8/FIGURES/14

Baruah, M., & Bag, S. (2017). Influence of pulsation in thermo-mechanical analysis on laser micro-welding of Ti6Al4V alloy. *Optics & Laser Technology*, *90*, 40–51. https://doi.org/10.1016/J.OPTLASTEC.2016.11.006

Batistão, B. F., Bergmann, L. A., Gargarella, P., Alcântara, N. G. de, dos Santos, J. F., & Klusemann, B. (2020). Characterization of dissimilar friction stir welded lap joints of AA5083 and GL D36 steel. *Journal of Materials Research and Technology*, *9*(6), 15132–15142. https://doi.org/10.1016/J.JMRT.2020.10.078

Beegan, D., Chowdhury, S., & Laugier, M. T. (2005). Work of indentation methods for determining copper film hardness. *Surface and Coatings Technology*, *192*(1), 57–63. https://doi.org/10.1016/J.SURFCOAT.2004.02.003

Bergmann, C. P., & Alessioomalandruccolo, S. (n.d.). *Topics in Mining, Metallurgy and Materials Engineering Series Editor: Aerospace Alloys*. http://www.springer.com/series/11054

Biwa, S., & Storåkers, B. (1995). An analysis of fully plastic Brinell indentation. *Journal of the Mechanics and Physics of Solids*, *43*(8), 1303–1333. https://doi.org/10.1016/0022-5096(95)00031-D

Blackburn, J. E., Allen, C. M., Hilton, P. A., Li, L., Hoque, M. I., & Khan, A. H. (2010). Modulated Nd : YAG laser welding of Ti–6Al–4V. *Science and Technology of Welding and Joining*, *15*(5), 433–439. https://doi.org/10.1179/136217110X12731414739718

Blakey-Milner, B., Gradl, P., Snedden, G., Brooks, M., Pitot, J., Lopez, E., Leary, M., Berto, F., & du Plessis, A. (2021). Metal additive manufacturing in aerospace: A review. *Materials & Design*, *209*, 110008. https://doi.org/10.1016/J.MATDES.2021.110008

Bohn, M. J., & Petkie, D. T. (2013). Terahertz applications in the aerospace industry. *Handbook of Terahertz Technology for Imaging, Sensing and Communications*, 510–546. https://doi.org/10.1533/9780857096494.3.510

Bolshakov, A., & Pharr, G. M. (1998). Influences of pileup on the measurement of mechanical properties by load and depth sensing indentation techniques. *Journal of Materials Research*, *13*(4), 1049–1058. https://doi.org/10.1557/JMR.1998.0146

Bolton, F. C., & Canada, O. (2011). Welding and Joining of Magnesium Alloys. *Magnesium Alloys - Design, Processing and Properties*. https://doi.org/10.5772/13947

Boyer, R. R. (1996). An overview on the use of titanium in the aerospace industry. *Materials Science and Engineering: A*, *213*(1–2), 103–114. https://doi.org/10.1016/0921-5093(96)10233-1

Bückle, H. (1959). PROGRESS IN MICRO-INDENTATION HARDNESS TESTING. *Metallurgical Reviews*, *4*(1), 49–100. https://doi.org/10.1179/095066059790421746

Bulychev, S. I., Alekhin, V. P., Shorshorov, M. Kh., Ternovskij, A. P., & Shnyrev, G. D. (1975). Determination of Young modulus by the hardness indentation diagram. *Zavodskaya Laboratoriya*, *41*(9), 1137–1140. http://inis.iaea.org/Search/search.aspx?orig_q=RN:10423096

Bunaziv, I., Akselsen, O. M., Ren, X., Nyhus, B., Eriksson, M., & Gulbrandsen-Dahl, S. (2021). A Review on Laser-Assisted Joining of Aluminium Alloys to Other Metals. *Metals 2021, Vol. 11, Page 1680*, *11*(11), 1680. https://doi.org/10.3390/MET11111680

Cabibbo, M., Marrone, S., & Quadrini, E. (2005). Mechanical and microstructural characteristics of laser welded titanium-aluminium joints. *Welding International*, *19*(2), 125–129. https://doi.org/10.1533/WINT.2005.3379/ASSET//CMS/ASSET/BA4EC598-5DDD-43A2-A9BC-2ADA63B1D0FF/WINT.2005.3379.FP.PNG

Cai, W., Daehn, G., Vivek, A., Li, J., Khan, H., Mishra, R. S., & Komarasamy, M. (2019). A state-of-the-art review on solid-state metal joining. *Journal of Manufacturing Science and Engineering, Transactions of the ASME*, *141*(3). https://doi.org/10.1115/1.4041182/369169

Cao, X., & Jahazi, M. (2009). Effect of welding speed on butt joint quality of Ti–6Al–4V alloy welded using a high-power Nd:YAG laser. *Optics and Lasers in Engineering*, *47*(11), 1231–1241. https://doi.org/10.1016/J.OPTLASENG.2009.05.010

Carlone, P., & Astarita, A. (2019). Dissimilar Metal Welding. *Metals 2019, Vol. 9, Page 1206*, *9*(11), 1206. https://doi.org/10.3390/MET9111206

Casalino, G., D'Ostuni, S., Guglielmi, P., Leo, P., Mortello, M., Palumbo, G., & Piccininni, A. (2017a). Mechanical and microstructure analysis of AA6061 and Ti6Al4V fiber laser butt weld. *Optik*, *148*, 151–156. https://doi.org/10.1016/J.IJLEO.2017.08.138

Casalino, G., D'Ostuni, S., Guglielmi, P., Leo, P., Mortello, M., Palumbo, G., & Piccininni, A. (2017b). Mechanical and microstructure analysis of AA6061 and Ti6Al4V fiber laser butt weld. *Optik*, *148*, 151–156. https://doi.org/10.1016/J.IJLEO.2017.08.138

Casalino, G., D'Ostuni, S., Guglielmi, P., Leo, P., Palumbo, G., & Piccininni, A. (2018). Off-Set and Focus Effects on Grade 5 Titanium to 6061 Aluminum Alloy Fiber Laser Weld. *Materials 2018, Vol. 11, Page 2337*, *11*(11), 2337. https://doi.org/10.3390/MA11112337

Casalino, G., & Mortello, M. (2016). Modeling and experimental analysis of fiber laser offset welding of Al-Ti butt joints. *International Journal of Advanced Manufacturing Technology*, *83*(1–4), 89–98. https://doi.org/10.1007/S00170-015-7562-8/METRICS

Casalino, G., Mortello, M., & Peyre, P. (2015). Yb–YAG laser offset welding of AA5754 and T40 butt joint. *Journal of Materials Processing Technology*, *223*, 139–149. https://doi.org/10.1016/J.JMATPROTEC.2015.04.003

Charitidis, C. A., Dragatogiannis, D. A., Koumoulos, E. P., & Kartsonakis, I. A. (2012a). Residual stress and deformation mechanism of friction stir welded aluminum alloys by nanoindentation. *Materials Science and Engineering: A*, *540*, 226–234. https://doi.org/10.1016/J.MSEA.2012.01.129

Charitidis, C. A., Dragatogiannis, D. A., Koumoulos, E. P., & Kartsonakis, I. A. (2012b). Residual stress and deformation mechanism of friction stir welded aluminum alloys by nanoindentation. *Materials Science and Engineering: A*, *540*, 226–234. https://doi.org/10.1016/J.MSEA.2012.01.129

Charitidis, C. A., Dragatogiannis, D. A., Koumoulos, E. P., & Kartsonakis, I. A. (2012c). Residual stress and deformation mechanism of friction stir welded aluminum alloys by nanoindentation. *Materials Science and Engineering: A*, *540*, 226–234. https://doi.org/10.1016/J.MSEA.2012.01.129

Charitidis, C. A., Dragatogiannis, D. A., Koumoulos, E. P., & Kartsonakis, I. A. (2012d). Residual stress and deformation mechanism of friction stir welded aluminum alloys by nanoindentation. *Materials Science and Engineering: A*, *540*, 226–234. https://doi.org/10.1016/J.MSEA.2012.01.129

Cheepu, M., Ashfaq, M., & Muthupandi, V. (2017). A New Approach for Using Interlayer and Analysis of the Friction Welding of Titanium to Stainless Steel. *Transactions of the Indian Institute of Metals*, *70*(10), 2591–2600. https://doi.org/10.1007/S12666-017-1114-X/FIGURES/13

Chen, S. H., Li, L. Q., & Chen, Y. B. (2010). Interfacial reaction mode and its influence on tensile strength in laser joining Al alloy to Ti alloy. *Materials Science and Technology*, *26*(2), 230–235. https://doi.org/10.1179/174328409X399056

CHEN, S. hai, LI, L. qun, CHEN, Y. bin, & LIU, D. jian. (2010). Si diffusion behavior during laser welding-brazing of Al alloy and Ti alloy with Al-12Si filler wire. *Transactions of*

Nonferrous Metals Society of China, *20*(1), 64–70. https://doi.org/10.1016/S1003-6326(09)60098-4

Chen, S., Li, L., Chen, Y., Dai, J., & Huang, J. (2011a). Improving interfacial reaction nonhomogeneity during laser welding–brazing aluminum to titanium. *Materials & Design*, *32*(8–9), 4408–4416. https://doi.org/10.1016/J.MATDES.2011.03.074

Chen, S., Li, L., Chen, Y., Dai, J., & Huang, J. (2011b). Improving interfacial reaction nonhomogeneity during laser welding–brazing aluminum to titanium. *Materials & Design*, *32*(8–9), 4408–4416. https://doi.org/10.1016/J.MATDES.2011.03.074

Chen, S., Li, L., Chen, Y., & Huang, J. (2011a). Joining mechanism of Ti/Al dissimilar alloys during laser welding-brazing process. *Journal of Alloys and Compounds*, *509*(3), 891–898. https://doi.org/10.1016/J.JALLCOM.2010.09.125

Chen, S., Li, L., Chen, Y., & Huang, J. (2011b). Joining mechanism of Ti/Al dissimilar alloys during laser welding-brazing process. *Journal of Alloys and Compounds*, *509*(3), 891–898. https://doi.org/10.1016/J.JALLCOM.2010.09.125

Chen, S., Yang, D., Li, M., Zhang, Y., Huang, J., Yang, J., & Zhao, X. (2016). Laser penetration welding of an overlap titanium-on-aluminum configuration. *International Journal of Advanced Manufacturing Technology*, *87*(9–12), 3069–3079. https://doi.org/10.1007/S00170-016-8732-Z/METRICS

Chen, X., Lei, Z., Chen, Y., Jiang, M., Jiang, N., Bi, J., & Lin, S. (2021). Enhanced wetting behavior using femtosecond laser-textured surface in laser welding-brazing of Ti/Al butt joint. *Optics & Laser Technology*, *142*, 107212.

Chen, Y., Chen, S., & Li, L. (2008). Effects of heat input on microstructure and mechanical property of Al/Ti joints by rectangular spot laser welding-brazing method. *The International Journal of Advanced Manufacturing Technology 2008 44:3*, *44*(3), 265–272. https://doi.org/10.1007/S00170-008-1837-2

Chen, Y., Chen, S., & Li, L. (2009). Effects of heat input on microstructure and mechanical property of Al/Ti joints by rectangular spot laser welding-brazing method. *International Journal of Advanced Manufacturing Technology*, *44*(3–4), 265–272. https://doi.org/10.1007/S00170-008-1837-2/METRICS

Chen, Y., Chen, S., & Li, L. (2010). Influence of interfacial reaction layer morphologies on crack initiation and propagation in Ti/Al joint by laser welding–brazing. *Materials & Design*, *31*(1), 227–233. https://doi.org/10.1016/J.MATDES.2009.06.029

Cheng, H., Kang, L., Pang, J., Xue, B., Du, D., & Chang, B. (2021). Effect of the welding position on weld quality when laser welding Inconel 617 Ni-based superalloy. *Optics & Laser Technology*, *139*, 106962. https://doi.org/10.1016/J.OPTLASTEC.2021.106962

Choi, D. H., Ahn, B. W., Lee, C. Y., Yeon, Y. M., Song, K., & Jung, S. B. (2011). Formation of intermetallic compounds in Al and Mg alloy interface during friction stir spot welding. *Intermetallics*, *19*(2), 125–130. https://doi.org/10.1016/J.INTERMET.2010.08.030

Constantinides, G., & Ulm, F. J. (2007). The nanogranular nature of C–S–H. *Journal of the Mechanics and Physics of Solids*, *55*(1), 64–90. https://doi.org/10.1016/J.JMPS.2006.06.003

Cooke, K. O., & Atieh, A. M. (2020). Current Trends in Dissimilar Diffusion Bonding of Titanium Alloys to Stainless Steels, Aluminium and Magnesium. *Journal of Manufacturing and Materials Processing 2020, Vol. 4, Page 39*, *4*(2), 39. https://doi.org/10.3390/JMMP4020039

Correa, E. O., Costa, S. C., & Santos, J. N. (2009). Studies on weldability of iron-based powder metal alloys using pulsed gas tungsten arc welding process. *Journal of Materials Processing Technology*, *209*(8), 3937–3942. https://doi.org/10.1016/J.JMATPROTEC.2008.09.008

Correia, A. N., Braga, D. F. O., Moreira, P. M. G. P., & Infante, V. (2021). Review on dissimilar structures joints failure. *Engineering Failure Analysis*, *129*, 105652. https://doi.org/10.1016/J.ENGFAILANAL.2021.105652

Cross, C. E. (2005). On the Origin of Weld Solidification Cracking. *Hot Cracking Phenomena in Welds*, 3–18. https://doi.org/10.1007/3-540-27460-X_1

Dak, G., & Pandey, C. (2020). A critical review on dissimilar welds joint between martensitic and austenitic steel for power plant application. *Journal of Manufacturing Processes*, *58*, 377–406.

Dean, J., Aldrich-Smith, G., & Clyne, T. W. (2011). Use of nanoindentation to measure residual stresses in surface layers. *Acta Materialia*, *59*(7), 2749–2761. https://doi.org/10.1016/J.ACTAMAT.2011.01.014

Deng, S., Yuan, R., Tang, X., & Lu, F. (2020). Migration behavior of IMC layer in twin-spot laser welding-brazing of aluminum to steel. *Materials & Design*, *188*, 108489. https://doi.org/10.1016/J.MATDES.2020.108489

Deng, Y., Sheng, G., & Yin, L. (2015). Impulse Pressuring Diffusion Bonding of Titanium to Stainless Steel Using a Copper Interlayer. *Rare Metal Materials and Engineering*, *44*(5), 1041–1045. https://doi.org/10.1016/S1875-5372(15)30063-1

Ehsan, M. A., Kumar, A. M., Suleiman, R. K., Javid, M., & Younas, M. (2024). Development of trimetallic cobalt-nickel-vanadium oxide anticorrosion coatings for the protection of AA2024 Al alloy specimens against sodium chloride solutions. *Materials Chemistry and Physics*, *313*, 128696. https://doi.org/10.1016/J.MATCHEMPHYS.2023.128696

Esmaeili, A., Sbarufatti, C., & Hamouda, A. M. S. (2019). Characteristics of Intermetallic Compounds in Dissimilar Friction Stir Welding: A Review. *Metallography, Microstructure, and Analysis*, *8*(4), 445–461. https://doi.org/10.1007/S13632-019-00557-W/METRICS

Ezugwu, E. O., Bonney, J., & Yamane, Y. (2003). An overview of the machinability of aeroengine alloys. *Journal of Materials Processing Technology*, *134*(2), 233–253. https://doi.org/10.1016/S0924-0136(02)01042-7

Fadaeifard, F., Pakmanesh, M. R., Esfahani, M. S., Matori, K. A., Chicot, D., Fadaeifard, F., Pakmanesh, M. R., Esfahani, M. S., Matori, K. A., & Chicot, D. (2019). Nanoindentation Analysis of Friction Stir Welded 6061-T6 Al Alloy in As-Weld and Post Weld Heat Treatment. *PMM*, *120*(5), 483–491. https://doi.org/10.1134/S0031918X1905003X

Fan, M., Yu, W., Wang, W., Guo, X. Z., Jin, K., Miao, R., Hou, W., Kim, N., & Tao, J. (2017). Microstructure and Mechanical Properties of Thin-Multilayer Ti/Al Laminates Prepared by One-Step Explosive Bonding. *Journal of Materials Engineering and Performance*, *26*(1), 277–284. https://doi.org/10.1007/S11665-016-2410-Z/FIGURES/10

Fang, Y., Jiang, X., Mo, D., Zhu, D., & Luo, Z. (2019). A review on dissimilar metals' welding methods and mechanisms with interlayer. *International Journal of Advanced Manufacturing Technology*, *102*(9–12), 2845–2863. https://doi.org/10.1007/S00170-019-03353-6/METRICS

Fernandes, F. A. O., Gonçalves, J. J. M., & Pereira, A. B. (2023). Evaluation of Laser Lap Weldability between the Titanium Alloy Ti-6Al-4V and Aluminum Alloy 6060-T6. *Crystals*, *13*(10), 1448.

Firouz Fadaeifard, Pakmanesh, M. R., Esfahani, M. S., Matori, K. A., & Chicot, D. (2019). Nanoindentation Analysis of Friction Stir Welded 6061-T6 Al Alloy in As-Weld and Post Weld Heat Treatment. *Physics of Metals and Metallography*, *120*(5), 483–491. https://doi.org/10.1134/S0031918X1905003X/FIGURES/7

Fischer-Cripps, A. C. (2011). *Nanoindentation*. 279. https://books.google.com/books/about/Nanoindentation.html?id=D23TpyBM_EcC

Gadakh, V. S., Badheka, V. J., & Mulay, A. S. (2021). Solid-state joining of aluminum to titanium: A review. *Proceedings of the Institution of Mechanical Engineers, Part L: Journal of Materials: Design and Applications*, *235*(8), 1757–1799. https://doi.org/10.1177/14644207211010839/ASSET/IMAGES/LARGE/10.1177_14644207211010839-FIG20.JPEG

Gagliardi, F., Palaia, D., & Ambrogio, G. (2019). Energy consumption and CO2 emissions of joining processes for manufacturing hybrid structures. *Journal of Cleaner Production*, *228*, 425–436.

Gale, J. D., & Achuthan, A. (2014). The effect of work-hardening and pile-up on nanoindentation measurements. *Journal of Materials Science*, *49*(14), 5066–5075. https://doi.org/10.1007/S10853-014-8213-4/FIGURES/10

Gammon, L. M., Briggs, R. D., Packard, J. M., Batson, K. W., Boyer, R., & Domby, C. W. (2004). Metallography and Microstructures of Titanium and Its Alloys. *Metallography and Microstructures*, 899–917. https://doi.org/10.31399/ASM.HB.V09.A0003779

Gao, M., Chen, C., Gu, Y., & Zeng, X. (2014). Microstructure and Tensile Behavior of Laser Arc Hybrid Welded Dissimilar Al and Ti Alloys. *Materials 2014, Vol. 7, Pages 1590-1602*, *7*(3), 1590–1602. https://doi.org/10.3390/MA7031590

Gao, X. L., Zhang, L. J., Liu, J., & Zhang, J. X. (2014). Effects of weld cross-section profiles and microstructure on properties of pulsed Nd:YAG laser welding of Ti6Al4V sheet. *International Journal of Advanced Manufacturing Technology*, *72*(5–8), 895–903. https://doi.org/10.1007/S00170-014-5722-X/METRICS

Gharavi, F., Matori, K. A., Yunus, R., & Othman, N. K. (2014). Corrosion behavior of friction stir welded lap joints of AA6061-T6 aluminum alloy. *Materials Research*, *17*(3), 672–681. https://doi.org/10.1590/S1516-14392014005000053

Ghosh, A., Sivaprasad, S., Bhattacharjee, A., & Kar, S. K. (2013). Microstructure–fracture toughness correlation in an aircraft structural component alloy Ti–5Al–5V–5Mo–3Cr.

Materials Science and Engineering: A, *568*, 61–67. https://doi.org/10.1016/J.MSEA.2013.01.017

Gialanella, S., & Malandruccolo, A. (2020). Titanium and Titanium Alloys. *Topics in Mining, Metallurgy and Materials Engineering*, 129–189. https://doi.org/10.1007/978-3-030-24440-8_4/FIGURES/39

Gloria, A., Montanari, R., Richetta, M., & Varone, A. (2019). Alloys for Aeronautic Applications: State of the Art and Perspectives. *Metals 2019, Vol. 9, Page 662*, *9*(6), 662. https://doi.org/10.3390/MET9060662

González, C., Vilatela, J. J., Molina-Aldareguía, J. M., Lopes, C. S., & LLorca, J. (2017). Structural composites for multifunctional applications: Current challenges and future trends. *Progress in Materials Science*, *89*, 194–251. https://doi.org/10.1016/J.PMATSCI.2017.04.005

Gu, X., Cui, M., Chen, J., Sun, D., Gu, X., & Liu, L. (2021a). Laser welding of 6082 aluminum alloy to TC4 titanium alloy via pure niobium as a transition layer. *Journal of Materials Research and Technology*, *13*, 2202–2209. https://doi.org/10.1016/J.JMRT.2021.06.015

Gu, X., Cui, M., Chen, J., Sun, D., Gu, X., & Liu, L. (2021b). Laser welding of 6082 aluminum alloy to TC4 titanium alloy via pure niobium as a transition layer. *Journal of Materials Research and Technology*, *13*, 2202–2209. https://doi.org/10.1016/J.JMRT.2021.06.015

Guo, W., You, G., Yuan, G., & Zhang, X. (2017). Microstructure and mechanical properties of dissimilar inertia friction welding of 7A04 aluminum alloy to AZ31 magnesium alloy. *Journal of Alloys and Compounds*, *695*, 3267–3277. https://doi.org/10.1016/J.JALLCOM.2016.11.218

Gupta, R. K., Anilkumar, V., Xavier, X. R., & Ramkumar, P. (2018). Electron beam welding study of grade 1 CP Titanium. *Materials Today: Proceedings*, *5*(2), 8464–8470. https://doi.org/10.1016/J.MATPR.2017.11.542

Gupta, S. P. (2002). Intermetallic compounds in diffusion couples of Ti with an Al–Si eutectic alloy. *Materials Characterization*, *49*(4), 321–330. https://doi.org/10.1016/S1044-5803(02)00342-X

Hainsworth, S. V., Chandler, H. W., & Page, T. F. (1996). Analysis of nanoindentation load-displacement loading curves. *Journal of Materials Research*, *11*(8), 1987–1995. https://doi.org/10.1557/JMR.1996.0250/METRICS

Hassaan, M., Junaid, M., Shahbaz, T., Ilyas, M., Khan, F. N., & Haider, J. (2021). Nanomechanical Response of Pulsed Tungsten Inert Gas Welded Titanium Alloy by Nanoindentation and Atomic Force Microscopy. *Journal of Materials Engineering and Performance*, *30*(2), 1490–1503. https://doi.org/10.1007/S11665-020-05413-5/TABLES/3

Hepworth, J. K. (1984). The effect of residual stress on the creep deformation of welded pipe. *International Journal of Pressure Vessels and Piping*, *15*(4), 271–290. https://doi.org/10.1016/0308-0161(84)90012-7

Holmberg, H. (2000). Influence of grain angle on Brinell hardness of Scots pine (Pinus sylvestris L.). *Holz Als Roh - Und Werkstoff*, *58*(1–2), 91–95. https://doi.org/10.1007/S001070050392/METRICS

Hong, J. K., Park, J. H., Park, N. K., Eom, I. S., Kim, M. B., & Kang, C. Y. (2008). Microstructures and mechanical properties of Inconel 718 welds by CO2 laser welding. *Journal of Materials Processing Technology*, *201*(1–3), 515–520. https://doi.org/10.1016/J.JMATPROTEC.2007.11.224

Honnorat, Y. (1996). Issues and breakthrough in the manufacture of turboengine titanium parts. *Materials Science and Engineering: A*, *213*(1–2), 115–123. https://doi.org/10.1016/0921-5093(96)10229-X

Hu, J., Sun, G., Zhang, X., Wang, G., Jiang, Z., Han, S., Zhang, J., & Lian, J. (2015a). Effects of loading strain rate and stacking fault energy on nanoindentation creep behaviors of nanocrystalline Cu, Ni-20 wt.%Fe and Ni. *Journal of Alloys and Compounds*, *647*, 670–680. https://doi.org/10.1016/J.JALLCOM.2015.06.094

Hu, J., Sun, G., Zhang, X., Wang, G., Jiang, Z., Han, S., Zhang, J., & Lian, J. (2015b). Effects of loading strain rate and stacking fault energy on nanoindentation creep behaviors of nanocrystalline Cu, Ni-20 wt.%Fe and Ni. *Journal of Alloys and Compounds*, *647*, 670–680. https://doi.org/10.1016/J.JALLCOM.2015.06.094

Hu, J., Sun, G., Zhang, X., Wang, G., Jiang, Z., Han, S., Zhang, J., & Lian, J. (2015c). Effects of loading strain rate and stacking fault energy on nanoindentation creep behaviors of nanocrystalline Cu, Ni-20 wt.%Fe and Ni. *Journal of Alloys and Compounds*, *647*, 670–680. https://doi.org/10.1016/J.JALLCOM.2015.06.094

Iltaf, A., Barka, N., & Dehghan, S. (2024). Effect of Ag interlayer on the microstructural properties and nanocreep behavior of Ti6Al4V/AA7075 dissimilar laser weldments. *Proceedings of the Institution of Mechanical Engineers, Part L: Journal of Materials: Design and Applications*. https://doi.org/10.1177/14644207241243351/ASSET/IMAGES/LARGE/10.1177_14644207241243351-FIG17.JPEG

Iltaf, A., Dehghan, S., Barka, N., & Belzile, C. (2024). Laser butt welding of AA7075 aluminium alloy and Ti6Al4V titanium alloy using a Cu interlayer. *Https://Doi.Org/10.1177/02670836241235847*. https://doi.org/10.1177/02670836241235847

Iltaf, A., Junaid, M., Khan, F. N., Bakhsh, N., & Rehman, M. U. (2023). Influence of electron beam oscillation patterns on the microstructure, texture, residual stress and mechanical properties of Ti-5Al-2.5Sn alloy weldments. *Proceedings of the Institution of Mechanical Engineers, Part B: Journal of Engineering Manufacture*, *237*(13), 2047–2061. https://doi.org/10.1177/0954405420937537/ASSET/IMAGES/LARGE/10.1177_0954405420937537-FIG20.JPEG

Iltaf, A., Karim, M. R. A., Taimoor, A. A., Junaid, M., Khan, F. N., Raza, S. A., & Khan, M. Z. (2021). Effect of Beam Oscillation Patterns on the Electrochemical Corrosion Behavior of Electron Beam Welded Ti-5Al-2.5Sn Alloy in Simulated Marine Environment. *Journal of Materials Engineering and Performance*, *30*(6), 4518–4528. https://doi.org/10.1007/S11665-021-05734-Z/FIGURES/11

Iltaf, A., Khan, F. N., Shehbaz, T., & Junaid, M. (2021). Influence of filler material on the microstructure, mechanical properties, and residual stresses in tungsten inert gas welded Ti-5Al-2.5Sn alloy joints. *Proceedings of the Institution of Mechanical Engineers, Part L: Journal of Materials: Design and Applications*, *235*(8), 1952–1966. https://doi.org/10.1177/14644207211012433/ASSET/IMAGES/LARGE/10.1177_14644207211012433-FIG20.JPEG

Jadhav, S., Powar, A., Patil, S., Supare, A., Farane, B., & Singh, R. (2017). Effect of volume fraction of alpha and transformed beta on the high cycle fatigue properties of bimodal Ti6Al4V alloy. *IOP Conference Series: Materials Science and Engineering*, *201*(1), 012035. https://doi.org/10.1088/1757-899X/201/1/012035

Jamleh, A., Sadr, A., Nomura, N., Yahata, Y., Ebihara, A., Hanawa, T., Tagami, J., & Suda, H. (2012). Nano-indentation testing of new and fractured nickel-titanium endodontic instruments. *International Endodontic Journal*, *45*(5), 462–468. https://doi.org/10.1111/J.1365-2591.2011.01997.X

Jandaghi, M. R., Pouraliakbar, H., Hong, S. I., & Pavese, M. (2020). Grain boundary transition associated intergranular failure analysis at TMAZ/SZ interface of dissimilar AA7475-AA2198 joints by friction stir welding. *Materials Letters*, *280*, 128557. https://doi.org/10.1016/J.MATLET.2020.128557

Jandaghi, M. R., Pouraliakbar, H., Saboori, A., Hong, S. I., & Pavese, M. (2021). Comparative Insight into the Interfacial Phase Evolutions during Solution Treatment of Dissimilar Friction Stir Welded AA2198-AA7475 and AA2198-AA6013 Aluminum Sheets. *Materials 2021, Vol. 14, Page 1290*, *14*(5), 1290. https://doi.org/10.3390/MA14051290

Jang, J. (2009). *Estimation of residual stress by instrumented indentation: A review*.

Jiang, P., & Chen, R. (2019). Research on interfacial layer of laser-welded aluminum to titanium. *Materials Characterization*, *154*, 264–268. https://doi.org/10.1016/J.MATCHAR.2019.06.012

Junaid, M., Rahman, K., Khan, F. N., Bakhsh, N., & Baig, M. N. (2017). Comparison of microstructure, mechanical properties, and residual stresses in tungsten inert gas, laser, and electron beam welding of Ti–5Al–2.5Sn titanium alloy. *Proceedings of the Institution of Mechanical Engineers, Part L: Journal of Materials: Design and Applications*, *0*(0), 1–16. https://doi.org/10.1177/1464420717748345

Kah, P., & Jukka Martikainen, M. S. (2014). Trends in Joining Dissimilar Metals by Welding. *Applied Mechanics and Materials*, *440*, 269–276. https://doi.org/10.4028/WWW.SCIENTIFIC.NET/AMM.440.269

Kalinenko, A., Kim, K., Vysotskiy, I., Zuiko, I., Malopheyev, S., Mironov, S., & Kaibyshev, R. (2020). Microstructure-strength relationship in friction-stir welded 6061-T6 aluminum alloy. *Materials Science and Engineering: A*, *793*, 139858. https://doi.org/10.1016/J.MSEA.2020.139858

Kar, A., Singh, K., & Kumar, L. (2023). Effect of Tool Rotational Speed and Mechanisms Associated with Microstructure Evolution and Intermetallics Formation in Friction Stir Welding of Aluminum Alloy to Titanium Alloy. *Journal of Materials Engineering and Performance*, 1–12. https://doi.org/10.1007/S11665-023-08407-1/FIGURES/9

Ke, W., Zeng, Z., Oliveira, J. P., Peng, B., Shen, J., Tan, C., Song, X., & Yan, W. (2023). Heat transfer and melt flow of keyhole, transition and conduction modes in laser beam oscillating welding. *International Journal of Heat and Mass Transfer*, *203*, 123821. https://doi.org/10.1016/J.IJHEATMASSTRANSFER.2022.123821

Kese, K. O., Li, Z. C., & Bergman, B. (2004a). Influence of residual stress on elastic modulus and hardness of soda-lime glass measured by nanoindentation. *Journal of Materials Research*, *19*(10), 3109–3119. https://doi.org/10.1557/JMR.2004.0404/METRICS

Kese, K. O., Li, Z. C., & Bergman, B. (2004b). Influence of residual stress on elastic modulus and hardness of soda-lime glass measured by nanoindentation. *Journal of Materials Research*, *19*(10), 3109–3119. https://doi.org/10.1557/JMR.2004.0404/METRICS

Khalil, A. M., Loginova, I. S., Pozdniakov, A. V., Mosleh, A. O., & Solonin, A. N. (2019). Evaluation of the Microstructure and Mechanical Properties of a New Modified Cast and Laser-Melted AA7075 Alloy. *Materials*, *12*(20). https://doi.org/10.3390/MA12203430

Khan, M. K., Fitzpatrick, M. E., Hainsworth, S. V., & Edwards, L. (2011). Effect of residual stress on the nanoindentation response of aerospace aluminium alloys. *Computational Materials Science*, *50*(10), 2967–2976. https://doi.org/10.1016/J.COMMATSCI.2011.05.015

Klueh, R. L., King, J. F., & Griffith, J. L. (1983). Simple test for dissimilar-metal welds. *Weld. Res. (Miami); (United States)*.

Kocik, R., Kaschel, S., Kreimeyer, M., Schumacher, J., & Vollertsen, F. (2004). Development of a new joining technology for hybrid metal aircraft structures. *ICALEO*

2004 - 23rd International Congress on Applications of Laser and Electro-Optics, Congress Proceedings. https://doi.org/10.2351/1.5060292/1000891

Kreimeyer, M., Wagner, F., & Vollertsen, F. (2005). Laser processing of aluminum–titanium-tailored blanks. *Optics and Lasers in Engineering*, *43*(9), 1021–1035. https://doi.org/10.1016/J.OPTLASENG.2004.07.005

Kulkarni, A., Dwivedi, D. K., & Vasudevan, M. (2019). Dissimilar metal welding of P91 steel-AISI 316L SS with Incoloy 800 and Inconel 600 interlayers by using activated TIG welding process and its effect on the microstructure and mechanical properties. *Journal of Materials Processing Technology*, *274*, 116280. https://doi.org/10.1016/J.JMATPROTEC.2019.116280

Kumar, M. R., Tomashchuk, I., Jouvard, J. M., & Duband, M. (2022). The investigation of keyhole behavior in dissimilar aluminum/titanium interface. *Procedia CIRP*, *111*, 507–512. https://doi.org/10.1016/J.PROCIR.2022.08.080

Kundu, S., Bhola, S. M., Mishra, B., & Chatterjee, S. (2014). Structure and properties of solid state diffusion bonding of 17-4PH stainless steel and titanium. *Materials Science and Technology (United Kingdom)*, *30*(2), 248–256. https://doi.org/10.1179/1743284713Y.0000000352/ASSET/IMAGES/LARGE/10.1179_1743284713Y.0000000352-FIG11.JPEG

Kuphasuk, C., Oshida, Y., Andres, C. J., Hovijitra, S. T., Barco, M. T., & Brown, D. T. (2001). Electrochemical corrosion of titanium and titanium-based alloys. *The Journal of Prosthetic Dentistry*, *85*(2), 195–202. https://doi.org/10.1067/MPR.2001.113029

Kuryntsev, S. V. (2019a). Microstructure, mechanical and electrical properties of laser-welded overlap joint of CP Ti and AA2024. *Optics and Lasers in Engineering*, *112*, 77–86.

Kuryntsev, S. V. (2019b). Microstructure, mechanical and electrical properties of laser-welded overlap joint of CP Ti and AA2024. *Optics and Lasers in Engineering*, *112*, 77–86. https://doi.org/10.1016/J.OPTLASENG.2018.09.001

Lathabai, S., Jarvis, B. L., & Barton, K. J. (2001). Comparison of keyhole and conventional gas tungsten arc welds in commercially pure titanium. *Materials Science and Engineering: A*, *299*(1–2), 81–93. https://doi.org/10.1016/S0921-5093(00)01408-8

Lee, K. soo, Kim, W., Lee, J. geun, Park, C. yong, Yang, J. seok, Kim, T. ryong, & Park, J. hak. (2009). Finite element analysis and measurement for residual stress of dissimilar metal weld in pressurizer safety nozzle mockup. *Journal of Mechanical Science and Technology*, *23*(11), 2948–2955. https://doi.org/10.1007/S12206-009-0809-2/METRICS

Lee, S. J., Nakamura, H., Kawahito, Y., & Katayama, S. (2013). Weldability of Ti and Al dissimilar metals using single-mode fiber laser. *Journal of Laser Micro Nanoengineering*, *8*(2), 149–154. https://doi.org/10.2961/jlmn.2013.02.0006

Lee. S, Katayama. S, & Kim. J. (n.d.). *Microstructural behavior on weld fusion zone of Al-Ti and Ti-Al dissimilar lap welding using single-mode fiber laser - 한국마린엔지니어링학회지 - 한국마린엔지니어링학회 - KISS*. https://kiss.kstudy.com/DetailOa/Ar?key=51385931

Lee, S.-J. ;, Nakamura, H. ;, Kawahito, Y., Lee, S.-J., Nakamura, H., & Katayama, S. (2013). Microstructural Characteristics and Mechanical Properties of Single-Mode Fiber Laser Lap-Welded Joint in Ti and Al Dissimilar Metals Microstructural Characteristics and Mechanical Properties of Single-Mode Fiber Laser Lap-Welded Joint in Ti and Al Dissimilar Metals †. *Citation Transactions of JWRI*, *42*(1), 17–21. https://doi.org/10.18910/26600

Leo, P., D'Ostuni, S., & Casalino, G. (2018a). Low temperature heat treatments of AA5754-Ti6Al4V dissimilar laser welds: Microstructure evolution and mechanical properties.

Optics & Laser Technology, *100*, 109–118. https://doi.org/10.1016/J.OPTLASTEC.2017.09.039

Leo, P., D'Ostuni, S., & Casalino, G. (2018b). Low temperature heat treatments of AA5754-Ti6Al4V dissimilar laser welds: Microstructure evolution and mechanical properties. *Optics & Laser Technology*, *100*, 109–118. https://doi.org/10.1016/J.OPTLASTEC.2017.09.039

Li, C., Zhao, W., Wang, Y., Duan, K., & Zhao, B. (2010). Experimental study on high power all-fiber laser. *Chinese Optics Letters, Vol. 8, Issue 4, Pp. 404-406*, *8*(4), 404–406. https://opg.optica.org/abstract.cfm?uri=col-8-4-404

Li, F., Ding, J., Fabbro, R., Qu, F., & Peyre, P. (2005). Investigation on laser brazing AA6056 Al alloy to XC18 low-carbon steel. *Chinese Optics Letters, Vol. 3, Issue 1, Pp. 31-34*, *3*(1), 31–34. https://opg.optica.org/abstract.cfm?uri=col-3-1-31

Li, J., Gao, H., Kong, C., & Yu, H. (2022). Insight into the bonding mechanism in Cu/Al/Cu clad sheets via introduction of thin SUS304 interlayer. *Journal of Materials Research and Technology*, *21*, 4619–4635. https://doi.org/10.1016/J.JMRT.2022.11.076

Li, J., Hu, D., Mu, G., Wang, S., Zhang, Z., Zhang, X., Lv, X., Li, D., & Wang, J. (2020). Optimal control strategy for large-scale VRB energy storage auxiliary power system in peak shaving. *International Journal of Electrical Power & Energy Systems*, *120*, 106007. https://doi.org/10.1016/J.IJEPES.2020.106007

Li, J., Liu, Y., Gao, Y., Jin, P., Sun, Q., & Feng, J. (2020). Benefits of interfacial regulation with interlayers in laser welding Ti6Al4V/316L steel. *Optics & Laser Technology*, *125*, 106007. https://doi.org/10.1016/J.OPTLASTEC.2019.106007

Li, L., Zhao, B., & Wu, X. (2019). Tungsten inert gas welding of dissimilar metals aluminum to titanium with aluminum based wire. *Materials Research Express*, *6*(5), 056561. https://doi.org/10.1088/2053-1591/AB056F

Li, P., Lei, Z., Zhang, X., & Chen, Y. (2020a). Influence of Si content on interfacial reactions and mechanical properties of dual-spot laser welded-brazed Ti/Al joints. *Journal of Manufacturing Processes*, *56*, 950–966. https://doi.org/10.1016/J.JMAPRO.2020.06.001

Li, P., Lei, Z., Zhang, X., & Chen, Y. (2020b). Influence of Si content on interfacial reactions and mechanical properties of dual-spot laser welded-brazed Ti/Al joints. *Journal of Manufacturing Processes*, *56*, 950–966. https://doi.org/10.1016/J.JMAPRO.2020.06.001

Li, P., Lei, Z., Zhang, X., & Chen, Y. (2020c). Influence of Si content on interfacial reactions and mechanical properties of dual-spot laser welded-brazed Ti/Al joints. *Journal of Manufacturing Processes*, *56*, 950–966. https://doi.org/10.1016/J.JMAPRO.2020.06.001

Li, P., Lei, Z., Zhang, X., & Chen, Y. (2020d). Influence of Si content on interfacial reactions and mechanical properties of dual-spot laser welded-brazed Ti/Al joints. *Journal of Manufacturing Processes*, *56*, 950–966. https://doi.org/10.1016/J.JMAPRO.2020.06.001

Li, P., Lei, Z., Zhang, X., Liu, J., & Chen, Y. (2020). Effects of laser power on the interfacial intermetallic compounds and mechanical properties of dual-spot laser welded–brazed Ti/Al butt joint. *Optics & Laser Technology*, *124*, 105987. https://doi.org/10.1016/J.OPTLASTEC.2019.105987

Li, T., Shi, J., Li, R., Qi, K., Liu, Z., Zhang, X., & Qiao, L. (2024). Interfacial microstructure and corrosion behaviors of TC4/DP780 steel joints by laser welding with H62 interlayer. *Journal of Materials Research and Technology*, *29*, 4470–4479. https://doi.org/10.1016/J.JMRT.2024.02.140

Li, W. B., Henshall, J. L., Hooper, R. M., & Easterling, K. E. (1991a). The mechanisms of indentation creep. *Acta Metallurgica et Materialia*, *39*(12), 3099–3110. https://doi.org/10.1016/0956-7151(91)90043-Z

Li, W. B., Henshall, J. L., Hooper, R. M., & Easterling, K. E. (1991b). The mechanisms of indentation creep. *Acta Metallurgica et Materialia*, *39*(12), 3099–3110. https://doi.org/10.1016/0956-7151(91)90043-Z

Li, X., Xie, J., & Zhou, Y. (2005). Effects of oxygen contamination in the argon shielding gas in laser welding of commercially pure titanium thin sheet. *Journal of Materials Science*, *40*(13), 3437–3443. https://doi.org/10.1007/S10853-005-0447-8/METRICS

Li, Z., Liu, Z., Chen, D., Mo, F., Fu, Y., Dai, Y., Wu, X., & Cong, D. (2022). Study of Microstructure and Properties of Aluminum/Steel Inertia Radial Friction Welding. *Metals 2022, Vol. 12, Page 2023*, *12*(12), 2023. https://doi.org/10.3390/MET12122023

Lin, Y. J., & Lin, C. S. (2021). Galvanic corrosion behavior of friction stir welded AZ31B magnesium alloy and 6N01 aluminum alloy dissimilar joints. *Corrosion Science*, *180*, 109203. https://doi.org/10.1016/J.CORSCI.2020.109203

Liu, S., Chew, Y., Weng, F., Sui, S., Du, Z., Man, Y., Ng, F. L., & Bi, G. (2022a). Effects of laser pulse modulation on intermetallic compounds formation for welding of Ti-6Al-4V and AA7075 using AA4047 filler. *Materials & Design*, *213*, 110325. https://doi.org/10.1016/J.MATDES.2021.110325

Liu, S., Chew, Y., Weng, F., Sui, S., Du, Z., Man, Y., Ng, F. L., & Bi, G. (2022b). Effects of laser pulse modulation on intermetallic compounds formation for welding of Ti-6Al-4V and AA7075 using AA4047 filler. *Materials & Design*, *213*, 110325.

Liu, S., Chew, Y., Weng, F., Sui, S., Du, Z., Man, Y., Ng, F. L., & Bi, G. (2022c). Effects of laser pulse modulation on intermetallic compounds formation for welding of Ti-6Al-4V and AA7075 using AA4047 filler. *Materials & Design*, *213*, 110325. https://doi.org/10.1016/J.MATDES.2021.110325

Liu, X., Zhang, Q., Zhao, X., Yang, X., & Luo, L. (2016). Ambient-temperature nanoindentation creep in ultrafine-grained titanium processed by ECAP. *Materials Science and Engineering: A*, *676*, 73–79. https://doi.org/10.1016/J.MSEA.2016.08.111

Lou, Y., Zhang, S., & Yoon, J. W. (2019). A reduced Yld2004 function for modeling of anisotropic plastic deformation of metals under triaxial loading. *International Journal of Mechanical Sciences*, *161–162*, 105027. https://doi.org/10.1016/J.IJMECSCI.2019.105027

Lu, H., Xu, W., Wang, H., & Wang, X. Z. (2023). Microstructure evolution and its effect on the corrosion of dissimilar aluminum alloys friction stir welding joint. *Corrosion Science*, *220*, 111249. https://doi.org/10.1016/J.CORSCI.2023.111249

Lucas, B. N., & Oliver, W. C. (1999). Indentation power-law creep of high-purity indium. *Metallurgical and Materials Transactions A: Physical Metallurgy and Materials Science*, *30*(3), 601–610. https://doi.org/10.1007/S11661-999-0051-7/METRICS

Lv, S. X., Jing, X. J., Huang, Y. X., Xu, Y. Q., Zheng, C. Q., & Yang, S. Q. (2012). Investigation on TIG arc welding-brazing of Ti/Al dissimilar alloys with Al based fillers. *Science and Technology of Welding and Joining*, *17*(7), 519–524. https://doi.org/10.1179/1362171812Y.0000000041/ASSET/IMAGES/LARGE/10.1179_1362171812Y.0000000041-FIG7.JPEG

Lv, X., Liu, L., & Song, G. (2022). Laser welding of AZ31Mg alloy with 6061Al alloy via Ti interlayer based on two kinds of bonding mechanisms. *Journal of Manufacturing Processes*, *83*, 678–684. https://doi.org/10.1016/J.JMAPRO.2022.09.034

Ma, Z., Long, S., Pan, Y., & Zhou, Y. (2008a). Loading rate sensitivity of nanoindentation creep in polycrystalline Ni films. *Journal of Materials Science*, *43*(17), 5952–5955. https://doi.org/10.1007/S10853-008-2838-0/FIGURES/4

Ma, Z., Long, S., Pan, Y., & Zhou, Y. (2008b). Loading rate sensitivity of nanoindentation creep in polycrystalline Ni films. *Journal of Materials Science*, *43*(17), 5952–5955. https://doi.org/10.1007/S10853-008-2838-0/FIGURES/4

Madadi, F., Ashrafizadeh, F., & Shamanian, M. (2012). Optimization of pulsed TIG cladding process of stellite alloy on carbon steel using RSM. *Journal of Alloys and Compounds*, *510*(1), 71–77. https://doi.org/10.1016/J.JALLCOM.2011.08.073

Mahmudi, R., Pourmajidian, M., Geranmayeh, A. R., Gorgannejad, S., & Hashemizadeh, S. (2013). Indentation creep of lead-free Sn–3.5Ag solder alloy: Effects of cooling rate and Zn/Sb addition. *Materials Science and Engineering: A*, *565*, 236–242. https://doi.org/10.1016/J.MSEA.2012.12.048

Maier, P., Richter, A., Tober, G., & Hort, N. (2013). Effect of Grain Size and Structure, Solid Solution Elements, Precipitates and Twinning on Nanohardness of Mg-RE Alloys. *Materials Science Forum*, *765*, 491–495. https://doi.org/10.4028/WWW.SCIENTIFIC.NET/MSF.765.491

Maier, V., Merle, B., Göken, M., & Durst, K. (2013). An improved long-term nanoindentation creep testing approach for studying the local deformation processes in nanocrystalline metals at room and elevated temperatures. *Journal of Materials Research*, *28*(9), 1177–1188. https://doi.org/10.1557/JMR.2013.39

Malekshahi Beiranvand, Z., Malek Ghaini, F., Naffakh Moosavy, H., Sheikhi, M., Torkamany, M. J., & Moradi, M. (2020). The relation between magnesium evaporation and laser absorption and weld penetration in pulsed laser welding of aluminum alloys: Experimental and numerical investigations. *Optics & Laser Technology*, *128*, 106170. https://doi.org/10.1016/J.OPTLASTEC.2020.106170

Mali, V. I., Bataev, A. A., Maliutina, I. N., Kurguzov, V. D., Bataev, I. A., Esikov, M. A., & Lozhkin, V. S. (2017). Microstructure and mechanical properties of Ti/Ta/Cu/Ni alloy laminate composite materials produced by explosive welding. *International Journal of*

Advanced Manufacturing Technology, *93*(9–12), 4285–4294. https://doi.org/10.1007/S00170-017-0887-8/METRICS

Malikov, A., Vitoshkin, I., Orishich, A., Filippov, A., & Karpov, E. (2020). Effect of the aluminum alloy composition (Al-Cu-Li or Al-Mg-Li) on structure and mechanical properties of dissimilar laser welds with the Ti-Al-V alloy. *Optics & Laser Technology*, *126*, 106135. https://doi.org/10.1016/J.OPTLASTEC.2020.106135

Manjunath, B. N., Jayaprakash, P., Mishra, A., Karthik, H. S., Arulkirubakaran, D., Kiran, D. V., & Venkaiah, N. (2023). Joining dissimilar metals using cold metal transfer process: a review. *Welding in the World*, *1*, 1–13. https://doi.org/10.1007/S40194-023-01639-8/FIGURES/13

Mansor, M. S. M., Yusof, F., Ariga, T., & Miyashita, Y. (2018). Microstructure and mechanical properties of micro-resistance spot welding between stainless steel 316L and Ti-6Al-4V. *International Journal of Advanced Manufacturing Technology*, *96*(5–8), 2567–2581. https://doi.org/10.1007/S00170-018-1688-4/METRICS

Mante, F. K., Baran, G. R., & Lucas, B. (1999). Nanoindentation studies of titanium single crystals. *Biomaterials*, *20*(11), 1051–1055. https://doi.org/10.1016/S0142-9612(98)00257-9

Marinkovic, N., Sasaki, K., Adzic, R. R., Guisbiers, G., & Buchaillot, L. (2008). Size and shape effects on creep and diffusion at the nanoscale. *Nanotechnology*, *19*(43), 435701. https://doi.org/10.1088/0957-4484/19/43/435701

Mathieu, A., Matteï, S., Deschamps, A., Martin, B., & Grevey, D. (2006). Temperature control in laser brazing of a steel/aluminium assembly using thermographic measurements. *NDT & E International*, *39*(4), 272–276. https://doi.org/10.1016/J.NDTEINT.2005.08.005

McKeen, L. W. (2009). The Effect of Creep and Other Time Related Factors on Plastics and Elastomers. *The Effect of Creep and Other Time Related Factors on Plastics and Elastomers*. https://doi.org/10.1016/c2013-0-19368-3

Mei, Y., Liu, Y., Liu, C., Li, C., Yu, L., Guo, Q., & Li, H. (2016). Effect of base metal and welding speed on fusion zone microstructure and HAZ hot-cracking of electron-beam welded Inconel 718. *Materials & Design*, *89*, 964–977. https://doi.org/10.1016/J.MATDES.2015.10.082

Meng, Y., Gu, X., Cui, M., Gu, X., & Zhao, X. (2022). Laser assisted diffusion bonding of TC4 titanium alloy to 301 stainless steel using a Ni interlayer. *Journal of Materials Research and Technology*, *21*, 739–748. https://doi.org/10.1016/J.JMRT.2022.09.065

Moon, S., Paek, J. H., Jang, Y. H., & Kang, K. (2024). Mixing behavior of Ti–Al interface during the ultrasonic welding process and its welding strength: Molecular dynamics study. *Heliyon*, e25116. https://doi.org/10.1016/J.HELIYON.2024.E25116

Mouritz, A. P. (2012). Introduction to Aerospace Materials. In *Introduction to Aerospace Materials*. Elsevier Inc. https://doi.org/10.2514/4.869198

Nagarajan, B. M., & Manoharan, M. (2023). Assessment of dissimilar joining between metal and polymer hybrid structure with different joining processes. *Journal of Thermoplastic Composite Materials*, *36*(5), 2169–2211. https://doi.org/10.1177/08927057211048534/ASSET/IMAGES/LARGE/10.1177_08927057211048534-FIG20.JPEG

Nguyen, N. V., Pham, T. H., & Kim, S. E. (2019a). Microstructure and strain rate sensitivity behavior of SM490 structural steel weld zone investigated using indentation. *Construction and Building Materials*, *206*, 410–418. https://doi.org/10.1016/J.CONBUILDMAT.2019.02.013

Nguyen, N. V., Pham, T. H., & Kim, S. E. (2019b). Microstructure and strain rate sensitivity behavior of SM490 structural steel weld zone investigated using indentation.

Construction and Building Materials, *206*, 410–418. https://doi.org/10.1016/J.CONBUILDMAT.2019.02.013

Nguyen, N. V., Pham, T. H., & Kim, S. E. (2019c). Microstructure and strain rate sensitivity behavior of SM490 structural steel weld zone investigated using indentation. *Construction and Building Materials*, *206*, 410–418. https://doi.org/10.1016/J.CONBUILDMAT.2019.02.013

Nguyen, N. V., Pham, T. H., & Kim, S. E. (2019d). Strain rate sensitivity behavior of a structural steel during low-cycle fatigue investigated using indentation. *Materials Science and Engineering: A*, *744*, 490–499. https://doi.org/10.1016/J.MSEA.2018.12.025

Nguyen, N. V., Pham, T. H., & Kim, S. E. (2019e). Strain rate sensitivity behavior of a structural steel during low-cycle fatigue investigated using indentation. *Materials Science and Engineering: A*, *744*, 490–499. https://doi.org/10.1016/J.MSEA.2018.12.025

Ohnuma, I., Fujita, Y., Mitsui, H., Ishikawa, K., Kainuma, R., & Ishida, K. (2000a). Phase equilibria in the Ti–Al binary system. *Acta Materialia*, *48*(12), 3113–3123. https://doi.org/10.1016/S1359-6454(00)00118-X

Ohnuma, I., Fujita, Y., Mitsui, H., Ishikawa, K., Kainuma, R., & Ishida, K. (2000b). Phase equilibria in the Ti–Al binary system. *Acta Materialia*, *48*(12), 3113–3123. https://doi.org/10.1016/S1359-6454(00)00118-X

Olivares, E. A. G., & Díaz, V. M. V. (2018). Study of the hot-wire TIG process with AISI-316L filler material, analysing the effect of magnetic arc blow on the dilution of the weld bead. *Welding International*, *32*(2), 139–148. https://doi.org/10.1080/09507116.2017.1347327

Oliveira, J. P., Santos, T. G., & Miranda, R. M. (2020). Revisiting fundamental welding concepts to improve additive manufacturing: From theory to practice. *Progress in Materials Science*, *107*, 100590. https://doi.org/10.1016/J.PMATSCI.2019.100590

Oliveira, J. P., Zeng, Z., Andrei, C., Braz Fernandes, F. M., Miranda, R. M., Ramirez, A. J., Omori, T., & Zhou, N. (2017). Dissimilar laser welding of superelastic NiTi and CuAlMn shape memory alloys. *Materials & Design*, *128*, 166–175. https://doi.org/10.1016/J.MATDES.2017.05.011

Oliver, W. C., & Fabes, B. D. (1995). The relationship between indentation and uniaxial creep in amorphous selenium. *Journal of Materials Research*, *10*(8), 2024–2032. https://doi.org/10.1557/JMR.1995.2024/METRICS

Oliver, W. C., & Pharr, G. M. (1992a). An improved technique for determining hardness and elastic modulus using load and displacement sensing indentation experiments. *Journal of Materials Research*, *7*(6), 1564–1583. https://doi.org/10.1557/JMR.1992.1564

Oliver, W. C., & Pharr, G. M. (1992b). An improved technique for determining hardness and elastic modulus using load and displacement sensing indentation experiments. *Journal of Materials Research*, *7*(6), 1564–1583. https://doi.org/10.1557/JMR.1992.1564/METRICS

Oliver, W. C., & Pharr, G. M. (1992c). An improved technique for determining hardness and elastic modulus using load and displacement sensing indentation experiments. *Journal of Materials Research*, *7*(6), 1564–1583. https://doi.org/10.1557/JMR.1992.1564

Oliver, W. C., & Pharr, G. M. (1992d). An improved technique for determining hardness and elastic modulus using load and displacement sensing indentation experiments. *Journal of Materials Research*, *7*(6), 1564–1583. https://doi.org/10.1557/JMR.1992.1564/METRICS

Oliver, W. C., & Pharr, G. M. (1992e). An improved technique for determining hardness and elastic modulus using load and displacement sensing indentation experiments. *Journal*

of Materials Research, *7*(6), 1564–1583. https://doi.org/10.1557/JMR.1992.1564/METRICS

Oliver, W. C., & Pharr, G. M. (2004a). Measurement of hardness and elastic modulus by instrumented indentation: Advances in understanding and refinements to methodology. *Journal of Materials Research*, *19*(1), 3–20. https://doi.org/10.1557/JMR.2004.19.1.3/METRICS

Oliver, W. C., & Pharr, G. M. (2004b). Measurement of hardness and elastic modulus by instrumented indentation: Advances in understanding and refinements to methodology. *Journal of Materials Research*, *19*(1), 3–20. https://doi.org/10.1557/JMR.2004.19.1.3/METRICS

Palanivel, R., Dinaharan, I., & Laubscher, R. F. (2017). Assessment of microstructure and tensile behavior of continuous drive friction welded titanium tubes. *Materials Science and Engineering: A*, *687*, 249–258. https://doi.org/10.1016/J.MSEA.2017.01.090

Patel, V., Li, W., Wang, G., Wang, F., Vairis, A., & Niu, P. (2019). Friction Stir Welding of Dissimilar Aluminum Alloy Combinations: State-of-the-Art. *Metals 2019, Vol. 9, Page 270*, *9*(3), 270. https://doi.org/10.3390/MET9030270

Patel, V., Sali, A., Hyder, J., Corliss, M., Hyder, D., & Hung, W. (2020). Electron Beam Welding of Inconel 718. *Procedia Manufacturing*, *48*, 428–435. https://doi.org/10.1016/J.PROMFG.2020.05.065

Peng, G., Ma, Y., Hu, J., Jiang, W., Huan, Y., Chen, Z., & Zhang, T. (2018). Nanoindentation Hardness Distribution and Strain Field and Fracture Evolution in Dissimilar Friction Stir-Welded AA 6061-AA 5A06 Aluminum Alloy Joints. *Advances in Materials Science and Engineering*, *2018*. https://doi.org/10.1155/2018/4873571

Peters, M., Kumpfert, J., Ward, C. H., & Leyens, C. (2003). Titanium Alloys for Aerospace Applications. *Advanced Engineering Materials*, *5*(6), 419–427. https://doi.org/10.1002/ADEM.200310095

Peyre, P., Berthe, L., Dal, M., Pouzet, S., Sallamand, P., & Tomashchuk, I. (2014). Generation and characterization of T40/A5754 interfaces with lasers. *Journal of Materials Processing Technology*, *214*(9), 1946–1953. https://doi.org/10.1016/J.JMATPROTEC.2014.04.019

Pham, T. H., Kim, J. J., & Kim, S. E. (2014). Estimation of microstructural compositions in the weld zone of structural steel using nanoindentation. *Journal of Constructional Steel Research*, *99*, 121–128. https://doi.org/10.1016/J.JCSR.2014.04.011

Plaine, A. H., Suhuddin, U. F. H., Alcântara, N. G., & dos Santos, J. F. (2017). Microstructure and mechanical behavior of friction spot welded AA6181-T4/Ti6Al4V dissimilar joints. *International Journal of Advanced Manufacturing Technology*, *92*(9–12), 3703–3714. https://doi.org/10.1007/S00170-017-0439-2/METRICS

Quazi, M. M., Ishak, M., Fazal, M. A., Arslan, A., Rubaiee, S., Qaban, A., Aiman, M. H., Sultan, T., Ali, M. M., & Manladan, S. M. (2020). Current research and development status of dissimilar materials laser welding of titanium and its alloys. *Optics & Laser Technology*, *126*, 106090. https://doi.org/10.1016/J.OPTLASTEC.2020.106090

Qun li Li, L. (2007). *Characteristics of laser welding-brazing joint of Al/Ti dissimilar alloys*. https://www.researchgate.net/publication/274381064

Raj, S., & Biswas, P. (2022). Mechanical and microstructural characterizations of friction stir welded dissimilar butt joints of Inconel 718 and AISI 204Cu austenitic stainless steel. *Materials Characterization*, *185*, 111763. https://doi.org/10.1016/J.MATCHAR.2022.111763

Raja Kumar, M., Jouvard, J. M., Tomashchuk, I., & Sallamand, P. (2020). Vapor plume and melted zone behavior during dissimilar laser welding of titanium to aluminum alloy. *Proceedings of the Institution of Mechanical Engineers, Part L: Journal of Materials: Design and Applications*, *234*(5), 681–696.

https://doi.org/10.1177/1464420720907936/ASSET/IMAGES/LARGE/10.1177_1464420720907936-FIG11.JPEG

Raja Kumar, M., Tomashchuk, I., Jouvard, J. M., & Duband, M. (2022). High-speed imaging of vapor plume in the treatment of dissimilar Aluminum/Titanium interface with Yb:YAG laser pulse. *Journal of Advanced Joining Processes*, *5*, 100097. https://doi.org/10.1016/J.JAJP.2022.100097

Ramezani, M., Mohd Ripin, Z., Pasang, T., & Jiang, C. P. (2023). Surface Engineering of Metals: Techniques, Characterizations and Applications. *Metals 2023, Vol. 13, Page 1299*, *13*(7), 1299. https://doi.org/10.3390/MET13071299

Ramkumar, T., Selvakumar, M., Narayanasamy, P., Begam, A. A., Mathavan, P., & Raj, A. A. (2017). Studies on the structural property, mechanical relationships and corrosion behaviour of Inconel 718 and SS 316L dissimilar joints by TIG welding without using activated flux. *Journal of Manufacturing Processes*, *30*, 290–298. https://doi.org/10.1016/J.JMAPRO.2017.09.028

Ribeiro, A. C. N., de Siqueira, R. H. M., de Lima, M. S. F., Giorjão, R. A. R., & Abdalla, A. J. (2021). Improvement weldability of dissimilar joints (Ti6Al4V/Al6013) for aerospace industry by laser beam welding. *International Journal of Advanced Manufacturing Technology*, *116*(3–4), 1053–1070. https://doi.org/10.1007/S00170-021-07506-4/FIGURES/21

Rossini, N. S., Dassisti, M., Benyounis, K. Y., & Olabi, A. G. (2012). Methods of measuring residual stresses in components. *Materials & Design*, *35*, 572–588. https://doi.org/10.1016/J.MATDES.2011.08.022

Ruano, O. A., Wadsworth, J., Wolfenstine, J., & Sherby, O. D. (1993). Evidence for Nabarro-Herring creep in metals: fiction or reality? *Materials Science and Engineering: A*, *165*(2), 133–141. https://doi.org/10.1016/0921-5093(93)90747-3

Rzaij, D. R., Ahmed, N. Y., & Alhaboubi, N. (2022). Coating Performance of SiO_2 / Epoxy Composites as a Corrosion Protector. *Corrosion Science and Technology*, *21*(2), 111–120. https://doi.org/10.14773/CST.2022.21.2.111

Saha, R., & Nix, W. D. (2001a). Soft films on hard substrates — nanoindentation of tungsten films on sapphire substrates. *Materials Science and Engineering: A*, *319–321*, 898–901. https://doi.org/10.1016/S0921-5093(01)01076-0

Saha, R., & Nix, W. D. (2001b). Soft films on hard substrates — nanoindentation of tungsten films on sapphire substrates. *Materials Science and Engineering: A*, *319–321*, 898–901. https://doi.org/10.1016/S0921-5093(01)01076-0

Sahul, M., Sahul, M., Vyskoč, M., Čaplovič, Ľ., & Pašák, M. (2017). Disk Laser Weld Brazing of AW5083 Aluminum Alloy with Titanium Grade 2. *Journal of Materials Engineering and Performance*, *26*(3), 1346–1357. https://doi.org/10.1007/S11665-017-2529-6/FIGURES/16

Schauerte, O. (2003). Titanium in Automotive Production. *Advanced Engineering Materials*, *5*(6), 411–418. https://doi.org/10.1002/ADEM.200310094

Schubert, E., Klassen, M., Zerner, I., Walz, C., & Sepold, G. (2001). Light-weight structures produced by laser beam joining for future applications in automobile and aerospace industry. *Journal of Materials Processing Technology*, *115*(1), 2–8. https://doi.org/10.1016/S0924-0136(01)00756-7

Schuh, C. A. (2006a). Nanoindentation studies of materials. *Materials Today*, *9*(5), 32–40. https://doi.org/10.1016/S1369-7021(06)71495-X

Schuh, C. A. (2006b). Nanoindentation studies of materials. *Materials Today*, *9*(5), 32–40. https://doi.org/10.1016/S1369-7021(06)71495-X

Selvamani, S. T. (2022). Various welding processes for joining aluminium alloy with steel: Effect of process parameters and observations–a review. *Proceedings of the Institution*

of Mechanical Engineers, Part C: Journal of Mechanical Engineering Science, *236*(10), 5428–5454. https://doi.org/10.1177/09544062211059695/ASSET/IMAGES/LARGE/10.1177_09544062211059695-FIG20.JPEG

Semiatin, S. L., Levkulich, N. C., Salem, A. A., & Pilchak, A. L. (2020). Plastic Flow During Hot Working of Ti-7Al. *Metallurgical and Materials Transactions A: Physical Metallurgy and Materials Science*, *51*(9), 4695–4710. https://doi.org/10.1007/S11661-020-05884-0

Shojaei Zoeram, A., Rahmani, A., & Akbari Mousavi, S. A. A. (2017). Microstructure and properties analysis of laser-welded Ni–Ti and 316l sheets using copper interlayer. *Journal of Manufacturing Processes*, *26*, 355–363. https://doi.org/10.1016/J.JMAPRO.2017.02.005

Sibum, H. (2003). Titanium and Titanium Alloys—From Raw Material to Semi-finished Products. *Advanced Engineering Materials*, *5*(6), 393–398. https://doi.org/10.1002/ADEM.200310092

Singh, K. (2014). Advanced Materials for Land Based Gas Turbines. *Transactions of the Indian Institute of Metals*, *67*(5), 601–615. https://doi.org/10.1007/S12666-014-0398-3/FIGURES/16

Singh, N., Hameed, P., Ummethala, R., Manivasagam, G., Prashanth, K. G., & Eckert, J. (2020). Selective laser manufacturing of Ti-based alloys and composites: impact of process parameters, application trends, and future prospects. *Materials Today Advances*, *8*, 100097. https://doi.org/10.1016/J.MTADV.2020.100097

Sonar, T., Balasubramanian, V., Malarvizhi, S., Venkateswaran, T., & Sivakumar, D. (2021). An overview on welding of Inconel 718 alloy - Effect of welding processes on microstructural evolution and mechanical properties of joints. *Materials Characterization*, *174*, 110997. https://doi.org/10.1016/J.MATCHAR.2021.110997

Song, Y., Huang, X., Gao, Z., Li, X., & Ma, Y. (2020a). Nanoindentation creep behavior of RPV's weld joint at room temperature. *Mechanics of Time-Dependent Materials*, *24*(3), 253–263. https://doi.org/10.1007/S11043-019-09419-Y/FIGURES/6

Song, Y., Huang, X., Gao, Z., Li, X., & Ma, Y. (2020b). Nanoindentation creep behavior of RPV's weld joint at room temperature. *Mechanics of Time-Dependent Materials*, *24*(3), 253–263. https://doi.org/10.1007/S11043-019-09419-Y/FIGURES/6

Song, Y., Huang, X., Gao, Z., Li, X., & Ma, Y. (2020c). Nanoindentation creep behavior of RPV's weld joint at room temperature. *Mechanics of Time-Dependent Materials*, *24*(3), 253–263. https://doi.org/10.1007/S11043-019-09419-Y/FIGURES/6

Song, Z., Nakata, K., Wu, A., & Liao, J. (2013). Interfacial microstructure and mechanical property of Ti6Al4V/A6061 dissimilar joint by direct laser brazing without filler metal and groove. *Materials Science and Engineering: A*, *560*, 111–120. https://doi.org/10.1016/J.MSEA.2012.09.044

Song, Z., & Tegus, O. (2023). The Corrosion Properties of Bronze Alloys in NaCl Solutions. *Materials 2023, Vol. 16, Page 5144*, *16*(14), 5144. https://doi.org/10.3390/MA16145144

Squillace, A., Prisco, U., Ciliberto, S., & Astarita, A. (2012). Effect of welding parameters on morphology and mechanical properties of Ti-6Al-4V laser beam welded butt joints. *Journal of Materials Processing Technology*, *212*(2), 427–436. https://doi.org/10.1016/j.jmatprotec.2011.10.005

Su, C., Herbert, E. G., Sohn, S., LaManna, J. A., Oliver, W. C., & Pharr, G. M. (2013a). Measurement of power-law creep parameters by instrumented indentation methods. *Journal of the Mechanics and Physics of Solids*, *61*(2), 517–536. https://doi.org/10.1016/J.JMPS.2012.09.009

Su, C., Herbert, E. G., Sohn, S., LaManna, J. A., Oliver, W. C., & Pharr, G. M. (2013b). Measurement of power-law creep parameters by instrumented indentation methods.

Journal of the Mechanics and Physics of Solids, *61*(2), 517–536. https://doi.org/10.1016/J.JMPS.2012.09.009

Sujata, M., Bhargava, S., & Sangal, S. (1997). On the formation of TiAl3 during reaction between solid Ti and liquid Al. *Journal of Materials Science Letters*, *16*(13), 1175–1178. https://doi.org/10.1007/BF02765402/METRICS

Sun, H., Han, Y., & Li, Y. (2023). Microstructure and strength of diffusion bonding W alloy/304 stainless steel joint using a Cu interlayer. *International Journal of Refractory Metals and Hard Materials*, *113*, 106188. https://doi.org/10.1016/J.IJRMHM.2023.106188

Sun, S., & Lv, W. (2016). Microstructure and Mechanical Properties of TC18 Titanium Alloy. *Rare Metal Materials and Engineering*, *45*(5), 1138–1141. https://doi.org/10.1016/S1875-5372(16)30108-4

Sun, Z., & Karppi, R. (1996). The application of electron beam welding for the joining of dissimilar metals: an overview. *Journal of Materials Processing Technology*, *59*(3), 257–267. https://doi.org/10.1016/0924-0136(95)02150-7

Tabor, D. (1996). Indentation hardness: Fifty years on a personal view. *Philosophical Magazine A*, *74*(5), 1207–1212. https://doi.org/10.1080/01418619608239720

Tavares, S. M. O., Castro, R. A. S., Richter-Trummer, V., Vilaça, P., Moreira, P. M. G. P., & De Castro, P. M. S. T. (2010). Friction stir welding of T-joints with dissimilar aluminium alloys: Mechanical joint characterisation. *Https://Doi.Org/10.1179/136217109X12562846839114*, *15*(4), 312–318. https://doi.org/10.1179/136217109X12562846839114

Teshome, F. B., Peng, B., Oliveira, J. P., Shen, J., Ao, S., Li, H., Chen, L., Tan, C., Song, X., Zhou, N., & Zeng, Z. (2023a). Role of Pd interlayer on NiTi to Ti6Al4V laser welded joints: Microstructural evolution and strengthening mechanisms. *Materials & Design*, *228*, 111845. https://doi.org/10.1016/J.MATDES.2023.111845

Teshome, F. B., Peng, B., Oliveira, J. P., Shen, J., Ao, S., Li, H., Chen, L., Tan, C., Song, X., Zhou, N., & Zeng, Z. (2023b). Role of Pd interlayer on NiTi to Ti6Al4V laser welded joints: Microstructural evolution and strengthening mechanisms. *Materials & Design*, *228*, 111845. https://doi.org/10.1016/J.MATDES.2023.111845

Tey, C. F., Tan, X., Sing, S. L., & Yeong, W. Y. (2020). Additive manufacturing of multiple materials by selective laser melting: Ti-alloy to stainless steel via a Cu-alloy interlayer. *Additive Manufacturing*, *31*, 100970. https://doi.org/10.1016/J.ADDMA.2019.100970

Titanium and Titanium Alloys. (2003). *Titanium and Titanium Alloys*. https://doi.org/10.1002/3527602119

Tohid, R. R., & Bull, S. J. (2007). Getting accurate nanoindentation data from time-dependent and microstructural effects of zinc. *International Journal of Materials Research*, *98*(5), 353–359. https://doi.org/10.3139/146.101477/MACHINEREADABLECITATION/RIS

Tomashchuk, I., Sallamand, P., Cicala, E., Peyre, P., & Grevey, D. (2015a). Direct keyhole laser welding of aluminum alloy AA5754 to titanium alloy Ti6Al4V. *Journal of Materials Processing Technology*, *217*, 96–104. https://doi.org/10.1016/J.JMATPROTEC.2014.10.025

Tomashchuk, I., Sallamand, P., Cicala, E., Peyre, P., & Grevey, D. (2015b). Direct keyhole laser welding of aluminum alloy AA5754 to titanium alloy Ti6Al4V. *Journal of Materials Processing Technology*, *217*, 96–104. https://doi.org/10.1016/J.JMATPROTEC.2014.10.025

Tomashchuk, I., Sallamand, P., Cicala, E., Peyre, P., & Grevey, D. (2015c). Direct keyhole laser welding of aluminum alloy AA5754 to titanium alloy Ti6Al4V. *Journal of Materials Processing Technology*, *217*, 96–104. https://doi.org/10.1016/J.JMATPROTEC.2014.10.025

Tomashchuk, I., Sallamand, P., Méasson, A., Cicala, E., Duband, M., & Peyre, P. (2017a). Aluminum to titanium laser welding-brazing in V-shaped groove. *Journal of Materials Processing Technology*, *245*, 24–36. https://doi.org/10.1016/J.JMATPROTEC.2017.02.009

Tomashchuk, I., Sallamand, P., Méasson, A., Cicala, E., Duband, M., & Peyre, P. (2017b). Aluminum to titanium laser welding-brazing in V-shaped groove. *Journal of Materials Processing Technology*, *245*, 24–36. https://doi.org/10.1016/J.JMATPROTEC.2017.02.009

Tomashchuk, I., Sallamand, P., Méasson, A., Cicala, E., Duband, M., & Peyre, P. (2017c). Aluminum to titanium laser welding-brazing in V-shaped groove. *Journal of Materials Processing Technology*, *245*, 24–36. https://doi.org/10.1016/J.JMATPROTEC.2017.02.009

Torkamany, M. J., Malek Ghaini, F., & Poursalehi, R. (2014). Dissimilar pulsed Nd:YAG laser welding of pure niobium to Ti–6Al–4V. *Materials & Design*, *53*, 915–920. https://doi.org/10.1016/J.MATDES.2013.07.094

Tsai, C. J., & Wang, L. M. (2014). Improved mechanical properties of Ti–6Al–4V alloy by electron beam welding process plus annealing treatments and its microstructural evolution. *Materials & Design*, *60*, 587–598. https://doi.org/10.1016/J.MATDES.2014.04.037

Tuck, J. R., Korsunskyl, A. M., Bull, S. J., & Davidson, R. I. (2001a). On the application of the work-of-indentation approach to depth-sensing indentation experiments in coated systems. *Https://Eprints.Ncl.Ac.Uk*, *137*(2–3), 217–224. https://doi.org/10.1016/S0257-8972(00)01063-X

Tuck, J. R., Korsunskyl, A. M., Bull, S. J., & Davidson, R. I. (2001b). On the application of the work-of-indentation approach to depth-sensing indentation experiments in coated

systems. *Surface and Coatings Technology*, *137*(2–3), 217–224. https://doi.org/10.1016/S0257-8972(00)01063-X

Tuck, J. R., Korsunskyl, A. M., Bull, S. J., & Davidson, R. I. (2001c). On the application of the work-of-indentation approach to depth-sensing indentation experiments in coated systems. *Surface and Coatings Technology*, *137*(2–3), 217–224. https://doi.org/10.1016/S0257-8972(00)01063-X

Tuck, J. R., Korsunskyl, A. M., Bull, S. J., & Davidson, R. I. (2001d). On the application of the work-of-indentation approach to depth-sensing indentation experiments in coated systems. *Surface and Coatings Technology*, *137*(2–3), 217–224. https://doi.org/10.1016/S0257-8972(00)01063-X

Vacchi, G. S., Plaine, A. H., Silva, R., Sordi, V. L., Suhuddin, U. F. H., Alcântara, N. G., Kuri, S. E., & Rovere, C. A. D. (2017). Effect of friction spot welding (FSpW) on the surface corrosion behavior of overlapping AA6181-T4/Ti-6Al-4V joints. *Materials & Design*, *131*, 127–134. https://doi.org/10.1016/J.MATDES.2017.06.005

Vafaeenezhad, H., & Shahverdi, H. R. (2024). Impact of Vanadium Presence on the Mechanical and Microstructural Characteristics of a Dilute Al–Sc–Zr–Si Alloy During Isothermal Aging. *Journal of Materials Research and Technology*, *30*, 2406–2419. https://doi.org/10.1016/J.JMRT.2024.03.145

Vaidya, W. V., Horstmann, M., Ventzke, V., Petrovski, B., Koçak, M., Kocik, R., & Tempus, G. (2009). Structure-property investigations on a laser beam welded dissimilar joint of aluminium AA6056 and titanium Ti6Al4V for aeronautical applications Part I: Local gradients in microstructure, hardness and strength. *Materialwissenschaft Und Werkstofftechnik*, *40*(8), 623–633. https://doi.org/10.1002/MAWE.200900366

Van Swygenhoven, H., & Derlet, P. M. (2001). Grain-boundary sliding in nanocrystalline fcc metals. *Physical Review B*, *64*(22), 224105. https://doi.org/10.1103/PhysRevB.64.224105

Varshney, D., & Kumar, K. (2021). Application and use of different aluminium alloys with respect to workability, strength and welding parameter optimization. *Ain Shams Engineering Journal*, *12*(1), 1143–1152. https://doi.org/10.1016/J.ASEJ.2020.05.013

Vijayan, D., Ananthapadmanaban, D., & Ravikumar, E. (2022). Analysis of bend angle variation in aluminium – copper friction welding in the presence and absence of nickel interlayer. *Materials Today: Proceedings*, *62*, 793–798. https://doi.org/10.1016/J.MATPR.2022.03.688

Vitek, J. M., & Babu, S. S. (2011). Multiscale characterisation of weldments. *Science and Technology of Welding and Joining*, *16*(1), 3–11. https://doi.org/10.1179/1362171810Y.0000000003

Viteri, V. S. de, Fuentes, E., Viteri, V. S. de, & Fuentes, E. (2013). Titanium and Titanium Alloys as Biomaterials. *Tribology - Fundamentals and Advancements*. https://doi.org/10.5772/55860

Wadsworth, J., Palmer, I. G., & Crooks, D. D. (1983). Superplasticity in Al Li based alloys. *Scripta Metallurgica*, *17*(3), 347–352. https://doi.org/10.1016/0036-9748(83)90171-0

Walley, S. M. (2012). Historical origins of indentation hardness testing. *Materials Science and Technology (United Kingdom)*, *28*(9–10), 1028–1044. https://doi.org/10.1179/1743284711Y.0000000127/ASSET/IMAGES/LARGE/10.1179_1743284711Y.0000000127-FIG16.JPEG

Wang, H. T., Wang, G. Z., Xuan, F. Z., & Tu, S. T. (2013). Fracture mechanism of a dissimilar metal welded joint in nuclear power plant. *Engineering Failure Analysis*, *28*, 134–148. https://doi.org/10.1016/J.ENGFAILANAL.2012.10.005

Wang, H., & Wang, Y. (2019). High-Velocity Impact Welding Process: A Review. *Metals 2019, Vol. 9, Page 144*, *9*(2), 144. https://doi.org/10.3390/MET9020144

Wang, J., Cui, X., Jin, G., Zhao, Y., Wen, X., & Zhang, Y. (2023). Effect of in-situ Ni interlayer on the microstructure and corrosion resistance of underwater wet 316L stainless steel laser cladding layer. *Surface and Coatings Technology*, *458*, 129341. https://doi.org/10.1016/J.SURFCOAT.2023.129341

Wang, P., Chen, X., Pan, Q., Madigan, B., & Long, J. (2016). Laser welding dissimilar materials of aluminum to steel: an overview. *International Journal of Advanced Manufacturing Technology*, *87*(9–12), 3081–3090. https://doi.org/10.1007/S00170-016-8725-Y/METRICS

Wang, S., & Wu, X. (2012). Investigation on the microstructure and mechanical properties of Ti–6Al–4V alloy joints with electron beam welding. *Materials & Design (1980-2015)*, *36*, 663–670. https://doi.org/10.1016/J.MATDES.2011.11.068

Wang, T., Zhang, B., Wang, H., & Feng, J. (2014). Microstructures and mechanical properties of electron beam-welded titanium-steel joints with vanadium, nickel, copper and silver filler metals. *Journal of Materials Engineering and Performance*, *23*(4), 1498–1504. https://doi.org/10.1007/S11665-014-0897-8/FIGURES/9

Wang, W., Meng, X., Dong, W., Xie, Y., Ma, X., Mao, D., Zhang, Z., & Huang, Y. (2024). In-situ rolling friction stir welding of aluminum alloys towards corrosion resistance. *Corrosion Science*, *230*, 111920. https://doi.org/10.1016/J.CORSCI.2024.111920

Wang, Z., Shen, J., Hu, S., Wang, T., & Bu, X. (2020a). Investigation of welding crack in laser welding-brazing welded TC4/6061 and TC4/2024 dissimilar butt joints. *Journal of Manufacturing Processes*, *60*, 54–60. https://doi.org/10.1016/J.JMAPRO.2020.10.029

Wang, Z., Shen, J., Hu, S., Wang, T., & Bu, X. (2020b). Investigation of welding crack in laser welding-brazing welded TC4/6061 and TC4/2024 dissimilar butt joints. *Journal of Manufacturing Processes*, *60*, 54–60. https://doi.org/10.1016/J.JMAPRO.2020.10.029

Węglowski, M. S., Błacha, S., & Phillips, A. (2016). Electron beam welding – Techniques and trends – Review. *Vacuum*, *130*, 72–92. https://doi.org/10.1016/J.VACUUM.2016.05.004

Weglowski, M. St., Błacha, S., & Phillips, A. (2012). Electron beam welding—Techniques and trends. *Welding and Joining of Aerospace Materials*, 157–198. https://doi.org/10.1016/B978-0-12-819140-8.00006-7

Wei, H., Zhang, Y., Tan, L., & Zhong, Z. (2015). Energy efficiency evaluation of hot-wire laser welding based on process characteristic and power consumption. *Journal of Cleaner Production*, *87*(C), 255–262. https://doi.org/10.1016/J.JCLEPRO.2014.10.009

Williams, J. C., & Boyer, R. R. (2020). Opportunities and Issues in the Application of Titanium Alloys for Aerospace Components. *Metals 2020, Vol. 10, Page 705*, *10*(6), 705. https://doi.org/10.3390/MET10060705

Wu, Y. E., & Wang, Y. T. (2010). Effect of filler metal and postwelding heat treatment on mechanical properties of Al-Zn-Mg alloy weldments. *Journal of Materials Engineering and Performance*, *19*(9), 1362–1369. https://doi.org/10.1007/S11665-010-9638-9/FIGURES/12

Wu, Y. E., Wang, Y. T., Wu, Y. E., & Wang, Y. T. (2010). Effect of Filler Metal and Postwelding Heat Treatment on Mechanical Properties of Al-Zn-Mg Alloy Weldments. *JMEP*, *19*(9), 1362–1369. https://doi.org/10.1007/S11665-010-9638-9

Xiong, J., Peng, Y., Zhang, H., Li, J., & Zhang, F. (2018). Microstructure and mechanical properties of Al-Cu joints diffusion-bonded with Ni or Ag interlayer. *Vacuum*, *147*, 187–193. https://doi.org/10.1016/J.VACUUM.2017.10.033

Xu, L., Cui, Y. Y., Hao, Y. L., & Yang, R. (2006). Growth of intermetallic layer in multi-laminated Ti/Al diffusion couples. *Materials Science and Engineering: A*, *435–436*, 638–647. https://doi.org/10.1016/J.MSEA.2006.07.077

Xu, Y., Hou, X., Shi, Y., Zhang, W., Gu, Y., Feng, C., & Volodymyr, K. (2021). Correlation between the microstructure and corrosion behaviour of copper/316 L stainless-steel dissimilar-metal welded joints. *Corrosion Science*, *191*, 109729. https://doi.org/10.1016/J.CORSCI.2021.109729

Xue, X., Pereira, A., Vincze, G., Wu, X., & Liao, J. (2019). Interfacial Characteristics of Dissimilar Ti6Al4V/AA6060 Lap Joint by Pulsed Nd:YAG Laser Welding. *Metals 2019, Vol. 9, Page 71*, *9*(1), 71. https://doi.org/10.3390/MET9010071

XUE, X., WU, X., & LIAO, J. (2021). Hot-cracking susceptibility and shear fracture behavior of dissimilar Ti6Al4V/AA6060 alloys in pulsed Nd:YAG laser welding. *Chinese Journal of Aeronautics*, *34*(4), 375–386. https://doi.org/10.1016/J.CJA.2020.12.015

Yan, X. Y., Chang, Y. A., Xie, F. Y., Chen, S. L., Zhang, F., & Daniel, S. (2001). Calculated phase diagrams of aluminum alloys from binary Al-Cu to multicomponent commercial alloys. *Journal of Alloys and Compounds*, *320*(2), 151–160. https://doi.org/10.1016/S0925-8388(00)01469-9

Yang, B., & Vehoff, H. (2005a). Grain size effects on the mechanical properties of nanonickel examined by nanoindentation. *Materials Science and Engineering: A*, *400–401*(1-2 SUPPL.), 467–470. https://doi.org/10.1016/J.MSEA.2005.01.077

Yang, B., & Vehoff, H. (2005b). Grain size effects on the mechanical properties of nanonickel examined by nanoindentation. *Materials Science and Engineering: A*, *400–401*(1-2 SUPPL.), 467–470. https://doi.org/10.1016/J.MSEA.2005.01.077

Yang, J., Oliveira, J. P., Li, Y., Tan, C., Gao, C., Zhao, Y., & Yu, Z. (2022). Laser techniques for dissimilar joining of aluminum alloys to steels: A critical review. *Journal of Materials Processing Technology*, *301*, 117443. https://doi.org/10.1016/J.JMATPROTEC.2021.117443

Yin, Q., Liu, Z., Wang, B., Song, Q., & Cai, Y. (2020). Recent progress of machinability and surface integrity for mechanical machining Inconel 718: a review. *International Journal of Advanced Manufacturing Technology*, *109*(1–2), 215–245. https://doi.org/10.1007/S00170-020-05665-4/FIGURES/38

Yunlian, Q., Ju, D., Quan, H., & Liying, Z. (2000). Electron beam welding, laser beam welding and gas tungsten arc welding of titanium sheet. *Materials Science and Engineering: A*, *280*(1), 177–181. https://doi.org/10.1016/S0921-5093(99)00662-0

Zengliang, G., Yuxuan, S., Zhouxin, P., Jianan, C., & Yi, M. (2020a). Nanoindentation investigation on the creep behavior of P92 steel weld joint after creep-fatigue loading. *International Journal of Fatigue*, *134*, 105506. https://doi.org/10.1016/J.IJFATIGUE.2020.105506

Zengliang, G., Yuxuan, S., Zhouxin, P., Jianan, C., & Yi, M. (2020b). Nanoindentation investigation on the creep behavior of P92 steel weld joint after creep-fatigue loading. *International Journal of Fatigue*, *134*, 105506. https://doi.org/10.1016/J.IJFATIGUE.2020.105506

Zengliang, G., Yuxuan, S., Zhouxin, P., Jianan, C., & Yi, M. (2020c). Nanoindentation investigation on the creep behavior of P92 steel weld joint after creep-fatigue loading. *International Journal of Fatigue*, *134*, 105506. https://doi.org/10.1016/J.IJFATIGUE.2020.105506

Zengliang, G., Yuxuan, S., Zhouxin, P., Jianan, C., & Yi, M. (2020d). Nanoindentation investigation on the creep behavior of P92 steel weld joint after creep-fatigue loading. *International Journal of Fatigue*, *134*, 105506. https://doi.org/10.1016/J.IJFATIGUE.2020.105506

Zhang, H., Li, J. K., Guan, Z. W., Liu, Y. J., Qi, D. K., & Wang, Q. Y. (2018). Electron beam welding of Nimonic 80A: Integrity and microstructure evaluation. *Vacuum*, *151*, 266–274. https://doi.org/10.1016/J.VACUUM.2018.01.021

Zhang, H., Qin, W., Man, C., Cui, H., Kong, D., Cui, Z., Wang, X., & Dong, C. (2022). Effect of heat treatment on microstructure and corrosion behavior of Ti6Al4V fabricated by laser beam powder bed fusion. *Corrosion Science*, *209*, 110789. https://doi.org/10.1016/J.CORSCI.2022.110789

Zhang, J., Zhao, J., Hu, K., Gao, Q., & Zhan, X. (2022). Improving intermetallic compounds inhomogeneity of Ti/Al butt joints by dual laser-beam bilateral synchronous welding-brazing. *Optics & Laser Technology*, *146*, 107533. https://doi.org/10.1016/J.OPTLASTEC.2021.107533

Zhang, W. D., Liu, Y., Wu, H., Lan, X. D., Qiu, J., Hu, T., & Tang, H. P. (2016). Room temperature creep behavior of Ti–Nb–Ta–Zr–O alloy. *Materials Characterization*, *118*, 29–36. https://doi.org/10.1016/J.MATCHAR.2016.05.001

Zhang, Y., Bi, Y. B., Zhou, J. P., Sun, D. Q., & Gu, X. Y. (2020). Butt laser welding of TC4 Titanium alloy and 304 stainless steel with Ag-base filler metal based on a hybrid connection mechanism. *Optics & Laser Technology*, *124*, 105957. https://doi.org/10.1016/J.OPTLASTEC.2019.105957

Zhang, Y., Bi, Y. B., Zhou, J. P., Sun, D. Q., & Li, H. M. (2021). Weldability and machinability of the dissimilar joints of Ti alloy and stainless steel-A review. *International Journal of Materials Research*, *112*(10), 826–847. https://doi.org/10.1515/IJMR-2020-8165/XML

Zhang, Y., Huang, J., Ye, Z., & Cheng, Z. (2017). An investigation on butt joints of Ti6Al4V and 5A06 using MIG/TIG double-side arc welding-brazing. *Journal of Manufacturing Processes*, *27*, 221–225. https://doi.org/10.1016/J.JMAPRO.2017.05.010

Zhang, Z., Huang, J., Dai, Y., Zhang, X., & Yao, C. (2021). Effect of tungsten mesh interlayer on microstructure and mechanical performance of A6061/Ti6Al4V dissimilar joints. *Materials Characterization*, *182*, 111569. https://doi.org/10.1016/J.MATCHAR.2021.111569

Zhang, Z., Huang, J., Fu, J., Nie, P., & Zhang, S. (2022). Microstructure and mechanical properties of laser welded-brazed titanium/aluminum joints assisted by titanium mesh interlayer. *Journal of Materials Processing Technology*, *302*, 117502. https://doi.org/10.1016/J.JMATPROTEC.2022.117502

Zhao, J., Jiang, P., Geng, S., Wang, Y., & Xu, B. (2023). Effect of pulsed laser pretreatment induced pit-structure on the formation of intermetallic compounds in titanium-aluminum dissimilar welded joints. *Optics & Laser Technology*, *167*, 109589. https://doi.org/10.1016/J.OPTLASTEC.2023.109589

Zhao, S., Jing, Y., Liu, T., Zhao, W., & Li, F. (2024). Corrosion behavior and mechanism of carbon steel in industrial circulating cooling water system operated by electrochemical descaling technology. *Journal of Cleaner Production*, *434*, 139817. https://doi.org/10.1016/J.JCLEPRO.2023.139817

Zheng, M., Yang, J., Xu, J., Jiang, J., Zhang, H., Oliveira, J. P., Lv, X., Xue, J., & Li, Z. (2023). Interfacial microstructure and strengthening mechanism of dissimilar laser al/steel joint via a porous high entropy alloy coating. *Journal of Materials Research and Technology*, *23*, 3997–4011. https://doi.org/10.1016/J.JMRT.2023.02.040

Zhou, J., Zhou, D., & Liu, J. (2021). Numerical and experimental investigation of magnesium/aluminum laser welding with magnetic field. *International Journal of Advanced Manufacturing Technology*, *116*(1–2), 545–559. https://doi.org/10.1007/S00170-021-07483-8/FIGURES/16

Zhou, X., Duan, J., Zhang, F., & Zhong, S. (2019). The Study on Mechanical Strength of Titanium-Aluminum Dissimilar Butt Joints by Laser Welding-Brazing Process. *Materials 2019, Vol. 12, Page 712*, *12*(5), 712. https://doi.org/10.3390/MA12050712

Zhu, Z., Wang, W., Li, Y., & Chen, H. (2019). Effect of laser-arc offset and laser-deviation angle on the control of a Ti-Al interlayer. *Journal of Materials Processing Technology*, *271*, 336–345. https://doi.org/10.1016/J.JMATPROTEC.2019.04.010